AFIT/DS/ENG/98-01

MICROELECTROMECHANICAL OPTICAL BEAM STEERING SYSTEMS

DISSERTATION

David M. Burns, Major, USAF

AFIT/DS/ENG/98-01

AFIT/DS/ENG/98-01

MICROELECTROMECHANICAL OPTICAL BEAM STEERING SYSTEMS

DISSERTATION

Presented to the Faculty of the Graduate School of Engineering

of the Air Force Institute of Technology

Air University in Partial Fulfillment of the

Requirements for the Degree of

Doctor of Philosophy

David M. Burns, B.S.E.E., M.S.E.E.,
Major, USAF

December 1997

AFIT/DS/ENG/98-01

MICROELECTROMECHANICAL OPTICAL BEAM STEERING SYSTEMS

David M. Burns, B.S.E.E., M.S.E.E., Major, USAF

Approved:

Victor M. Bright, Ph.D. (Chairman)
AFIT Department of Electrical and Computer Engineering — 12-11-97 Date

Byron M. Welsh, Ph.D.
AFIT Department of Electrical and Computer Engineering — 12-11-97 Date

Jeffrey W. Grantham, Ph.D., Major, USAF
AFIT Department of Engineering Physics — 11 Dec 97 Date

Edward A. Watson, Ph.D.
Air Force Research Laboratory, AFRL/AAJT — 11 Dec 97 Date

Steven C. Gustafson, Ph.D.
University of Dayton Research Institute — 11 Dec 97 Date

Glen P. Perram, Ph.D., Lt Col, USAF (Dean's Representative)
AFIT Department of Engineering Physics — 15 Dec 97 Date

Accepted:

Robert A. Calico, Jr.
Dean, Graduate School of Engineering

Acknowledgements

Many people contributed to the success of this dissertation. My sponsors: Dr. Jeff Grantham, Dr. Ed Watson, and Dr. Steve Gustafson, made this research possible. I would not have been able to fabricate the many micromachined dies without their funding. Their support also provided laboratory equipment and enabled me to present papers at four national and two international conferences (Nagoya, Japan and Heidelburg, Germany). Many of the ideas presented in this dissertation resulted from discussing topics at these conferences with fellow researchers. Thanks to Dr. Byron Welsh for directing me into optical MEMS research.

Dr. Victor Bright could not have been a better advisor. Dr. Bright gave encouragement and support as well as the freedom to pursue the development of novel devices. I was never burdened with unnecessary tasks or irrelevant research. Dr. Bright also provided a "push to publish" that generated many ideas and ultimately made the MEMS community aware of our research. Publishing made this research both successful and available to other researchers.

Charlie Powers and Bill Trop provided direct assistance throughout this research. Charlie and Bill are dedicated professionals who always found a way to get the job done. The quality of education at AFIT would be greatly diminished if these individuals were not here.

Thanks to my fellow researchers for their ideas and support. Special thanks to Dr. John Comtois for his legacy at AFIT. Many of my ideas began with the simple, yet proven, microelectromechanical building blocks that he left in our databases. I cannot imagine how difficult it would have been for me to build a micromotor or a micromirror if our toolboxes had been empty.

My dear wife, Cheryl Ann, provided constant assistance. She spent countless hours proof-reading papers, watching the kids when I worked weekends and nights, finding money for extra textbooks and computer equipment, and providing encouragement. Getting a doctorate in electrical engineering has been a specific goal of mine since I first attended high school; it would not have been possible without Cheryl. Thanks to my kids – Alex, Eric, Rachel, and Leah – for letting me stay inside and use the computer. I hope that now we can play the games that I was too busy to play before.

David M. Burns

Table of Contents

List of Figures

List of Tables

Abstract

The development of microelectromechanical systems (MEMS) has matured to the point where the fabrication of micron-sized devices is feasible. State-of-the-art MEMS construction processes now support the fabrication of novel optical devices that could not previously be built. This dissertation reports on the development of innovative micro-optical devices such as Variable Blaze Gratings (VBGs) using state-of-the-art MEMS construction processes. The principle application of the micro-optical devices described in this dissertation is steering optical beams; however other applications such as spectral analysis are identified. Specific optical beam steering systems developed and characterized in this work include: optical phased arrays, VBGs, decentered microlens arrays, and integrated Vertical Cavity Surface Emitting Laser (VCSEL) micromirror systems. Optical power induced damage to micromachined mirrors is also modeled and tested. In addition a number of new MEMS devices were created during this research including: double hot arm thermal actuators, optical hybrid devices such as variable blaze phased arrays and focusing micromirrors, and nonlinear flexures. Extensive Fourier analysis and optical testing of the micro-optical devices was used to verify device operation.

1 Introduction

This chapter presents the objectives of the author's research, the organization of this dissertation, and answers the questions:

What are Microelectromechanical Systems (MEMS)?

Why use MEMS for optical beam steering?

Why conduct this research at AFIT?

This chapter is organized into four sections. Section 1.1 addresses the questions listed above. Section 1.2 contains the objectives of the author's research. Section 1.3 defines the organization of this dissertation. Section 1.4 lists the author's publications relevant to this work.

1.1 Preliminary Questions

1.1.1 What Are Microelectromechanical Systems (MEMS)?

MEMS are electrical, mechanical, and optical systems designed and fabricated with dimensions measured in millimeters, microns, or even nanometers. MEMS were first postulated by Nobel Prize Laureate R. P. Feynman in 1959 [1]. The development and production of MEMS has increased dramatically in the last ten years; this increase is primarily due to the application of mature integrated circuit manufacturing processes to the construction of MEMS [2]. MEMS designers have been able to apply the manufacturing technology research aimed at reducing the size and cost of integrated circuits directly to the fabrication of MEMS. Making "dual use" of integrated circuit manufacturing research has enabled companies such as Ford Microelectronics Inc. to develop and field MEMS applications at a relatively low cost.

Figure 1.1 is a picture of an automotive microelectromechanical accelerometer and control circuitry developed by Ford Microelectronics Inc. to detect collisions and determine when to deploy airbags. If the

airbag deployment sensor is accelerated, then the capacitance of the collision detection microstructure will increase. If the capacitance value exceeds a threshold value (set in read-only memory on the interface and deployment decision circuit die), then the interface and deployment decision circuit die will output a control signal to activate the automobile's airbags [3]. This device is packaged in an integrated circuit Dual In-line Package (DIP) and is on every new Ford Taurus automobile in North America. Ford would not have fielded this technology if the only benefits were cost and weight; a few inadvertent airbag deployments could easily result in multi-million dollar lawsuits. It was the combination of cost, weight, and reliability that convinced Ford to field the MEMS airbag deployment sensor.

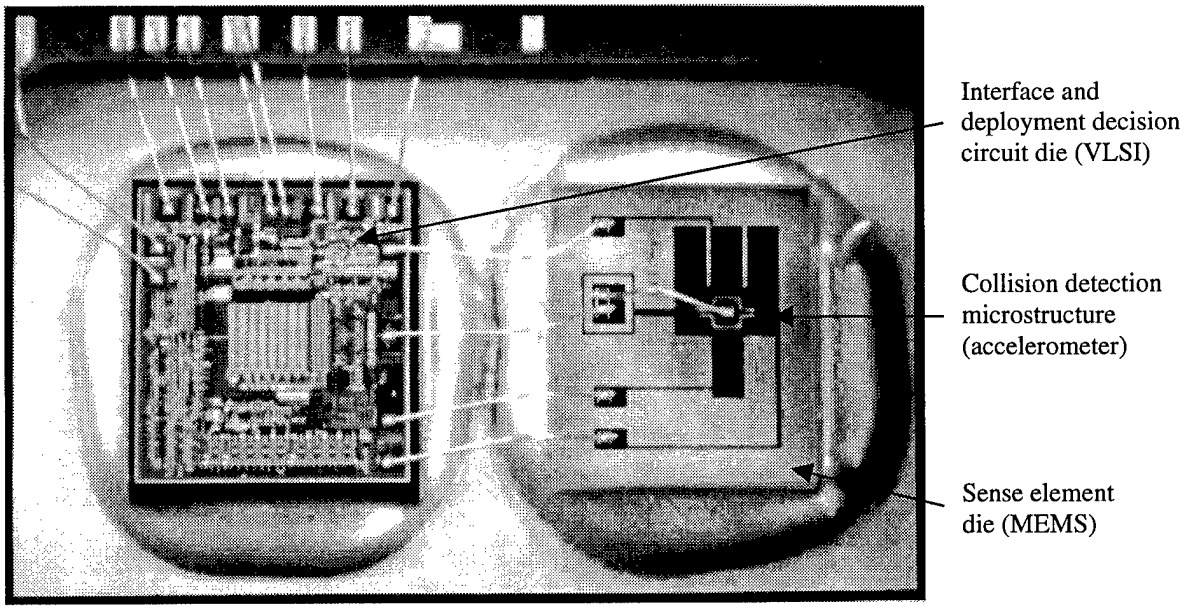

Figure 1.1. Close-up view of the Ford MEMS airbag deployment sensor [3].

1.1.2 Why Use MEMS for Optical Beam Steering?

MEMS have many advantages over traditional macro-systems. Because many MEMS fabrication techniques were borrowed from the semiconductor industry, MEMS typically have low unit cost, low power consumption, high yield, improved operational performance, and excellent reliability. Figure 1.2 is a comparison of a conventional Inertial Navigation Unit (INU) with an equivalent microelectromechanical INU. Table 1.1 compares the two devices shown in Figure 1.2.

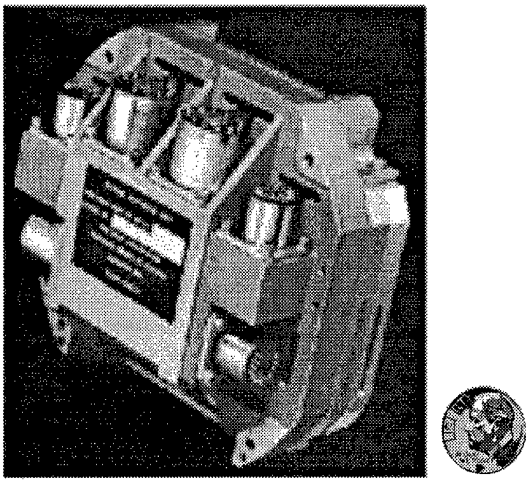

(a) Conventional

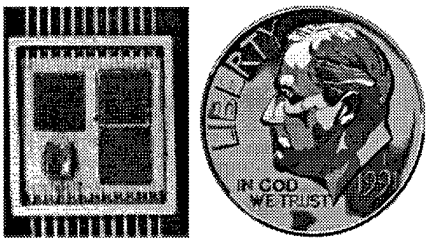

(b) MEMS

Figure 1.2. Comparison of inertial navigation units fabricated using (a) conventional and (b) MEMS manufacturing techniques. A dime is shown next to both devices for size comparison [4].

Table 1.1. Comparision of Conventional and MEMS INUs [4].

	Conventional INU	MEMS INU
Mass	1587.5 grams	10 grams
Size	15 cm × 8 cm × 5 cm	2 cm × 2 cm × 0.5 cm
Power	35 W	~ 1 mW
Survivability	35 g's	100K g's
Cost	$20,000	$500

Conventional optical beam steering systems are often expensive in terms of cost, weight, and power. Using MEMS for optical beam steering can reduce production and maintenance costs, decrease weight and power requirements, and improve system performance. In some cases MEMS are the only possible solutions; the application may simply not have enough room for traditional components. New applications for optical beam steering on Air Force platforms may be created by the use of MEMS. For example a "smart" aircraft

counter-measure flare could be developed that would use MEMS optical beam steering to direct the optical radiance emitted by the flare's energy source towards an adversary's optical detectors. Because flares must be small and expendable, a MEMS optical beam steering system is the only viable solution (in terms of cost, size, weight, and power) for this application.

1.1.3 Why Conduct This Research at AFIT?

Microelectromechanical optical beam steering has many potential Air Force applications. MEMS-based laser scanning could be used for producing small airborne laser imaging systems; these systems could guide low cost, highly accurate munitions or unmanned aerial vehicles. A MEMS-based laser scanning system on an aircraft's skin could be used to blind thermally guided enemy air-to-air missiles attacking the host air vehicle. Another application of MEMS-based optical beam steering is the Holographic Data Storage Initiative (HDSI). The HDSI project may dramatically improve the computer memory capacities of future airborne platforms (see Chapter 5 for a complete description of HDSI). The key benefits of MEMS (cost, weight, performance, reliability, and power) are perhaps more critical to the development of aerospace platforms than any other application.

Research at AFIT directly supports Air Force requirements so AFIT is a logical choice for the investigation of MEMS-based optical beam steering systems. More importantly AFIT is the only organization doing basic research in a number of fields within MEMS-based optical beam steering. For example Variable Blaze Gratings (VBGs) developed by the author are the only proven MEMS device suitable for steering large aperture (10 cm or more) optical beams. A VBG could be constructed using an entire semiconductor wafer; a large aperture could steer high power optical beams (100 watts or more).

Research at AFIT is also cost-effective. A portion of the research conducted by the author (in support of the HDSI project) was sponsored by the University of Dayton Research Institute. By using civilian funding, the author was able to more thoroughly investigate MEMS-based optical beam steering systems at no additional cost to the Air Force. AFIT is well equipped for conducting research into MEMS-based optical beam steering (see Appendix C). Most of this equipment was at AFIT at the beginning of the author's research. As a result, less Air Force funding was required to support this research.

In addition to the three questions answered in this section, the reader may have more questions such as:

What accomplishments did the author make in his research?

What are the Air Force applications for this research?

These questions are specifically answered in Chapter 10.

1.2 Research Objectives

The author's research objectives were first documented on page 73 of his dissertation research prospectus: *Microelectromechanical Optical Beam Steering Systems Design and Performance* approved on August 29, 1996. The author's research objectives are given in Table 1.2. Although the author investigated a wide variety of MEMS-based optical beam steering systems, his research was primarily focused on the topics in Table 1.2.

The author was part of a team conducting research on the last topic in Table 1.2; Captain Joseph Bouchard directed his Master's degree research towards developing an integrated semiconductor laser beam steering system. The author developed a number of microdevices for the integrated semiconductor laser beam steering project; these microdevices are presented in Chapter 9 of this dissertation. A complete description of the author's and Captain Bouchard's research on the integrated semiconductor laser beam steering project can be found in Captain Bouchard's Master's degree thesis [5].

1.3 Research Organization

This dissertation is organized into ten chapters. The first chapter is an introduction to the author's research. Chapter 2 is a review of a wide variety of MEMS constructed both in industry and at universities. The objective of Chapter 2 is to provide a background for the reader on the current state-of-the-art in MEMS. Chapter 2 also introduces the principle methods for constructing MEMS devices and defines surface micromachining, bulk micromachining, and micromachining using X-ray lithography and electroplating (known by the German acronym: LIGA).

Table 1.2. Research Objectives.

	Topic
1.	Investigate microelectromechanical optical beam steering for the HDSI project.
2.	Investigate microelectromechanical optical beam steering using variable blaze gratings.
3.	Investigate microelectromechanical optical beam steering using decentered microlens arrays.
4.	Determine the maximum optical power rating for a microelectromechanical optical beam steering system.
5.	Investigate microelectromechanical optical beam steering using an integrated semiconductor laser.

Chapter 3 discusses the Multi-User MEMS Processes (MUMPs) initially sponsored by the Defense Advanced Research Projects Agency (DARPA) [6]. MUMPs became self-supporting in March 1997. MUMPs is an affordable surface micromachining process with a regularly scheduled production run every other month. The author used MUMPs to construct the majority of his MEMS-based optical beam steering systems. Chapter 3 also includes a discussion of a number of design techniques pioneered by the author for MUMPs. Many of these techniques were published by the author separate from this dissertation and are available to other users of MUMPs.

Chapter 4 contains all the theory and modeling used by the author in his research, except for optical power modeling. Optical power modeling is presented separately in Chapter 8. Chapter 4 is intended to be a reference for the reader and addresses optical beam steering theory using the systems listed in Table 1.2. Chapter 4 includes formulas for calculating the deflection of electrostatically actuated micromirrors. Chapter 4 also includes optical modeling using Fast Fourier Transform (FFT) based software and mechanical modeling using stand-alone programs.

Chapters 5, 6, 7, and 8 present the author's research into the first four topics in Table 1.2, respectively. Chapter 5 addresses optical beam steering for the HDSI project. Chapter 6 addresses optical beam steering using variable blaze gratings. Chapter 7 addresses optical beam steering using decentered microlens arrays. Chapter 8 addresses optical power induced damage to micromirrors. Each of these chapters is independent of the others; however all four chapters depend on the theory and modeling presented in Chapter 4.

Chapter 9 is a review of the other microelectromechanical devices developed by the author as part of this research. Devices developed by the author to support the fifth topic in Table 1.2 (optical beam steering using an integrated semiconductor laser) are presented in Chapter 9. Many other devices created by the author as part of his research have applications beyond optical beam steering; these other devices (such as double hot arm thermal actuators and nonlinear flexures) are detailed in Chapter 9. Chapter 10 summarizes the author's research accomplishments and offers research areas for further investigation. Chapter 10 also discusses potential Air Force applications for the author's research.

1.4 Author's Publications Relevant to This Dissertation

1. D. M. Burns and V. M. Bright, "Micro-electro-mechanical variable blaze gratings," *IEEE MEMS-97 Workshop*, Nagoya Japan, pp. 55-60, January 26, 1997.
2. D. M. Burns and V. M. Bright, "Designs to improve polysilicon micromirror surface topology," *Proc. SPIE*, San Jose, CA, vol. 3008, pp. 100-110, February 10, 1997.
3. D. M. Burns and V. M. Bright, "Investigation of the maximum optical power rating for a micro-electro-mechanical device," *Digest of Technical Papers, 1997 International Conference on Solid-State Sensors and Actuators (Transducers-97)*, Chicago, IL, vol. 1, pp. 335-338, June 16, 1997.
4. D. M. Burns, V. M. Bright, S. C. Gustafson, and E. A. Watson, "Optical beam steering using surface micromachined gratings and optical phased arrays," *Proc. SPIE*, San Diego, CA, vol. 3131, pp. 99-110, July 30, 1997.
5. D. M. Burns and V. M. Bright, "Design and performance of a double hot arm polysilicon thermal actuator," *Proc. SPIE*, Austin, TX, vol. 3224, pp. 296-306, September 29, 1997.

6. D. M. Burns and V. M. Bright, "Nonlinear flexures for stable deflection of an electrostatically actuated micromirror," *Proc. SPIE*, Austin, TX, vol. 3226, pp. 125-136, September 29, 1997.
7. D. M. Burns and V. M. Bright, "Development of microelectromechanical variable blaze gratings," to be published in *Sensors and Actuators (A: Physical)*, vol. 64, no. 1, January 1998.
8. V. M. Bright, J. T. Butler, W. D. Cowan, D. M. Burns, and J. R. Reid, "Automated assembly of micro-electro-mechanical systems," to be published in *The International Journal of Advanced Manufacturing Systems*.
9. J. G. Bouchard, V. M. Bright, and D. M. Burns, "Techniques and applications for integrating a semiconductor laser on a surface micromachined die," to be published in *Proc. SPIE*, vol. 3289, San Jose, CA, January 26, 1998.
10. D. M. Burns and V. M. Bright, "Micro-electro-mechanical focusing mirrors," to be published in *IEEE MEMS-98 Workshop*, Heidelburg, Germany, January 25, 1998.
11. D. M. Burns and V. M. Bright, "Optical power induced damage to microelectromechanical mirrors," to be published in *Sensors and Actuators (A: Physical)*, estimated date of publication is June, 1998.

Table 1.3 relates the author's publications to the author's research areas. Often a published paper would present investigation results into several of the author's research topics; for example the paper "Designs to improve polysilicon micromirror surface topology" (publication # 2) addressed design techniques used in all areas of the author's research.

Table 1.3. Cross-reference of the Author's Publications with the Author's Research Topics.

Publication Number	Research Topics (from Table 1.2)				
	1 HDSI Project	2 VBGs	3 Microlens	4 Optical Power	5 Integrated laser
1		×			
2	×	×	×	×	×
3				×	
4	×	×			
5					×
6	×	×			
7		×			
8	×				
9			×		×
10			×		×
11				×	

1.5 References

[1] R. P. Feynman, "There's plenty of room at the bottom," *Journal of Microelectromechanical Systems*, vol. 1, no. 1, pp. 60-66, March 1992.

[2] J. W. Gardner, *Microsensors: Principles and Applications*, Chichester: John Wiley & Sons Ltd., 1994.

[3] L. C. Spangler and C. J. Kemp, "ISAAC: integrated silicon automotive accelerometer," *Sensors and Actuators (A: Physical)*, vol. 54, pp. 523-529, 1996.

[4] K. Gabriel, "Microelectromechanical systems program: summary of research activities," *Defense Advanced Research Projects Agency*, July 1994.

[5] J. G. Bouchard, "Microelectromechanical scanner using a vertical cavity surface emitting laser," *Master's Thesis*, Air Force Institute of Technology, Wright-Patterson AFB, OH, AFIT/GCS/ENG/97D-04, December 1997.

[6] D. Koester, R. Majedevan, A. Shishkoff, and K. Marcus, *Multi-User MEMS Processes (MUMPs) Introduction and Design Rules*, rev. 4, July 15, 1996, MCNC MEMS Technology Applications Center, Research Triangle Park, NC, 27709.

2 Microelectromechanical Systems

This chapter presents the state-of-the-art in MEMS. The first section describes the basic fabrication techniques currently used to construct MEMS. The second section reviews state-of-the-art optical MEMS devices and their applications.

2.1 MEMS Fabrication Techniques

Fabrication of MEMS devices typically starts with a bare silicon wafer. Several basic processes are then invoked to fabricate microelectromechanical devices. Bulk micromachining uses etchants sensitive to the orientation of the crystal lattice to remove bulk regions of the silicon until the desired MEMS device is left etched in the wafer. This process is similar to the carving of a sculpture by a stone mason – the mason removes all the stone that is not part of the sculpture and only the work of art is left. Silicon fusion bonding uses fused bulk micromachined wafers to form a MEMS device with multiple layers. Surface micromachined MEMS are constructed from thin films deposited on the surface of the wafer. The films are then selectively etched to form a MEMS device. LIGA can be used to create a thick (100 μm or more) layer of metal on the wafer. A combination of these micromachining processes is possible, and can be used to exploit the strengths of each. These processes are discussed in detail in the next few sections.

2.1.1 Bulk Micromachining

Bulk micromachining uses chemical etchants to remove volumes of the single-crystal silicon wafer, leaving the desired MEMS device. The removal of bulk silicon is controlled by masking the surface of the wafer with etchant-resistive masks. Then an anisotropic etchant that is sensitive to crystal plane orientation is used to remove the unwanted silicon. The speed and crystal plane sensitivity of the etching process often depend on dopant concentration in the wafer and etching conditions such as temperature, etchant concentration, and duration [1].

The Miller indices indicate the orientation of the crystal plane in the wafer as shown in Figure 2.1. The (100) direction is perpendicular to the (100) plane. The (100) direction is the x-axis in Figure 2.1. In general the etch rates of an anisotropic etchant are faster in the (100) and (110) directions than the (111) direction. The selectivity of an etchant is the ratio of the etch rate in the desired direction to the etch rate in an undesired direction. For an isotropic etchant, the selectivity is always unity. For anisotropic etchants such as potassium hydroxide (KOH), the etching selectivity of the (110) plane over the (111) plane can be as high as 500 [1].

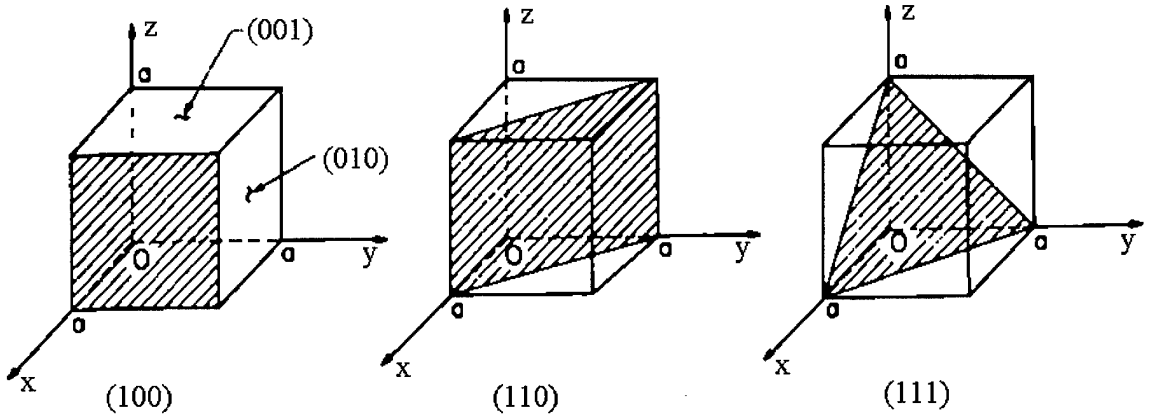

Figure 2.1. Miller indices of some important planes in a cubic crystal [2].

Some etchants are also sensitive to the presence of dopants in the crystal lattice. For example in Ethylene Diamine, Pyrocatechol and water (EDP) etchant, the removal of silicon doped with boron at a level of 3×10^{19} atoms/cm^3 occurs at half the rate of the undoped silicon [1]. The etching process can be controlled by making highly doped etch stops in the bulk region that exploit this sensitivity. Figure 2.2 shows an etch stop controlled bulk micromachining process. The boron doped region on the bottom of the wafer is resistant to the etchant and is not removed. The trench on the left of Figure 2.2 does not have an etch stop and continues to grow until a hole is made in the wafer. The V-shaped trench on the right side of the wafer is formed in an anisotropic etchant because the bottom of the trench is in the (100) direction and the sides of the trench are in the (111) orientation. This configuration results in the sides of the trench being removed very slowly compared

to the bottom of the trench. Etching continues until the trench is V-shaped and no surface in the (100) direction remains in the trench. At this time, the trench almost stops growing for a highly selective etchant.

Silicon nitride is easily grown by low pressure chemical vapor deposition (LPCVD) and is very resistant to both EDP and KOH. It is often used to mask the surface of the wafer so the etching process removes only exposed silicon. Silicon oxide can also be used to mask portions of the wafer surface; however it is not as resistant as silicon nitride to most etchants [1].

Silicon fusion can be used to join bulk etched wafers. Fusion joins two or more wafers in a permanent bond. The fusion occurs when the wafers are cleaned and pressed together. Because the wafers are flat, clean, and have similar microscopic structure, Van der Waals forces hold them in position prior to placement in the furnace. When the wafers are heated to temperatures up to 1000° C, they fuse in a bond that is as strong as each of the wafers [1,3].

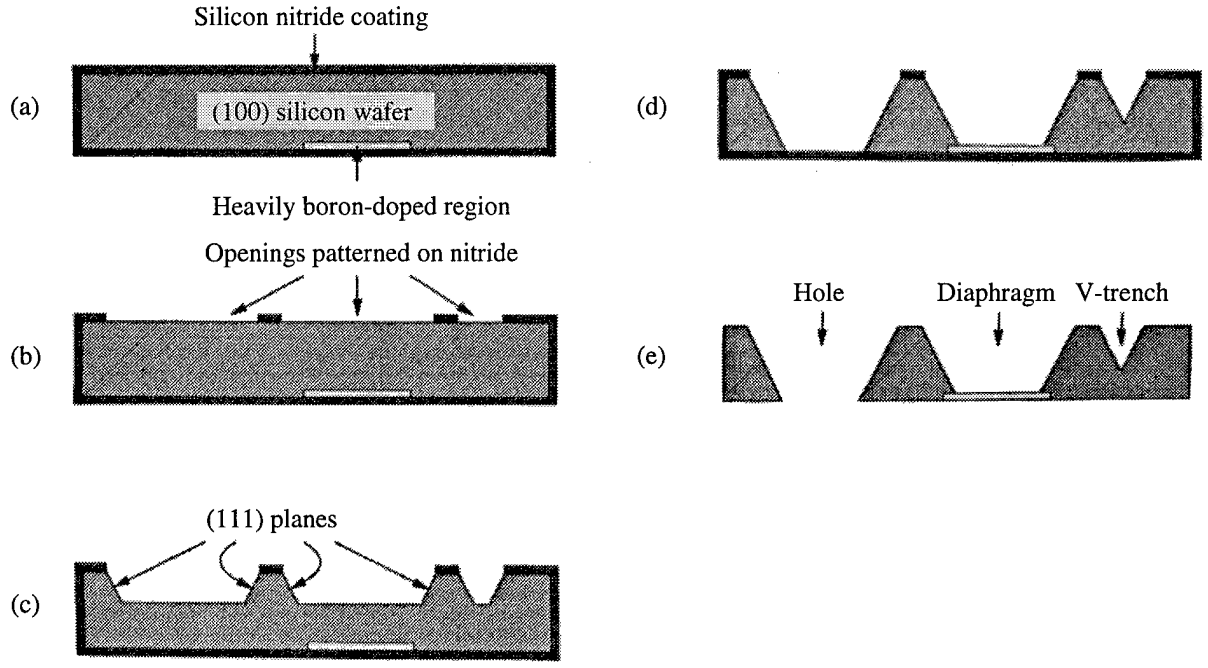

Figure 2.2. Bulk etching of a wafer with an etch stop [1].

An example of a MEMS device constructed with fusion bonding is the micropump illustrated in Figure 2.3. Four wafers were patterned using bulk micromachining and fused. The bottom two wafers are identical; one of the wafers was inverted after fabrication. The top wafer, referred to as the counter-electrode in the diagram, was electrically isolated from the other wafers by a thin layer of pyrex glass. This isolation allows a voltage to be placed between the top wafer and the other three wafers. If 150 volts is applied to the micropump, the pump diaphragm will be pulled to the counter-electrode by electrostatic attraction. This action will pull in fluid through the inlet valve. The diaphragm returns to its original position when the voltage returns to zero, pumping the fluid out the outlet valve [4]. Because the actuation mechanism relies on electrostatic force, the device consumes virtually no current.

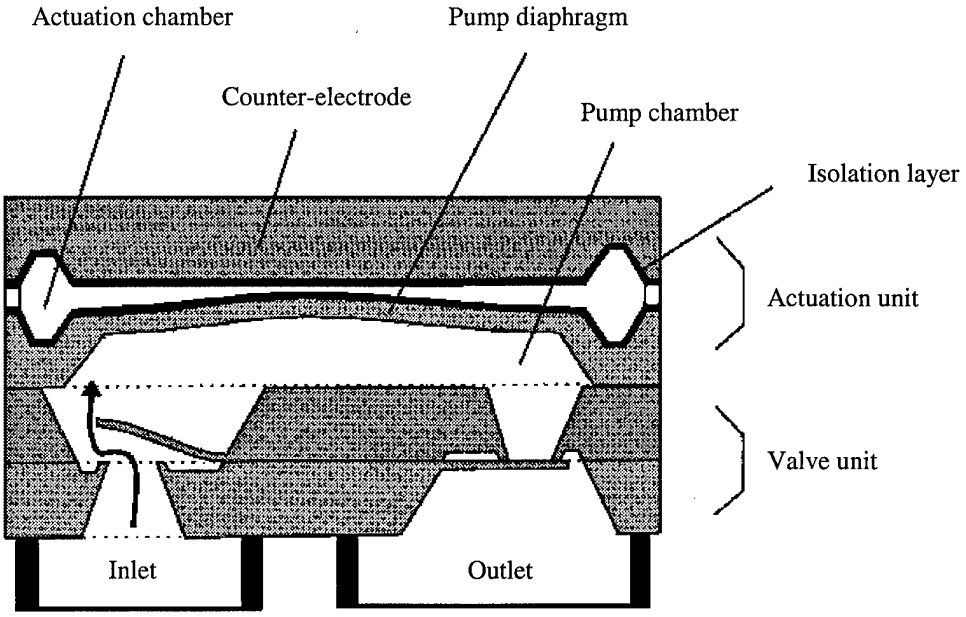

Figure 2.3. Micropump formed by bulk micromachining and silicon fusion bonding [4].

2.1.2 Surface Micromachining

Surface micromachined devices are constructed from thin films deposited on the surface of the wafer. The films are then selectively etched to form a MEMS device. Sacrificial layers of phosphosilicate glass (PSG)

are often used to isolate adjacent polycrystalline silicon (polysilicon) film layers. Phosphosilicate glass is silicon oxide doped with phosphorous. The PSG layers are removed at the end of device fabrication, creating device components from the polysilicon layers. The thickness and patterning of the films can be controlled to finer tolerances than typically possible in bulk micromachining, making surface micromachining the preferred technique for the fabrication of the smallest MEMS devices. Figure 2.4 is a diagram of the process for manufacturing a flip-up micromirror. POLY-1 and POLY-2 are two separate polysilicon layers. Each layer (PSG and polysilicon) is patterned before the next layer is added. The last step uses an isotropic etchant such as hydrofluoric acid to remove all sacrificial PSG layers, which "releases" the movable portion of the device [5].

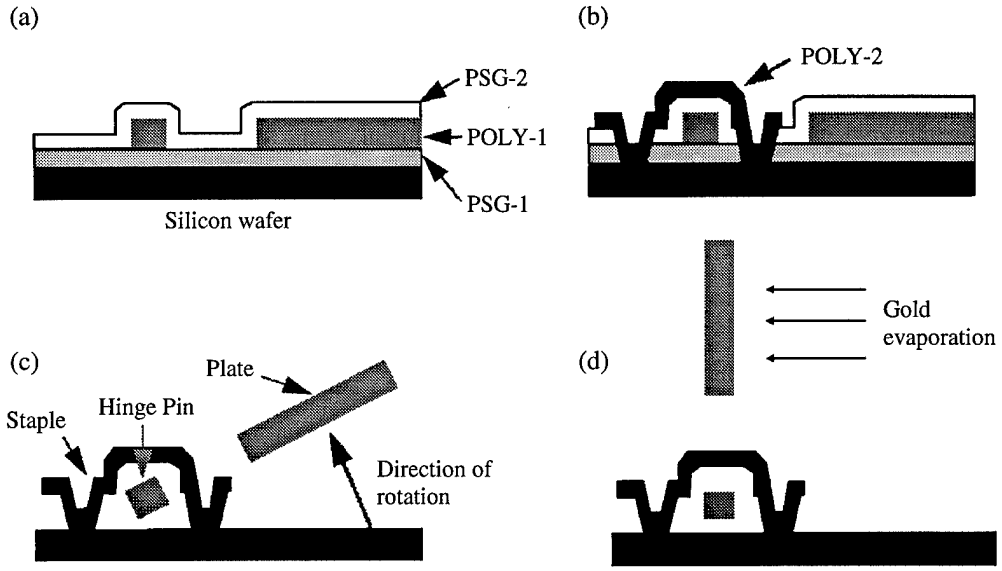

Figure 2.4. Construction process for manufacturing a flip-up micromirror [5].

There are several surface micromachining fabrication facilities. The processes used by each are similar, differing only in the number of releasable layers, thickness of each layer, and the materials used for each layer. This section briefly reviews the surface micromachining processes used at the University of California at Berkeley and Sandia National Laboratories at Albuquerque, New Mexico. An in-depth review of the Multi-User MEMS Processes (MUMPs) used at AFIT will be presented in Chapter 3.

The University of California at Berkeley uses four layers of polysilicon to create the micromirrors shown in the Scanning Electron Microscope (SEM) micrograph in Figure 2.5. Three of these layers are releasable because they are deposited over a sacrificial layer. The left mirror rotates on an axis parallel to the substrate and the right mirror rotates on an axis perpendicular to the substrate. The mirrors are both 300 μm × 500 μm in size and are electrostatically operated [6,7].

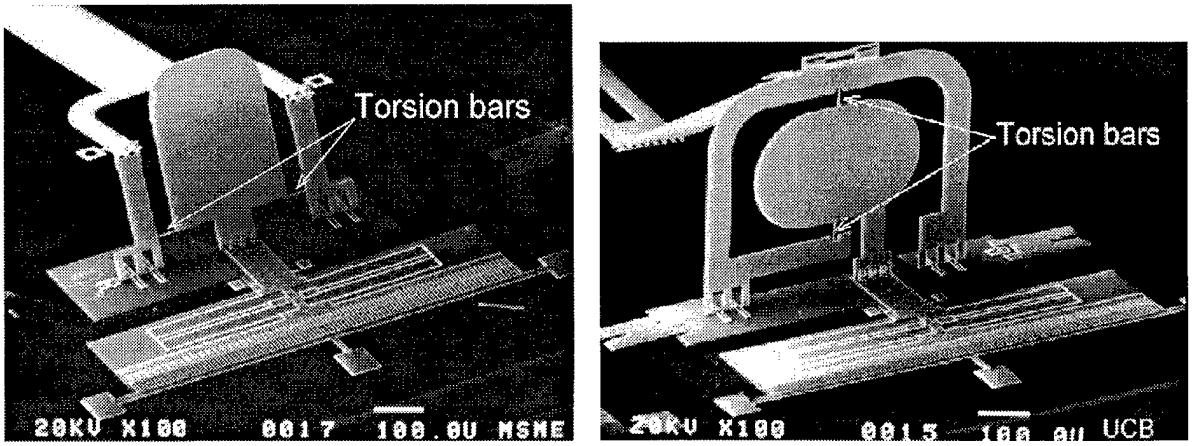

Figure 2.5. Two scanning micromirrors developed at the University of California, Berkeley [6].

The surface micromachining process at Sandia National Laboratories also uses three releasable layers of polysilicon. The key difference between the Berkeley and Sandia processes is that the Sandia process allows the integration of Complementary Metal-Oxide Semiconductor (CMOS) circuitry with MEMS using chemical-mechanical polishing (CMP) planarization. These hybrid MEMS devices are fabricated by using bulk etching to make a trench in the wafer and building a surface micromachined MEMS device in the trench. The MEMS device is then buried in a sacrificial layer of oxide and the wafer is planarized using CMP. The wafer then can be processed in a CMOS production line [8].

The electrostatically operated micromotor shown in Figure 2.6 was constructed using the Sandia process. The rectangular regions in the top and left of the image are electrostatic comb drives that pull an actuator arm around a gear, which turns the larger wheel. The large wheel in the lower right is an optical shutter rotated to open or close an optical path perpendicular to the substrate. Figure 2.7 is a close-up view of the actuator arm, and the linkages to the electrostatic comb drives [9].

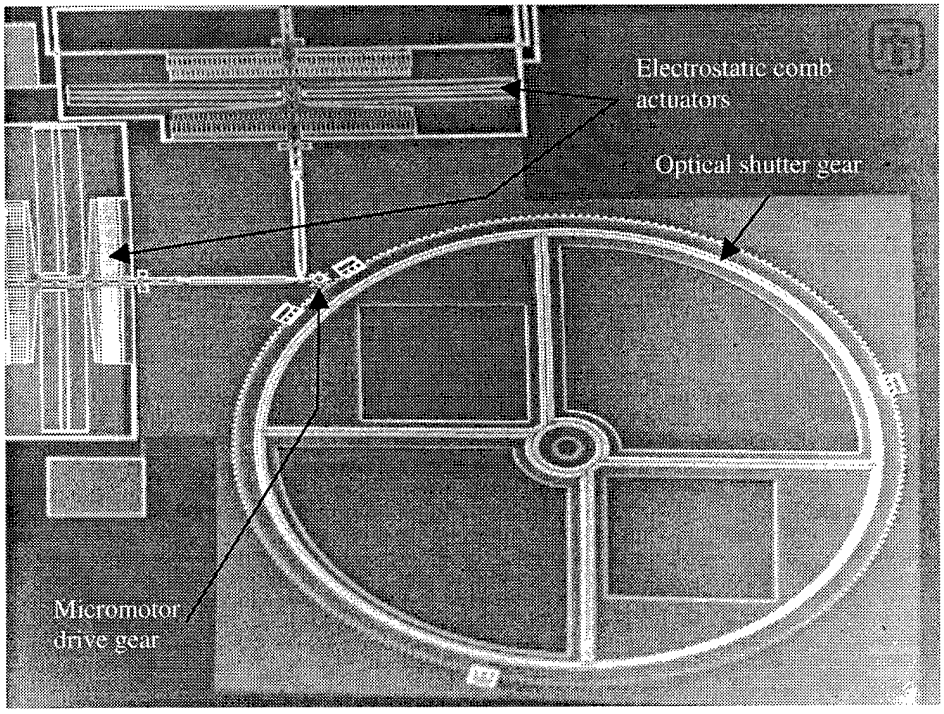

Figure 2.6. Scanning electron micrograph of the Sandia micromotor coupled to a 1600 μm optical shutter gear. This image was taken at an angle (optical shutter gear appears elliptical) [9].

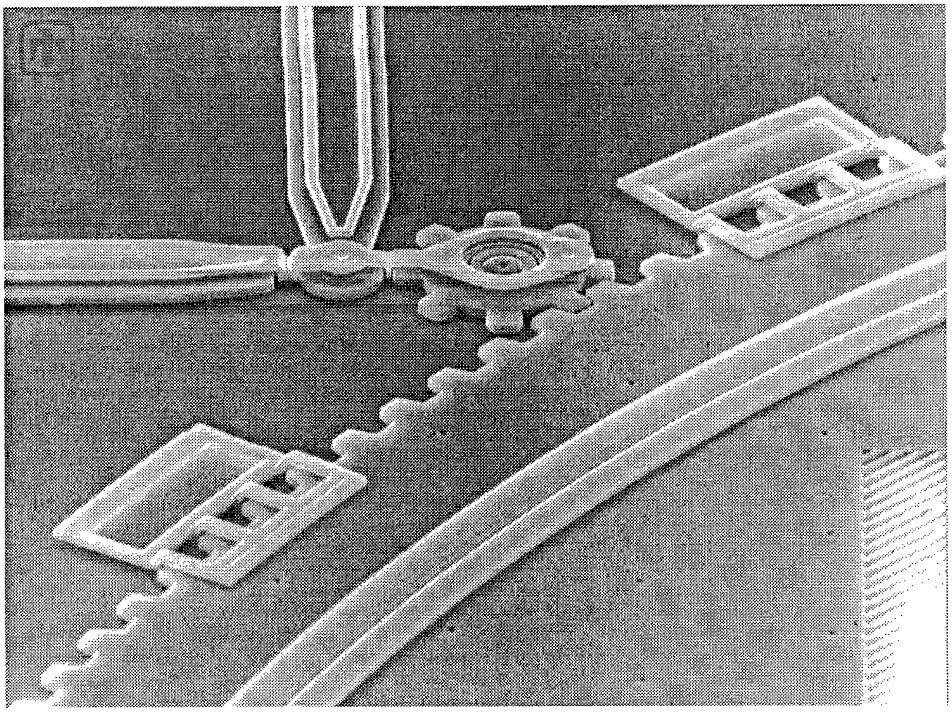

Figure 2.7. Scanning electron micrograph close-up of the Sandia micromotor drive gear in Figure 2.6. The micromotor drive gear has a diameter of 25 μm [9].

In surface micromachining, each layer conforms to the layer below it so the topology of the top layer grows may become more convoluted as additional layers are added to the process. This effect is illustrated for a stacked gear train in Figure 2.8. The gear on the top overlaps a portion of the gear on the bottom and is patterned by the shape of the bottom gear's teeth. This patterning can cause device malfunction; this particular MEMS device occasionally stuck in position when the depressions in the top gear fell into the teeth of the bottom gear.

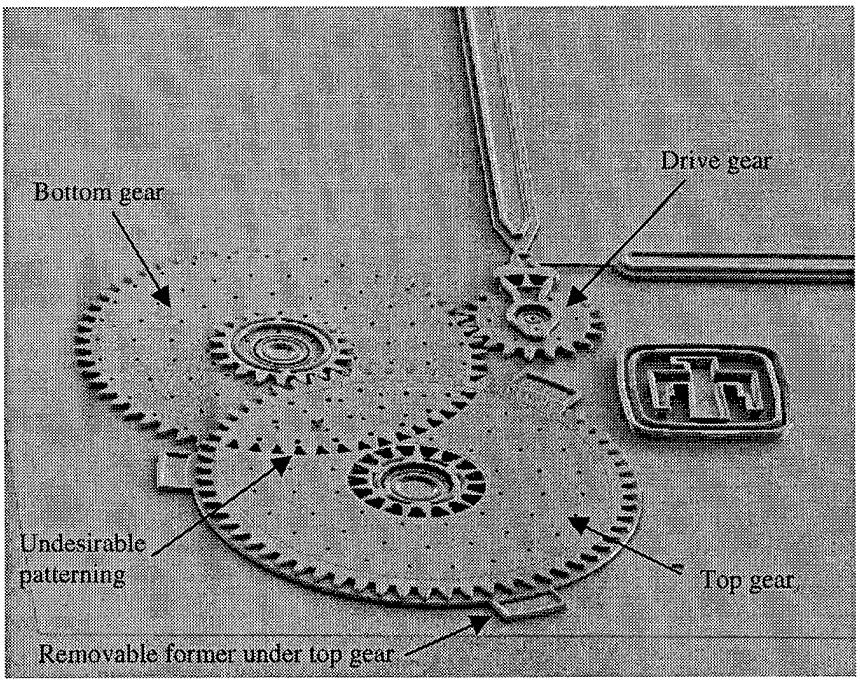

Figure 2.8. Scanning electron micrograph of a stacked gear train. The diameter of the micromotor drive gear is 50 μm [9].

2.1.3 LIGA

In the LIGA process, MEMS devices are realized from electroplated metal. This is a one metal layer process, so devices are often assembled manually using micromanipulators after the metal parts have been etched off the substrate. LIGA fabricated devices have straight, smooth walls and are very durable. Figure 2.9 is a collection of gears fabricated at the University of Wisconsin. The metal is a permalloy, approximately 78% nickel and 22% iron.

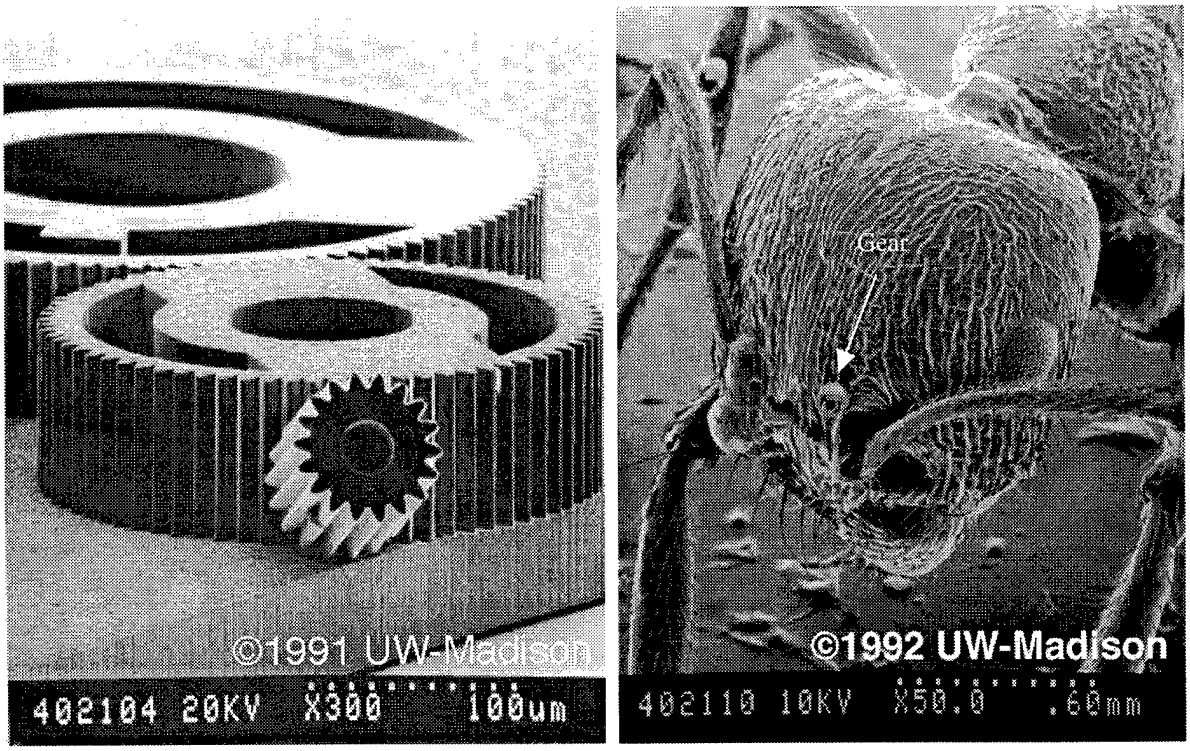

Figure 2.9. Gears fabricated using LIGA: (a) three 80 μm thick gears and (b) a 100 μm wide gear on the head of an ant [10].

LIGA uses a high energy X-ray source to pattern a thick layer of x-ray sensitive polymer. The x-ray synchrotron is expensive and may require exposures over several hours. If thinner layers (less than 50 μm) are acceptable to the system designer, conventional lithographic techniques using ultraviolet source may be used [1]. LIGA processing is commercially available through organizations such as the Microelectronics Center of North Carolina (MCNC) [11]. The principle advantage of LIGA is the capability to construct thick (100 μm or more) metal structures. A drawback to using LIGA is the restriction to a single layer. LIGA systems must be assembled by hand after the metal layer has been patterned.

LIGA processing can be combined with other micromachining processes. Figure 2.10 is a micromirror made at the California Institute of Technology using LIGA over a cavity formed by bulk micromachining. The micromirror operates with electromagnetic actuation; a strong (approximately 24,000 A/m) magnetic field forces the mirror up when a current is passed through the mirror in embedded electroplated copper wiring. Figure 2.10 shows the mirror in the flat state with no current applied (left picture) and deflected as a result of applying 30 mA to the copper wiring (right picture) [12].

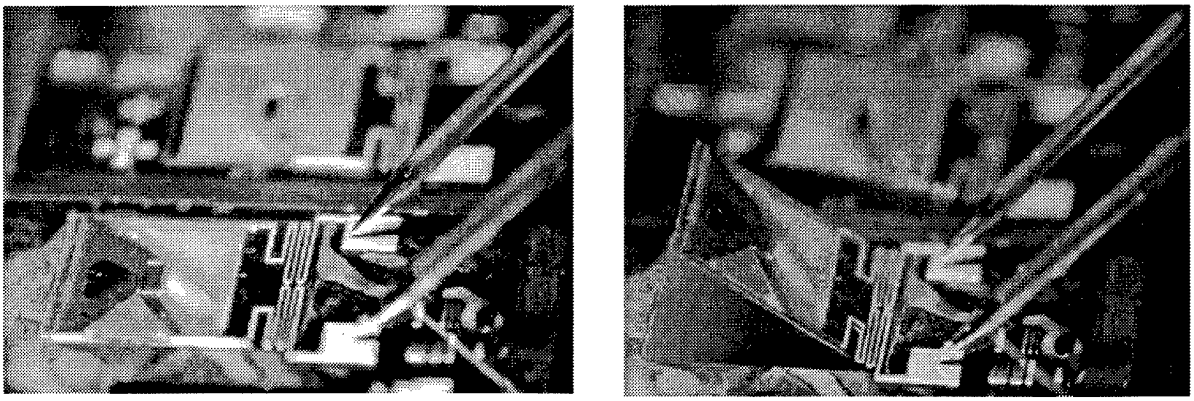

Figure 2.10. A micromirror fabricated with LIGA and bulk micromachining processes [12].

2.2 State-of-the-art Optical MEMS and Their Applications

Optical MEMS devices presented in this section are: Digital Mirror Display (DMD), tunable infrared filter, barcode scanner, Grating Light Valve (GLV), free space optical bench, fiber optical switch, and a micro-turbine-engine. Many of these devices rely on electrostatic actuation. Electrostatic actuation uses charge distributions not current flow so it is an excellent choice for high speed or low power applications.

2.2.1 Digital Mirror Display (DMD)

One of the most publicized micromirror designs under active development is an electrostatically tilted mirror from Texas Instruments, Inc. An array of these mirrors is used to reflect the light from a common source on to a display screen [13]. Each mirror controls the light for one pixel of the display. Figure 2.11 shows this MEMS device.

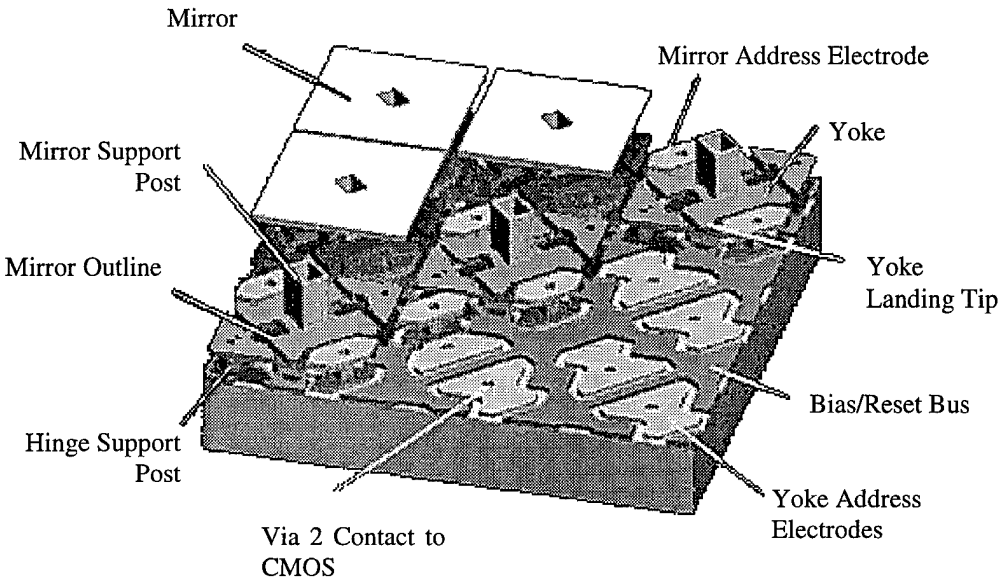

Figure 2.11. The Texas Instruments Digital Micromirror Device™ (DMD) [14].

The angle of the light source is off the optical axis perpendicular to the face of the mirror. The mirror operates by tilting to steer the incident light towards the display. Non-tilted mirrors reflect the incident light away from the display and on to an absorbing flat. This results in illuminated pixels caused by tilted mirrors and dark pixels caused by flat, or non-powered, mirrors. Addressing of individual pixels is controlled by CMOS circuitry on the substrate under the MEMS device. The steering angle of the incident light is constant; the duty cycle of the drive voltage controls the brightness of individual pixels. A color filter wheel in front of the light source determines the color of the pixel. Arrays of hundreds of thousands of micromirrors are currently under development.

2.2.2 Tunable Infrared Filter

A tunable infrared (IR) transmission filter developed at the University of Wisconsin for the Honeywell Corporation is shown in Figure 2.12 [15]. The device is tuned using a electromagnetic stepper motor (not shown) to compress and expand the optical filter elements. The yoke is used to compress the filter elements and shorten the wavelength of the light permitted to pass through the filter. The IR filter was fabricated using

LIGA. The design of the springs at each end of the filter elements is critical; the springs must hold the filter elements at a constant separation distance as the yoke is moved.

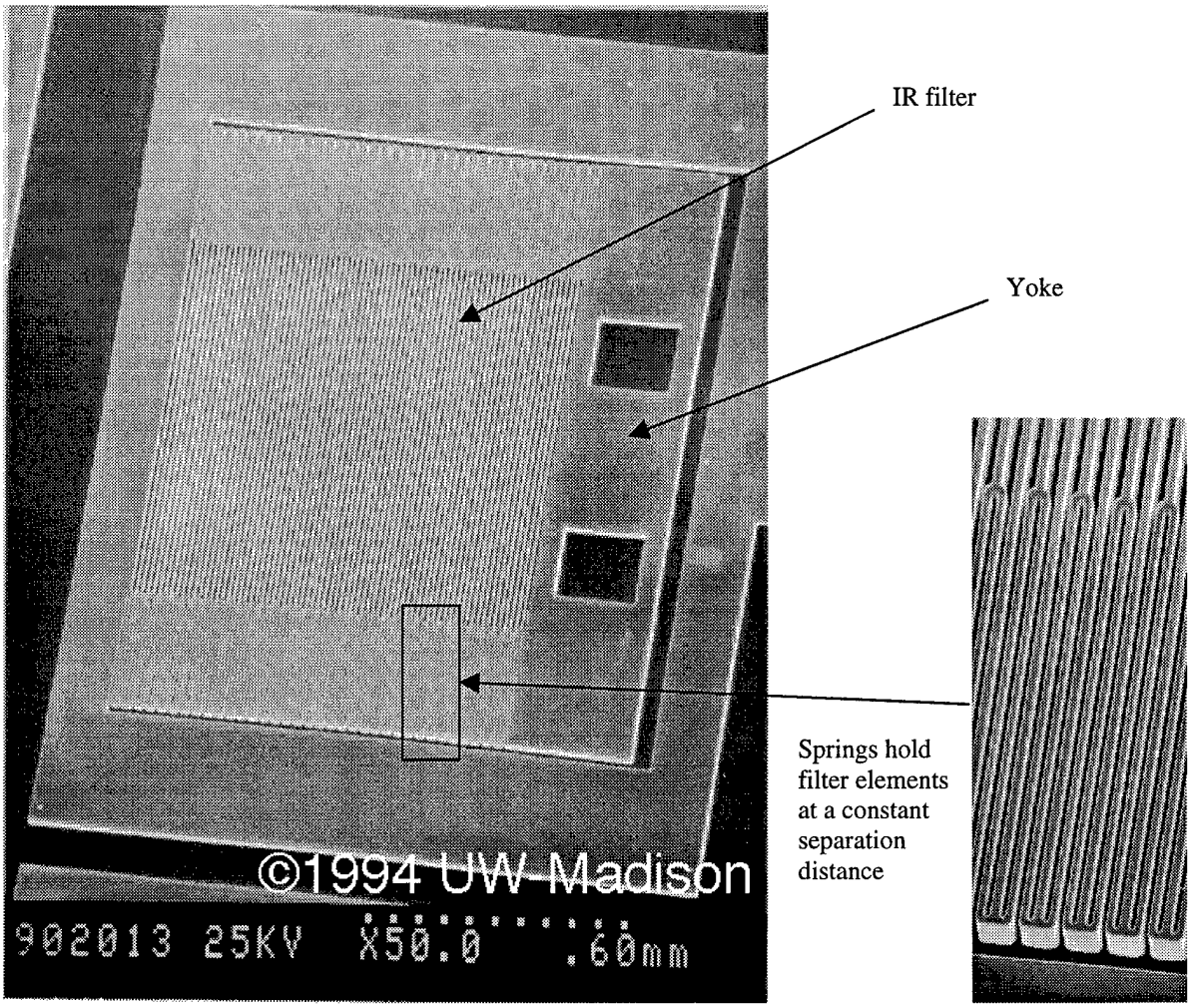

Figure 2.12. Tunable IR filter fabricated using LIGA [16].

Applications for the tunable IR filter include thermally guided air-to-air missiles. The tunable IR filter could be used to prevent background thermal signatures or enemy counter-measures (such as flares and lasers) from reaching the missile's detector and guidance unit.

2.2.3 Barcode Scanner

An electrostatically actuated micromirror designed for scanning barcodes is depicted in Figure 2.13. The barcode scanner was fabricated at the University of California, Berkeley, using their four layer polysilicon surface micromachining process described in Section 2.1.2 [7]. The barcode scanner is part of a single chip barcode reading system. An integrated semiconductor laser and detector are constructed within the barcode scanner's line-of-sight on the surface of the die. The micromirror is continually scanned over a 28° wide arc when the barcode scanner is driven at its resonant frequency (3.1 kHz).

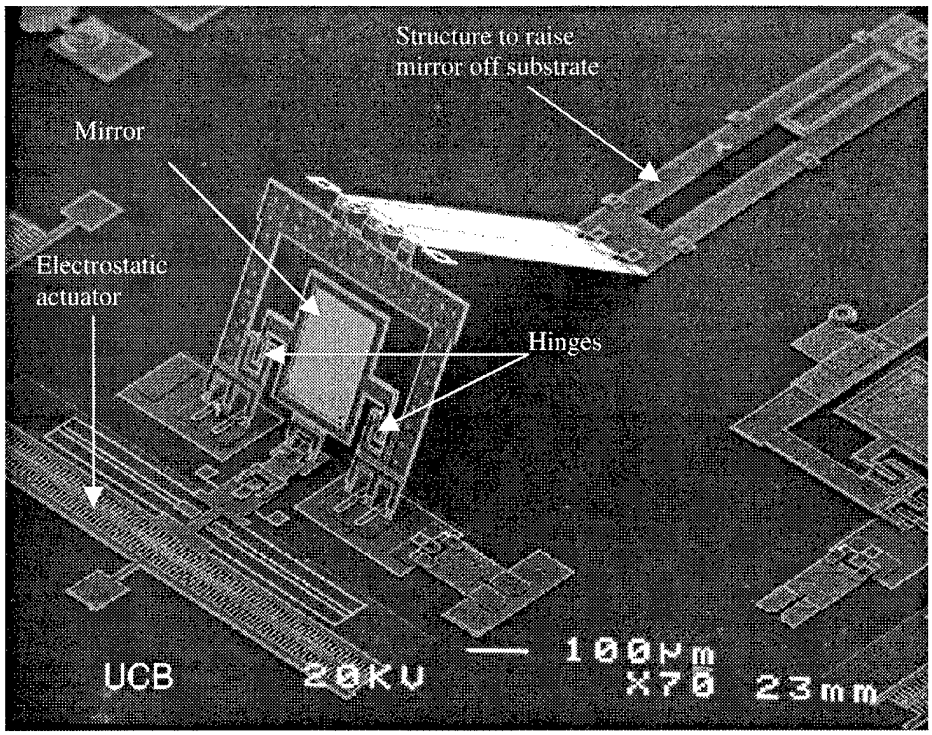

Figure 2.13. Barcode scanner developed at the University of California, Berkeley [17].

2.2.4 Grating Light Valve (GLV)

Pull-down gratings work by changing the optical path length for periodically spaced elements in the grating. The element spacing determines the location of the first diffraction order. Scientists at Stanford have developed a MEMS grating called the Grating Light Valve (GLV) [18]. A side view schematic diagram of this device is shown in Figure 2.14. This MEMS device is part of an array designed for video display applications.

If no voltage is applied, the top electrode is in the up position and all the incident light is reflected back. When approximately 20 volts is placed between the top and bottom electrodes, the top electrode snaps down to the bottom electrode. The difference in optical path lengths for light falling on the surfaces of the top and bottom electrodes causes diffraction, and light is shifted to the diffracted orders of the grating. The MEMS device operates in a digital mode, either in the up or down position. Pixel intensity is controlled by adjusting the duty cycle of the GLV. Increasing the down position percentage in the duty cycle causes an increase in pixel brightness. A full color display can be created using red, blue, and green pixels. Each pixel has a top electrode grating that has dimensions fixed to steer the first diffracted order in a direction so that the desired color passes through a mask. The GLV is currently being marketed by Silicon Light Machines, Inc.

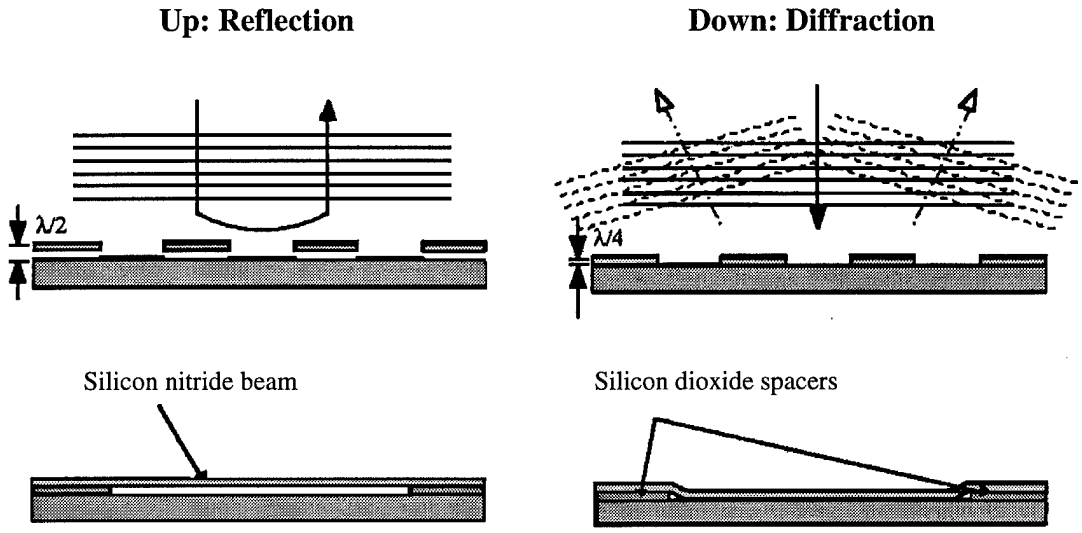

Figure 2.14. Side view of a GLV in operation [18].

2.2.5 Free Space Optical Bench

The University of California at Los Angeles (UCLA) has fabricated a number of surface micromachined optical devices; many of these devices are approximations for large scale optical components found on optical benches in a typical optics laboratory. Figure 2.15 shows an edge emitting semiconductor laser (left side of picture) mounted on a surface micromachined die. The Fresnel lens is used to collimate the

light emitted by the laser. UCLA also developed flip-up micromirrors and beam splitters [19]. One proposed application for free space optical benches is a read/write head for an optical disk drive [20].

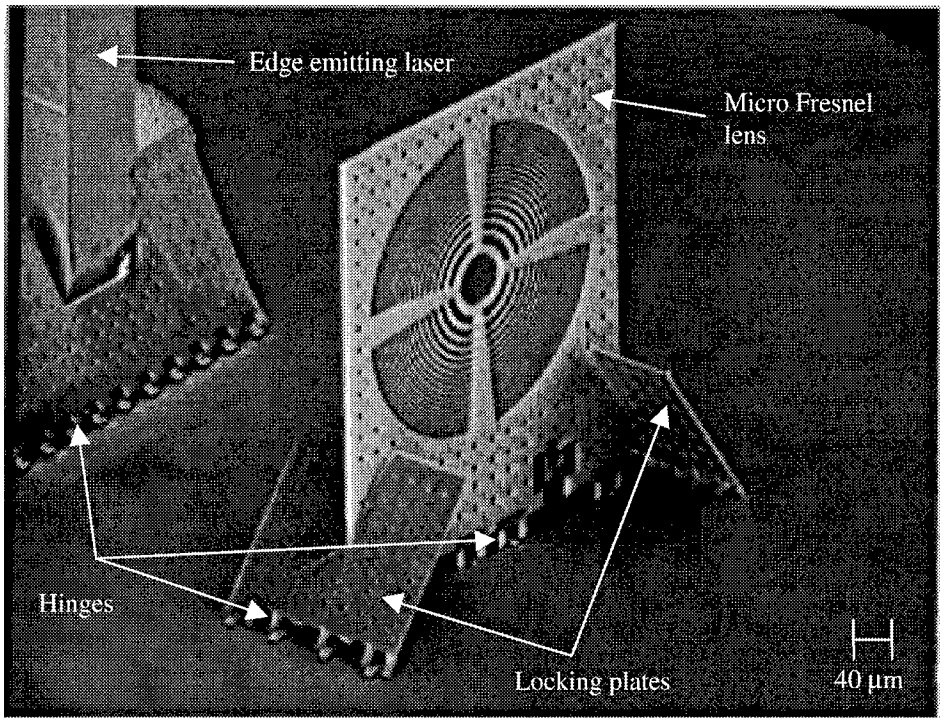

Figure 2.15. Scanning electronic micrograph of an edge emitting semiconductor laser coupled to a flip-up Fresnel microlens [19].

2.2.6 Fiber Optics Switch

A high efficiency switch for fiber optics was developed at the University of Neuchatel, Switzerland, and is depicted in Figure 2.16. When the bulk fabricated switch is open (shutter withdrawn), light from one fiber passes across the switch to the opposite fiber. When the switch is closed (shutter extended across gap), light from one fiber is reflected off the shutter into the other fiber on the same side of the switch. The silicon shutter is coated with aluminum after etching and is 76% reflective (at a wavelength of 1.3 µm - commonly used for fiber optical communication). The switching time is below 200 µs and the device is electrostatically actuated [21]. This fiber optics switch can be used in almost any fiber optics network.

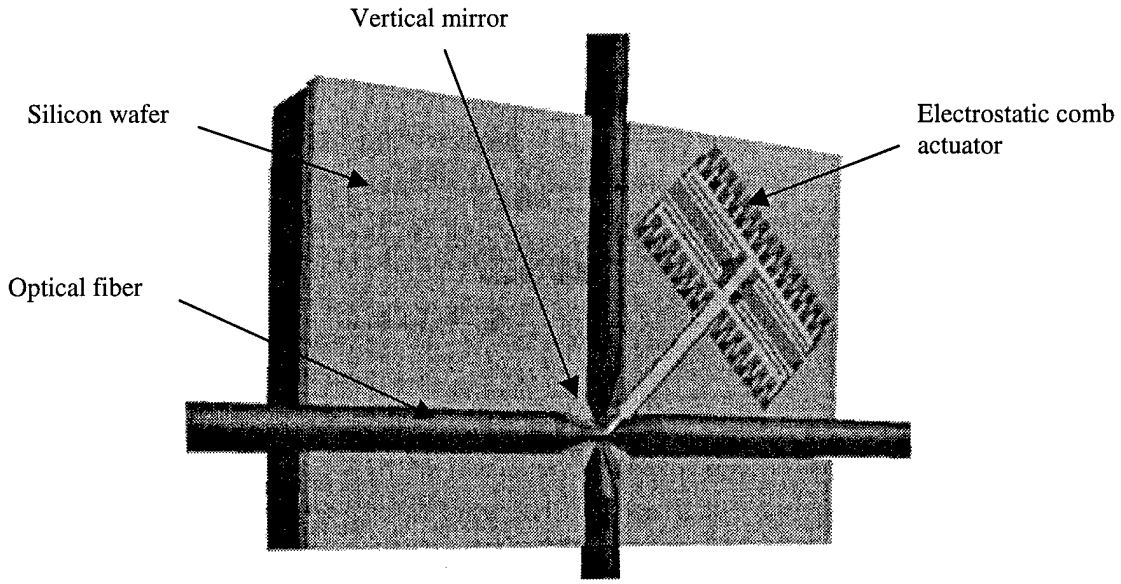

Figure 2.16. Bulk fabricated fiber optical switch [21].

2.2.7 Micro-turbine-engine

Micro-turbine-engines have been constructed using bulk micromachining at the Massachusetts Institute of Technology (MIT). Figure 2.17 depicts an 80 watt micro-engine designed to combust hydrogen. Future versions of this micro-engine could produce up to 100 watts of power using hydrocarbon fuels. Micro-turbine-engines have demonstrated performance equivalent to the best full sized turbine engines. The predicted performance of micro-turbine-engines currently under development at MIT is in the range 10 to 100 watts in sub-cubic centimeter sized packaging [22].

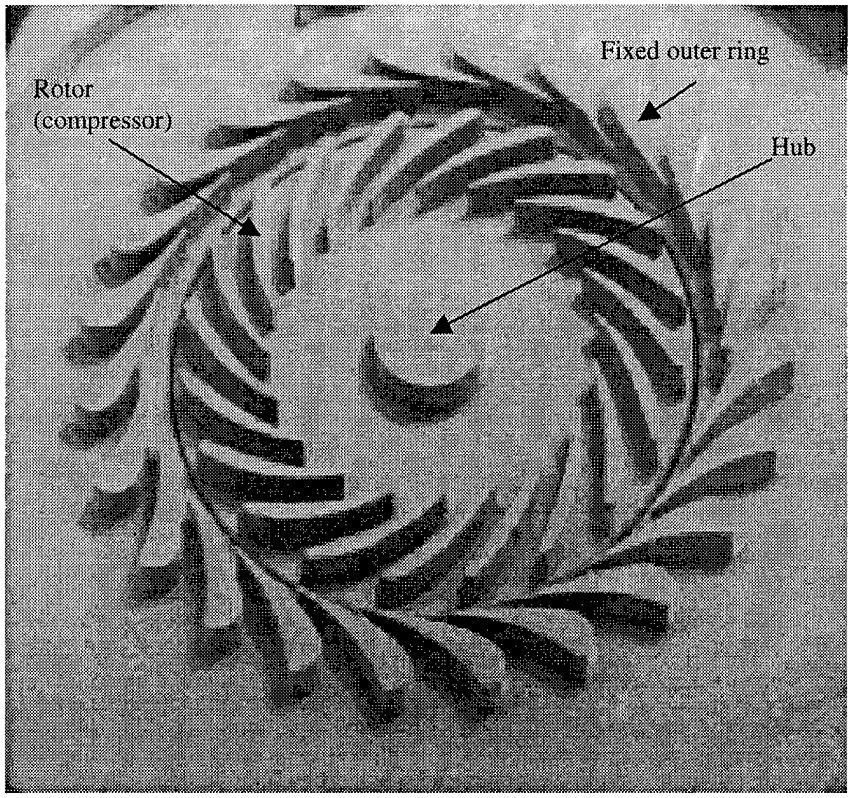

Figure 2.17. An 80 watt micro-turbine-engine developed at MIT after the top of the engine was removed. The diameter of the rotor is 3 mm [22].

2.3 References

[1] S. M. Sze, *Semiconductor Sensors*, New York, NY: John Wiley & Sons, 1994.

[2] S. M. Sze, *Semiconductor Devices - Physics and Technology*, New York, NY: John Wiley & Sons, 1985.

[3] M. Mehregany, "Microelectromechanical systems," *IEEE Circuits and Devices*, vol. 9, no. 7, pp. 14-22, July 1993.

[4] R. Zengerle, S. Kluge, M. Ricter, and A. Richter, "A bi-directional silicon micropump," *Proc. IEEE Micro Electro Mechanical Systems Symposium*, Amsterdam, the Netherlands, pp. 19-24, January 29 - February 2, 1995.

[5] M. C. Wu, L. Y. Lin, and S. S. Lee, "Micromachined free-space integrated optics," *Proc. SPIE Integrated Optics and Microstructures II*, San Diego, CA, vol. 2291, pp. 40-51, 1994.

[6] M.–H. Kiang, O. Solgaard, R. Muller, and K. Y. Lau, "High-precision silicon micromachined micromirrors for laser beam scanning and positioning," *Proc. Solid-State Sensor and Actuator Workshop - Late-News Poster Session Supplemental Digest*, Hilton Head Island, SC, pp. 33-34, June 3-6, 1996.

[7] M.–H. Kiang, O. Solgaard, R. S. Muller, and K. Y. Lau, "Surface-micromachined electrostatic-comb driven scanning micromirrors for barcode scanners," *Proc. IEEE Micro Electro Mechanical Systems-96*, San Diego, CA, pp. 175-180, Feb 12-16, 1996.

[8] R. D. Nasby, J. J. Sniegowski, J. H. Smith, S. Montague, C. C. Barron, W. P. Eaton, and P. J. McWhorter, "Application of chemical-mechanical polishing to planarization of surface-micromachined devices," *Proc. Solid-State Sensor and Actuator Workshop*, Hilton Head Island, SC, pp. 48-53, June 3-6, 1996.

[9] J. J. Sniegowski, S. L. Miller, G. F. LaVigne, M. S. Rodgers, and P. J. McWhorter, "Monolithic geared-mechanisms driven by a polysilicon surface-micromachined on-chip electrostatic microengine," *Proc. Solid-State Sensor and Actuator Workshop*, Hilton Head Island, SC, pp. 178-182, June 3-6, 1996.

[10] Images downloaded from the University of Wisconsin's Internet website, *www.engr.wisc.edu*, on October 2, 1997.

[11] D. Koester, R. Majedevan, A. Shishkoff, and K. Marcus, *Multi-User MEMS Processes (MUMPS) Introduction and Design Rules*, rev. 4, July 15, 1996, MCNC MEMS Technology Applications Center, 3021 Cornwallis Road, Research Triangle Park, NC, 27709.

[12] R. Miller, G. W. Burr, Y. C. Tai, and D. Psaltis, "Electromagnetic MEMS scanning mirrors for holographic data storage," *Proc. Solid-State Sensor and Actuator Workshop*, Hilton Head Island, SC, pp. 183-186, June 3-6, 1996.

[13] T. H. Lin, "Implementation and characterization of a flexure-beam micromechanical spatial light modulator," *Optical Engineering*, vol. 33, no. 11, pp. 3643-3648, November 1994.

[14] Picture downloaded from the Texas Instruments Corporation Internet website, *www.ti.com/corp/dos/pressrel/pressreleases.html*, July 31, 1996.

[15] T. R. Ohnstein, J. D. Zook, and H. B. French, "Tunable IR filters with integral electromagnetic actuators," *Proc. Solid-State Sensor and Actuator Workshop*, Hilton Head Island, SC, pp. 196-199, June 3-6, 1996.

[16] Picture downloaded from the University of Wisconsin Internet website, www.*mems.engr/wisc.edu/images/linear*, August 14, 1996.

[17] M.–H. Kiang, O. Solgaard, R. S. Muller, and K. Y. Lau, "Micromachined microscanners for optical scanning," *Proc. SPIE*, vol. 3008, pp. 82-90, February 10-12, 1997.

[18] R. B. Apte, F. S. A. Sandejas, W. C Banyai and D. M. Bloom, "Deformable grating light valves for high resolution displays," *Proc. Solid-State Sensor and Actuator Workshop*, Hilton Head Island, SC, pp. 1-6, June 13-16, 1994.

[19] M. E. Motamedi, M. C. Wu, and K. S. Pister, "Micro-opto-electro-mechanical devices and on-chip optical processing," *Optical Engineering*, vol. 36, no. 5, pp. 1282-1297, May 1997.

[20] L. Y. Lin, J. L. Shen, S. S. Lee, and M. C. Wu, "Realization of novel monolithic free-space optical disk pickup heads by surface micromachining," *Optics Letters*, vol. 21, no. 2, pp. 155-157, January 15, 1996.

[21] C. Marxer, M.–A. Gretillat, N. F. de Rooij, R. Battig, O. Anthamatten, B. Valk, and P. Vogel, "Vertical mirrors fabricated by reactive ion etching for fiber optical switching applications," *Proc. IEEE Micro Electro Mechanical Systems Workshop 97*, Nagoya, Japan, pp. 49-54, January 26-30, 1997.

[22] A. H. Epstein, S. D. Senturia, G. Anathasuresh, A. Ayon, K. Breuer, K.-S. Chen, F. E. Ehrich, G. Gauba, R. Ghodssi, C. Groshenry, S. Jacobson, J. H. Lang, C.-C. Lin, A. Mehra, J. M. Miranda, S. Nagle, D. J. Orr, E. Piekos, M. A. Schmidt, G. Shirley, M. S. Spearing, C. S. Tan, Y.-S. Tzeng, and I. A. Waits, "Power MEMS and microengines," *Proc. 1997 International Conference on Solid-State Sensors and Actuators (Transducers-97)*, Chicago, IL, pp.753-756, June 16, 1997.

3 Multi-User MEMS Processes

The author fabricated most of his microelectromechanical structures using the Multi-User MEMS Processes (MUMPs) provided by the Microelectronics Center of North Carolina (MCNC). MUMPs was initially sponsored by the Defense Advanced Research Projects Agency (DARPA). Originally derived from work at the University of California at Berkeley, MUMPs has two releasable polysilicon layers and a top layer of gold that can be used as a reflective surface for a micromirror or as a power bus. This chapter describes the MUMPs fabrication process and presents the author's solutions to design challenges such as residual material stress induced micromirror curvature.

3.1 Overview of the MUMPs Fabrication Process

MUMPs starts with a (100) n-type silicon wafer that is highly conductive. A 600 nm thick silicon nitride layer is deposited on the top of the wafer, using Low Pressure Chemical Vapor Deposition (LPCVD). This layer electrically isolates subsequent polysilicon layers from the conductive substrate. Next, alternate layers of polysilicon and phosphosilicate glass (PSG) are deposited using LPCVD. The PSG layers are often referred to as "oxide" layers because they are composed of silicon oxide highly doped with phosphorous (approximately 10^{20} phosphorous atoms/cm^3). A 500 nm thick layer of gold is evaporated onto the wafer after three layers of polysilicon have been deposited. Each layer of polysilicon, PSG, and gold is patternable. Table 3.1 shows the layering order and thickness used in the MUMPs process. The nomenclature "POLY-#" refers to the order number of the polysilicon layer (e.g. POLY-0 refers to the initial polysilicon layer placed on the wafer) [1].

All the layers, except the silicon nitride layer, are deposited and patterned before the next layer is deposited. The silicon nitride layer cannot be directly patterned, however Comtois developed a method of indirectly patterning the silicon nitride layer [2]. The direct patterning of layers is accomplished using a photoresistive mask and a reactive ion etch. After all polysilicon and PSG layers are deposited, the wafer is

annealed at 1050° C for one hour. This step lowers the internal stresses in the polysilicon and drives in phosphorus from the PSG. Driving phosphorous into the polysilicon reduces the electrical resistance of the polysilicon. After annealing, gold is evaporated onto the wafer and patterned. When the process is complete, the wafer is cut into individual 1 cm^2 dies, coated in a thick photoresist layer to protect the die during shipment, and sent to the users.

Table 3.1. Film Layers Used in the MUMPs Process [1].

Layer Name	Thickness (μm)
Silicon Nitride	0.6
POLY-0	0.5
1st PSG Layer (sacrificial oxide)	2.0
POLY-1	2.0
2nd PSG Layer (sacrificial oxide)	0.75
POLY-2	1.5
Gold	0.5

AFIT originally used the steps in Table 3.2 to "release" each die. The release process removes the PSG layers and allows MEMS devices such as the slide-up mirror in Figure 3.1 to move freely. The steps described in Table 3.2 were modified from MCNC's recommended release procedures [1]. These modifications were a result of the author's and other researchers' experience with MUMPs and were optimized for releasing large micromirrors. The author modified this release process further to reduce stiction (inadvertent bonding of a polysilicon layer to another polysilicon layer or the nitride layer). The author's improved release process is presented in Section 3.2. Rectangular etch access holes in the micromirror in Figure 3.1 are used to allow the hydrofluoric acid to etch under the mirror surface.

Figure 3.2 is a cross-sectional diagram of a device fabricated using MUMPs before the sacrificial layers are removed. Each layer conforms to the topology of the underlying layers. "Anchor 1" is a complete removal of a section of the 1st oxide layer before the POLY-1 layer is deposited. "Anchor 2" is a complete removal of a section of the 1st and 2nd oxide layers before the POLY-2 layer is deposited. Anchors are used to adhere a polysilicon layer to the nitride layer and prevent a structure from floating off the die during the release

process. Anchors also support the top electrode of electrostatically actuated micromirrors. A "dimple" is a partial (750 nm deep) removal of a section of the 1st oxide layer before the POLY-1 layer is deposited. Dimples are used to reduce the amount of polysilicon in contact with the nitride layer to reduce stiction. Dimples can also be used to corrugate polysilicon layers and increase a structure's resistance to bending. A "via" is a complete removal of a section of the 2nd oxide layer before the POLY-2 layer is deposited. Vias are used to bond POLY-1 and POLY-2 layers together. If an anchor-1 and a via or an anchor-1 and an anchor-2 are used together (with no intervening POLY-1 layer), the silicon nitride layer will be breached. Breaching the silicon nitride layer allows a POLY-2 layer to be in electrical contact with the underlying substrate [2].

Table 3.2. MCNC's Recommended Procedures for Releasing MUMPs Die.

Step	Process
1.	Remove shipment photoresist by immersing the die in acetone for 10 minutes and then rinsing the die in deionized water for 5 minutes.
2.	Dry the die by rinsing it in 2-propanol for 10 minutes. This step removes residual acetone and water that could dilute the hydrofluoric acid used to etch the die.
3.	Allow the remaining 2-propanol to evaporate (approximately 5 minutes).
4.	Remove the sacrificial PSG layers by etching the die in 49% pure hydrofluoric acid for 3 minutes.
5.	Rinse in deionized water for 10 minutes to remove all of the etchant.
6.	Rinse the die in 2-propanol for 20 minutes. This step reduces stiction of the polysilicon layers caused by capillary forces.
7.	Allow the remaining 2-propanol to evaporate (approximately 5 minutes).

3.2 MUMPs Design Challenges

Many potential applications including holographic data storage addressing [3], optical beam steering [4], optical gratings (Chapter 6), and optical display generation [5], require an optically flat reflective surface (less than 10% of a wavelength variation across the device's surface). This level of flatness has often been difficult to achieve because of unintentional embossing and mirror curvature. Unintentional embossing results from the thin film process used to construct surface micromachined devices. As each film is added to the substrate, the film conforms to the topology of the previously patterned layers. This conformal shaping causes the top layer to have depressions corresponding to the removed areas of the lower layers as shown in Figure 3.2.

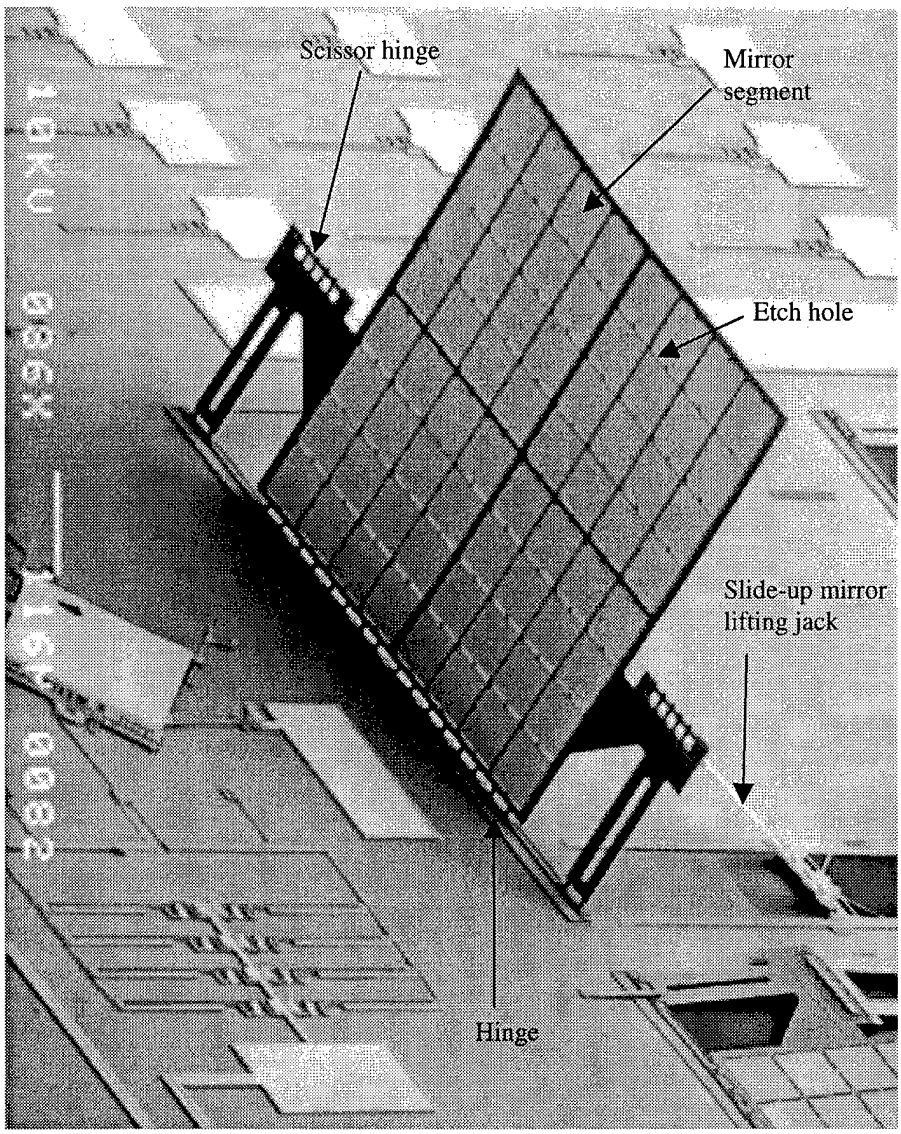

Figure 3.1. A large slide-up mirror. The reflective region of the mirror is 0.9 mm wide, 0.9 mm tall, and only 4 μm thick. The mirror is composed of 64 square mirror segments; the sides of all mirror segments are 100 μm long. Etch holes are located around the edges of each mirror segment. The mirror is easily visible on the die with the naked eye (fabricated by the author in MUMPs 18).

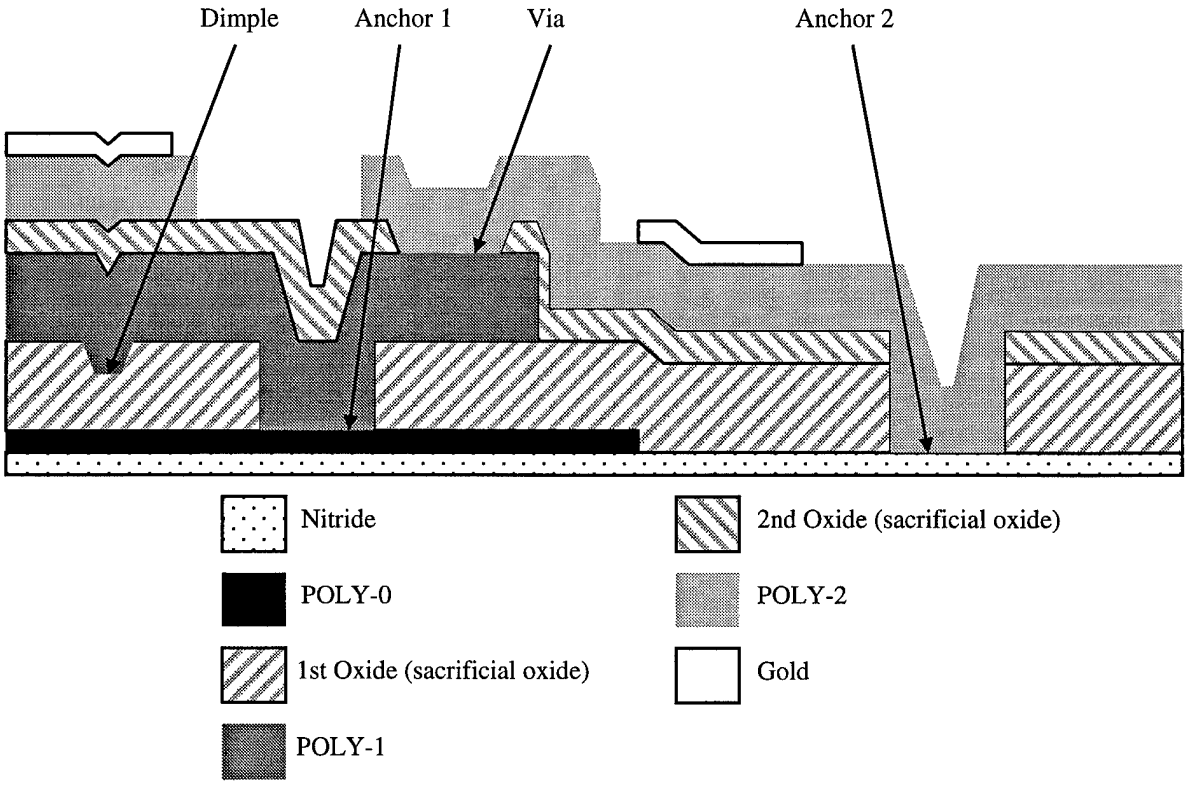

Figure 3.2. Schematic diagram of the layers used in MUMPs (after [1]).

Another source of distortion to the reflective surface is curvature resulting from the differences in the internal material stress between the top metal layer and the immediately lower polysilicon layer. When the sacrificial layers are removed, the metal layer and its supporting polysilicon layer curl into a concave shape. Although the curvature is difficult to detect with a traditional microscope, it can be measured with an interferometric microscope. For larger mirrors (100 μm or more in diameter), the curvature may result in the center of a POLY-2 and gold mirror dropping 500 nm or more towards the substrate. A large curvature is not only detrimental to optical applications of the mirror, it can also significantly change the electrical actuation properties of the mirror.

Stiction may limit the life span of a microdevice or completely prevent any operation. Stiction is often caused by capillary forces during the release process. Capillary forces can bring a polysilicon layer in a high force contact with another polysilicon layer or the silicon nitride layer; Van der Waals forces then bond the layers together.

Section 3.2.1 presents a baseline micromirror; subsequent sections report the author's design solutions to the problems of unintentional embossing, residual stress induced curvature, and stiction. The baseline micromirror was used as a control to evaluate the effects of the design techniques on mirror topology and stiction.

3.2.1 Baseline Micromirror Design

A round mirror with a top electrode diameter of 106 μm was used as the baseline micromirror. The baseline micromirror is composed of a top electrode consisting of a 1.5 μm thick structural layer of polysilicon (POLY-2) with a 500 nm thick top layer of gold as the reflective surface. The mirror is suspended 2.75 μm (the thickness of the two sacrificial oxide layers) over four bottom electrodes. A 500 nm thick layer of polysilicon (POLY-0) is used for the bottom electrodes. The diameter of the reflective portion of the mirror is 100 μm. The bottom electrode has been separated into four regions so that the mirror can be simultaneously tilted on two axis to steer incident light in two dimensions. Figure 3.3 is a schematic diagram of the mirror and its supporting flexures; the supporting flexures in this diagram were straightened for clarity. Figure 3.4 depicts the micromirror after fabrication and release.

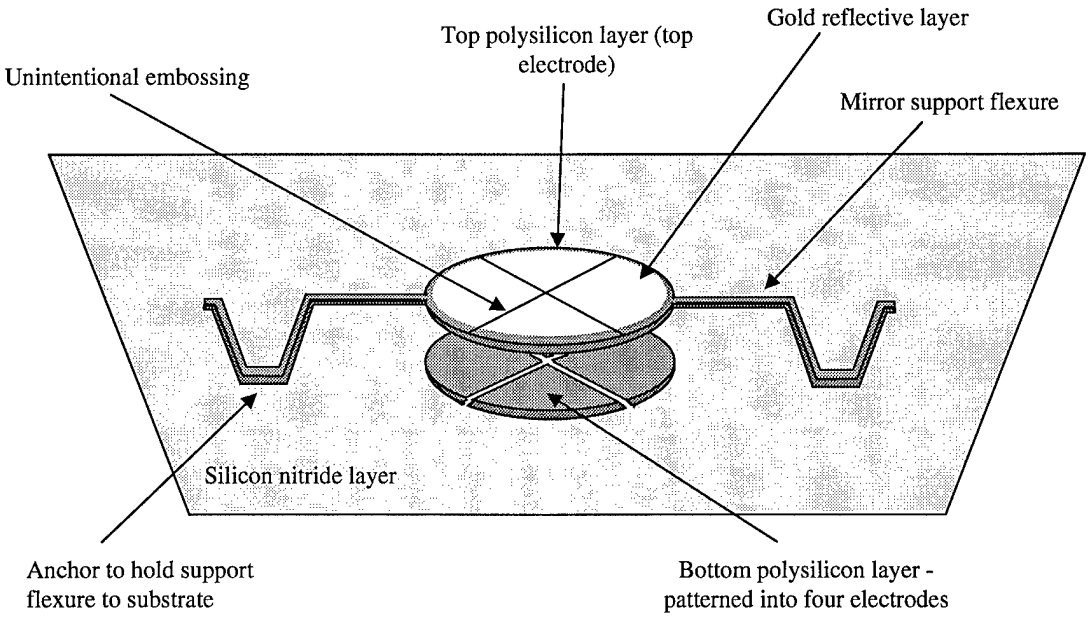

Figure 3.3. Schematic diagram of the baseline electrostatically-driven tilt mirror.

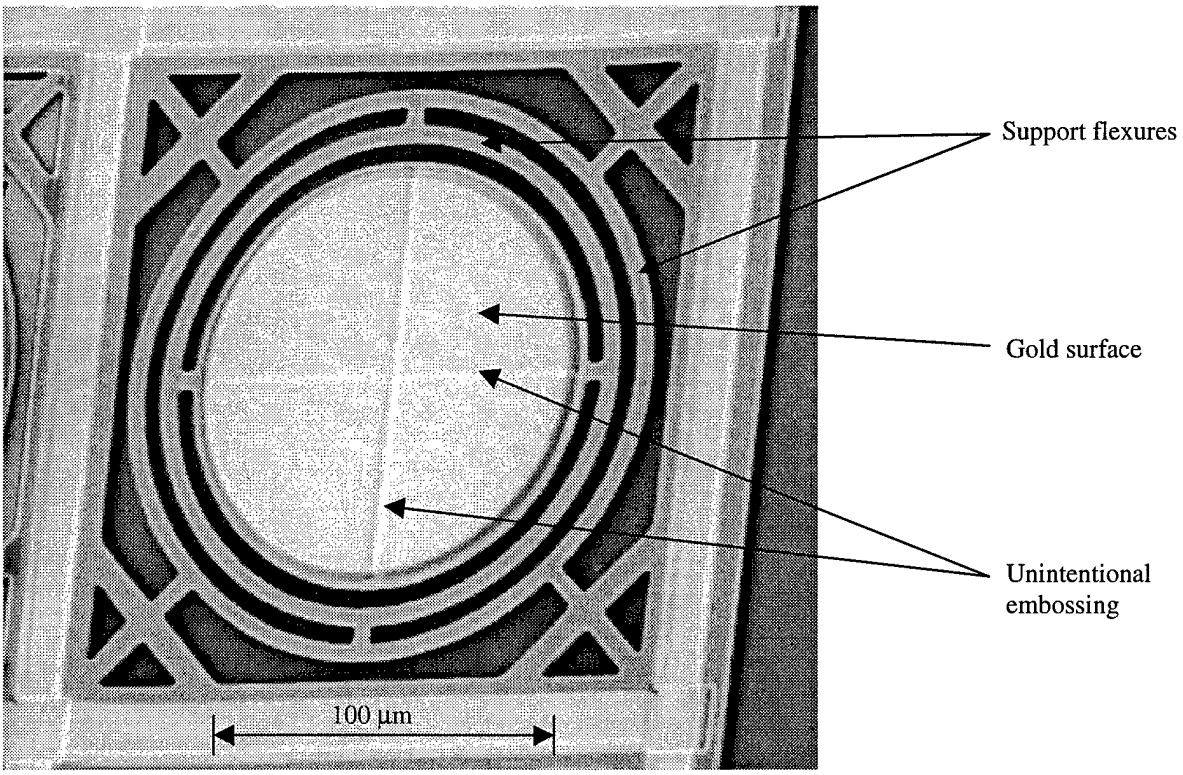

Figure 3.4. Scanning electron micrograph of the baseline electrostatically-driven tilt mirror after release (fabricated by the author in MUMPs 14).

When the top electrode is grounded and a voltage is placed on one of the bottom electrodes, electrostatic attraction tilts the mirror's surface towards the selected bottom electrode. If the voltage is reduced, the supporting flexures will pull the top electrode up towards the initial flat position. By using two bottom electrodes, the mirror can be tilted on two axis simultaneously. If all four bottom electrodes are used, the mirror can be pulled down without tilting (pistoned) to change the system's optical path length. After the top electrode is displaced a third of the initial distance to the bottom electrode, the top electrode's position becomes unstable. This instability causes the top electrode to quickly travel the remaining distance down to the bottom electrode [6]. This phenomenon is known as "snap-through" and it results from using a linear force (the support flexures) to counteract a non-linear force (electrostatic attraction). Snap-through is discussed in depth in Chapter 4. The four bottom electrodes are separated by 4 µm wide trenches (for electrical isolation) and this creates a "cross" pattern on the top electrode because subsequent layers conform to the gap between individual bottom electrodes.

The underlying bottom electrodes and the differences in material stresses between the gold and the polysilicon (POLY-2) resulted in the surface distortions graphed in Figure 3.5. The plot in Figure 3.5 was created by a Zygo interferometric microscope, model Maxim 3D, at a magnification of 40x and it indicates that the center of the mirror is 527.5 nm lower than the edge of the mirror as a result of internal material stress-induced curvature. Also a cross-shaped embossing pattern is evident in Figure 3.5 due to the top layer conforming to the four bottom electrodes. The Zygo interferometric microscope was unable to measure the depth of the embossed region because the edge of the embossed region created a phase discontinuity; Figure 3.5 shows an absence of data for the embossed region. Measurements at a higher magnification (100x) determined that the width of the embossed trench is 3.1 μm and the depth is 527.7 nm. The embossment and curvature distortions are significant and may limit potential applications of this mirror. The curvature also reduces the distance the mirror can be electrostatically actuated before snap-through occurs; the center of the mirror is closer to the bottom electrodes than it would be if no curvature was present.

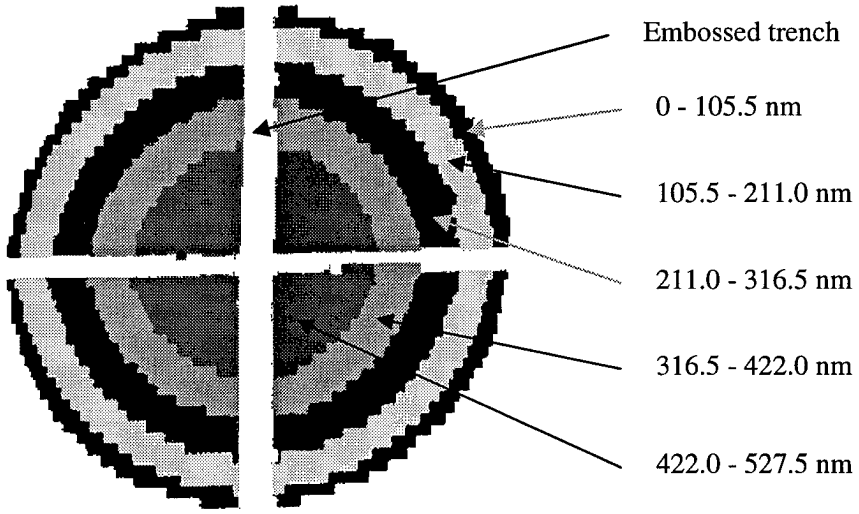

Figure 3.5. Surface topology plot of the baseline mirror. The mirror diameter is 100 μm (fabricated by the author in MUMPs 15).

3.2.2 Unintentional Embossing

The author investigated three techniques for reducing unintentional embossing of the mirror's surface without changing the MUMPs fabrication process. These techniques are separate top and bottom electrode formation areas, an alternate actuator design, and a polysilicon pull-out layer. The first two techniques relied on modifying the design of the mirror so that the mirror's reflective surface is formed over a flat area of the substrate. The last technique used an additional polysilicon layer to absorb some of the distortion caused by the patterning of the bottom electrodes.

3.2.2.1 Separate Top and Bottom Electrode Formation Areas

The first technique was accomplished by forming the mirror's reflective surface and top electrode in an area that was not directly over the bottom patterned electrodes and then sliding the top electrode over the bottom electrodes after the die was fabricated and released. Figure 3.6 and Figure 3.7 depict the mirror before and after the sliding top electrode was positioned over the bottom electrodes with a manual probe. This technique eliminated all embossing effects but required an extra manual step to prepare the mirror for use. The extra manual step could be eliminated if a linear motor was used to position the top electrode. A sliding mirror coupled to a linear motor is shown in Figure 3.8. A complete description of the linear motor used in Figure 3.8 is presented in Chapter 5. The measured peak-to-valley curvature for the sliding top electrode mirror was 501.2 nm.

3.2.2.2 Alternate Actuator Design

The alternate actuator design used a non-electrostatic actuator mechanism to remove the requirement for the bottom electrodes. Figure 3.9 shows a 100 μm diameter mirror driven by vertical thermal actuators instead of electrostatic attraction. When a current passes through the vertical thermal actuator, it curls up from the substrate and lifts the nearest edge of the mirror [7]. If a pair of vertical thermal actuators are used, then the mirror can be tilted on two axis simultaneously. This actuator design does not use bottom electrodes so the top mirror surface is free of unintentional embossing. The interferometric microscope plot of the surface of this

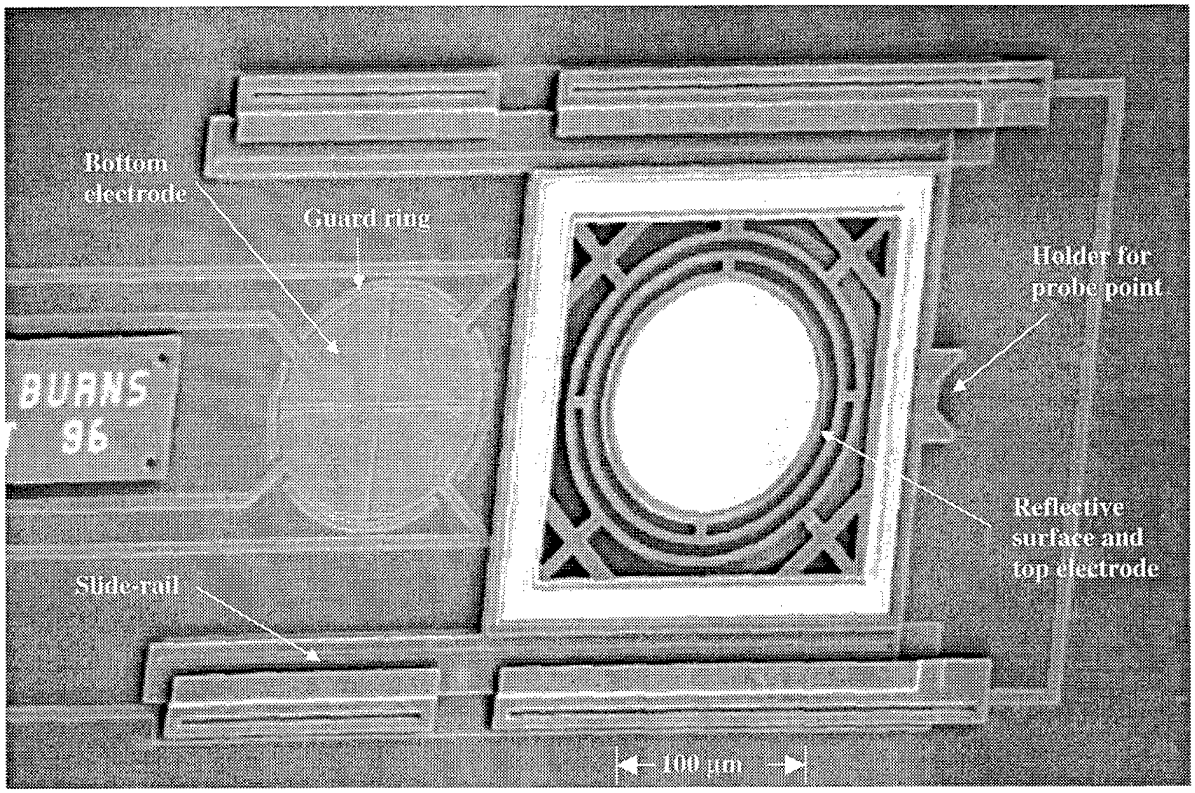

Figure 3.6. Scanning electron micrograph of the sliding top electrode mirror in open position (fabricated by the author in MUMPs 13).

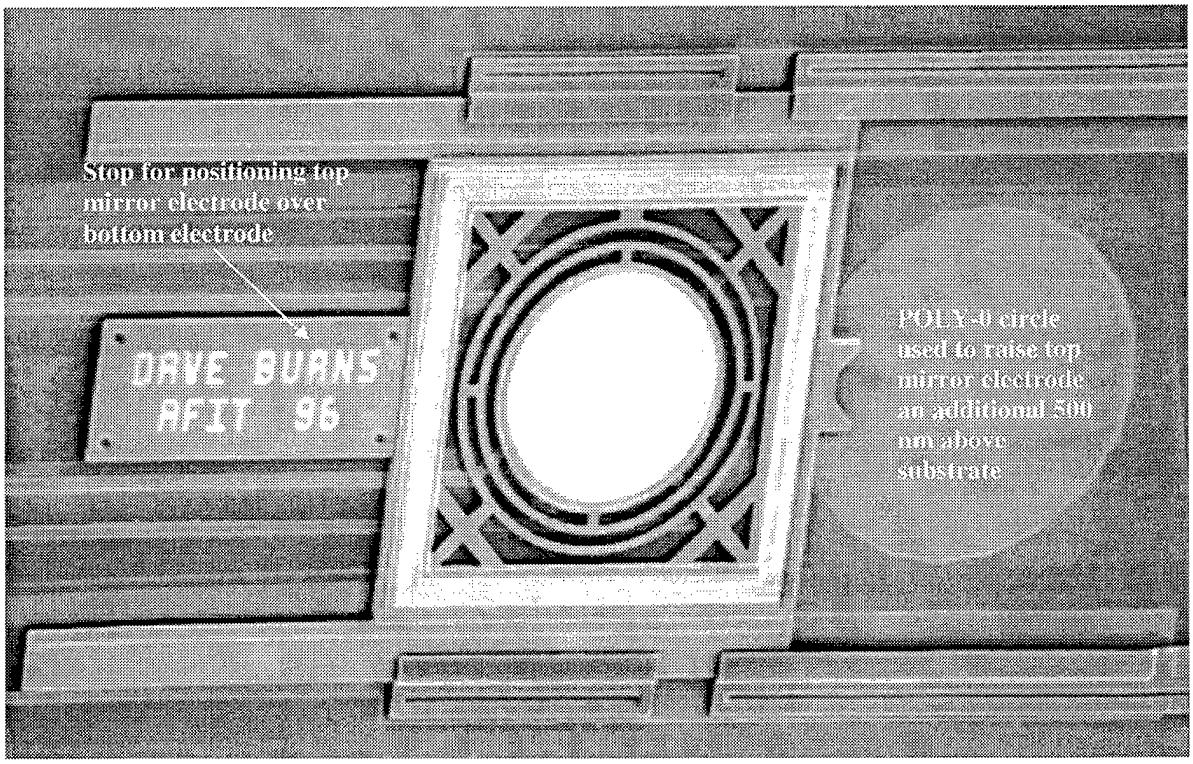

Figure 3.7. Scanning electron micrograph of the sliding top electrode mirror after assembly (fabricated by the author in MUMPs 13).

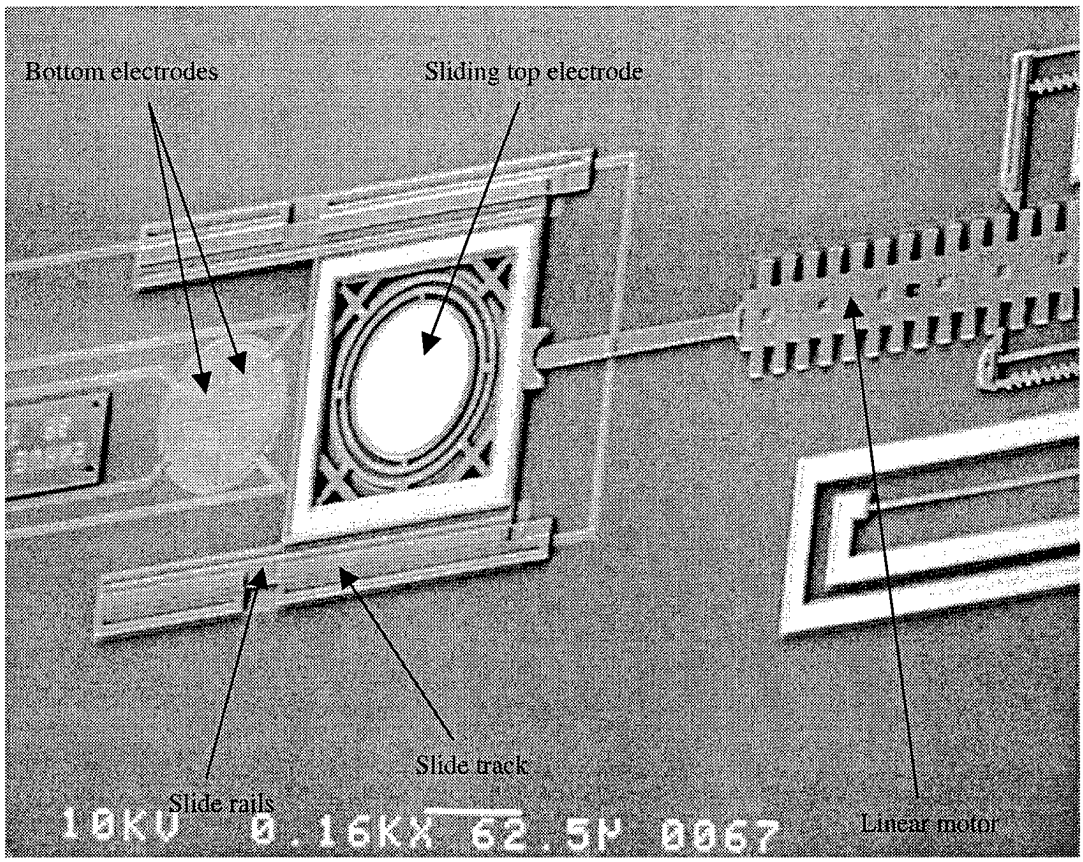

Figure 3.8. Sliding top electrode mirror coupled to a linear motor (fabricated by the author in MUMPs 14).

mirror is identical to the plot of the sliding top electrode mirror measured in Figure 3.7. An advantage of this design is that it can tilt the mirror over a larger angle than the electrostatic-driven baseline mirror; vertical thermal actuators lift the mirror up from the die and do not exhibit the snap-through instability present in electrostatic actuators. The maximum operating frequency of the vertical thermal actuators is only a few hundred hertz; if a higher operating frequency is needed, an electrostatically-driven mirror design may be required [8]. The measured peak-to-valley curvature for the vertical thermal actuator mirror was 501.2 nm. A more complete description of vertical thermal actuators is given in Chapter 9, Section 9.2.

3.2.2.3 Polysilicon Pull-out Layers

Polysilicon pull-outs are formed in a separate polysilicon layer (POLY-1) under the top electrode (POLY-2) [9]. The POLY-1 pull-out layer is removed from under the top electrode after the die is released.

Figure 3.10 shows a 100 μm diameter micromirror with a pull-out polysilicon layer partially removed. Figure 3.11 is a surface topology plot of the surface of the mirror after the POLY-1 layer has been removed. The polysilicon pull-out mirror has two advantages over the baseline mirror: reduced embossing and a larger tilt angle. The reduced embossing is a result of the POLY-1 layer imperfectly conforming to the bottom layers. The gap between the bottom electrodes is rounded over by the POLY-1 layer during fabrication. Measurements by the Zygo microscope at a high magnification (100x) determined that the width of the embossed trench is 2.6 μm, a 16% improvement over the baseline mirror. However the depth of the trench was unchanged from the baseline design. The larger tilt angle resulted from the top electrode being fabricated 2.0 μm higher than the baseline mirror (the thickness of the additional POLY-1 layer). The top electrode for the polysilicon pull-out mirror is 4.75 μm above the bottom electrodes. The POLY-1 layer can be removed with a linear motor, allowing the mirror to be assembled by remote means. Automated removal of a POLY-1 pull-out under the baseline mirror's top electrode will be presented in Chapter 5.

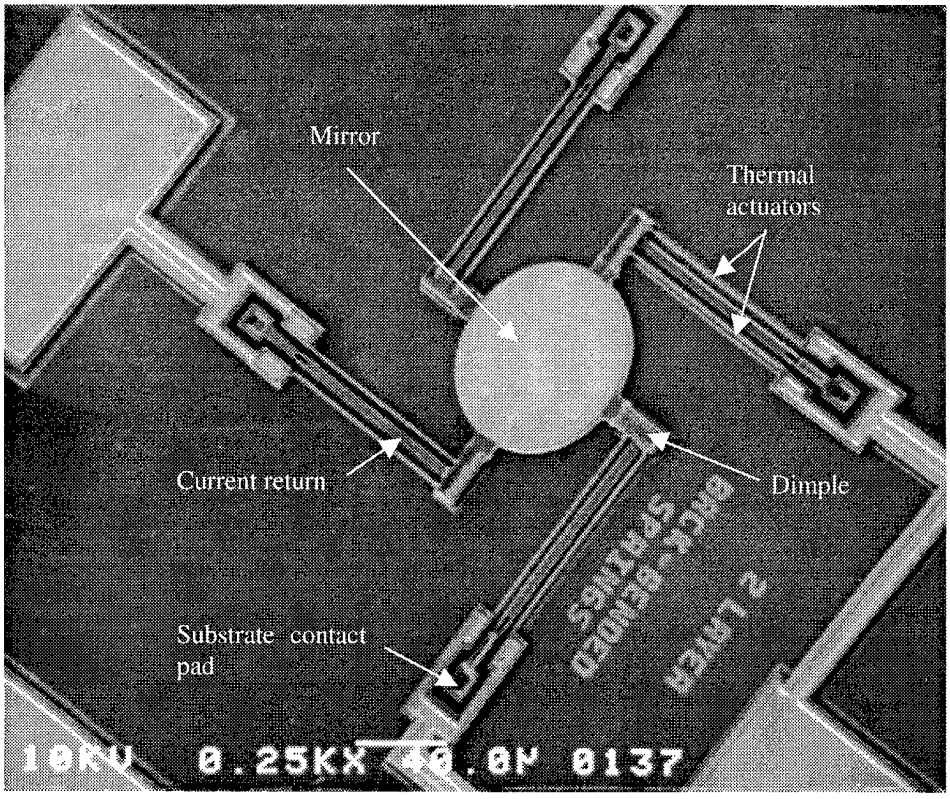

Figure 3.9. Tilt mirror (100 μm diameter) driven by vertical thermal actuators (fabricated by the author in MUMPs 14).

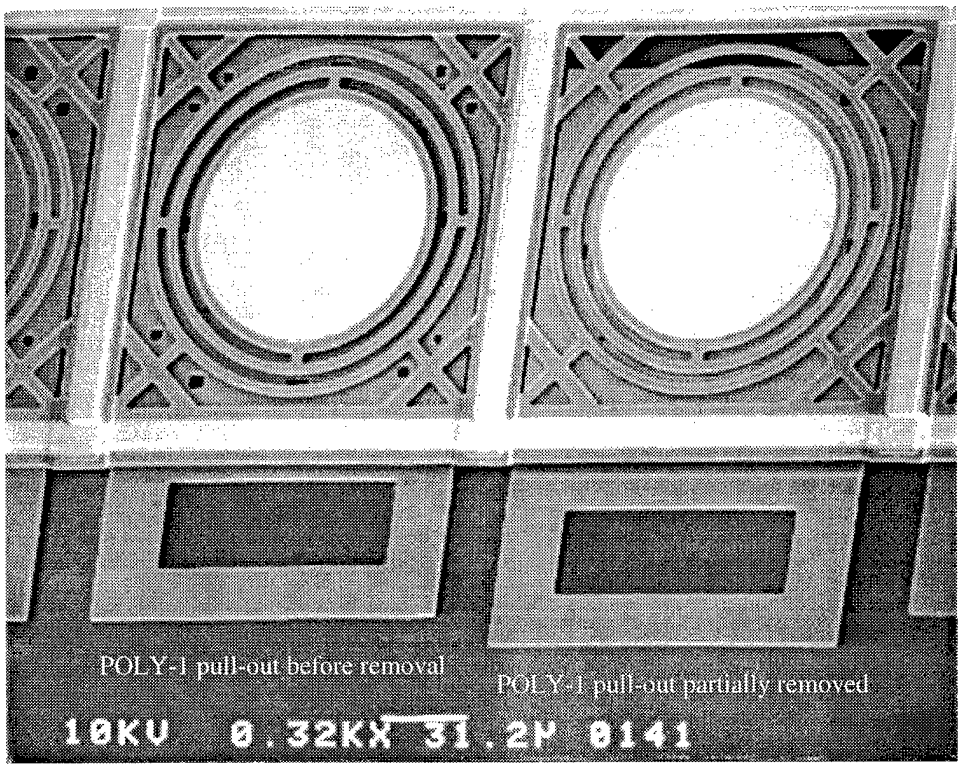

Figure 3.10. Scanning electron micrograph of the polysilicon pull-out mirror (fabricated by the author in MUMPs 14).

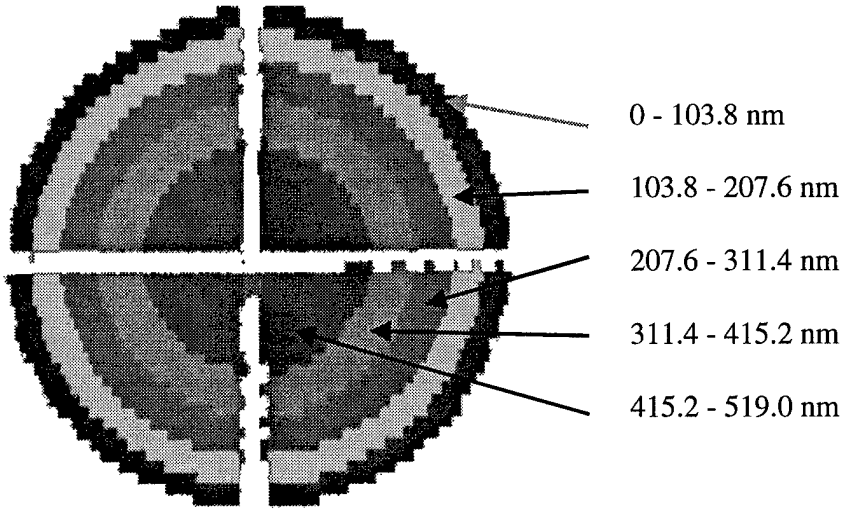

Figure 3.11. Surface topology plot of the polysilicon pull-out mirror (fabricated by the author in MUMPs 15).

3.2.3 Residual Material Stress Induced Curvature

Residual material stress induced curvature is due to a force imbalance between the compressive material stress in the top polysilicon layer and the tensile material stress in the gold. When the die is released the lower oxide layers are removed and the gold/POLY-2 layer stress difference immediately causes curvature in the mirror's reflective surface. Micromirrors fabricated with no gold on the top electrode had no measurable curvature and only a slight ripple in the top suspended polysilicon layer (less than 3 nm RMS). Four techniques were investigated by the author to minimize mirror curvature: stacked-polysilicon, trapped-oxide, alternate gold layer thickness, and thermal annealing. The first and second techniques were derived from earlier work at AFIT [9]. A summary of the unintentional embossing and curvature reduction techniques will be presented after all of the techniques are discussed.

3.2.3.1 Stacked-poly

The stacked polysilicon design (abbreviated as stacked-poly) relies on a bond between the middle polysilicon layer (POLY-1) and the top polysilicon layer (POLY-2) to increase the thickness of the polysilicon support under the gold layer. The two polysilicon layers are bonded by removing the intervening phosphosilicate glass (second oxide layer) during fabrication using a via (see Figure 3.2). The thickness of the resulting polysilicon support layer is increased from 1.5 μm (POLY-2 only) to 3.5 μm (combined POLY-1 and POLY-2 layers). The extra thickness of the combined polysilicon support layer is able to counteract the internal material stress in the gold layer more effectively than a single polysilicon layer.

Figure 3.12 is a cross-sectional diagram of a micromirror constructed using stacked-poly. Figure 3.13 is a surface topology plot of a 100 μm diameter micromirror designed with a bonded layer of POLY-1 and POLY-2. The micromirror is significantly flatter, however the distance from the top electrode to the bottom electrode has decreased from a maximum of 2.75 μm (the sum of the first and second oxides) to 2.0 μm (only the thickness of the first oxide).

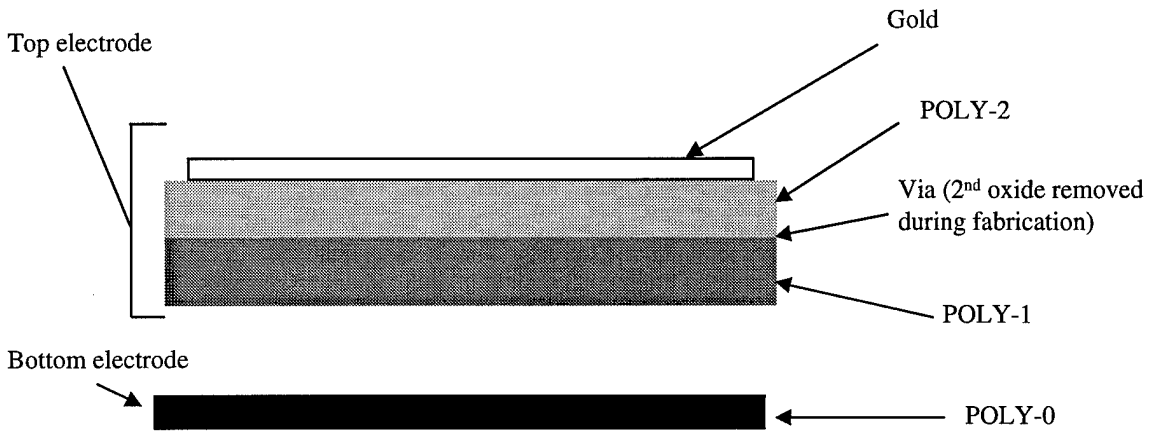

Figure 3.12. Cross-sectional view of a micromirror fabricated using stacked-poly.

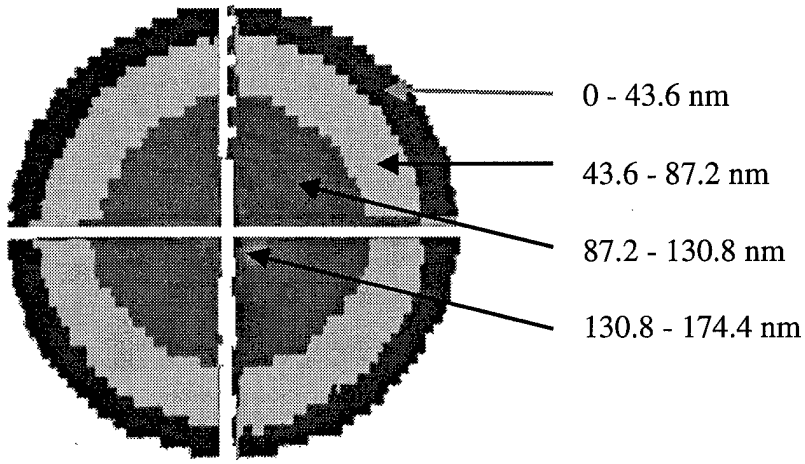

Figure 3.13. Surface topology plot of the stacked-poly mirror (fabricated by the author in MUMPs 15).

3.2.3.2 Trapped-oxide

Another curvature-reduction technique is to trap a portion of the second oxide layer in a sealed POLY-1 / POLY-2 cavity. This technique prevents the phosphosilicate glass present in the top electrode from being removed when the die is released and it increases the thickness of the support under the gold layer to 4.25

μm. The sealed cavity is formed by removing a ring of the second oxide around the edge of the mirror (using a via). This ring allows the POLY-1 and POLY-2 to bond around the outer edge of the mirror and conceals the inner second oxide layer from the hydrofluoric acid when the die is released. Figure 3.14 is a cross-sectional diagram of a micromirror constructed using trapped-oxide. Figure 3.15 is the surface topology plot of a 100 μm diameter mirror with a trapped second oxide layer. A further improvement in surface flatness is obtained, however the increased mass of the top electrode decreases the maximum operating frequency of the mirror.

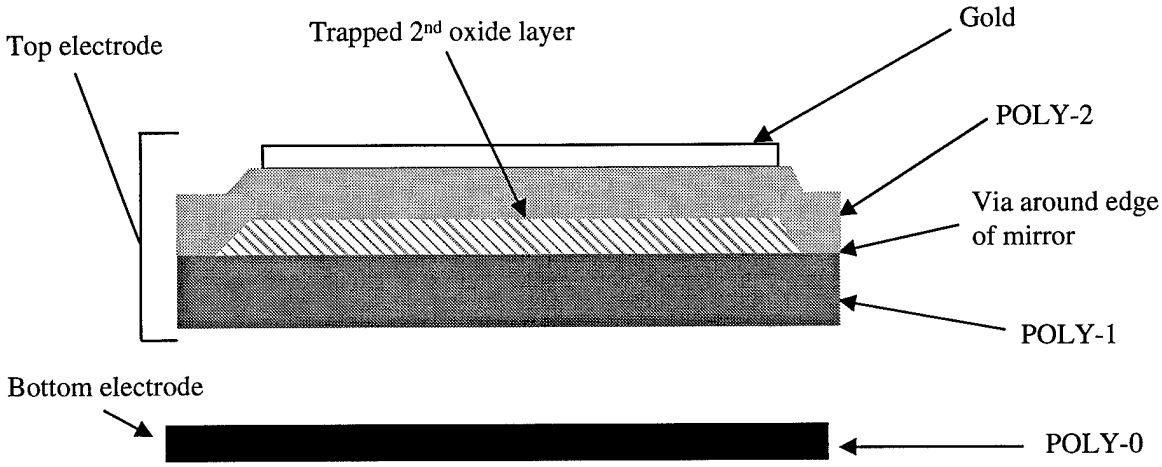

Figure 3.14. Cross-sectional view of a micromirror fabricated using trapped-oxide.

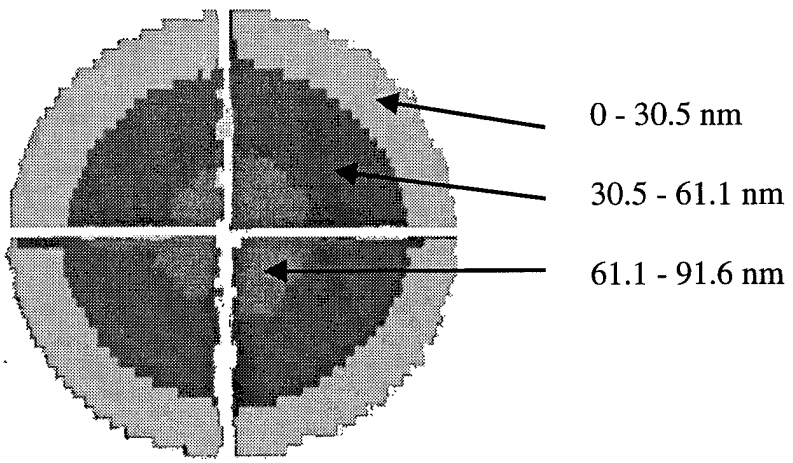

Figure 3.15. Surface topology plot of the trapped-oxide mirror (fabricated by the author in MUMPs 15).

3.2.3.3 Alternate Gold Layer Thickness

The next method of reducing micromirror curvature is to fabricate the mirrors without the standard top gold layer thickness used in the MUMPs process. This method was accomplished by designing the device without a gold layer and then depositing gold on the top electrode after the die was returned to AFIT. No photoresistive mask is required if the alternate gold layer is applied before the die is released because the removal of the underlying phosphosilicate glass will undercut and remove excess gold. However the gold layer may make the releasing process more difficult; the gold will have to be undercut by etchant before the sacrificial layer can be removed. It is possible to deposit thin films of gold using post-processing that provide the desired reflectance and are thinner than the MUMPs gold layer. The top polysilicon layer is able to resist curvature induced from thin layers of gold better than thick gold layers. The MUMPs process uses a 500 nm thick layer of gold, which is excellent for making low resistivity bondpads or wiring. However the MUMPs gold layer thickness is far more than required for a good mirror surface at visible wavelengths.

The author investigated mirror curvature resulting from a 150 nm layer of gold directly deposited on the top polysilicon layer after the die was released. The mirror curvature peak-to-valley distance for a 150 nm layer of gold deposited directly on a 100 μm diameter POLY-2 mirror was 44.5 nm. It is also possible to make a POLY-1 top electrode by depositing gold directly on a POLY-1 layer after the die was released; a POLY-1 and thin gold layer (150 nm) mirror had a mirror curvature peak-to-valley distance of 33.4 nm. Figure 3.16 is the surface topology plot of a 100 μm diameter POLY-2 mirror after a 150 nm layer of gold was deposited by the author (the MUMPs gold layer was not used).

3.2.3.4 Thermal Annealing

Attempts to reduce residual material stress induced curvature using thermal annealing were unsuccessful. MUMPs die (both released and unreleased) were baked in an electronic oven at temperatures ranging from 200°C to 700°C. The duration of the annealing varied from one hour to 24 hours. MUMPs dies subjected to 250°C or higher for more than 30 minutes had a decrease in the reflectivity of the gold layer of at least 25% (at a wavelength of 632.8 nm). A complete discussion of the effects of baking MUMPs micromirrors will be presented in Chapter 8. Thermal annealing did not reduce micromirror curvature in any experiment;

however thermal annealing actually increased micromirror curvature when micromirrors were baked at 500°C for 30 minutes or more.

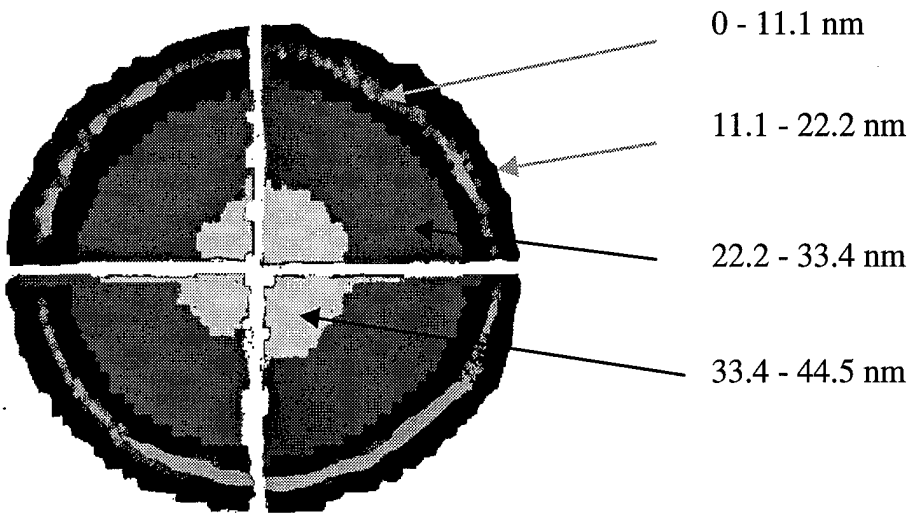

Figure 3.16. Surface topology plot of a POLY-2 and 150 nm thick gold layer mirror (fabricated by the author in MUMPs 15).

3.2.4 Summary of Topology Design Solutions

Figure 3.17 shows a cross-sectional view of the curvature resulting from the three successful curvature reduction techniques and compares results to the baseline mirror. The peak-to-valley curvature measurements in Figure 3.17 were collected on mirrors that did not have embossed-trenches. The best topology results were obtained by combining three of the techniques: separate formation of the top and bottom electrodes, using a top electrode with trapped-oxide, and using a thin gold layer. Table 3.3 summarizes the effects of each technique on surface topology.

Peak-to-valley curvature also varies as a function of the production run. Appendix A lists MUMPs parameters (such as material stress) that varied on each production run. Trapped-oxide was consistently the flattest construction technique possible if the MUMPs gold layer was used; stacked-poly was always second best. Figure 3.18 shows micromirror peak-to-valley curvature as a function of the MUMPs fabrication run.

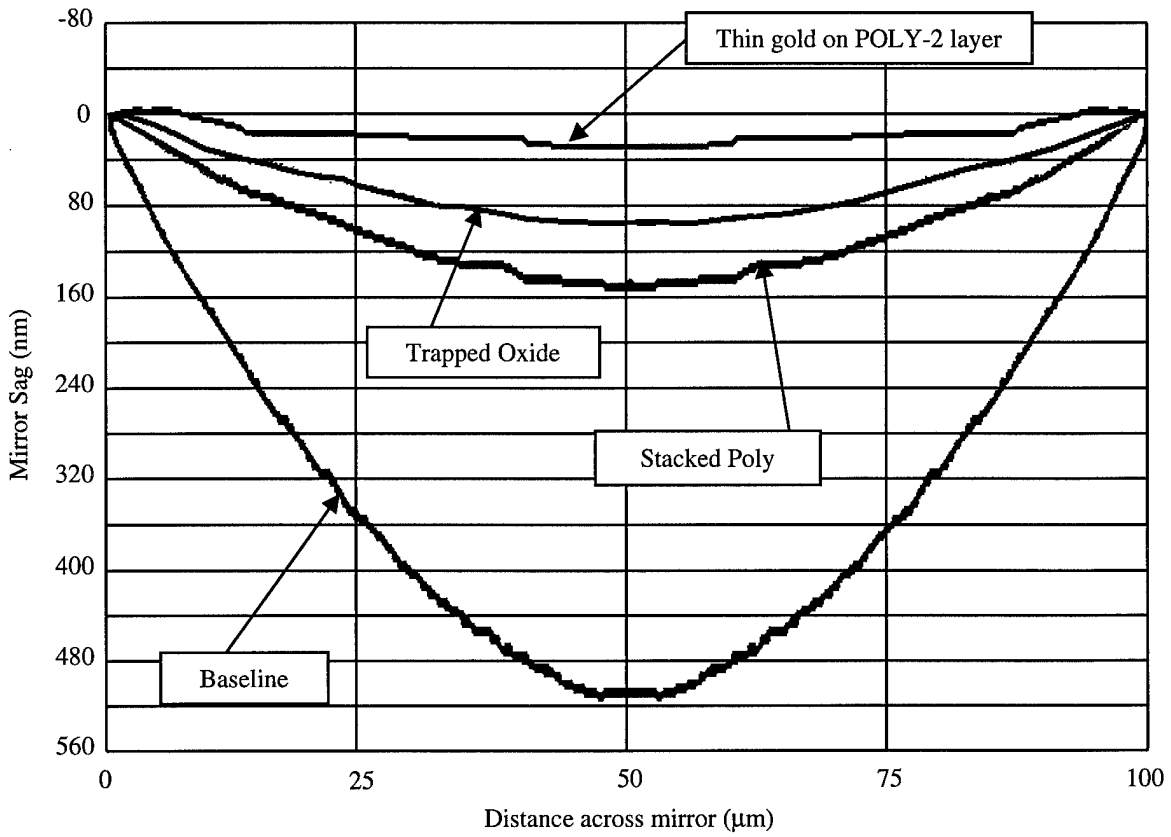

Figure 3.17. Cross-sectional comparison of residual stress induced curvature (all micromirrors fabricated in MUMPs 15).

Table 3.3. Summary of Topology Improvement Techniques for a 100 μm Diameter Mirror (all micromirrors fabricated in MUMPs 15).

Technique	Unintentional embossing present ?	Mirror curvature peak-to-valley distance (nm)
1. Baseline (no technique applied)	YES	527.5
2. Separate top and bottom electrode formation areas	NO	501.2
3. Alternate actuator design	NO	501.2
4. Polysilicon pull-out layer	YES	519.0
5. Stacked-polysilicon	YES	136.6
6. Trapped-oxide	YES	85.9
7. Thinner gold layer (150 nm thick) on POLY-2 layer	YES	44.5
8. Thermal annealing at 500°C for one hour	YES	755.5
9. Combination of techniques 2, 6, and 7	NO	25.7

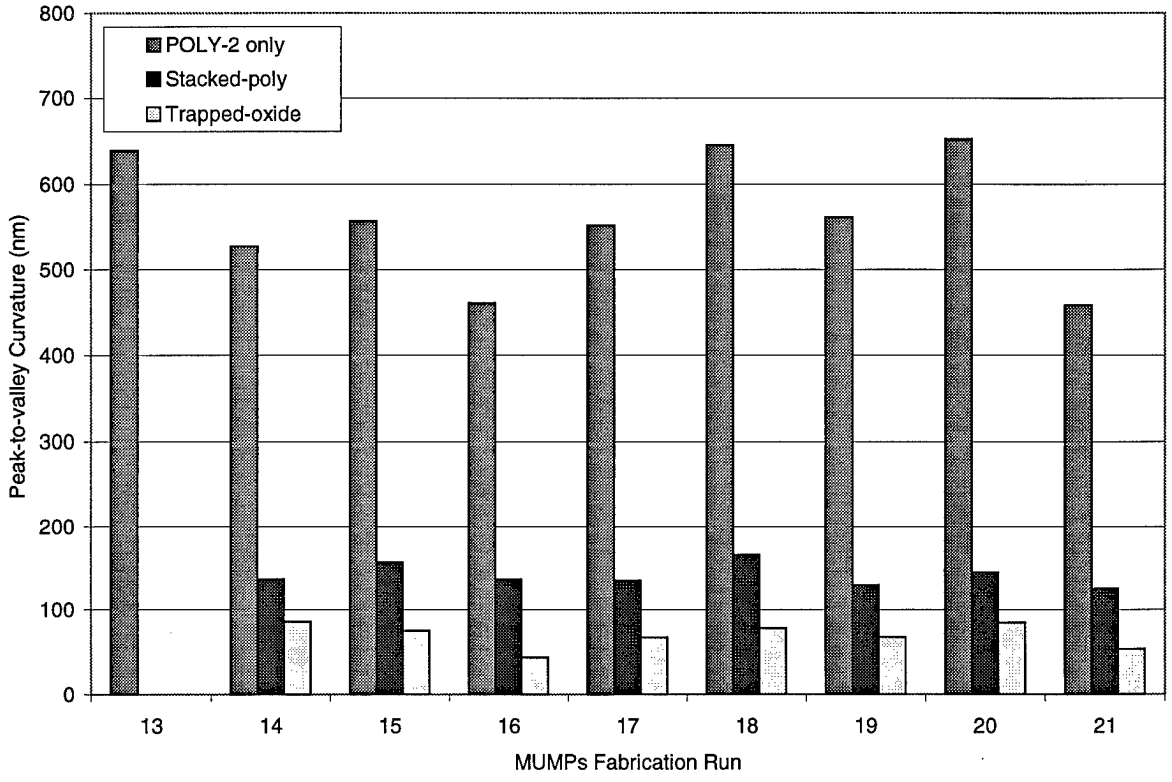

Figure 3.18. Peak-to-valley curvature for a round 100 μm micromirror as a function of MUMPs fabrication run.

3.2.5 Stiction

The author focused his stiction reduction investigation on the MUMPs release process. The existing release procedures exposed the MUMPs die to deionized water for ten minutes or more both before and after etching in hydrofluoric acid. The capillary force of water is very high so long duration baths in water increase the opportunity for stiction. The author experimented with shortened cycle times in the deionized water and eventually settled on a quick dip (2 second) in deionized water followed by a bath in methyl alcohol. The quick dip was used to rinse residual hydrofluoric acid off the die and prevent contaminating the methyl alcohol with hydrofluoric acid. The author's improved release procedures are listed in Table 3.4. The release procedures in Table 3.4 have been adopted by all of the other researchers at AFIT as the best low stiction release process. MCNC is currently investigating the author's release process and may recommend it as the standard release process to all MUMPs users.

Table 3.4. Author's Low Stiction Release Procedure.

Step	Procedure	Purpose
1.	Soak die in 1st acetone container for 2 minutes.	Removes packaging photoresist.
2.	Soak die in 2nd acetone container for 5 minutes.	Continues removal of packaging photoresist. Using two separate acetone containers improves the cleanliness of the die.
3.	Soak die in 1st methyl alcohol container for 5 minutes.	Removes residual acetone.
4.	Heat die on hot plate (90°C) for 3 minutes.	Evaporates methyl alcohol (prepares die for etching).
5.	Etch die in hydrofluoric acid for 3-5 minutes.	Removes sacrificial layers. Duration depends on the structures on the die. Three minutes is sufficient for most designs; however large structures with few etch holes may require up to five minutes.
6.	Dip die in deionized water (2 seconds).	Rinses off hydrofluoric acid (makes it easier to dispose of the methyl alcohol used in step 7).
7.	Soak die in 2nd methyl alcohol container for 10 minutes.	Removes the remaining traces of hydrofluoric acid.
8.	Heat die on hot plate (90°C) for 10 minutes.	Evaporates methyl alcohol.

3.3 References

[1] D. Koester, R.Majedevan, A. Shishkoff, and K. Marcus, *Multi-User MEMS Processes (MUMPS) Introduction and Design Rules*, rev. 4, July 15, 1996, MCNC MEMS Technology Applications Center, 3021 Cornwallis Road, Research Triangle Park, NC, 27709.

[2] J. H. Comtois, "Structures and techniques for implementing and packaging complex, large scale microelectromechanical systems using foundry fabrication processes", *Ph.D. Dissertation*, AFIT/DS/ENG/96-04, May 1996.

[3] S. C. Gustafson, G. R. Little, V. M. Bright, J. H. Comtois, and E. A. Watson, "Micromirror arrays for coherent beam steering and phase control," *Proc. SPIE*, vol. 2881, pp. 65-74, 1996.

[4] E. A. Watson and A. R. Miller, "Analysis of optical beam steering using phased micromirror arrays," *Proc. SPIE*, vol. 2687, pp. 60-67, 1996.

[5] M. A. Michalicek, V. M. Bright, and J. H. Comtois, "Design, fabrication, modeling, and testing of a surface-micromachined micromirror device," *Proc. 1996 ASME Dynamic Systems and Control Division*, DSC-vol. 57-2, pp. 981-985, 1995.

[6] P. M. Osterberg, R. K. Gupta, J. R. Gilbert, and S. D. Senturia, "Quantitative models for the measurement of residual stress, Poisson ratio and Young's modulus using electrostatic pull-in of beams and diaphragms," *Proc. Solid-State Sensor and Actuator Workshop*, Hilton Head Island, SC, pp. 184-188, June 13-16, 1994.

[7] J. H. Comtois, V. M. Bright, and M. W. Phipps, "Thermal microactuators for surface-micromachining processes," *Proc. SPIE*, vol. 2642, pp. 10-21, 1995.

[8] M. A. Michalicek, D. E. Sene, and V. M. Bright, "Advanced modeling of micromirror devices," *Proc. International Conference on Integrated Micro/Nanotechnology for Space Applications*, NASA & Aerospace Corp. Publications, pp. 214-229, 1995.

[9] J. H. Comtois and V. M. Bright, "Surface micromachined polysilicon thermal actuator arrays and applications," *Proc. Solid-State Sensor and Actuator Workshop*, Hilton Head Island, SC, pp. 174-177, June 3-6, 1996.

4 Optical Beam Steering Theory and Modeling

This chapter presents all of the optical and electro-mechanical theory used by the author in his research with one exception: theory on the optical power capacity of micromirrors will be presented in Chapter 8. Modeling presented in this chapter includes: far-field irradiance patterns for reflected light, electrostatic actuation of micromirrors, and micromirror curvature. This chapter is organized into two sections. The first section reviews theory and the second section introduces the modeling used in subsequent chapters. Unless stated otherwise, all optical sources discussed in this chapter are assumed to be coherent and monochromatic. If the reader prefers to skip this chapter, a brief review of Section 4.1.1.1 (radiometry) is recommended; notation introduced in this section is used in several other chapters.

4.1 Theory

The theory section describes how each of the MEMS devices constructed by the author can be used to steer an optical beam. Some of these microdevices have other applications in addition to beam steering, such as spectrum analysis. These other applications will also be discussed. This section is intended to be a reference for the reader, providing a single location for many of the formulas and equations used in this research. The theory section is organized into optical and electro-mechanical theory segments.

4.1.1 Optical Theory

The optical theory segment begins with an overview of the radiometric terms used by the author to describe optical power. Three optical systems capable of steering an optical beam are then described: linear optical phased arrays, variable blaze gratings, and decentered lens beam steering. Two additional topics relevant to optical beam steering are subsequently discussed: divergence angles and Fourier analysis. An example of Fourier analysis is presented at the end of the optical theory segment.

4.1.1.1 Radiometry

The author used the standard radiometric units for optical power defined by Boyd [1]. For a receiver, optical power densities are described in terms of irradiance. For an optical source, optical power densities are described in terms of radiance, exitance, and intensity. Table 4.1 lists the definitions, symbols, and units for each of these terms. The units are in terms of watts (W), meters (m), and steradians (str). The beam solid angle (Ω) is defined as an *angular area*. Figure 4.1 shows a diagram that can be used to determine the beam solid angle. Equation (4.1) provides a method for calculating the beam solid angle using the half angle, $\theta_{½}$, labeled in Figure 4.1. The units for the beam solid angle are steradians and range from zero to 4π (an entire sphere).

Table 4.1. Radiometric Units Used in the Author's Research.

Radiometric Term	Origin	Definition	Symbol	Units
Power	Receiver	$\int_{A_R} E \partial A_R$	P	W
Irradiance	Receiver	$\frac{\partial P}{\partial A_R}$	E	W/m^2
Radiance	Source	$\frac{\partial^2 P}{\partial A_{\perp S} \partial \Omega_S}$	$\mathscr{R}$	W/(m^2-str)
Exitance	Source	$\frac{\partial P}{\partial A_S}$	M	W/m^2
Intensity	Source	$\frac{\partial P}{\partial \Omega_S}$	I	W/str

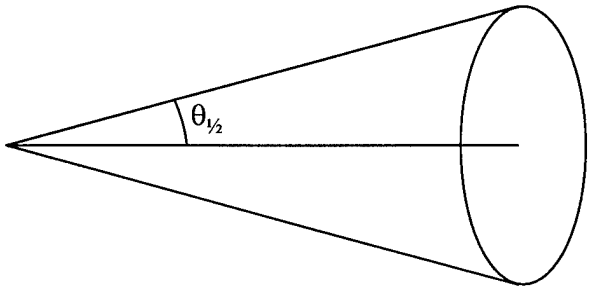

Figure 4.1. A circular cone for calculating the beam solid angle.

$$\Omega = 4\pi \sin^2\left(\frac{1}{2}\theta_{\frac{1}{2}}\right) \tag{4.1}$$

Although optical power can be defined either for the source or the receiver, the author is using the receiver because this definition is used in Chapter 8. Optical power is defined as the integral sum of the irradiance falling on the surface of a receiver (A_R). If the surface is flat and normal to the direction of propagation and the irradiance is constant over the surface, then the optical power on the receiver is defined as the product of the irradiance and the surface area of the receiver. Note that this definition does not account for reflection, transmission, or absorption of optical power; those effects are considered separately. Irradiance is defined as the optical power density (W/m^2) at the receiver.

Radiance is a method for describing the optical power produced by an optical source. Optical phased arrays and variable blaze gratings may be thought of as secondary sources, because they function by reflecting a large portion of the incident power. Radiance is the optical power emitted by a differential surface (dA_S) and projected in a beam solid angle ($d\Omega$) . Radiance defines how the optical power emitted from the surface of a source is distributed in angle. Incoherent sources such as a light bulb without additional optics are often isotropic over some large beam solid angle; their radiance is a weak function of angle in this range. The radiance for a coherent source such as a laser is typically a strong function of angle.

Exitance is similar to irradiance; it defines an optical power density as a function of surface area. However exitance is from the point of view of a source. Exitance is the optical power leaving the surface of a source as a function of the area of the surface (dA_S). Intensity is the optical power leaving a source in a beam solid angle ($d\Omega$).

All reflectances in this document are power reflectances (measured as a percent) unless otherwise noted. If a material has a reflectance of R and is illuminated so that a total optical power P falls on the surface of the object, then a power equal to $R \times P$ is reflected off the object. The E-field reflectance will be used in computing the Fourier transform of an optical transmittance; the E-field reflectance is equal to the square root of the power reflectance ($\sqrt{R}$).

4.1.1.2 Linear Optical Phased Arrays

All of the optical phased arrays constructed by the author were linear, consequently the theory presented in this section is for a linear optical phased array. Previous researchers at AFIT designed two-dimensional optical phased arrays that may have been capable of simultaneously steering a beam in two directions [2], however the author's application (the holographic data storage project) required a high fill factor and a single steering dimension. The previously designed two-dimensional optical phased arrays were unsuitable for this application because they had low fill factors (in addition to other considerations such as array period and array element curvature).

An optical phased array works by shifting the phase of the light reflected off each element in an array so that a wavefront is created in the desired direction. In the simplest case (a single reflected beam), a phased array is actually an approximation to a macromirror as shown in Figure 4.2. In Figure 4.2(a), a normally incident light is reflected off a macromirror that is tilted to an angle θ_r. The angle of the reflected light (with respect to the incident light) is equal to twice the tilt angle ($2\theta_r$) [3]. If the macromirror is divided into equal length segments (array elements), then the tilt angle can be approximated by shifting each array element down as shown in Figure 4.2(b). Although the individual array elements are not tilted, each array element is assumed to be small enough so that diffraction will spread the reflected light into the desired direction.

The distance that each array element is displaced causes a net phase change in the light reflected off the element. Equation (4.2) calculates the phase difference, δ, resulting from displacing an array element a distance d [3]:

$$\delta = \frac{2\pi}{\lambda} d \tag{4.2}$$

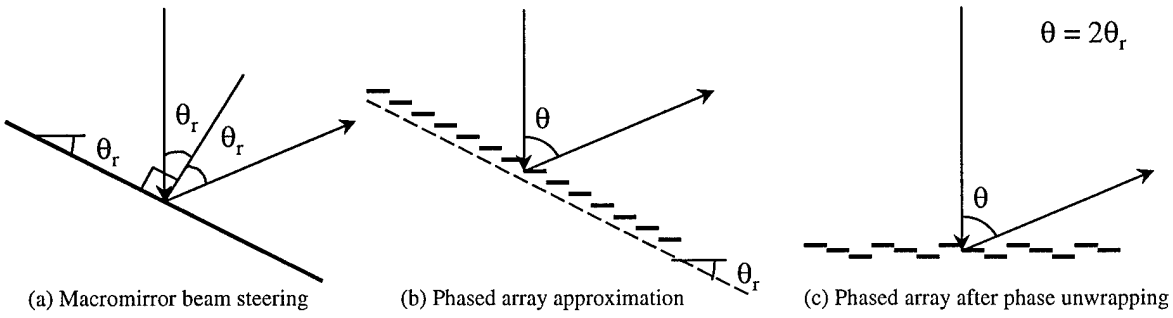

Figure 4.2 Principle of operation for a linear optical phased array.

where λ is the wavelength of the incident light. Phase differences of more than 2π radians can be unwrapped by repeatedly subtracting 2π until the net phase difference is in the range of 0 to 2π radians. So the displacement of each of the elements in Figure 4.2(b) can be reduced until the displacement results in a phase difference in the range of 0 to 2π radians; this displacement reduction was used to unwrap the phase in Figure 4.2(c). The key advantage of unwrapping the phase is that now the vertical displacement ranges from 0 to λ. Smaller array element vertical displacements reduces the complexity of the array. A disadvantage of using a phased array is wavelength dependence. Because the phased array relies on changing the phase of the reflected light using Equation (4.2), the incident light must be monochromatic (or nearly monochromatic).

Before the phase is unwrapped (Figure 4.2(b)), it is apparent that each array element is displaced a fixed distance from the previous array element (for a fixed array period). Figure 4.3 shows a method for calculating the inter-element deflection distance, α. In Figure 4.3, b is the array period and θ_r is tilt angle of the macromirror approximation line with respect to the horizon. The macromirror approximation line is simply a line through the center of each array element in Figure 4.2(b). The inter-element deflection distance can be calculated using Equation (4.3):

$$\alpha = b \tan \theta_r \tag{4.3}$$

Equation (4.3) can be used to calculate the beam steering angle, θ, by replacing θ_r with $\theta/2$ (as shown in Figure 4.2), and using a trigonometry identity:

$$\alpha = b \frac{\sin \theta}{1 + \cos \theta} \tag{4.4}$$

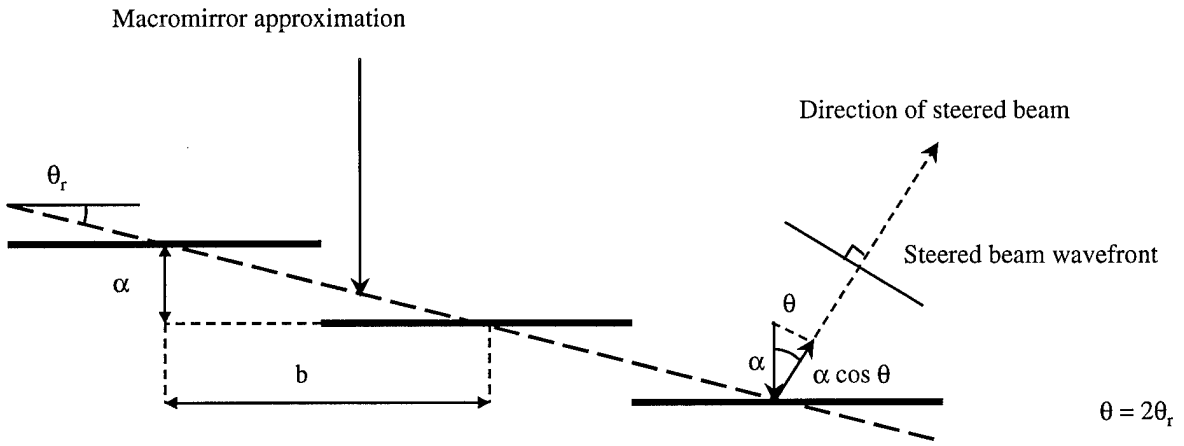

Figure 4.3 A method for calculating the inter-element deflection distance (α).

The inter-element phase difference, Ψ, can be calculated by multiplying Equation (4.4) by Equation (4.2) using an Optical Path Length (OPL) of $\alpha(1+\cos\theta)$:

$$\Psi = \frac{2\pi b}{\lambda}\sin\theta \tag{4.5}$$

The inter-element phase difference in Equation (4.5) is the round trip phase change for an inter-element deflection distance of α in the direction of the steered beam to the new steered beam wavefront (see the right hand side of Figure 4.3). The OPL used in Equation (4.5) is sometimes referred to as the obliquity factor [4]. Figure 4.2(c) was created by limiting Ψ to a range of 0 to 2π radians (unwrapping the phase). The beam steering angle resulting from a inter-element phase difference of Ψ is given by Equation (4.6):

$$\theta = \sin^{-1}\left(\frac{\Psi\lambda}{2\pi b}\right) \tag{4.6}$$

The maximum steering angle, θ_{max}, can be calculated from Equation (4.6) by substituting in $\Psi = 2\pi$:

$$\theta_{\max}\Big|_{\Psi=2\pi} = \sin^{-1}\left(\frac{\lambda}{b}\right) \tag{4.7}$$

For example, a linear optical phased array with a period of 30 μm that is illuminated by source at a wavelength of 632.8 nm has a maximum steering angle of 1.21°. Ideally, the array could steer a normally incident beam over the entire range of ±1.21°; however the existence of a secondary beam (a sidelobe) makes this impractical. When a fixed inter-element phase difference, Ψ, exists across the array in one direction, the

complement of inter-element phase difference, $2\pi-\Psi$, also exists on the array (in the opposite direction) as shown in Figure 4.4.

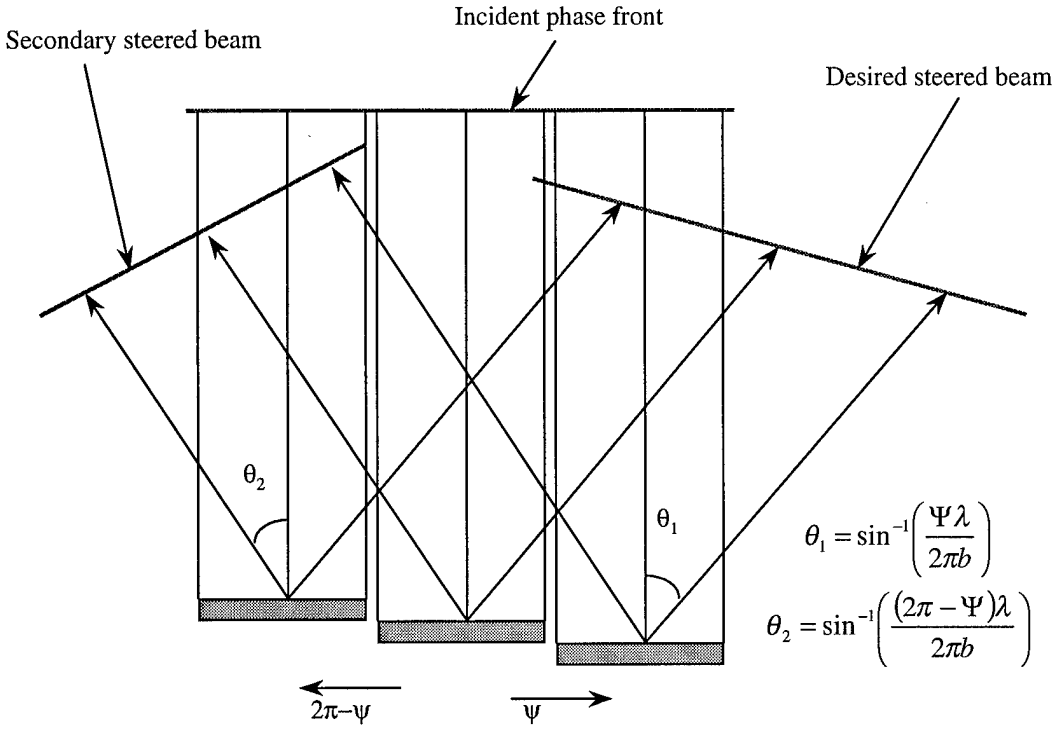

Figure 4.4 Existence of a secondary steered beam.

Because each element in the array is incrementally deflected, constant element to element phase differences exist in both directions on the array. The compliment of the desired inter-element phase difference creates a secondary steered beam moving in the opposite direction as Ψ. The secondary steered beam is usually undesirable because it steers light where the system designer may not want it. The secondary steered beam also reduces the intensity of the light in the intended steered direction by shifting some of the incident optical power into the secondary beam. These negative effects can be partially compensated by restricting Ψ to the range of $-\pi$ to $+\pi$ and using an aperture as shown in Figure 4.5. If Ψ is restricted to the range of $-\pi$ to $+\pi$, the maximum range of the beam steering angle can be calculated using Equation (4.8).

$$\theta_{\max}\Big|_{\Psi=\pi} = \sin^{-1}\left(\frac{\lambda}{2b}\right) \tag{4.8}$$

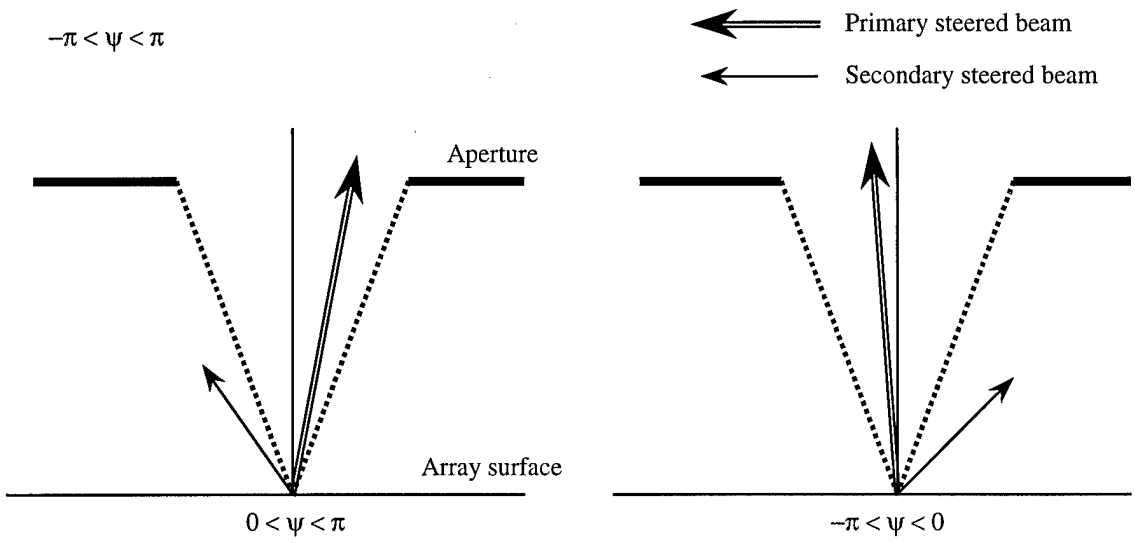

Figure 4.5 The use of an aperture to block the secondary steered beam. The image resulting from this aperture is the exit pupil.

All future calculations for a linear optical phased array's maximum beam steering angle are based on Equation (4.8). If Ψ is restricted to the range of $-\pi$ to $+\pi$, the range of the beam steering angle for the previous example is limited to the range of $\pm 0.604^{\circ}$. For a perfect array (all incident energy is reflected with no diffraction losses), the maximum optical efficiency at $\Psi = \pi$ is 50% because the magnitudes of the primary and secondary steered beams are equal. Linear optical phased arrays rely on changing the phase of reflected light so that constructive interference of the diffracted light in the far field supports the intended optical beam direction. Because these devices rely on phase, the optical efficiency of the array is a direct function of individual element surface flatness and the reflective region fill factor; these features will be modeled in Section 4.2.1.2.

4.1.1.3 Variable Blaze Gratings

Reflection gratings are often used to disperse incident light into angular directions (called interference orders) corresponding to the incident light's wavelength and the construction properties of the grating. Blazing, or contouring individual grating elements, is used to improve the ratio of light diffracted in a specific direction to the incident light (defined as the diffraction efficiency). Typical blazed gratings have a blaze angle that is

fixed at the time of construction. A variable blaze grating has an adjustable blaze angle that can be set as often as required after construction.

Grating interference orders result when light reflected off grating elements combines constructively in the far field. Figure 4.6 is a schematic diagram of a flat reflective grating producing constructive interference. The interference orders shown in Figure 4.6 result when light reflected off each grating element arrives at a location with the same phase. The location of constructive interference regions are sequentially numbered as diffraction orders (0,1,...,*m*). Light reflected off grating elements destructively adds in the regions between the orders. Because the phase of light arriving at the location of a diffraction order depends on the light's wavelength, the location of the orders in Figure 4.6 are wavelength dependent. The direction of a particular order, θ_m, resulting from normally incident light is given by Equation (4.9) [3]:

$$\theta_m = \sin^{-1}\left(\frac{m\lambda}{a}\right) \tag{4.9}$$

where m is the diffraction order number, λ is the wavelength of the source, and a is the grating's period (element width plus the width of the gap between two elements).

The intensity of light diffracted off a flat grating decreases rapidly as the interference order number increases. Blazing can be used to increase the intensity of light diffracted into a specific interference order. Variable blaze gratings operate by adjusting the blaze angle of each slat (VBG grating element) so that the specular reflection of the incident light matches a particular interference order. Figure 4.7 is a schematic diagram of a blazed grating. For normally incident light, the blaze angle γ_m required to select a particular diffraction order m is given by Equation (4.10).

$$\gamma_m = \frac{1}{2}\theta_m \tag{4.10}$$

The blaze angle is measured with respect to a plane parallel to the face of the grating. As the blaze angle increases, the optical efficiency declines. Optical efficiency is proportional to the fill factor (the ratio of the width of a VBG slat to the period). As the blaze angle increases, each VBG slat is tilted away from the horizon.

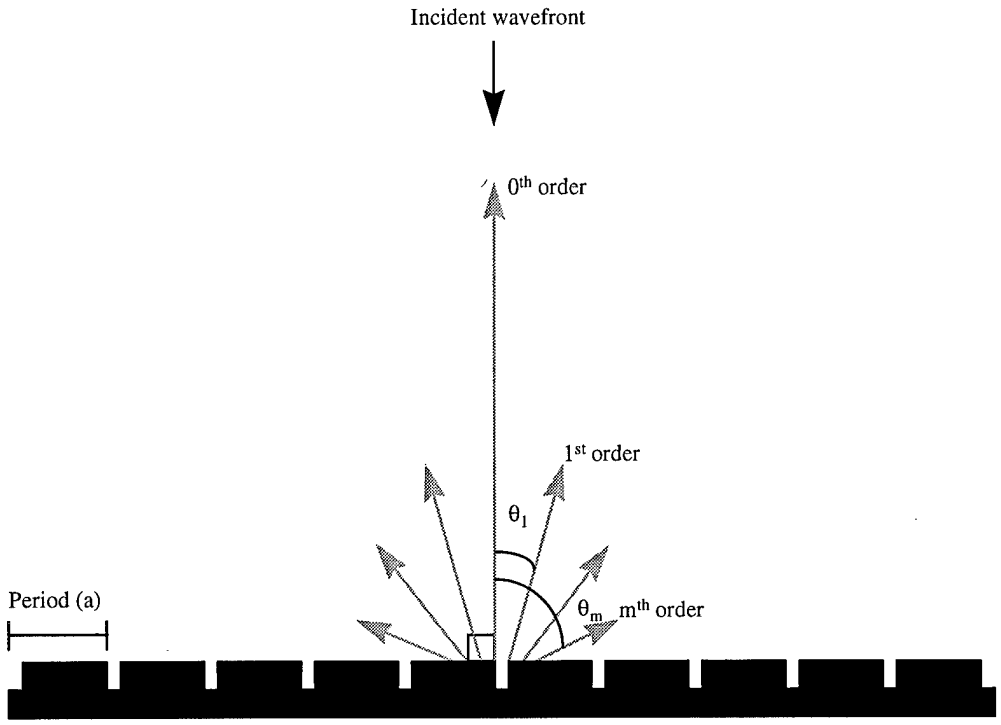

Figure 4.6 Schematic diagram of a reflective flat grating illuminated by normally incident light.

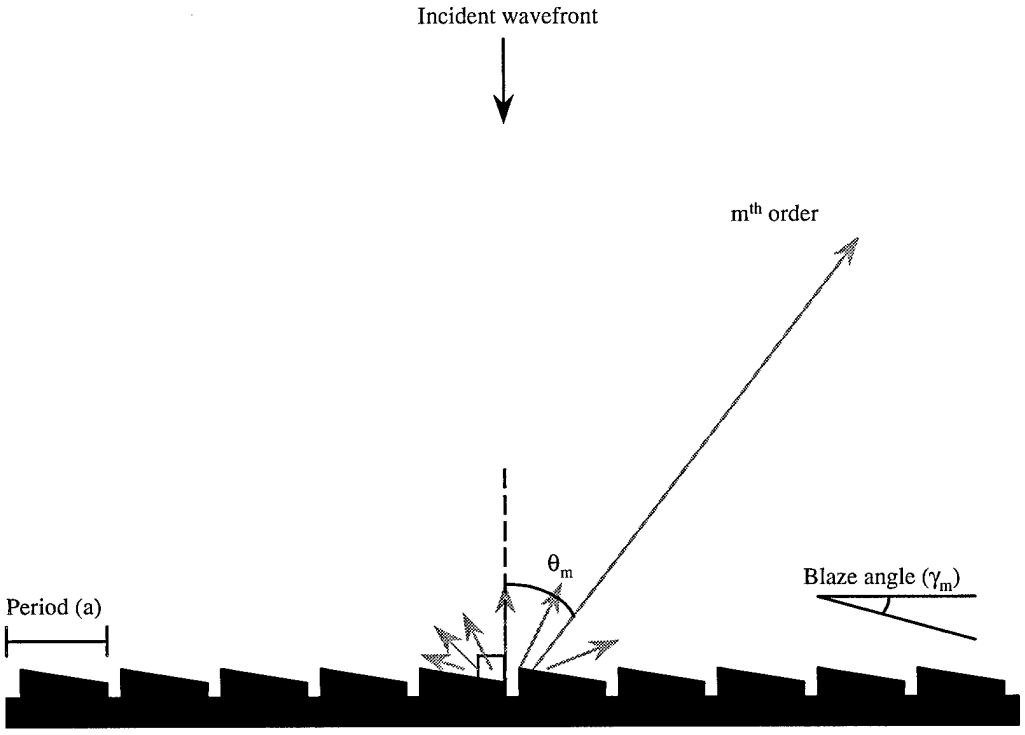

Figure 4.7 Schematic diagram of a reflective blazed grating illuminated by normally incident light.

The slat's cross-sectional area normal to the incident light is a function of the blaze angle:

$$f_m = \frac{w \cos \gamma_m}{a} \tag{4.11}$$

where f_m is the grating's fill factor for a particular interference order m and w is the width of the slat. Note that in Equation (4.11) the fill factor is independent of the slat's length.

Figure 4.8 presents the predicted diffraction pattern for 16 element and 32 element gratings blazed to support the first order (m=1). The gratings have a period of 38 μm and were illuminated by a normally incident 632.8 nm laser source. The elements in both gratings were flat (zero peak-to-valley curvature), constructed out of gold with a 1 μm polysilicon border on each side, and had a 2 μm gap between adjacent elements. Figure 4.8 was created using the author's Fast Fourier Transform (FFT) model presented in Section 4.2.1.3. The **y** axis in Figure 4.8 is the irradiance (W/m^2) on an object in the far field as a function of an angle measured from the **z** axis (normal to the face of the grating). The diffracted irradiance was normalized by setting the incident power on the whole grating equal to one watt. The definition of a far field will be presented in the next section.

The width of the main lobe (first order) for the gratings shown in Figure 4.8 is directly proportional to the number of elements; a grating's monochromatic divergence for a selected order can be improved by increasing the number of elements in the grating. A mathematical representation for a blazed grating's far field will be derived in Section 4.1.1.7. Most of the reflected light that does not go into the first order is distributed into the other diffraction orders. Increasing the diffraction efficiency of a diffraction order selected by the blaze angle therefore reduces the light in non-selected diffraction orders.

A promising application for VBGs is in spectrum analyzers. The chromatic resolving power, R, is a measure of a spectrum analyzer's ability to resolve small changes in the wavelength of incident light ($R=\lambda/\Delta\lambda$) and is given by Equation (4.12) for grating-based spectrum analyzers [3]:

$$R = mN \tag{4.12}$$

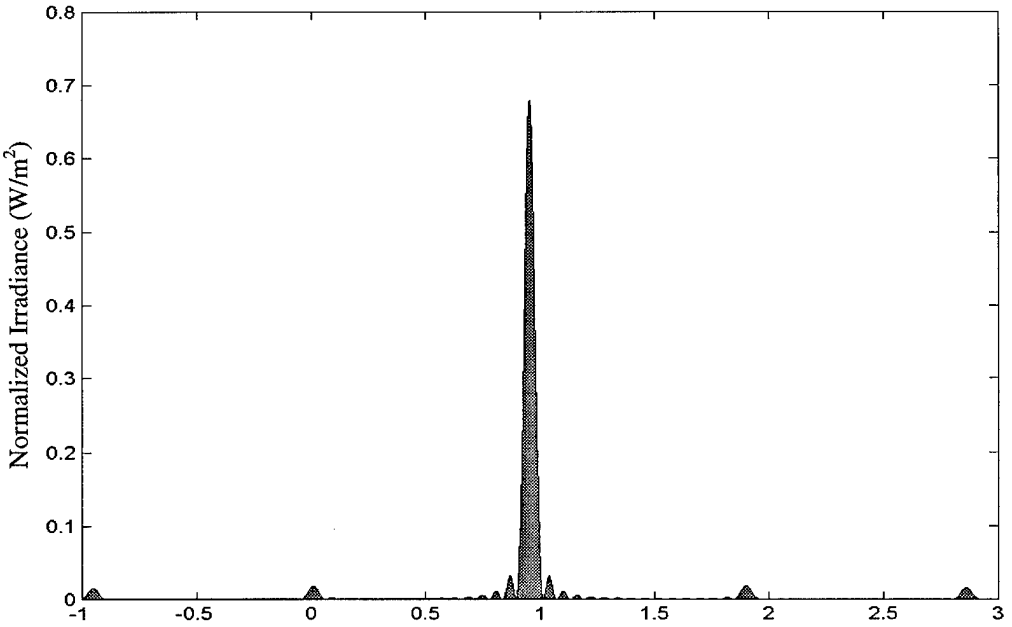

Steering Angle (degrees)
(a) 16 element

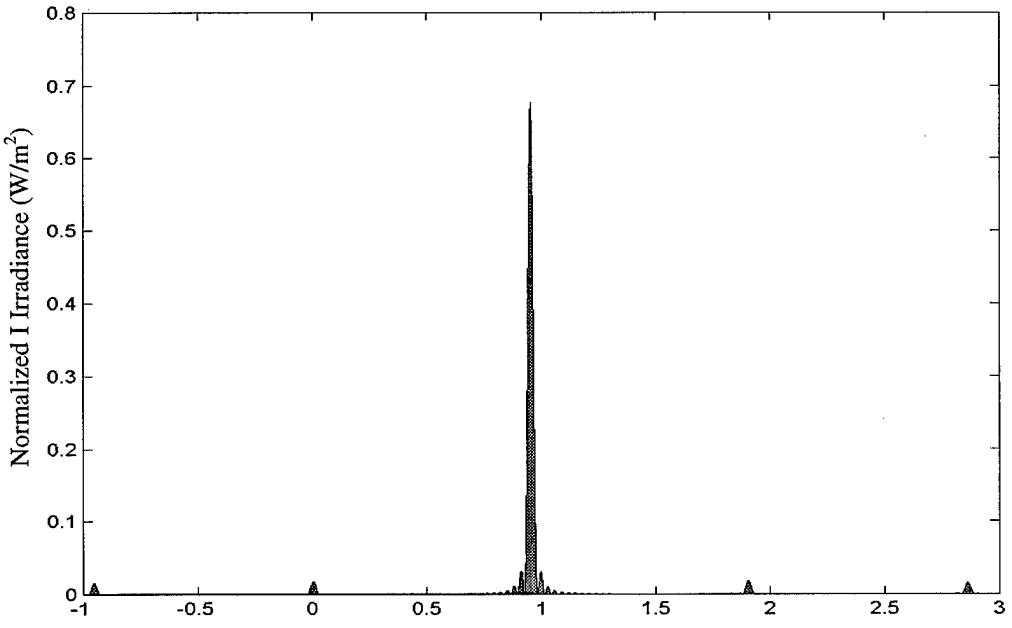

Steering Angle (degrees)
(b) 32 element

Figure 4.8. Far field patterns for gratings blazed to favor the first order. The main lobe is the first order and is located at +0.95 degrees. The zero order is located at 0.0 degrees, and the second order is located at +1.9 degrees.

where N is number of elements in the grating and m is the interference order number. The sensitivity of a grating-based spectrometer can be improved by increasing the number of grating elements and by operating at a higher interference order. Selectable blaze angles supporting multiple diffraction orders (unavailable until the invention of the VBG by the author) allow intelligent spectrum analyzers to trade receiver signal strength for frequency resolution in real time. Receiver signal strength is reduced as the interference order number increases (by Equation (4.11)); frequency resolution is increased as the interference order number increases.

4.1.1.4 Decentered Lens Beam Steering

This section presents an overview of the theory behind beam steering using microlenses (lenslets). Only the geometric theory relevant to the author's research will be discussed; a more complete discussion of beam steering using lenslets can be found in [5,6,7]. Fresnel lens properties and the lens-maker equation will also be introduced because they were used to develop the author's decentered lens beam steering system designs.

A double lens beam steering system is shown in Figure 4.9. The focal lengths of the first microlens (plane 1) and the second microlens (plane 3) are f_1 and f_2, respectively. The focal length of the first microlens is larger than the second microlens. L_1 and L_2 are the diameters of the first and second microlenses, respectively. Normally incident collimated light enters the first microlens at plane 0 from the left and is focused to it's minimum waist size at plane 2. The light then expands and is collimated again by the second microlens at plane 3. The distance the second microlens is displaced from the optical axis is Δ. The beam steering angle, θ, can be found by ray tracing. The formula for the beam steering angle is given by Equation (4.13).

$$\theta = \tan^{-1}\left(\frac{\Delta}{f_2}\right) \tag{4.13}$$

The maximum steering angle for the double lens system, θ_{max}, can be calculated using ray-tracing, and is given by Equation (4.14):

$$\theta_{max} = \tan^{-1}\left(\frac{L_2}{2f_2} - \frac{L_1}{f_1 + f_2}\right) \tag{4.14}$$

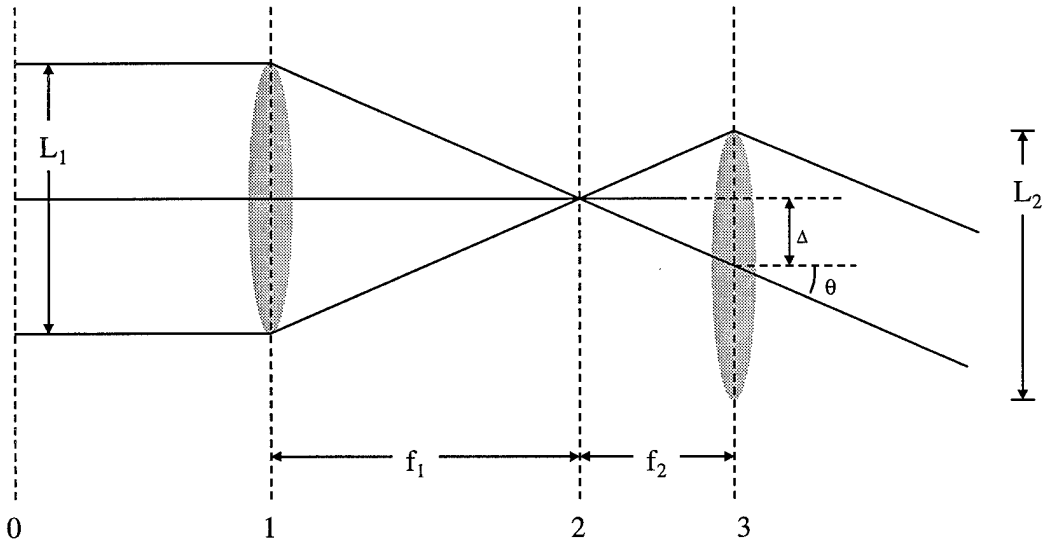

Figure 4.9. A double lens beam steering system [5].

Equation (4.14) was derived by limiting the steering angle so that all of the light passing through the first microlens falls on the second microlens. Note that if both lenses have identical construction properties (same diameter and focal length), then the maximum beam steering angle producing no scattered light is zero. The vertical displacement required to reach θ_{max} is Δ_{max} and is given by Equation (4.15):

$$\Delta_{max} = \frac{L_2}{2} - \frac{f_2 L_1}{f_1 + f_2} \tag{4.15}$$

The fill factor for light exiting the second microlens is less than unity (for non-identical microlenses) and is given by Equation (4.16):

$$fill\ factor = \frac{2f_2}{f_1 + f_2}\left(\frac{L_1}{L_2}\right) \tag{4.16}$$

For a discussion of non-normally incident light, see [8].

The triple lens beam steering system shown in Figure 4.10 was designed to improve the fill factor of the double lens system by inserting a field lens [5]. The field lens at plane 2 in Figure 4.10 is aligned with the second microlens; all three lens have equal diameters (L) and focal lengths (f). The beam steering angle, θ, for the triple lens system can be calculated using ray tracing and is given by Equation (4.17).

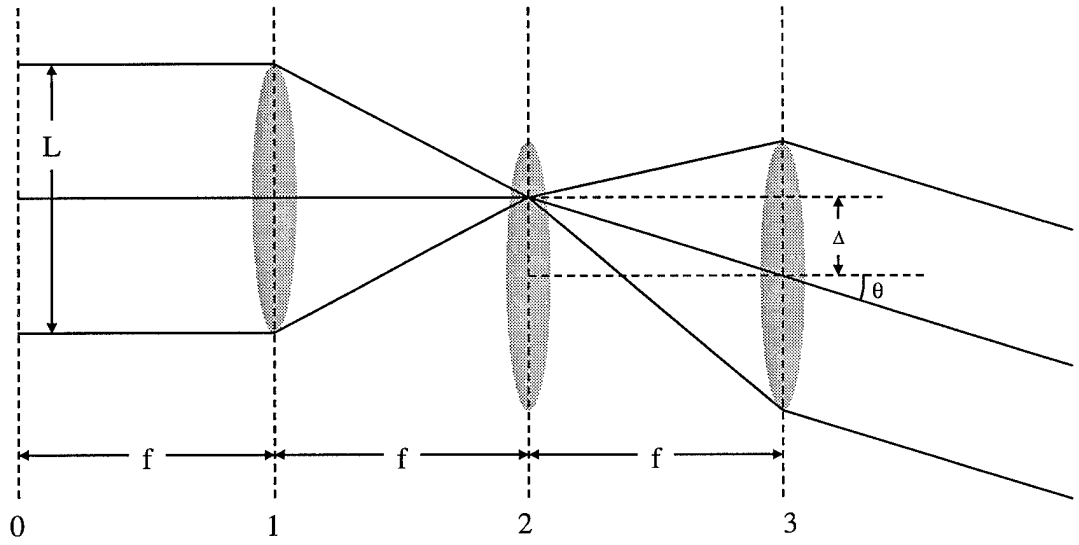

Figure 4.10. A triple lens beam steering system [5].

$$\theta = \tan^{-1}\left(\frac{\Delta}{f}\right) \tag{4.17}$$

The maximum steering angle for the triple lens system, θ_{max}, can be calculated using ray-tracing and is given by Equation (4.18):

$$\theta_{max} = \tan^{-1}\left(\frac{L}{2f}\right) \tag{4.18}$$

The vertical displacement required to reach θ_{max} for the triple lens system is Δ_{max} and is given by Equation (4.19):

$$\Delta_{max} = \frac{L}{2} \tag{4.19}$$

Ideally the fill factor for light exiting the triple lens system is unity. However diffraction losses reduce the intensity of the steered light. The addition of the field lens not only improves the fill factor for light exiting the system, it also increases the maximum beam steering angle (if the diameter of the second microlens in the double lens system, L_2, is equal to the diameter of the lens in the triple lens system, L).

Fresnel lenses (also called zone plates) use diffraction and constructive interference to shape the near-field intensity exiting the lens. Two types of Fresnel lenses have been extensively used: zone blocking plates and phase-reversing zone plates. Light diffracted through a circular aperture can be divided into positive and negative zones as a result of applying Huygen's principle to the light in the aperture [3]. Zone plates that block alternate zones are called zone blocking plates. Zone plates that retard the phase of light in alternate zones by π radians are called phase reversing plates. Figure 4.11 depicts two zone blocking plates.

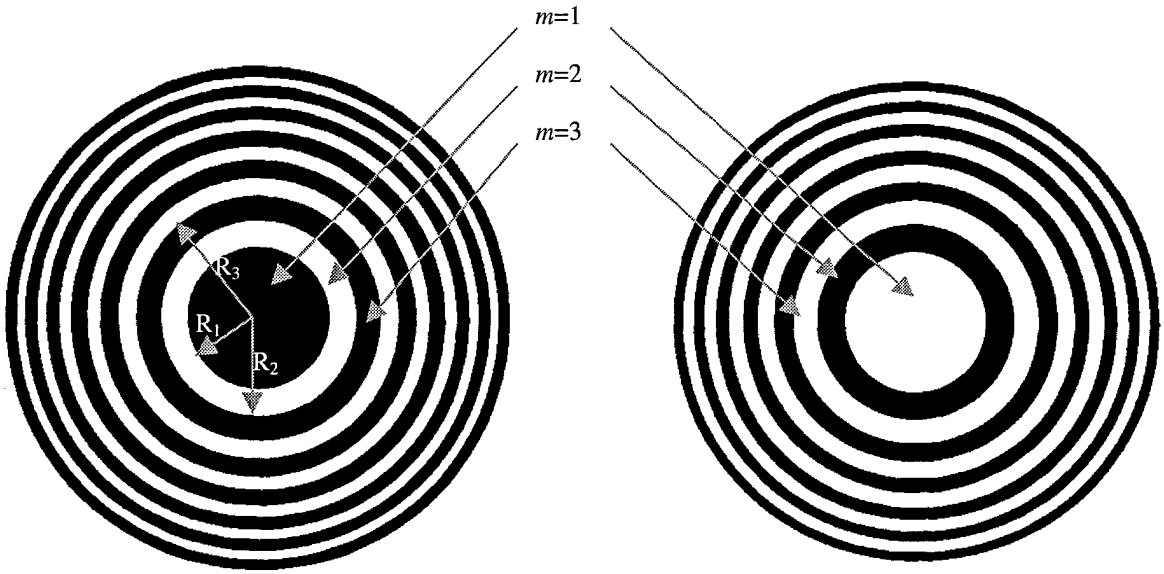

Figure 4.11. A pair of zone blocking plates. The plate on the left has odd numbered zones blocked; the plate on the right has even numbered plates blocked. If the black region in each plate transmitted incident light with a equivalent phase delay of π radians (compared to light passing through the white regions), then the plates would become phase reversing zone plates [3].

A zone plate can be constructed using surface micromachining by patterning a polysilicon layer so that the polysilicon is removed in the alternate zones. Chapter 7 presents a detailed review of Fresnel lens

fabrication using MUMPs and includes SEM micrographs of completed lenses; these lenses were constructed using the zone outer radius R_m calculated by Equation (4.20) [3]:

$$R_m = \sqrt{mf\lambda} \tag{4.20}$$

where m is the largest integer number of zones used in the lens, λ is the wavelength of the source, and f is the desired primary focal length. The same units (microns, nanometers, etc.) should be used for R_m, f, and λ in Equation (4.20). After the Fresnel lens is constructed, the primary focal length is:

$$f = \frac{R_m^2}{m\lambda} \tag{4.21}$$

The primary focal length is a direct function of the source wavelength, so Fresnel lenses are specifically designed for monochromatic (or nearly monochromatic) light.

Microlenses can be constructed from photoresist [9] or polyurethane. The focal length of the microlens can be calculated using the lens-maker equation provided the lens is thin. A thin lens is a lens that has a thickness that is much less than the focal length and the object and image distances [4]. A schematic diagram of a thin lens is shown in Figure 4.12. R and R' are the radius of curvature for the left and right lens surfaces, respectively. R' is negative because of the sign convention used in Figure 4.12 (concave to the left). D is the thickness of the lens and n is the index of refraction for the lens material.

The power P_{thin} of the thin lens shown in Figure 4.12 can be calculated using the lens-maker equation given in Equation (4.22) [4]:

$$P_{thin} = (n-1)\left(\frac{1}{R} - \frac{1}{R'}\right) \tag{4.22}$$

Equation (4.22) is for lens operation in air or a vacuum (n=1 outside the lens). The thin lens focal length f_{thin} can be calculated from the power by Equation (4.23):

$$f_{thin} = \frac{1}{P_{thin}} \tag{4.23}$$

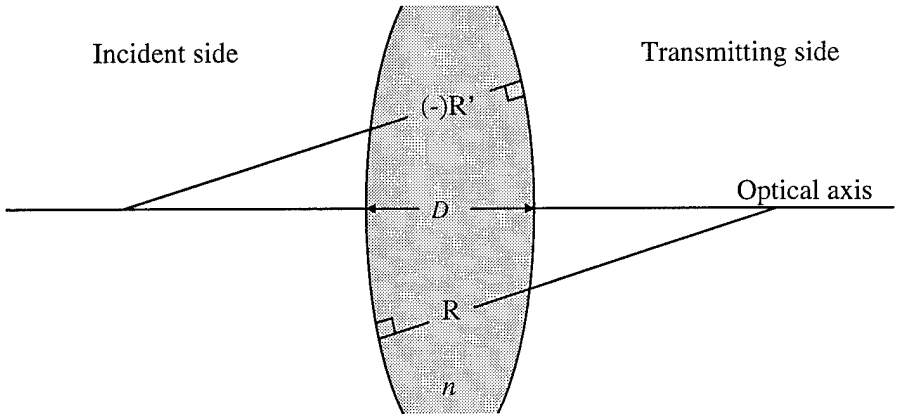

Figure 4.12. A schematic diagram of a thin lens.

Substituting Equation (4.22) into Equation (4.23) gives a direct calculation for the thin lens focal length:

$$f_{thin} = \frac{RR'}{(n-1)(R'-R)} \tag{4.24}$$

Note that when R' is equal to infinity (a single sided lens such as a lens fabricated using photoresist [9]), Equation (4.24) reduces to:

$$f_{thin} = \frac{R}{n-1} \tag{4.25}$$

4.1.1.5 Divergence Angle

Micromachining processes limit practical micromirrors to a maximum size, often several orders of magnitude less than the dimensions of the die. MUMPs, for example, limits releasable structures to a maximum width of about 100 μm, if etch holes are not used. State-of-the-art MUMPs-based micromirrors have a maximum diameter of 100 μm. If the illuminating beam is larger than the micromirror (typical case), the micromirror can be modeled as a plane wave illuminated aperture. Diffraction occurs as a result of reducing a plane wave from its theoretical infinite extent to a finite area. The degree of diffraction is inversely related to

the size of the aperture. Light passing through smaller apertures is diffracted more. The angle of divergence depends only on the beam diameter and the wavelength of the incident light, provided the micromirror is flat. The far field divergence angle, θ, for a round flat micromirror with a diameter of D at a source wavelength, λ, of 632.8 nm (a HeNe laser) can be approximated by Equation (4.26) [4,10]:

$$\theta = 1.22\frac{\lambda}{D} \tag{4.26}$$

At a distance d, the diameter of the Airy disk, s, resulting from this divergence angle is:

$$s = 2d\tan\left(\frac{\theta}{2}\right) \tag{4.27}$$

For example, if a 100 μm diameter round flat micromirror is illuminated by a laser operating at 632.8 nm, then the diameter of the Airy disk at a distance of 100 m is 77.2 cm. The large divergence of light reflected off single micro-optical devices makes the use of multi-element devices (such as linear optical phased arrays and VBGs) attractive for long distance applications. Long distance applications include laser radar, laser range-finding, and bomb guidance.

If the mirror is curved, perhaps as a result of residual material stress, the output beam will be defocused in the far field. Such curvature yields a larger divergence angle. Therefore if the divergence of a beam steered by a micromirror is too high, the physical or apparent size of the mirror must be increased and curvature must be reduced or corrected with additional optical components. The apparent size of the micromirror can be increased by using a source with a shorter wavelength or using arrays of micromirrors.

A micromirror curved by residual material stress is depicted in Figure 4.13. The peak-to-valley curvature of the micromirror is P and the linear diameter of the micromirror is D. The radius of curvature, R, can be estimated using Equation (4.28) derived from the Pythagorean theorem.

$$R^2 = (R-P)^2 + \left(\frac{D}{2}\right)^2 \tag{4.28}$$

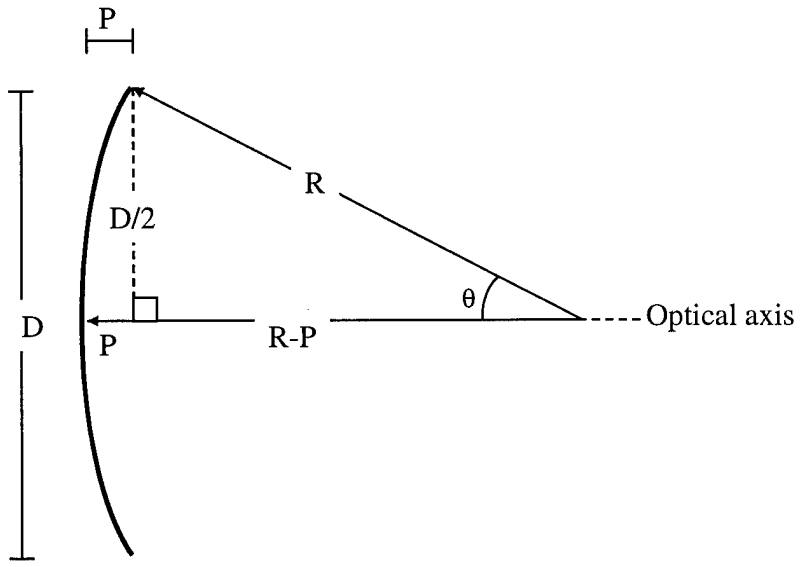

Figure 4.13. Diagram for estimating a radius of curvature, R, given a peak-to-valley curvature, P.

After simplification, Equation (4.28) reduces to:

$$R = \frac{P}{2} + \frac{D^2}{8P} \tag{4.29}$$

Equation (4.29) is useful because the peak-to-valley curvature for a given micromirror can be easily determined using an interferometric microscope such as the ZYGO model MAXIM-3D. Once the radius of curvature is known, the effects of the curvature can be predicted. Figure 4.14 depicts a curved micromirror illuminated by a coherent plane wave (not shown) with a wavelength of λ. The beam is focused to its minimum waist size at a distance f from the micromirror. The focal length for a spherical mirror is given by Equation (4.31) provided $D >> \lambda$ [3]:

$$f = \frac{R}{2} \tag{4.30}$$

The full divergence angle, θ_d, is given by Equation (4.31):

$$\theta_d = 2\sin^{-1}\left(\frac{D}{2R}\right) \tag{4.31}$$

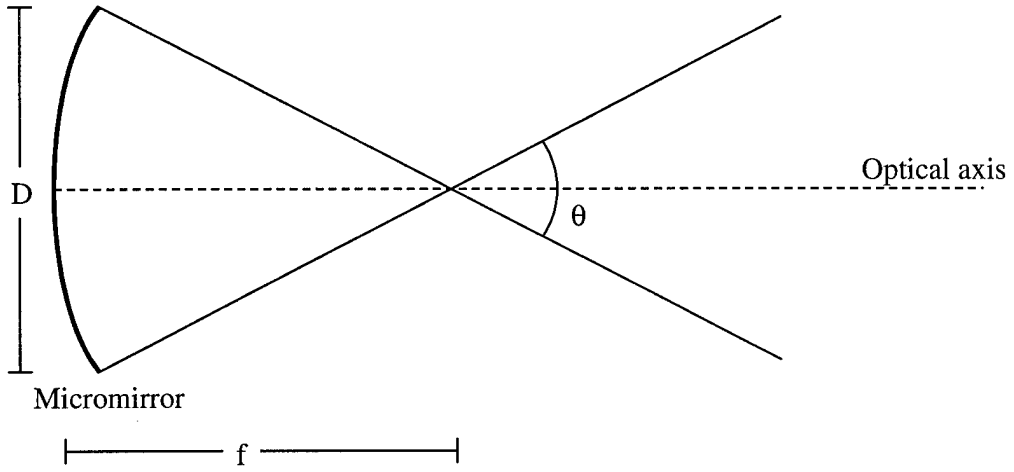

Figure 4.14. A schematic diagram of coherent light reflected off a curved micromirror.

provided $D >> \lambda$. Note that Equation (4.31) does not take into account the divergence from diffraction resulting when D is not much greater than λ; Equation (4.26) should be used in this case.

The micromirror's linear diameter is reduced from its design value by residual material stress induced curvature. If the micromirror's surface is modeled as spherical, then the linear diameter, D, is related to the design length L. The angle θ in Figure 4.13 can be used to calculate D as a function of L and P. L is an arc on a circle of radius R. If $\theta=2\pi$, then L would equal the circumference of this circle, $L=2\pi R$. Therefore L is directly proportional to θ and can be calculated using Equation (4.32):

$$\frac{L}{2} = 2\pi R\left(\frac{\theta}{2\pi}\right) \tag{4.32}$$

Note that in Figure 4.13 the angle θ is the half angle (corresponding to half of the micromirrors length); the design length L in Equation (4.32) is divided by two to compensate. The angle θ in Figure 4.13 can be derived using Equation (4.33):

$$\theta = \sin^{-1}\left(\frac{D}{2R}\right) \tag{4.33}$$

L can be related to D by substituting Equation (4.32) into Equation (4.33):

$$L = 2R\sin^{-1}\left(\frac{D}{2R}\right) \tag{4.34}$$

Solving Equation (4.34) for D yield Equation (4.35):

$$D = 2R\sin\left(\frac{L}{2R}\right) \tag{4.35}$$

To construct a 100 μm diameter (linear length after fabrication, D) micromirror using POLY-2 only (typical peak-to-valley curvature is 500 nm), the required design length, L, could be calculated by first estimating the radius of curvature using Equation (4.29). In this example, the radius of curvature would be 2,500.25 μm. The required design length L can now be calculated using Equation (4.34). In this example, the required design length L is 100.0067 μm (which is well below the design tolerances). So for the micromirrors designed by the author using MUMPs, the reduction in micromirror diameter caused by residual stress induced curvature is negligible.

4.1.1.6 Predicting the Far Field Using Fourier Analysis

The far field is the spatial intensity pattern at a distance z from an optical device. The optical device may be a source (a laser), a reflector (micromirrors in an optical phased array), or a transmitter (a lens). The distance z is many times the source wavelength so that the shape of the resulting image is invariant; however the size of the resulting image is proportional to the distance [11]. Equation (4.36) is the Fraunhofer condition and can be used to bound z [11]:

$$|z| >> \frac{\pi L^2}{\lambda} \tag{4.36}$$

where L is the maximum radial extent of the optical device and λ is the wavelength of the source. The distance z can be positive or negative depending on the coordinate system used. A factor of ten is commonly used as an estimate for the "much greater than" sign in Equation (4.36) [11]. Applying Equation (4.36) to a 3 mm wide VBG illuminated by a HeNe laser operating at 632.8 nm gives a far field distance of 1.2 m. In this far field

example, each VBG slat is 3 mm long (typical widths vary from 20 μm to 100 μm); when illuminated by a circular laser beam, the maximum radial extent of the illuminated region is 1.5 mm. Unless stated otherwise, all of the optical theory and modeling presented by the author will be in the far field.

The shape and relative phase distribution of the spatial intensity pattern resulting from an optical device is invariant in the far field and can be predicted using the Fraunhofer approximation to the Rayleigh-Sommerfeld diffraction formula. The Fraunhofer approximation is the square of the absolute value of the Fourier transform of the optical device's transmittance $t(x,y)$ scaled by $1/(z\lambda)$. The transmittance is the magnitude and phase at each point (x,y) on a plane across the face of the optical device. The resulting irradiance $E(x,y)$ on an observation plane at a distance z can be predicted by Equation (4.37):

$$E(x,y) = E_s\left(\frac{1}{z\lambda}\right)^2 \left|\Im\left[t\left(\frac{x}{z\lambda},\frac{y}{z\lambda}\right)\right]\right|^2 \tag{4.37}$$

where $\Im[t]$ is the Fourier transform of the transmittance function, t [11]. E_s is the irradiance from a source onto the device and is assumed to be uniform (not a function of (x,y)). Note that the variables x and y used to denote the position in the plane of the transmittance function have each been scaled by $1/(z\lambda)$. The SI units for irradiance are watts per square meter and the transmittance function is unitless. A transmittance function for an optical array or variable blaze grating consists of the E-field reflectivity and relative phase difference as a function of location on the array. Equation (4.37) is for Fraunhofer diffraction and will be applied to a variable blazed grating in the next section.

The two dimensional Fourier transform and inverse Fourier transform are defined in Equations (4.38) and (4.39):

$$\Im(f(x,y)) = \int_{-\infty}^{\infty}\int f(x,y)e^{-i2\pi(\xi x+\eta y)}dxdy = F(\xi,\eta) \tag{4.38}$$

$$\Im^{-1}(F(\xi,\eta)) = \int_{-\infty}^{\infty}\int F(\xi,\eta)e^{i2\pi(\xi x+\eta y)}d\xi d\eta = f(x,y) \tag{4.39}$$

Fourier analysis is a powerful tool because it relates physical dimensions (aperture and relative phase differences) and material properties (such as reflectance) to the far field. The author will use Equation (4.37) in

Section 4.2.1 to model the predicted far field intensity patterns of optical phased arrays and variable blaze gratings.

4.1.1.7 Example: Fourier Analysis of a Variable Blazed Grating

The Fourier analysis presented in the previous section will be applied to a variable blazed grating example in this section. The objective of this analysis is to develop a far field irradiance plot (similar to Figure 4.8) for a variable blazed grating. This example will be used to relate the diffraction efficiency to the far field irradiance plot. The resulting VBG far field irradiance equation will be used to validate the author's model of a VBG.

A cross-sectional view of a simplified variable blazed grating is shown in Figure 4.15. The reflective surface of each slat is tilted at a blaze angle θ_b. The width of each slat is w and the length of each slat is L (length is not shown in Figure 4.15). The initial gap between adjacent slats (θ_b=0) is g. The surface area of each slat that is normal to the face of the grating decreases as the blaze angle increases; the length of the gap between adjacent slats increases as the blaze angle increases. The array period a is equal to $w + g$. The OPL ($2x \tan \theta_b$) of light reflected off a grating element depends on the location (labeled as x in Figure 4.15) where it strikes the grating element. Equation (4.40) calculates the phase change $\phi(x)$ resulting from the tilted grating surface.

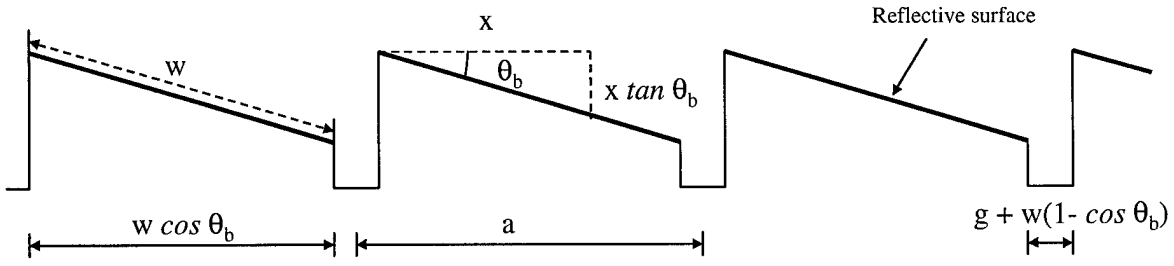

Figure 4.15. A cross-sectional view of a blazed grating.

$$\phi(x) = \frac{2\pi}{\lambda} 2x \tan\theta_b \tag{4.40}$$

The *rect* function is defined in Equation (4.41) and will be used to define a grating element [11]:

$$rect(x) = \begin{cases} 0 & for \quad \left|\frac{x - x_0}{b}\right| > \frac{1}{2} \\ \frac{1}{2} & for \quad \left|\frac{x - x_0}{b}\right| = \frac{1}{2} \\ 1 & for \quad \left|\frac{x - x_0}{b}\right| < \frac{1}{2} \end{cases} \tag{4.41}$$

where b is the length over which the *rect* function has a nonzero value. The center of the length over which the *rect* function has a nonzero value is x_0. The transmittance function for a single slat $t_e(x,y)$ can be written as:

$$rect\left(\frac{x}{w\cos\theta_b}\right) rect\left(\frac{y}{L}\right) e^{i\phi(x)} \tag{4.42}$$

Equation (4.42) includes both the sampled element area (the *rect* functions) and phase ($e^{i\phi(x)}$). If the transmittance functions for all of the elements in the grating are added together, a transmittance function, $t(x,y)$, for a blazed grating can be written as:

$$rect\left(\frac{x}{w\cos\theta_b}\right) rect\left(\frac{y}{L}\right) e^{i2\pi\frac{2x}{\lambda}\tan\theta_b} + rect\left(\frac{x-a}{w\cos\theta_b}\right) rect\left(\frac{y}{L}\right) e^{i2\pi\frac{2(x-a)}{\lambda}\tan\theta_b} + \cdots + rect\left(\frac{x-(N-1)a}{w\cos\theta_b}\right) rect\left(\frac{y}{L}\right) e^{i2\pi\frac{2(x-(N-1)a)}{\lambda}\tan\theta_b} \tag{4.43}$$

where N is the number of elements in the grating.

An *impulse* function $\delta(x)$ is any function that meets the restrictions of Equations (4.44) and (4.45) [11]:

$$\delta(x - x_0) = 0 \quad for \quad x \neq x_0 \tag{4.44}$$

$$\int_{x_1}^{x_2} f(x)\delta(x - x_0)\, dx = f(x_0) \quad iff \quad x_2 > x_0 > x_1 \tag{4.45}$$

An *impulse* function is often used to represent periodic functions. Equation (4.46) defines the shifting property of an *impulse* function [11]:

$$f(x) * \delta(x - x_0) = f(x - x_0) \tag{4.46}$$

The convolution operation, * , for two functions f(x) and g(x) is:

$$f(x) * g(x) = \int_{-\infty}^{\infty} f(\alpha)\, g(x-\alpha)\, d\alpha \tag{4.47}$$

Equation (4.43) can be rewritten as a convolution of a single element with an evenly spaced number of *impulse* functions:

$$t(x,y) = rect\left(\frac{x}{w\cos\theta_b}\right) rect\left(\frac{y}{L}\right) e^{i\frac{2\pi}{\lambda}2x\tan\theta_b} * \left[\sum_{n=1}^{N} \delta\left(x-(n-1)a\right)\right] \tag{4.48}$$

using the shifting property of the *impulse* function. The right hand side of Equation (4.48) is often called a *comb* function. The transmittance function in Equation (4.48) is unitless. Equation (4.48) is not symmetric about the **z** axis (located at x=0 and y=0); instead it has a range of:

$$-w\cos\theta_b \le x \le w\cos\theta_b + a(N-1) \tag{4.49}$$

$$-\frac{L}{2} \le y \le \frac{L}{2} \tag{4.50}$$

To avoid a non-symmetrical far field irradiance pattern, Equation (4.49) will have to be shifted on the **x** axis so that:

$$-\frac{a(N-1)}{2} - w\cos\theta_b \le x \le w\cos\theta_b + \frac{a(N-1)}{2} \tag{4.51}$$

Equation (4.52) is the result of shifting Equation (4.48) by $-a(N\text{-}1)/2$:

$$t(x) = rect\left(\frac{x}{w\cos\theta_b}\right) rect\left(\frac{y}{L}\right) e^{i\frac{2\pi}{\lambda}2x\tan\theta_b} * \sum_{n=1}^{N} \delta\left(x - \left(n-1-\frac{N-1}{2}\right)a\right) \tag{4.52}$$

The next step is a Fourier transform of Equation (4.52). Some important properties of the Fourier transform are listed in Appendix B. To obtain the Fraunhofer irradiance pattern for the variable blaze grating in this example, the Fourier transform of the transmittance function must be evaluated at $u=x/(\lambda z)$ and $v= y/(\lambda z)$. Equation (4.53) is repeated from the previous section for convenience:

$$E(u,v) = E_s\left(\frac{1}{z\lambda}\right)^2 \left|\Im[t(\varsigma,\eta)]\right|^2\Big|_{\varsigma=\frac{x}{z\lambda};\ \eta=\frac{y}{z\lambda}} \tag{4.53}$$

where u is on an axis parallel to the **x** axis and v is on an axis parallel to the **y** axis; u and v are both in the far field. Figure 4.16 is a diagram of the axis system used to calculate the far field irradiance pattern.

Applying the Fourier transform properties listed in Appendix B to Equation (4.52) yields:

$$\Im(t(x,y)) = \left[\Im\left(rect\left(\frac{x}{w\cos\theta_b}\right)rect\left(\frac{y}{L}\right)\right) * \Im\left(e^{i\frac{2\pi}{\lambda}2x\tan\theta_b}\right)\right]\Im\left(\sum_{n=1}^{N}\delta\left(x-\left(n-1-\frac{N-1}{2}\right)a\right)\right) \tag{4.54}$$

Equation (4.54) is the Fourier transform portion of Equation (4.53). After the Fourier transforms are evaluated, Equation (4.55) becomes:

$$T(u,v) \equiv \Im(t(x,y)) = \left[|wL\cos\theta_b|\,\mathrm{sinc}(w\cos\theta_b u)\mathrm{sinc}(Lv) * \delta\left(u-\frac{2\tan\theta_b}{\lambda}\right)\right]\sum_{n=1}^{N} e^{-i2\pi a\left(n-1-\frac{N-1}{2}\right)} \tag{4.55}$$

where the *sinc* function is defined as.

$$\mathrm{sinc}\left(\frac{x-x_0}{b}\right) = \frac{\sin\left(\pi\dfrac{x-x_0}{b}\right)}{\pi\left(\dfrac{x-x_0}{b}\right)} \tag{4.56}$$

The limit of *sinc(x)* for $x=0$ is 1 (using L'Hopital's rule) and the author is using Gaskill's definition for a *sinc* function that includes an embedded factor of π [11]. Equation (4.55) can be simplified using the identity:

$$\sum_{n=1}^{N} e^{-i2\pi u\left(n-1-\frac{N-1}{2}\right)a} = \frac{\sin(-N\pi ua)}{\sin(-\pi ua)} \tag{4.57}$$

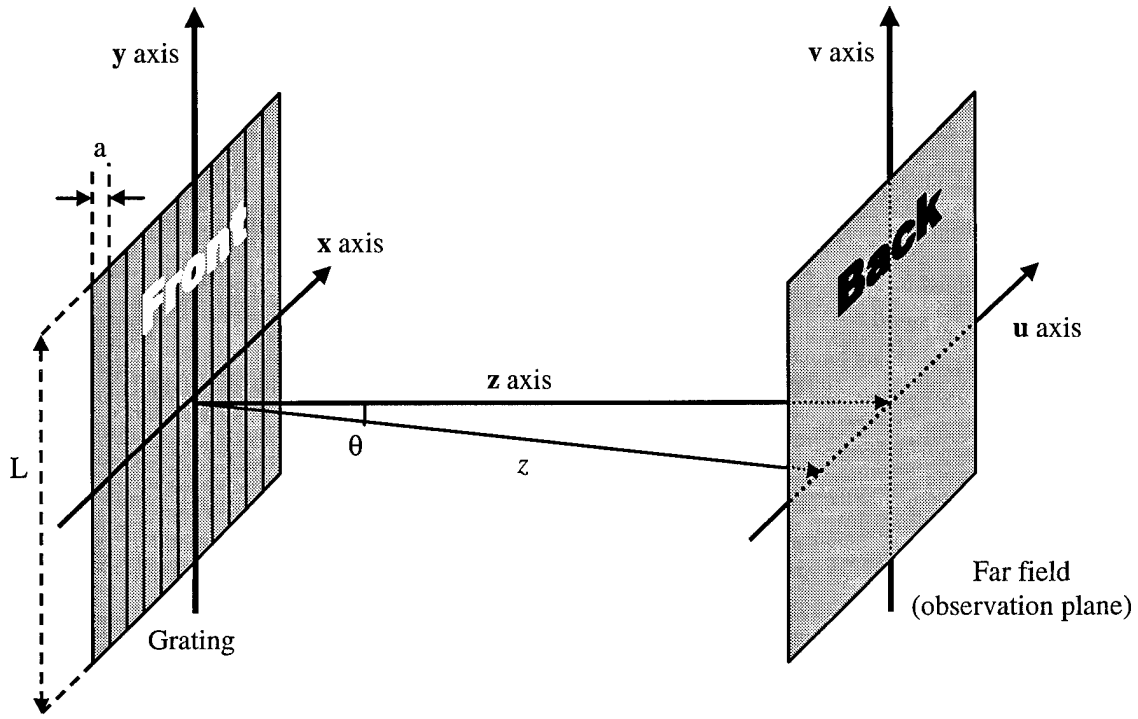

Figure 4.16. Diagram of the axis system used to calculate the Fraunhofer diffraction pattern. The grating is facing the right. The observation plane is transparent so that the locations of the **u** axis, **v** axis, and **z** axis are visible. Note that the axis perpendicular to the **x** axis and the **y** axis is the **z** axis and the distance from the grating to each element in the far field is z; the author uses bold letters for each axis title and italic letters for distances and variables.

The author provides a proof of Equation (4.57) in Appendix B. Substituting Equation (4.57) into Equation (4.55) and applying Equation (4.46) yields:

$$T(u,v) = \left|wL\cos\theta_b\right| \operatorname{sinc}\left(w\cos\theta_b \left(u - \frac{2\tan\theta_b}{\lambda} \right) \right) \operatorname{sinc}(Lv) \frac{\sin(-N\pi ua)}{\sin(-\pi ua)} \tag{4.58}$$

Expanding the terms in the first *sinc* function gives:

$$T(u,v) = \left|wL\cos\theta_b\right| \operatorname{sinc}\left(w\cos\theta_b u - \frac{2w\sin\theta_b}{\lambda} \right) \operatorname{sinc}(Lv) \frac{\sin(-N\pi ua)}{\sin(-\pi ua)} \tag{4.59}$$

Substituting Equation (4.59) into Equation (4.53) and scaling u and v by $1/(\lambda z)$ gives:

$$E(u,v) = E_s\left(\frac{wL\cos\theta_b}{z\lambda}\right)^2 \text{sinc}^2\left(\frac{w\cos\theta_b u}{z\lambda} - \frac{2w\ \sin\theta_b}{\lambda}\right)\text{sinc}^2\left(\frac{Lv}{z\lambda}\right)\frac{\sin^2\left(-\frac{N\pi ua}{z\lambda}\right)}{\sin^2\left(-\frac{\pi ua}{z\lambda}\right)} \tag{4.60}$$

The **v** axis is parallel to the length of a slat. Typically the length of a variable blaze grating slat is more than 100 times the width so diffraction effects across the **v** axis are much less than across the **u** axis. Also Equation (4.60) varies only in the shape of a *sinc*^{2} function on the **v** axis. The rest of the analysis in this example will be for the cross-section of the far field at v=0. The distance to the far field (z) may not be known, so it is often useful to convert Equation (4.61) to an angular function. If an angle θ is defined as shown in Figure 4.16, then the distance term (z) in Equation (4.60) can be removed from inside the *sinc* and *sine* functions:

$$E(\theta) = E_s\left(\frac{1}{z\lambda}\right)^2 (wL\cos\theta_b)^2 \text{sinc}^2\left(\frac{w}{\lambda}(\cos\theta_b \sin\theta - 2\ \sin\theta_b)\right)\frac{\sin^2\left(-\frac{N\pi a}{\lambda}\sin\theta\right)}{\sin^2\left(-\frac{\pi a}{\lambda}\sin\theta\right)} \tag{4.61}$$

where the angle θ is defined as:

$$\sin\theta = \frac{u}{z} \tag{4.62}$$

Note that z is the distance from the grating to each element in the far field and not the length of the **z** axis. E_s is equal to the irradiance (E_0) falling on the grating from an external source multiplied by the reflectivity of a grating element R (which is typically dependent on wavelength). Equation (4.63) calculates E_s:

$$E_s = E_0 R \tag{4.63}$$

The author will use a normalized source irradiance for this example; the normalized source irradiance is equal to the square of a unit electric field distributed across the surface area of the grating (N×a×L). Equation (4.64) gives the final form for the normalized E_s:

$$E_s = \left(\frac{1}{NaL}\right)^2 R \tag{4.64}$$

The final form of the normalized Fraunhofer diffraction pattern for a variable blaze grating (in the v=0 plane) is:

$$E(\theta) = R\left(\frac{1}{z\lambda}\right)^2\left(\frac{w\cos\theta_b}{Na}\right)^2 \operatorname{sinc}^2\left(\frac{w}{\lambda}(\cos\theta_b \sin\theta - 2\ \sin\theta_b)\right)\frac{\sin^2\left(-\frac{N\pi a}{\lambda}\sin\theta\right)}{\sin^2\left(-\frac{\pi a}{\lambda}\sin\theta\right)} \tag{4.65}$$

The term $(1/z\lambda)^2$ scales the irradiance as a function of distance and is similar to the inverse square law [3]. This term is not a function of θ, so the author will set it equal to one for the purpose of studying the distribution of irradiance in the far field. This term could also have been accounted for by increasing E_s to accommodate the reduction in irradiance due to $(1/z\lambda)^2$.

Figure 4.17 is a plot of Equation (4.65) with a blaze angle set to favor the first diffraction order. Table 4.2 lists the values used to create Figure 4.17. Figure 4.17 is very similar to Figure 4.8(a), created by the author's FFT optical modeling algorithm. Both have the same shape, but the maximum value of the main lobe in Figure 4.8(a) is 73.7%, and the maximum value of the main lobe in Figure 4.17 is 67.9%. This variation is caused by interference from the polysilicon border and silicon nitride layers which were modeled in Figure 4.8(a), but were not included in the calculations for Figure 4.17.

Equation (4.65) was based on a VBG model that did not include interference from polysilicon and silicon nitride layers (Figure 4.15). Figure 4.18 includes modifications to the basic grating slat model to account for the additional interference found on VBGs constructed using MUMPs. The width of the polysilicon border on each side of the gold layer is L_b. The finite thickness of the gold layer (500 nm in MUMPs) causes the polysilicon to be a distance h_p below the top surface of the gold layer. The silicon nitride layer is located a distance h_N below the top surface of the gold layer. The Fraunhofer irradiance pattern for a VBG based on the model in Figure 4.18 is given by Equation (4.66).

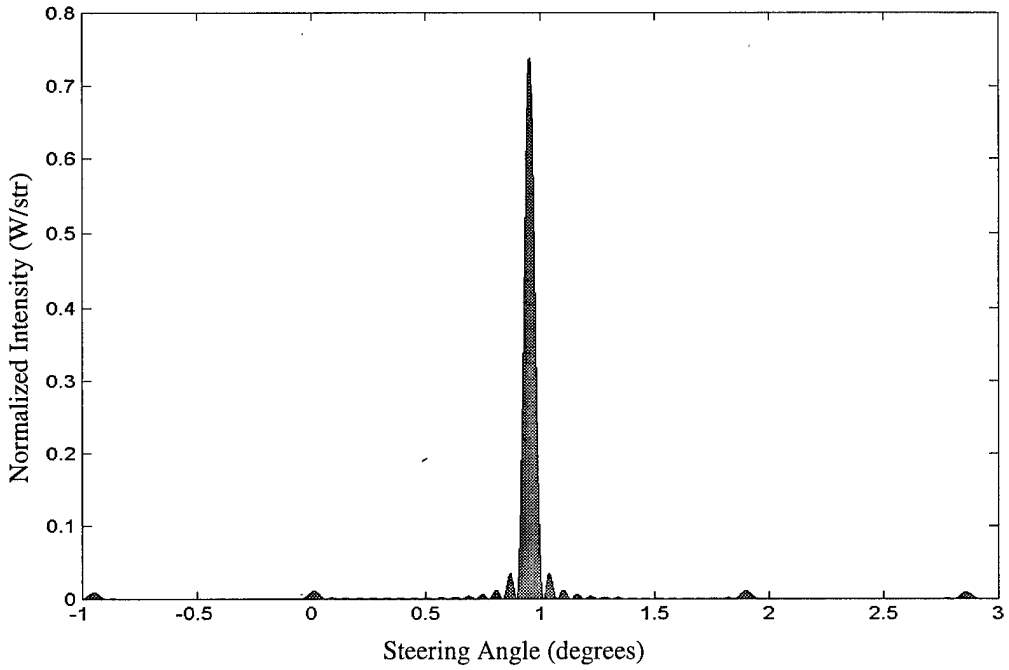

Figure 4.17. Calculated far field pattern for a grating blazed to favor the first diffraction order. The main lobe is the first diffraction order and is located at +0.95 degrees. The zero diffraction order is located at 0.0 degrees, and the second diffraction order is located at +1.9 degrees.

Table 4.2. Values Used to Plot Equations (4.65) and (4.66).

Variable	Value
Source wavelength (λ)	0.6328 μm
Reflectivity of gold at 632.8 nm (R)	91.5%
Reflectivity of polysilicon at 632.8 nm (R_p)	34.9%
Reflectivity of silicon nitride at 632.8 nm (R_N)	4.95%
Slat width (w)	34 μm
Period (a)	38 μm
Number of elements (N)	16
Blaze angle (θ_b)	0.47706°
Polysilicon border width (L_b)	1 μm
Vertical separation –gold to polysilicon (h_p)	500 nm
Vertical separation –gold to silicon nitride (h_N)	6.75 μm

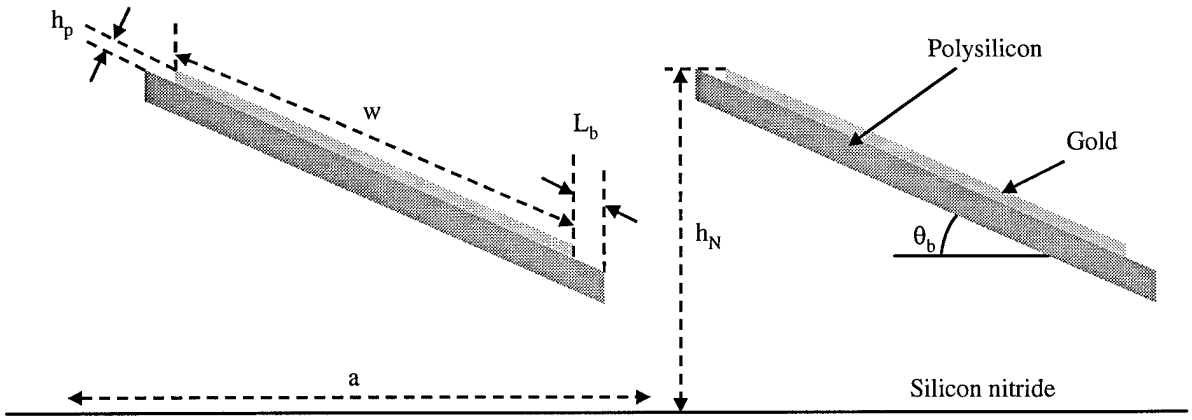

Figure 4.18. A cross-sectional view of a complete VBG model.

$$
\begin{aligned}
E(\theta) = & \left(\frac{1}{(N-1)a+\cos\theta_b(w+2L_b)}\right)^2\left(\frac{1}{z\lambda}\right)^2 \times \\
& \left| |w\cos\theta_b|\sqrt{R}\,\mathrm{sinc}\left(\frac{w}{\lambda}(\cos\theta_b\sin\theta-2\sin\theta_b)\right)\frac{\sin\left(\frac{-N\pi a}{\lambda}\sin\theta\right)}{\sin\left(\frac{-\pi a}{\lambda}\sin\theta\right)}+\right. \\
& 2|L_b\cos\theta_b|\sqrt{R_p}e^{i\frac{4\pi}{\lambda}h_p}\,\mathrm{sinc}\left(\frac{L_b}{\lambda}(\cos\theta_b\sin\theta-2\sin\theta_b)\right)\times \\
& \cos\left(\frac{\pi}{\lambda}(\cos\theta_b\sin\theta-2\sin\theta_b)(w+L_b)\right)\frac{\sin\left(\frac{-N\pi a}{\lambda}\sin\theta\right)}{\sin\left(\frac{-\pi a}{\lambda}\sin\theta\right)}+ \\
& \left.|a-\cos\theta_b(w+2L_b)|\sqrt{R_N}e^{i\frac{\pi}{\lambda}(4h_N+a\sin\theta)}\,\mathrm{sinc}\left(\frac{\sin\theta}{\lambda}(a-\cos\theta_b(w+2L_b))\right)\times\right. \\
& \left.\frac{\sin\left(\frac{-(N-1)\pi a}{\lambda}\sin\theta\right)}{\sin\left(\frac{-\pi a}{\lambda}\sin\theta\right)}\right|^2
\end{aligned}
\tag{4.66}
$$

R_p is the reflectance of polysilicon and R_N is the reflectance of silicon nitride. Equation (4.66) is derived in Appendix B.

Figure 4.19 compares the normalized irradiances of the far field diffraction formulas (Equations (4.65) and (4.66)) with the predictions of the author's FFT optical modeling algorithm (presented in Section 4.2.1.1) as a function of diffraction order. The Fourier transform plots in Figure 4.19 were calculated directly using Equations (4.66) and (4.65) for a gold only VBG and a gold, polysilicon, and nitride VBG, respectively. The "FFT simulation of VBG with poly and nitride layers" plot was made using an FFT simulation of a VBG with a 1 μm polysilicon border and silicon nitride between the adjacent slats (see Figure 4.8(a)). The "FFT simulation of gold-only VBG" plot was made using an FFT simulation of the same VBG used in the "FFT simulation of VBG with poly and nitride layers" plot except the reflectances of the polysilicon and nitride layers was set equal to zero. The results of the FFT simulation algorithm are in close agreement with the calculated far field diffraction patterns.

No significant amplitude loss occurs in any of the plots until the VBG reaches the 11^{th} diffraction order, a beam steering angle of 10.6^{o} from normal. Diffraction efficiency is defined as the percentage of the incident power that is diffracted by the grating into a single diffraction order. The $sinc^2$ function in Equation (4.65) only distributes the optical power over a beam solid angle; the rest of Equation (4.65) actually determines the diffraction efficiency [24]. At the center of each order, the value of the *sinc* function is unity. The maximum value of the normalized irradiance for each diffraction order in Figure 4.17 directly correlates to the diffraction efficiency for that order. VBG diffraction efficiency predictions by the author were made using the normalized irradiance of the far field in the direction of a specific diffraction order.

4.1.2 Electro-mechanical Theory

The electro-mechanical theory segment presents three topics on the actuation of micromirrors using electrostatic force. The topics are: deflection of micromirrors with linear force supporting flexures, deflection of micromirrors with nonlinear force supporting flexures, and deflection of micromirrors using the substrate as the bottom electrode.

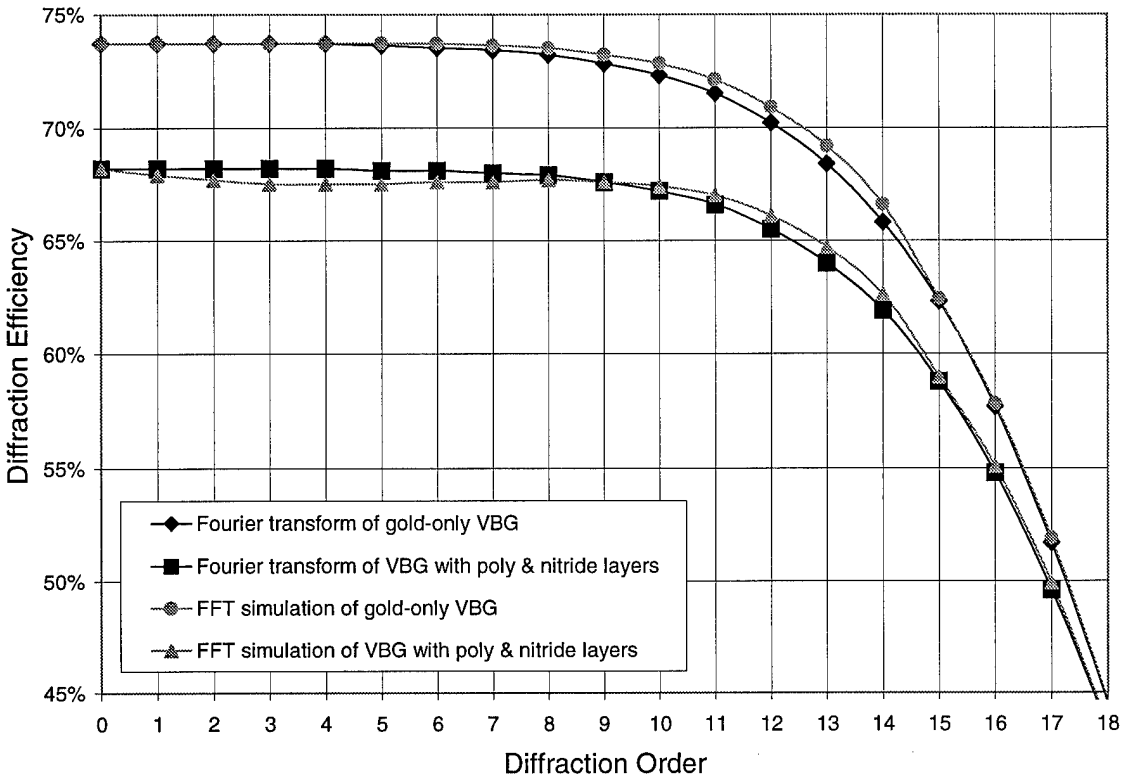

Figure 4.19. Comparison of the normalized irradiances for a variable blaze grating with blaze angles supporting the indicated diffraction orders.

4.1.2.1 Electrostatically Actuated Devices with Linear Force Flexures

Electrostatic force results from the attraction between unlike charges when a voltage is placed between two electrodes. Electrostatic actuation is the application of electrostatic force to a mechanical system. Low power applications are ideal candidates for electrostatic actuation because electrostatic force is generated by charge distributions not current flow. One drawback of electrostatic actuation is that electrostatic force is a nonlinear function of distance; electrostatic force increases exponentially as the distance between electrodes decreases. Supporting flexures typically provide a restorative force that is a linear function of distance. After the separation distance between the electrodes in a device with linear force flexures decreases by one-third, the positions of the electrodes become unstable and they quickly travel the remaining separation distance. This phenomenon is called "snap-through" [12].

Snap-through limits the useful range of motion in an electrostatic device with linear force flexures to one-third of the initial separation distance between electrodes. The piston micromirror shown in Figure 4.20 is driven by electrostatic actuation and was designed by the author. The phase of light reflected off the micromirror can be altered if the micromirror is pulled down towards the substrate. The top electrode is the center region of the micromirror supported by the flexures. The bottom electrode is a POLY-0 layer hidden from view by the top electrode.

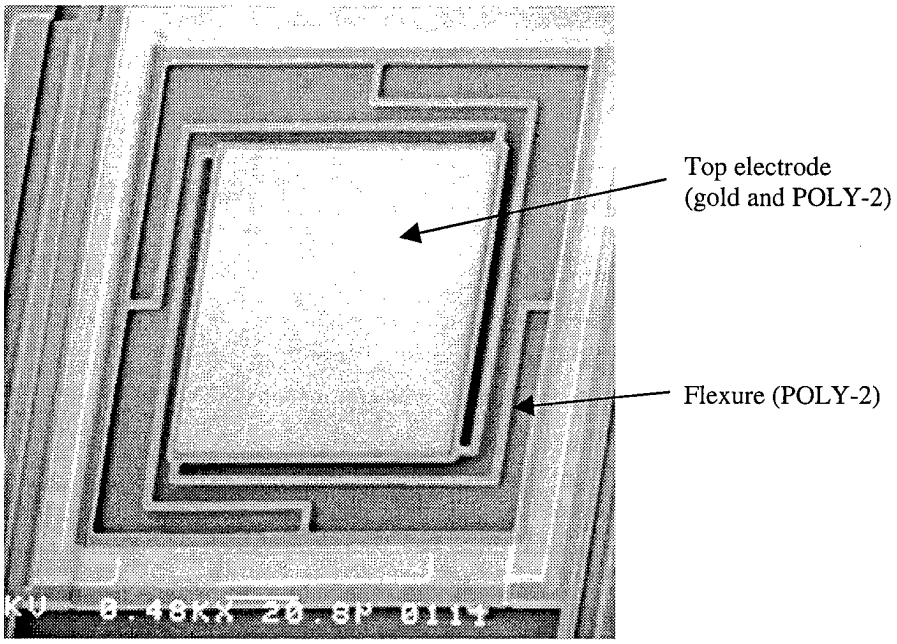

Figure 4.20. A 100 μm square electrostatically actuated piston micromirror with linear force flexures (fabricated by the author in MUMPs 13).

Equation (4.67) can be used to calculate electrostatic force, F_e, between two parallel plates [13]:

$$F_e = \frac{V^2 \varepsilon_0 A}{2D^2} \tag{4.67}$$

where A is the common surface area normal to both plates, D is the separation distance, ε_0 is the permittivity of free space, and V is the voltage potential between the plates. Equation (4.67) does not consider the effects of fringing losses or plate surface deformations resulting from the electric field; Michalicek and others demonstrated that a good model can be developed even if these effects are neglected [14,15]. The flexures for the micromirror pictured in Figure 4.20 can be modeled as cantilevers. For small deflections, a cantilever's force is given by Hooke's law [16]:

$$F_c = kd \tag{4.68}$$

where k is the spring constant, d is the deflection distance, and F_c is the cantilever's force. The flexure spring constant can be calculated by [14,17]:

$$k = \left[\frac{Ewt^3}{L^3} + \frac{\sigma(1-\nu)wt}{2L} \right] \tag{4.69}$$

where E is the modulus of elasticity, w is the flexure width, L is the flexure length, t is the flexure thickness, σ is the flexure material stress, and ν is the flexure material Poisson's ratio. The spring constant is determined during design and construction; it is not a function of voltage or deflection. For an electrostatically actuated micromirror in stable deflection (deflection distance less than the snap-through distance), the electrostatic force is balanced by the restorative flexure force. Setting Equation (4.67) equal to the number of flexures, N, times Equation (4.68) results in:

$$\frac{V^2 \varepsilon_0 A}{2D^2} = Nkd \tag{4.70}$$

Solving Equation (4.70) for applied voltage, V, as a function of micromirror deflection leads to [14,18]:

$$V = (z_0 - d)\sqrt{\frac{2Nkd}{\varepsilon_0 A}} \tag{4.71}$$

where the separation distance, D, in Equation (4.70) has been replaced by:

$$D = (z_0 - d) \tag{4.72}$$

where z_0 is the initial separation distance and d is the micromirror deflection distance. Equation (4.71) calculates the required voltage, V, to deflect the micromirror a distance, d, from rest.

4.1.2.2 Electrostatically Actuated Devices with Nonlinear Force Flexures

If a flexure can be designed to provide a higher order restorative force, such as:

$$F_c = kd^r \tag{4.73}$$

where r is order of the flexure's force (i.e. r=2 is a quadratic force flexure), then Equation (4.71) is no longer valid. For nonlinear flexures (r not equal to one), the value of the spring constant, k, will not be determined by

Equation (4.69); the flexure will not be a simple uniform cross-section cantilever. For an electrostatically actuated micromirror with nonlinear force flexures defined by Equation (4.71) in stable deflection, Equation (4.71) becomes:

$$V = (z_0 - d)\sqrt{\frac{2Nkd^r}{\varepsilon_0 A}} \tag{4.74}$$

Figure 4.21 is a normalized plot of Equation (4.74) for several values of r. Note that even though the distance before snap-through was increased, the snap-through phenomenon was not eliminated. Snap-through still occurs because electrostatic force and flexure force are not balanced over all of the micromirror's deflection range. An additional benefit of using a higher order force flexure is shown in Figure 4.21; a large segment of the micromirror deflection range for second and third order flexure force is closer to a linear function of applied voltage than deflection with linear flexure force.

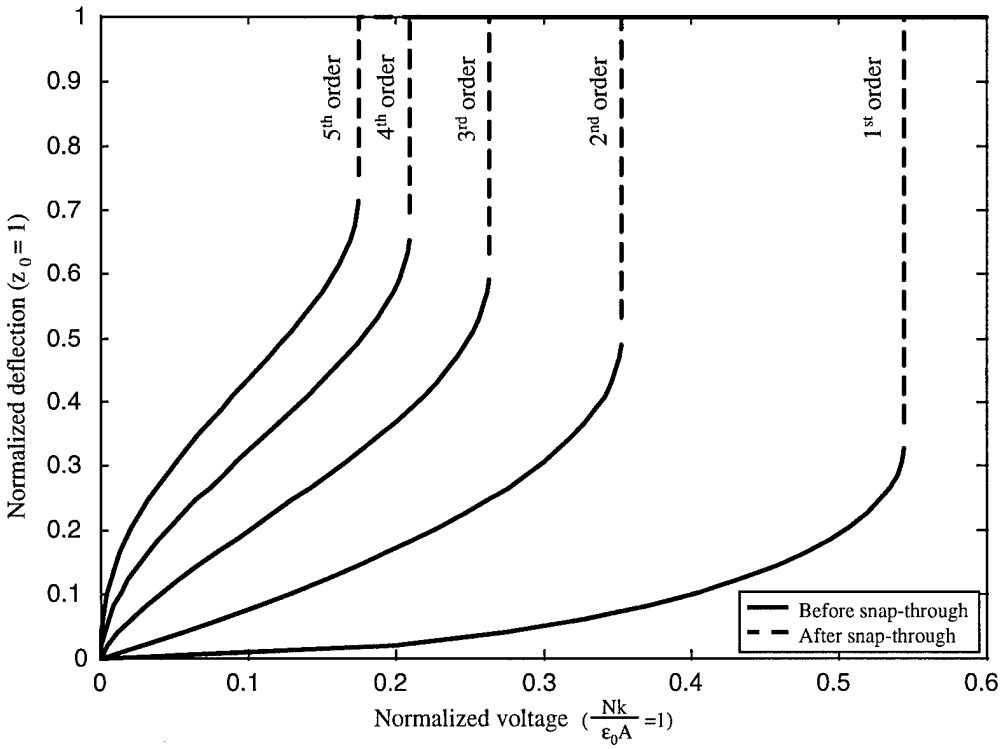

Figure 4.21. Deflection versus voltage plots for electrostatically-actuated micromirrors with nonlinear force flexures.

Snap-through occurs when the derivative of Equation (4.74) with respect to deflection changes sign, so it is possible to calculate the snap-through point for an electrostatically actuated device with any flexure force order. Setting the derivative of Equation (4.74) equal to zero results in the following solution for deflection:

$$d_{snap} = \frac{z_0 r}{2+r} \tag{4.75}$$

where d_{snap} is the deflection distance to snap-through, and r is the order of the flexure force. As r grows large, d_{snap} approaches the initial separation distance; however, the voltage versus deflection curve shown in Figure 4.21 becomes sharper. Micromirrors with continuously adjustable deflection distances may be difficult to control for high order (r greater than or equal to 5) flexure forces. Note that Equation (4.75) is independent of the number of flexures, the spring constant, and electrode surface area. Equation (4.71) will be applied in Section 4.2.2.3.

4.1.2.3 Electrostatic Actuation Using the Substrate as the Bottom Electrode

The substrate can be used as the bottom electrode if the substrate contact pad developed by Comtois [19] is used to ground the bulk silicon region under the silicon nitride layer and a drive voltage is placed on the micromirror's top electrode. Figure 4.22 is a trapped-oxide electrostatically actuated piston micromirror that uses the substrate as the bottom electrode. Three advantages of using the substrate as the bottom electrode are: snap-through current protection, simplified wiring, and reduced unintentional embossing.

After an electrostatically actuated device with POLY-0 bottom electrodes reaches snap-through, the top and bottom electrodes are in direct contact. A high current will pass between the electrodes if an external current limiting resister is not used. This high current can destroy the device by melting the support flexures. Silicon nitride is an excellent electrical insulator, consequently devices using the substrate as the bottom electrode are protected after snap-through. Simplified wiring also results when the substrate is used as the bottom electrode because wires for bottom POLY-0 electrodes are not needed. Any number of electrostatically actuated devices can all use the substrate as the bottom electrode. Reduced unintentional embossing results from removing the POLY-0 bottom electrode; additionally polysilicon and gold layers are formed over flat silicon nitride and sacrificial oxide layers.

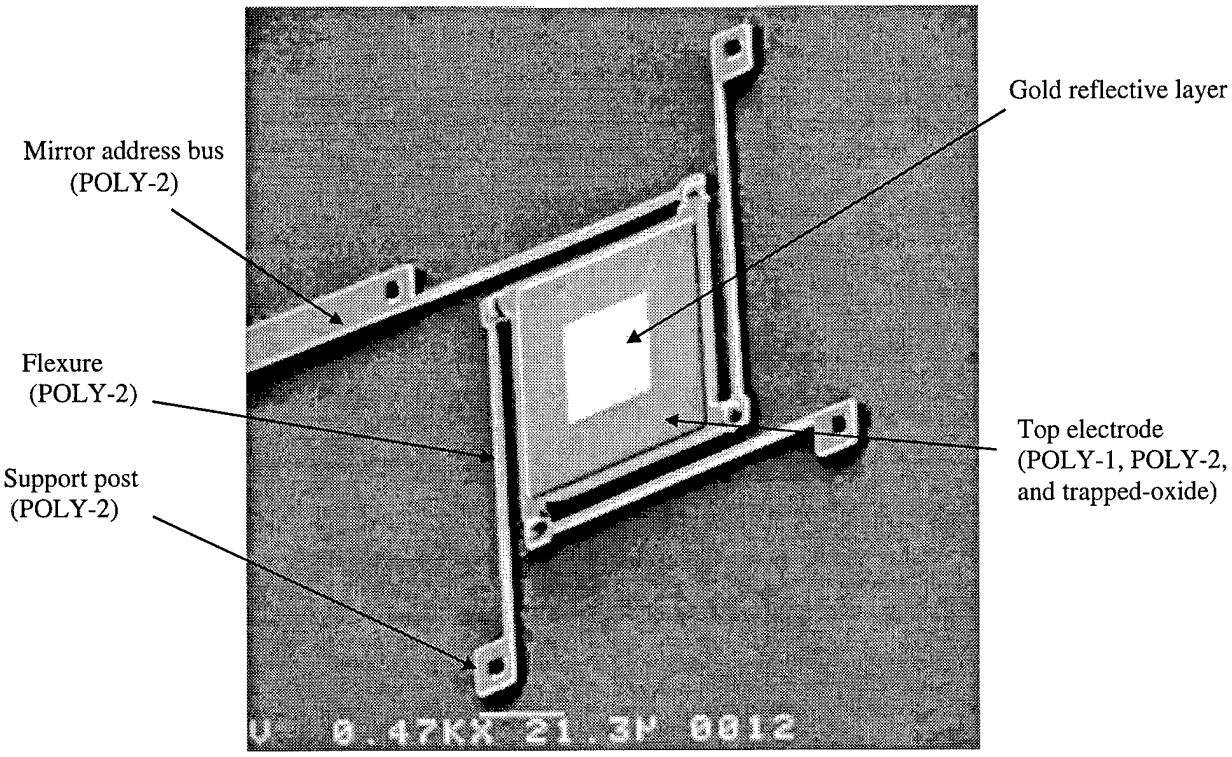

Figure 4.22. An electrostatically actuated piston micromirror using the substrate as the bottom electrode (fabricated by the author in MUMPs 18)

Two disadvantages of using the substrate as the bottom electrode are one dimensional motion and trapped charges. Micromirrors can tilt and piston if several bottom POLY-0 electrodes are used. If the substrate is used, then the device will be limited to a single bottom electrode. Electrostatically actuated devices with a single bottom electrode can either tilt on one axis (VBG slats) or piston (linear optical phased array elements). Silicon nitride can store trapped charges if a high electric field is placed across the silicon nitride layer. After the electric field is removed, the residual trapped charges can alter the device's deflection characteristics. The author observed this problem on several high voltage (over 50 volts) VBG designs. After several minutes of use, the VBG slats were no longer capable of reaching the zero order when voltage was removed; residual trapped charges partially deflected the VBG slats and prevented the slats from fully reaching their initial position (parallel to substrate). The trapped charges can be reduced by reversing the polarity of the drive voltage or by applying an Alternating Current (AC) signal.

The impact of the silicon nitride layer on deflection as a function of applied voltage can be calculated. Figure 4.23 shows a cross-sectional view of an electrostatically actuated micromirror using the substrate as the

bottom electrode. The capacitance of the system can be modeled as two capacitors in series: the first capacitor has a separation distance of D and a dielectric constant $\varepsilon_r = 1$, and the second capacitor has a separation distance of s and a dielectric constant $\varepsilon_r = 7.5$ [20]. The capacitance's of the first and second capacitors are given by Equations (4.76) and (4.77), respectively.

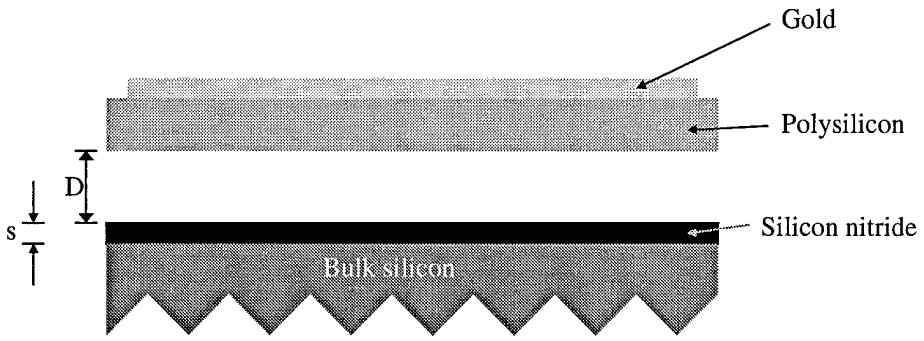

Figure 4.23. Cross-sectional view of an electrostatically actuated device using the substrate as the bottom electrode.

$$C_1 = \frac{\varepsilon_0 A}{D} \tag{4.76}$$

$$C_2 = \frac{\varepsilon_r \varepsilon_0 A}{s} \tag{4.77}$$

where A is the surface area normal to both electrodes, ε_0 is the free space permittivity, D is the gap between the top electrode and the silicon nitride layer, and s is the thickness of the silicon nitride layer. The equivalent capacitance C_{eq} for two capacitors in series is given by Equation (4.78) [21]:

$$C_{eq} = \frac{C_1 C_2}{C_1 + C_2} \tag{4.78}$$

For the micromirror in Figure 4.23, the equivalent capacitance is given by Equation (4.79):

$$C_{eq} = \frac{\varepsilon_r \varepsilon_0 A}{\varepsilon_r D + s} \tag{4.79}$$

The equivalent capacitance in Equation (4.79) can be used to calculate the force on the top electrode as a function of the applied voltage, V. The electrostatic force pulling the top electrode towards the substrate can be calculated using Equation (4.80) [22]:

$$F = \frac{1}{2(D + \frac{s}{\varepsilon_r})} C_{eq} V^2 \tag{4.80}$$

The separation distance ($D + s/\varepsilon_r$) in Equation (4.80) is the equivalent separation distance after accounting for the reduction in electric field caused by the silicon nitride layer. Equation (4.81) is the electrostatic force on the top electrode after substituting in the equivalent capacitance:

$$F = \frac{\varepsilon_0 A}{2} \left(\frac{V}{D + \frac{s}{\varepsilon_r}} \right)^2 \tag{4.81}$$

If Equation (4.79) is set equal to the restorative force provide by linear force flexures (given in Equation (4.68)) and the deflection distance d is substituted using $D = z_0 - d$, then deflection as a function of applied voltage can be calculated using Equation (4.82):

$$V = \left(z_0 + \frac{s}{\varepsilon_r} - d \right) \sqrt{\frac{2Nkd}{\varepsilon_0 A}} \tag{4.82}$$

where z_0 is the initial separation distance between the top electrode and the silicon nitride layer, N is the number of supporting flexures, and k is the spring constant of each flexure. The expression ($z_0 + s/\varepsilon_r$) is defined as the apparent separation distance for electrostatically actuated devices using the substrate as the bottom electrode. For stacked-poly and trapped-oxide designs, z_0 is 2.0 μm and s is 0.6 μm. The net result of using the substrate as the bottom electrode is a change in apparent electrode separation from 2.00 μm to 2.08 μm. This change in apparent electrode separation is small because it is close to the layer thickness tolerances of the MUMPs process (see Appendix A). However the micromirror's deflection characteristics do change when the substrate is used as the bottom electrode. Figure 4.24 is a plot of micromirror deflection versus applied voltage for micromirrors with bottom electrodes constructed out of POLY-0 and the substrate. The initial separation distance is 2.0 μm (i.e. micromirrors constructed with stacked-poly or trapped-oxide). The snap-through distance is virtually the same for both micromirrors, however the micromirror using the substrate as the bottom electrode has a 6.0% increase in the maximum applied voltage.

Snap-through occurs when the derivative of Equation (4.82) with respect to deflection changes sign. The snap-through point for an electrostatically actuated device with any flexure force order operated through the substrate can be calculated by setting the derivative of Equation (4.82) equal to zero:

$$d_{snap} = \frac{r}{2+r}\left(z_0 + \frac{s}{\varepsilon_r}\right) \tag{4.83}$$

where d_{snap} is the deflection distance to snap-through, and r is the order of the flexure force. For a micromirror fabricated using MUMPs with an initial electrode separation of 2 μm and linear force flexures, the increase in the distance to snap through is 22.2 nm if the substrate is used as the bottom electrode. This increased distance to snap-through is negligible because it is less than the layer thickness variations in the MUMPs process (see Appendix A).

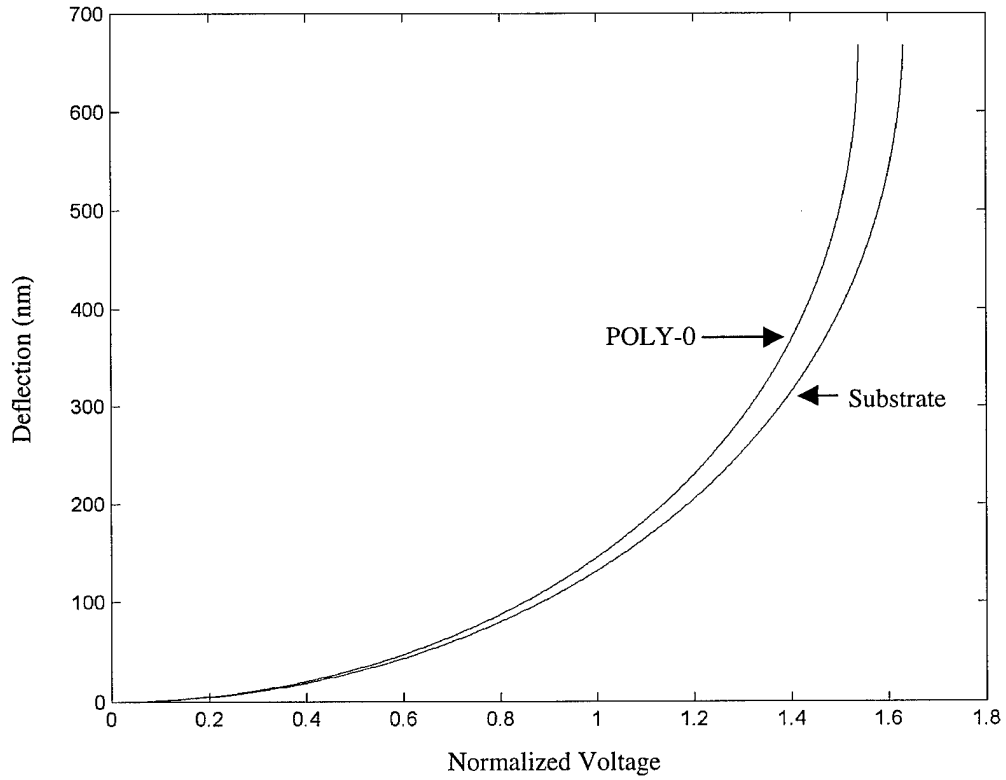

Figure 4.24. Plot of deflection versus voltage for micromirrors with POLY-0 and substrate bottom electrodes. The applied voltage was normalized by setting $(Nk)/(\varepsilon_0 A)=1$. The initial separation distance between the top electrode and the POLY-0 or silicon nitride layer (z_0) is 2.0 μm.

4.2 Modeling

The modeling segment covers both optical and electro-mechanical modeling. Most of the modeling in the author's research was conducted using MATLAB™ [23]. The author also created several stand-alone programs using the C++ programming language.

4.2.1 Optical Modeling

Optical modeling was used to evaluate linear optical phased arrays and variable blaze gratings. In Section 4.1.1.6, the Fourier transform was used to predict the far field irradiance pattern for a VBG. Although this technique gave accurate results (based on testing conducted in Chapter 6), it was time consuming and tedious. Also some optical features such as defocusing caused by residual material stress induced curvature can not be modeled using this technique because the transmittance function for a grating with curved slats has no direct analytical Fourier transform.

The author overcame the problems associated with the analytical Fourier transform by using a discrete Fourier transform conducted using a computational algorithm known as a Fast Fourier Transform (FFT). The following sections discuss the FFT simulation used by the author. The objective of the Fourier analysis conducted by the author was to optimize the performance of arrays and gratings designed by the author, and minimize the cost of the author's research. Cost was minimized by eliminating the fabrication of devices with moderate or low predicted optical and electro-mechanical performance.

4.2.1.1 Fast Fourier Transform

The Fast Fourier Transform (FFT) is an algorithm designed to compute a discrete Fourier transform. In Section 4.1.1.5, the far field irradiance pattern for an optical device with a transmittance function, $t(x,y)$, was given as:

$$E(x,y) = E_s\left(\frac{1}{z\lambda}\right)^2\left|\Im\left[t(\frac{x}{z\lambda},\frac{y}{z\lambda})\right]\right|^2 \tag{4.84}$$

Equation (4.84) is still valid; however the author used a discrete Fourier transform on the transmittance function. The discrete Fourier transform of a function t(x,y) is given by [24]:

$$T(p\Delta x, q\Delta y) = \sum_{m=0}^{N_x-1} \sum_{n=0}^{N_y-1} t(m\Delta\xi, n\Delta\eta) e^{i2\pi\left(\frac{pm}{N_x}+\frac{qn}{N_y}\right)} \tag{4.85}$$

where Δx and Δy are the sample sizes in the **x** axis and the **y** axis. N_x and N_y are the total number of samples on the **x** axis and the **y** axis. p and q are integers ranging from 0 to N_x or N_y, respectively. An FFT algorithm is a computationally efficient method of calculating the discrete Fourier transform in Equation (4.85). As was done in Section 4.1.1.6, the author used a one dimensional FFT; most of the optical beam steering devices designed by the author steer light over a single axis. A variety of FFT algorithms are in widespread use [25]; the author selected the MATLAB™ FFT algorithm because of its execution speed and ease of use [23].

Important factors in the use of an FFT are: sample size, number of samples, and output angular resolution. Sample size, Δx, must meet the Nyquist criteria [24]. The Nyquist criteria requires the sample size to be less than or equal to half the smallest sampled feature. Equation (4.86) bounds the maximum sample size for an optical device with a minimum optical feature size of L_{min}:

$$\Delta x \leq \frac{L_{\min}}{2} \tag{4.86}$$

The smallest feature of the author's MUMPs designs is typically the polysilicon border next to the gold layer; often this border is 1 μm, giving a maximum sample size of 500 nm. The number of samples, N, for the FFT should be equal to 2^m; m is the smallest integer such that the number of samples multiplied by the sample size is greater than or equal to the width of the optical device. Equation (4.87) gives the minimum number of samples for an optical device with a width w:

$$N = \frac{w}{\Delta x} \tag{4.87}$$

The output angular resolution, Δθ is given by Equation (4.88) [25]:

$$\Delta\theta = \frac{\lambda}{N\Delta x} \tag{4.88}$$

Therefore the angular resolution can be increased by increasing the number of samples and/or increasing the sample size (but keeping it within the Nyquist criteria). The sample size can be increased by "padding" or adding zeros to each size of the sampled array. Padding can be used to keep the number of samples constant and increase the sample size. If padding is used, then the magnitude of the output must be adjusted by the padding fill factor as shown in Equation (4.89):

$$M_{adjusted} = M_{raw} \frac{w + pad}{w} \tag{4.89}$$

where M_{raw} is the output of the FFT, $M_{adjusted}$ is the corrected output, and *pad* is the length of the padded region. The author used both of these techniques to improve the angular resolution in the modeling of optical phased arrays and VBGs. All of the author's FFT simulation routines follow the process shown in Table 4.3 to derive a normalized far field irradiance pattern. The steps shown in Table 4.3 were based on the normalized irradiance function presented in Equation (4.66) in Section 4.1.1.6.

4.2.1.2 Linear Optical Phased Array FFT Simulations

The author developed a MATLAB™ routine to create a far field irradiance plot as a function of steering angle for a linear optical phased array. The routine was used to model a fifth generation high yield array illuminated by a laser operating at a wavelength of 632.8 nm. Complete design characteristics for this 128 element, 30 μm period array are presented in Chapter 5, Section 5.3. Figures 4.25 through 4.28 show the Fraunhofer irradiance patterns for this array as the desired beam steering angle is increased from zero to its maximum value (+0.6°) corresponding to an inter-element phase difference of π radians. When the beam steering angle is set equal to zero, two secondary beams exist and are located at ±1.2°. Note that as the desired beam steering angle increases, the magnitudes of the desired and secondary beams decrease and increase, respectively. At the maximum beam steering angle (+0.6°), the magnitudes of the desired and secondary beams are equal.

Table 4.3 . Steps Used in the Author's FFT Simulation Routines.

Step	Description
1.	Determine sample size (Δx) and number of samples (N) using Equations (4.86) and (4.87).
2.	Create a discrete transmittance function ($t(x)$) by sampling the optical device. The transmittance function consists of a magnitude $\sqrt{R}$ multiplied by a phase term $e^{i4\pi d}$ for each sample. The magnitude is equal to the square root of the power reflectance at the sample's location. The phase is determined by the vertical distance d from the top of the sample to a reference plane.
3.	Compute the FFT of sampled transmittance function.
4.	Create an irradiance pattern by calculating the square of the absolute value of the FFT results as shown in Equation (4.85).
5.	Normalize the irradiance pattern by dividing the output magnitude by the square of the number of samples.
6.	Adjust the magnitude of the irradiance pattern to account for padding (Equation (4.89)).
7.	Calculate the x-axis for an irradiance pattern using Equation (4.88).

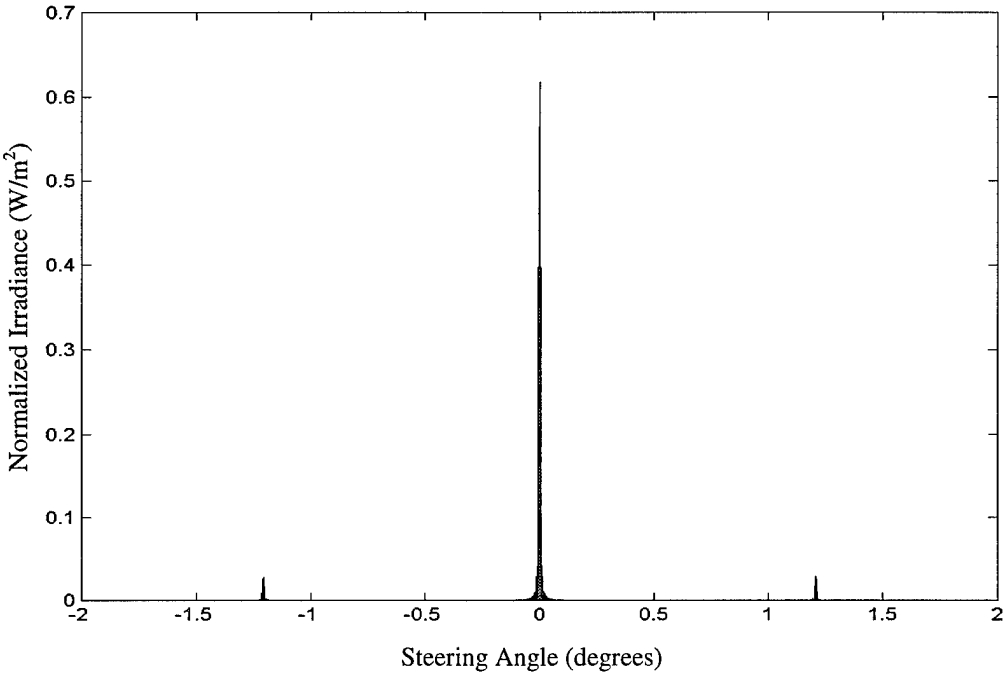

Figure 4.25. Normalized Fraunhofer irradiance pattern for an inter-element phase difference of 0 radians. The desired beam is located at 0°. Secondary beams are located at ±1.2°.

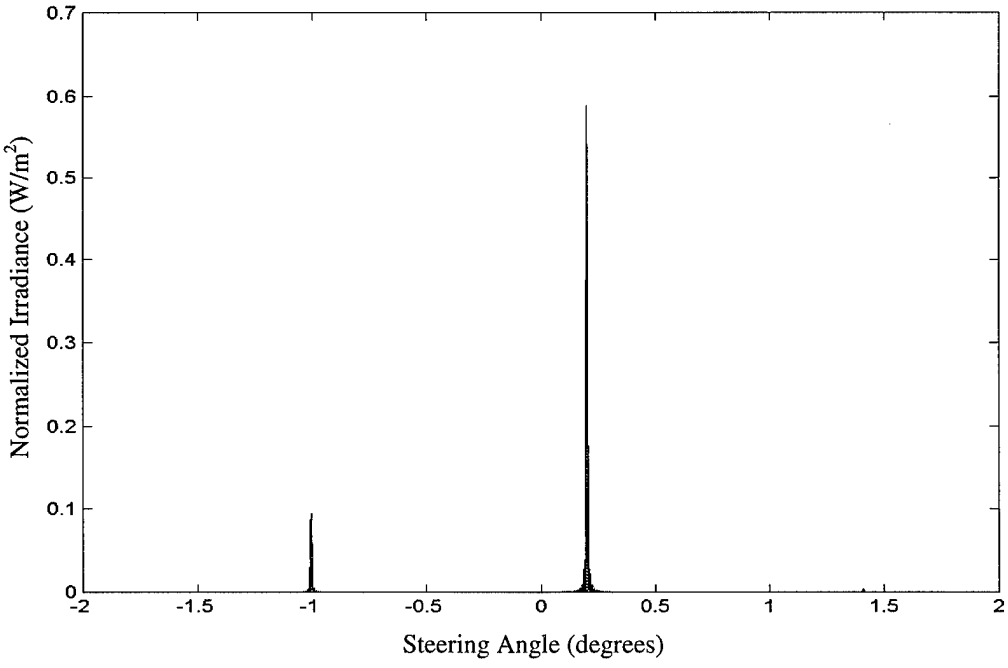

Figure 4.26. Normalized Fraunhofer irradiance pattern for an inter-element phase difference of $\pi/3$ radians. The desired beam is located at +0.2°. A secondary beam is located at -1.0°.

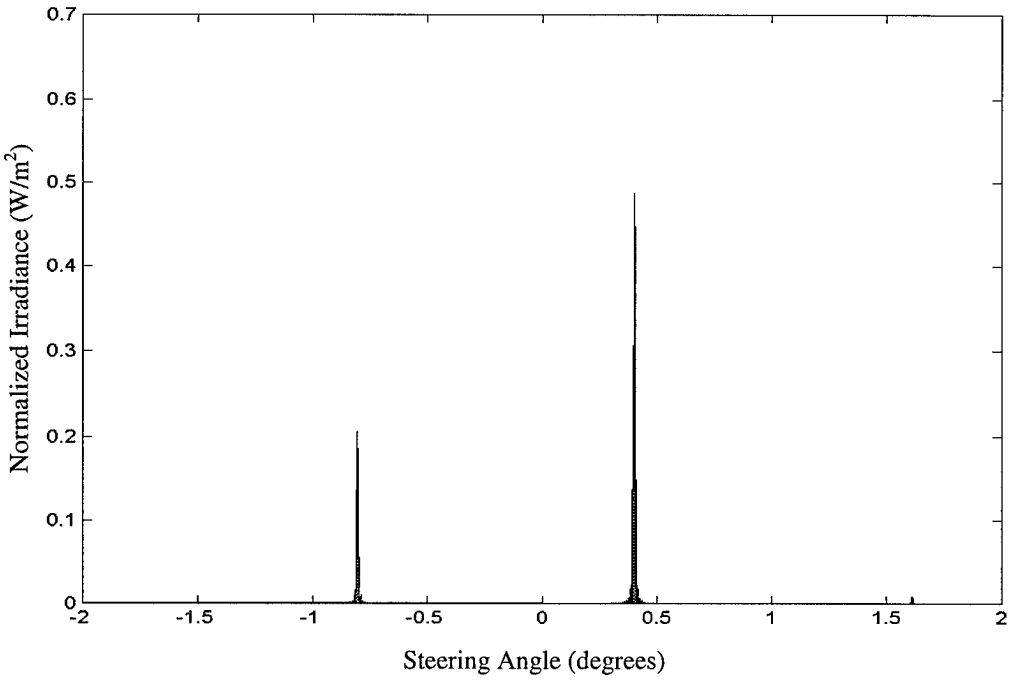

Figure 4.27. Normalized Fraunhofer irradiance pattern for an inter-element phase difference of $2\pi/3$ radians. The desired beam is located at $+0.4^{\circ}$. A secondary beam is located at -0.8°.

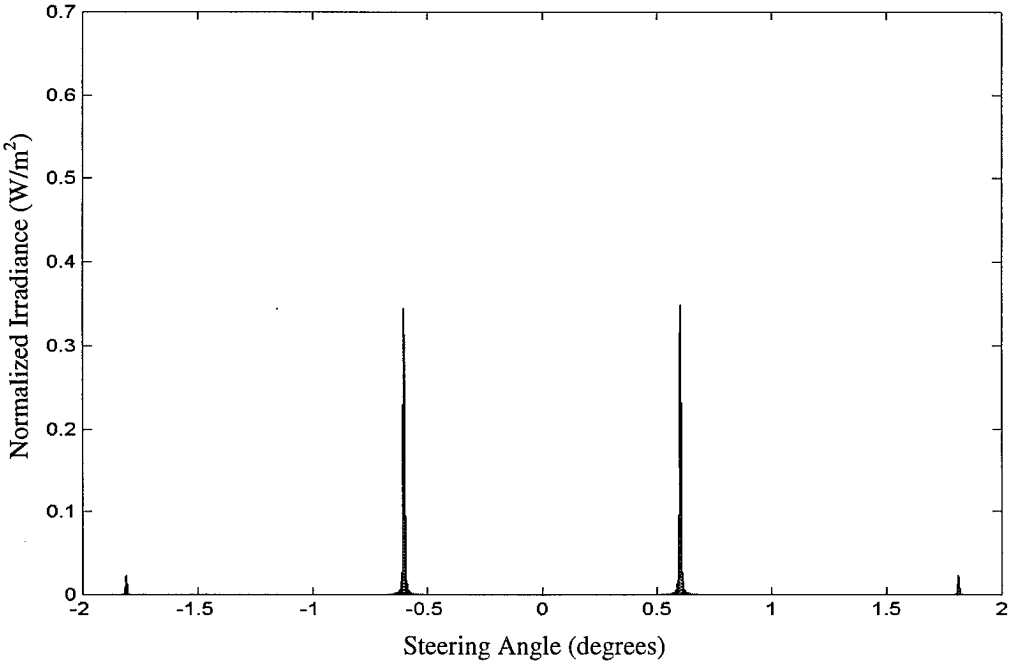

Figure 4.28. Normalized Fraunhofer irradiance pattern for an inter-element phase difference of π radians. The desired beam is located at $+0.6^{\circ}$. A secondary beam is located at -0.6°.

4.2.1.3 VBG FFT Simulations

The author developed a MATLAB™ routine to create a far field irradiance plot as a function of steering angle for a variable blaze grating. The routine was used to model a 36 slat VBG with a period of 80 μm illuminated by a laser operating at a wavelength of 632.8 nm. The peak-to-valley curvature across the width of each slat was 79.1 nm (typical for a trapped-oxide slat design). Each slat had a 2 μm polysilicon border on each side of the gold layer. Figures 4.29 through 4.32 show the Fraunhofer irradiance patterns for this VBG as the desired beam steering angle is incrementally increased from the first diffraction order to the second diffraction order. Note that the location of the orders does not change. As the slat tilt angle is increased from the blaze angle required for the first diffraction order (0.227°) to the second diffraction order (0.453°), the diffraction efficiency for the first order decreases and the diffraction efficiency for the second order increases. Power in the non-selected orders (m=-1 for example) increases when the slat tilt angle does not match the blaze angle for a diffraction order.

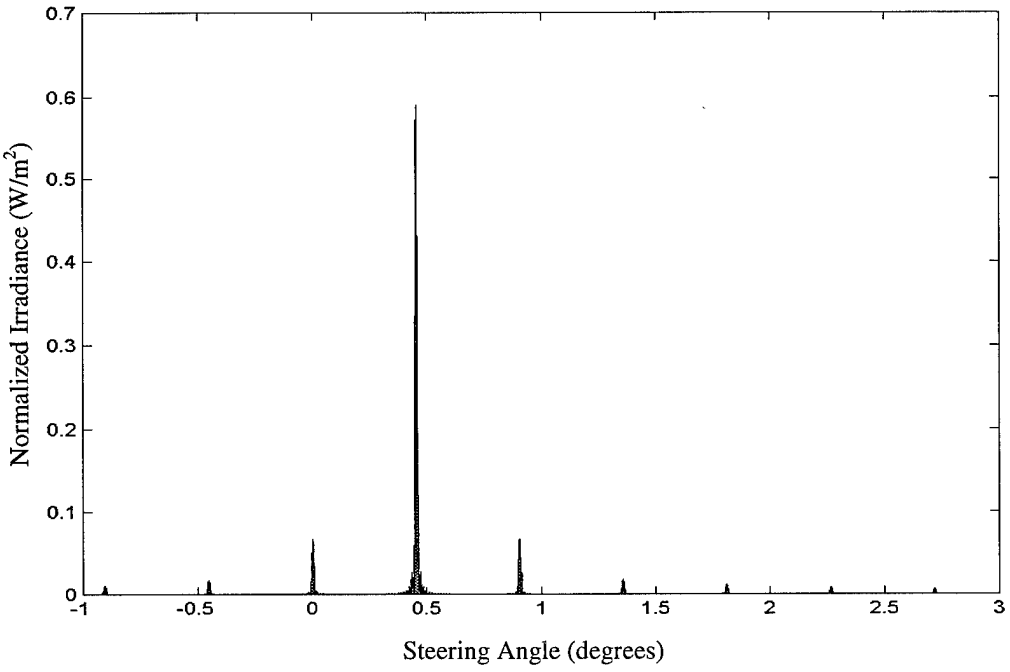

Figure 4.29. Normalized Fraunhofer irradiance pattern for a VBG with a blaze angle of 0.227° (m=1). The diffraction efficiency is 58.97%. The location of the first diffraction order is at 0.454°.

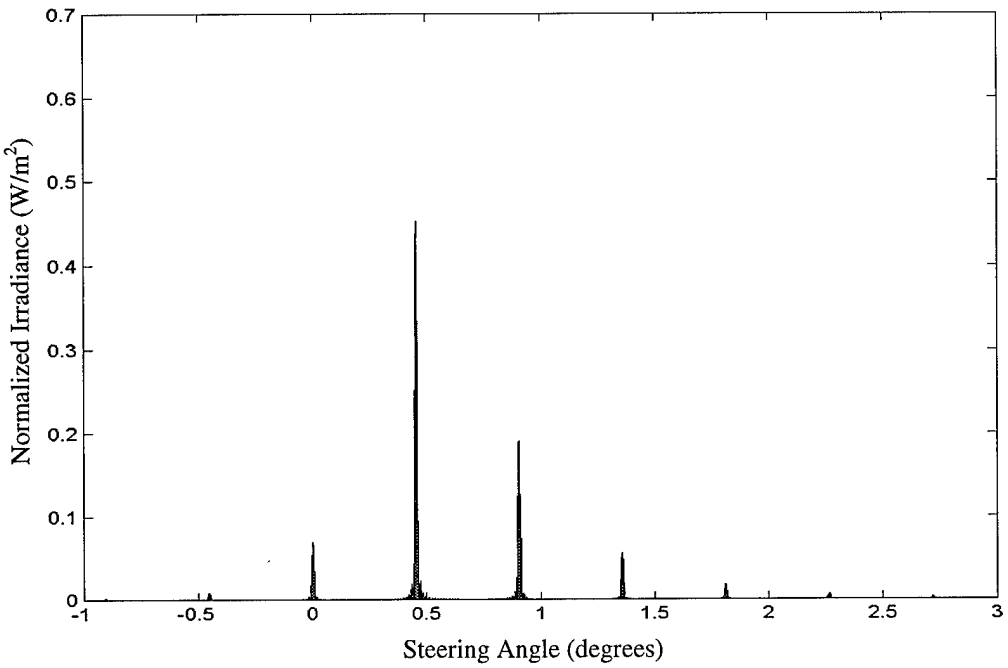

Figure 4.30. Normalized Fraunhofer irradiance pattern for a VBG with a blaze angle of 0.303°. The diffraction efficiency is 45.29%. The location of the first diffraction order is at 0.454°.

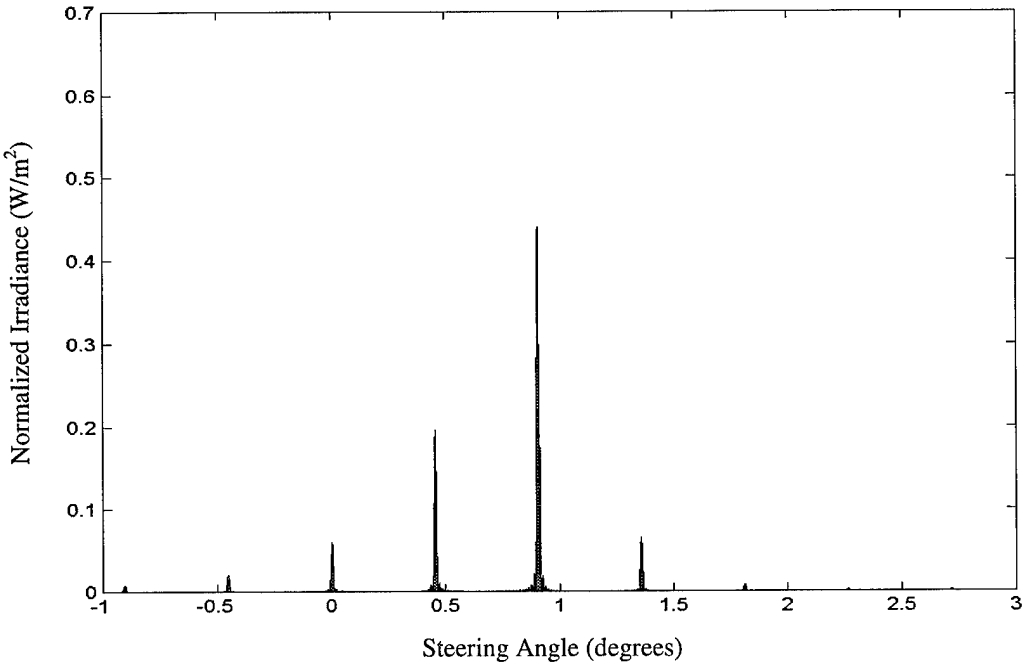

Figure 4.31. Normalized Fraunhofer irradiance pattern for a VBG with a blaze angle of 0.378°. The diffraction efficiency is 44.01%. The location of the second diffraction order is at 0.907°.

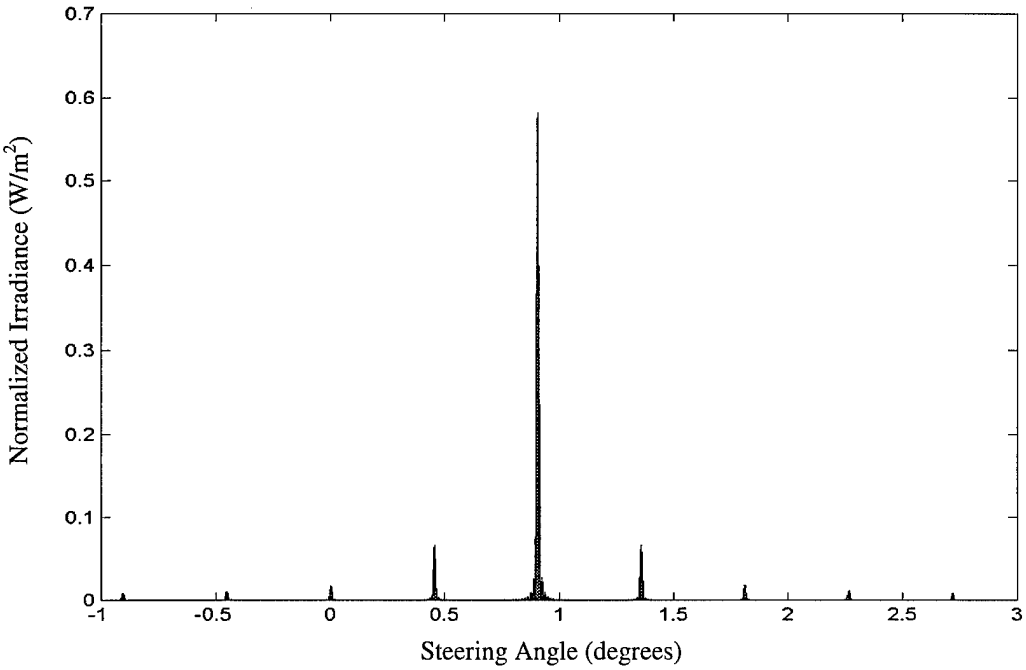

Figure 4.32. Normalized Fraunhofer irradiance pattern for a VBG with a blaze angle of 0.453° (m=2). The diffraction efficiency is 58.20%. The location of the second diffraction order is at 0.907°.

4.2.1.4 Ray Tracing

If a non-normally incident source is used to illuminate an optical array or a VBG, then it is possible to eliminate all the light in the far field reflected off the stationary silicon nitride layer; if all of the diffracted light is reflected off a movable surface (slats), the optical device will not show a bias towards a beam steering angle of zero or the zero diffraction order. Figure 4.33 depicts a cross-sectional view of the gap between two adjacent array elements or VBG slats. The width of the gap, g, is typically 2 μm for array elements or VBG slats constructed with MUMPs. The height of the outer POLY-2 edge, h, ranges from 4.25 μm (POLY-2 only) to 6.25 μm (stacked-poly or trapped-oxide). Equation (4.90) can be used to calculate the minimum incident angle, θ_t, that will ensure that none of the light reflected off the silicon nitride layer reaches the zero order.

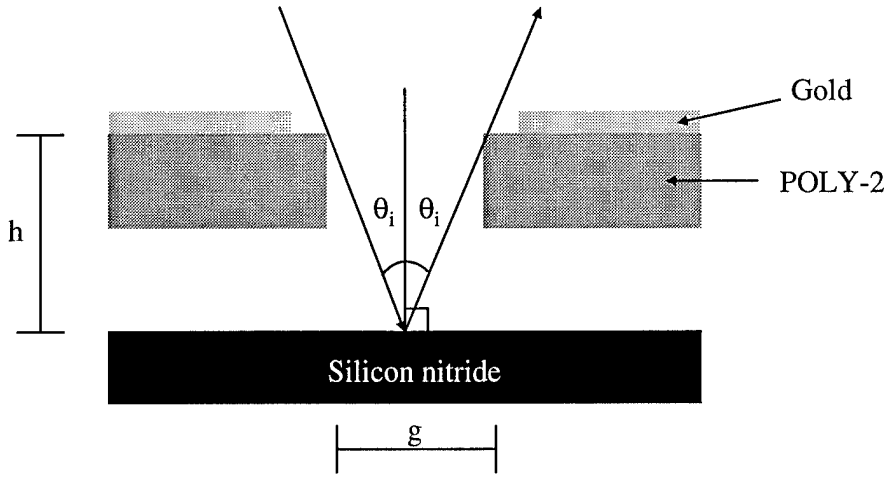

Figure 4.33 Cross-sectional view of the gap between adjacent VBG slats.

$$\theta_i > \tan^{-1}\left(\frac{g}{2h}\right) \tag{4.90}$$

For a POLY-2 only array element or VBG slat with a gap of 2 μm, θ_I is 13.2°. For a stacked-poly or trapped-oxide optical device with a gap of 2 μm, θ_I is 9.1°. The standard MATLAB™ simulations discussed in Section 4.2.1.3 assumed a normally incident source. The author created a separate program for FFT simulations on optical phased arrays and VBGs with a non-normally incident source. Ray-tracing is accomplished by applying Equation (4.92) to every sampled point on the array or VBG (including gold, polysilicon, and silicon nitride layers).

The locations of the diffraction orders for a variable blaze grating illuminated by a source at a nonzero angle θ_i (measured with respect to the axis normal to the face of the grating) are no longer given by Equation (4.9). Instead the location of the m^{th} order (θ_m) is given by [4]:

$$\sin(\theta_m) - \sin(\theta_i) = \frac{m\lambda}{a} \tag{4.91}$$

Figure 4.34 is the far field irradiance pattern for the same VBG used in Figure 4.32 illuminated by a source at an angle of 45° to normal. The VBG tilt angle was set to favor the second order (m=2). Note that the diffraction efficiency for Figure 4.34 is 70.0%, a 20.3% improvement (relative) over the same VBG illuminated

by normally incident light in Figure 4.32. Much of this increase in diffraction efficiency is a result of changing the destructive interference from the polysilicon borders in Figure 4.32 to constructive interference by changing the OPL difference between the gold and polysilicon layers.

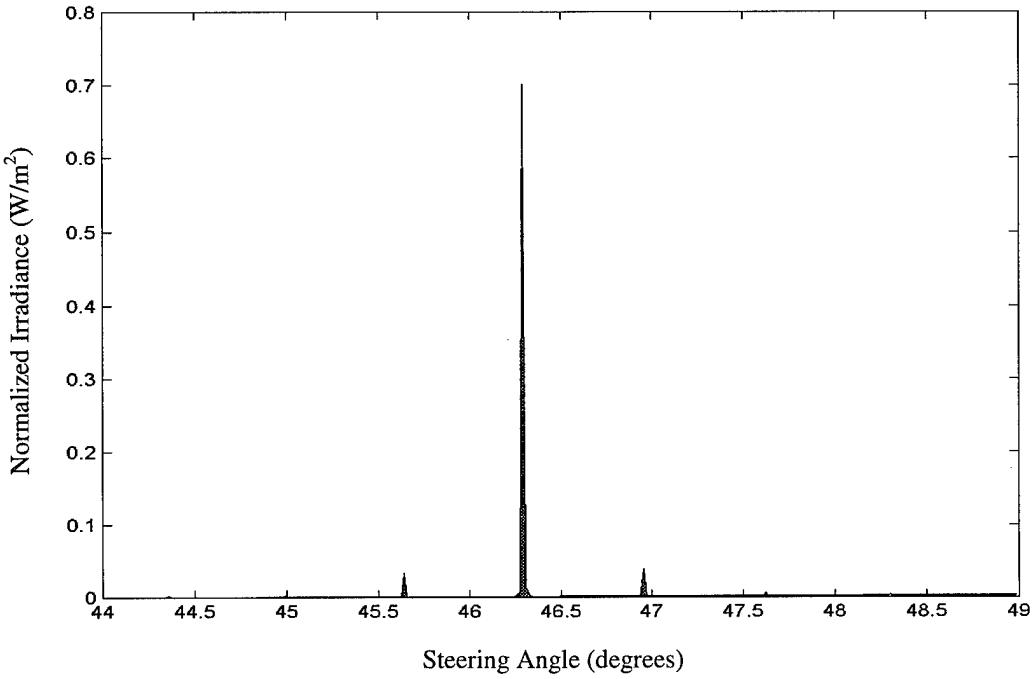

Figure 4.34. Normalized Fraunhofer irradiance pattern for a VBG with a blaze angle favoring the second diffraction order (m=2) illuminated by a source at θ_i=45°. The diffraction efficiency is 70.0%. The location of the second diffraction order is at 46.3°.

4.2.2 Electro-mechanical Modeling

This section presents the modeling used to estimate the material stress induced curvature of a micromirror and the deflection of an electrostatically actuated micromirror.

4.2.2.1 Peak-to-Valley Curvature

The peak-to-valley curvature for a micro-optic device varies as a direct function of the construction process and the width. Figure 4.35, Figure 4.36, and Figure 4.37 show measured peak-to-valley curvatures as a function of width for micromirrors constructed out of POLY-2/gold, stacked-poly/gold, and trapped-oxide/gold, respectively. The micromirrors are rectangular, with a constant length of 300 μm. The plot shown on each graph is an arc with the indicated radius of curvature (R) intersecting the origin. Do not confuse the graphs in Figure 4.35, Figure 4.36, and Figure 4.37 with a cross-sectional view of a micromirror with residual material stress induced curvature; each point in these graphs represents the measured peak-to-valley curvature for a micromirror constructed with the specified device width. Section 4.2.2.2 will discuss curvature modeling for a specific device (given the device's width and peak-to-valley curvature).

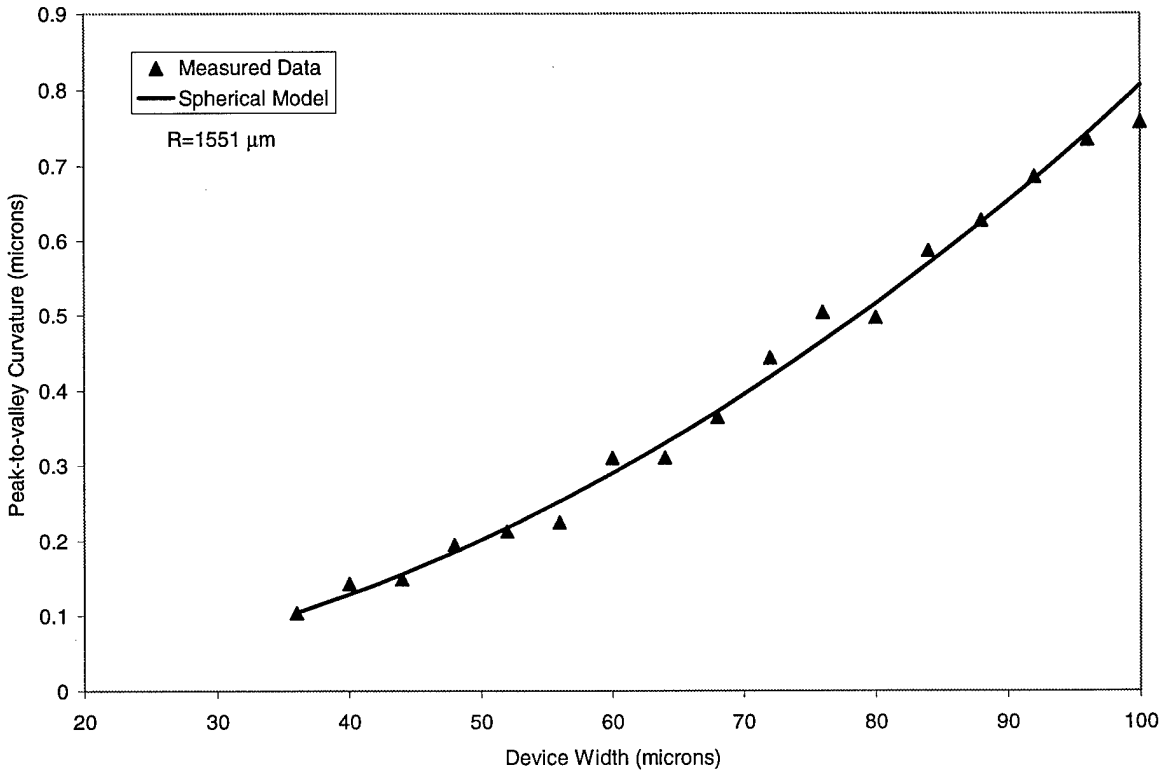

Figure 4.35. Peak-to-valley curvature for POLY-2 only/gold micromirrors varying widths (MUMPs 19).

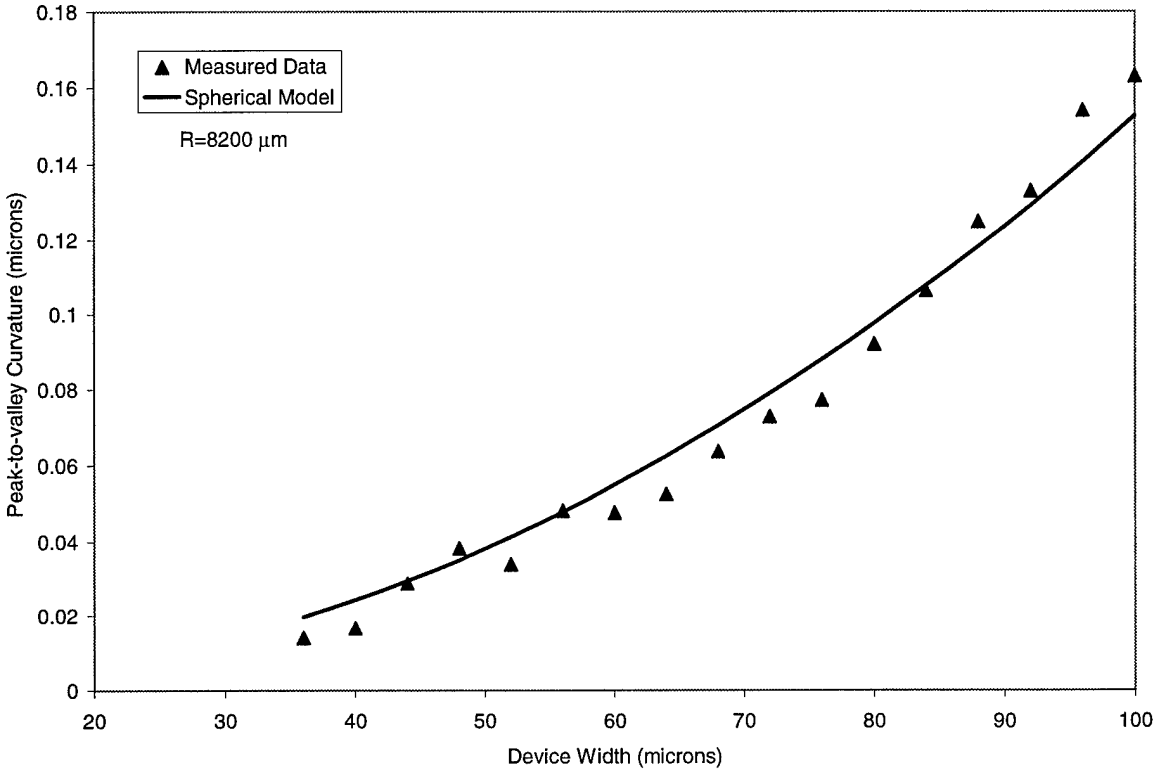

Figure 4.36. Peak-to-valley curvature for stacked-poly micromirrors with varying widths (MUMPs 19).

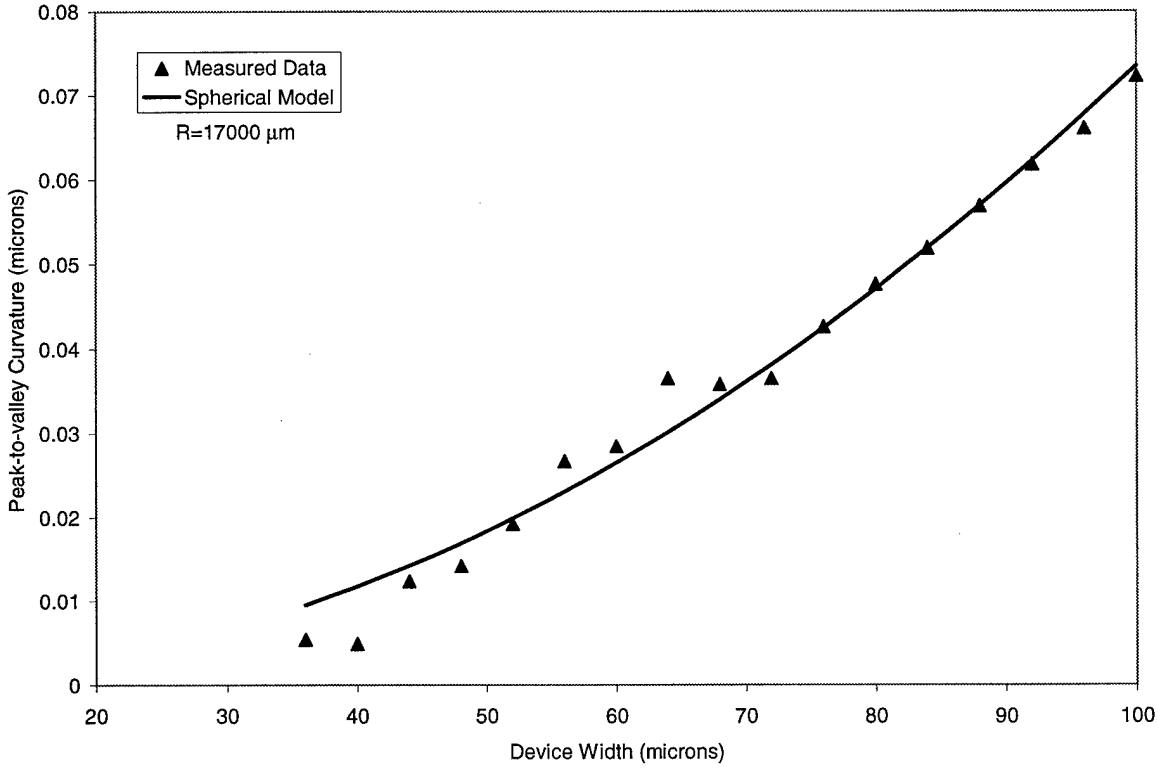

Figure 4.37. Peak-to-valley curvature for trapped-oxide/gold micromirrors varying widths (MUMPs 19).

The spherical model used to create the arcs in Figure 4.35, Figure 4.36, and Figure 4.37 is given in Equation (4.92).

$$P = R - \sqrt{R^2 - \frac{D^2}{4}} \tag{4.92}$$

Equation (4.92) was derived from Equation (4.29). D is the device width (**x** axis) and P is the peak-to-valley curvature (**y** axis). R is the radius of curvature and is an average value, calculated from the measured data using Equation (4.29). The spherical model is a good approximation of the measured data and can be used to estimate the peak-to-valley curvature for a given device width. A device's peak-to-valley curvature can be approximated if the peak-to-valley curvature is known for a similar device. Similar devices are defined as being nearly identical in shape (e.g. both rectangular) and construction (e.g. both constructed out of stacked-poly). For best accuracy, the sampled device's width should be as large as possible. Curvature plays an important role in calculating the diffraction efficiency of linear optical phased arrays and VBGs. Variations of the technique presented in this section are used in selecting the highest efficiency period for these devices. Curvature is a system design trade-off; larger period devices have a higher fill factor because the gap between adjacent devices is usually fixed at 2 μm. However the peak-to-valley curvature of a device increases exponentially. When the peak-to-valley curvature approaches a quarter of the wavelength of the source, the diffraction efficiency begins to drop sharply (this will be shown in FFT-simulations in Chapters 5 and 6).

4.2.2.2 Device Cross-sectional Curvature

Once the peak-to-valley curvature is known for a specific micromirror, the shape of the micromirror can be approximated. The micromirror shape approximation is used in FFT simulations to evaluate the impact of micromirror curvature on optical efficiency. Figure 4.38 is a cross-sectional diagram of a micromirror with residual stress induced curvature. Given the micromirror's peak to valley curvature, p, the radius of curvature, R, can be determined using Equation (4.29). The objective of this section is to define a function relating linear position (the **x** axis in Figure 4.38) to the micromirror's height (the **y** axis in Figure 4.38).

In Figure 4.38, D is the width of the micromirror, p is the peak-to-valley curvature, and R is the radius of curvature. (D_1,h_1) is a point on the micromirrors surface. The **x** and **y** axis are selected so that at $x=0$, the

micromirrors height is zero ($y=0$). The surface of the micromirror can be modeled as an arc with a radius equal to R (the radius of curvature); Equation (4.93) defines the circle that this arc belongs to:

$$\left(\frac{D}{2}-x\right)^2+\left((R-p)-y\right)^2=R^2 \tag{4.93}$$

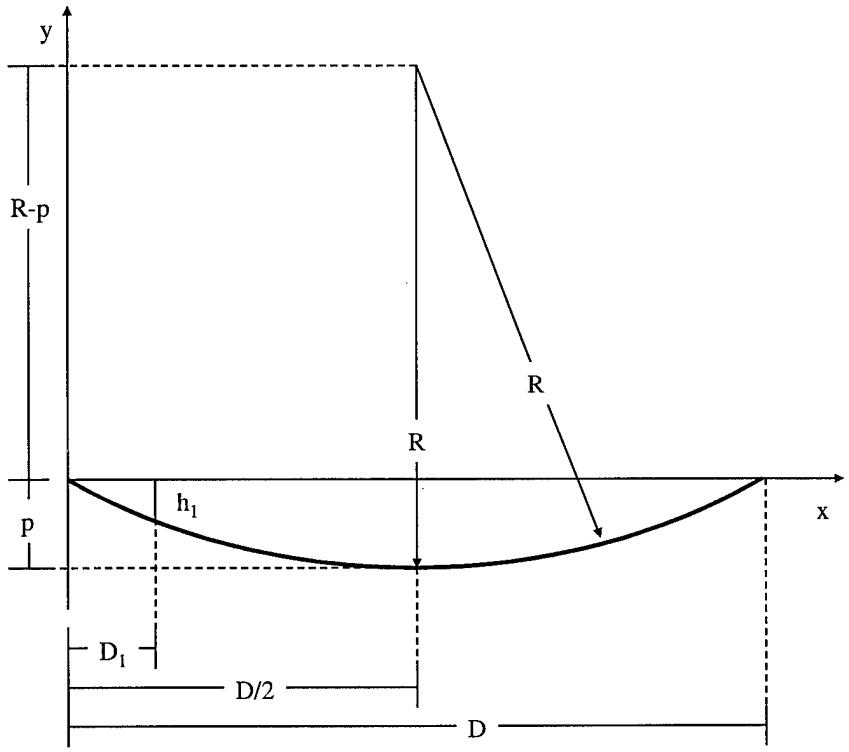

Figure 4.38. Diagram for modeling micromirror height variation as a function of position on a curved micromirror.

Solving Equation (4.93) for y yields:

$$y=R-p-\sqrt{R^2-\left(\frac{D}{2}-x\right)^2} \tag{4.94}$$

Equation (4.94) can be checked by using Figure 4.38. At $x=D/2$, y is equal to $-p$ (the maximum peak-to-valley curvature). For $x=0$ or $x=D$, Equation (4.94) becomes:

$$y=R-p-\sqrt{R^2-\left(\frac{D}{2}\right)^2} \tag{4.95}$$

If Equation (4.29) is substituted in for the radius of curvature, Equation (4.95) can be expanded to:

$$y = \left(\frac{p}{2} + \frac{D^2}{8p}\right) - p - \sqrt{\left(\frac{p}{2} + \frac{D^2}{8p}\right)^2 - \frac{D^2}{4}} \tag{4.96}$$

After simplification, Equation (4.96) becomes:

$$y = \frac{D^2}{8p} - \frac{p}{2} - \sqrt{\frac{p^2}{4} + \frac{D^2}{8} + \frac{D^4}{64p^2} - \frac{D^2}{4}} \tag{4.97}$$

The expression in the square root bracket can be reduced, yielding Equation (4.98):

$$y = \frac{D^2}{8p} - \frac{p}{2} - \left(\frac{D^2}{8p} - \frac{p}{2}\right) = 0 \tag{4.98}$$

Therefore y is equal to the peak-to-valley curvature p at $x=D/2$, and equal to zero at both ends ($x=0$ and $x=D$) of the micromirror. Equation (4.94) was embedded in a number of the author's MATLAB™ routines used to evaluate the impact of micromirror curvature on optical efficiency.

4.2.2.3 Spherical Versus Parabolic Micromirror Curvature

If the edges of a micromirror are not directly supported by a flexure, the residual stress induced curvature will deform the micromirror into the shape of a parabola. For the relatively low peak-to-valley curvature distances (compared to the length of the micromirror), this parabolic micromirror shape can be approximated by the spherical curvature equations presented in the previous section. Equation (4.99) presents the equation for a parabola through the points ($x=D/2$, $y=-p$), ($x=0$, $y=0$), and ($x=D$, $y=0$) from Figure 4.38:

$$y = \frac{p}{\left(\frac{D}{2}\right)^2}\left(\frac{D}{2} - x\right)^2 - p \tag{4.99}$$

The height error Δy between the parabolic curvature defined by Equation (4.99) and the spherical curvature defined by Equation (4.94) is:

$$\Delta y = \left| R - \sqrt{R^2 - \left(\frac{D}{2} - x\right)^2} - \frac{4p}{D^2}\left(\frac{D}{2} - x\right)^2 \right| \tag{4.100}$$

The location of the maximum height error on the **x** axis can be found by setting the derivative of Equation (4.100) with respect to x equal to zero and solving for x:

$$x = \frac{D}{2} - \sqrt{R^2 - \frac{D^4}{64p^2}} \tag{4.101}$$

If Equation (4.101) is substituted into Equation (4.100), the maximum height error, Δy_{max}, can be found for a given micromirror diameter, D, and peak-to-valley curvature, p:

$$\Delta y_{\max} = \left| R - R^2 \frac{4p}{D^2} - \frac{D^2}{16p} \right| \tag{4.102}$$

Equation (4.102) can be simplified by substituting in Equation (4.29) for the radius of curvature:

$$\Delta y_{\max} = \frac{p^3}{D^2} \tag{4.103}$$

The maximum height error between a spherical and a parabolic micromirror curvature model for a 100 μm diameter micromirror with a peak-to-valley curvature of 650 nm (the maximum peak-to-valley curvature ever measured by the author for this device) is less than 1 Å. The height error values for typical MUMPs structures are much less than the layer thickness variations in MUMPs and are less than 1% of visible wavelengths. The author used a spherical micromirror curvature approximation to model the surface of a micromirror.

4.2.2.4 Micromirror Deflection Modeling Using Equation (4.71)

Figure 4.39 is a plot of predicted deflection versus voltage for the micromirror pictured in Figure 4.22 using Equation (4.71). When the deflection distance is equal to one-third the initial separation distance, the required voltage stops increasing. Snap-through for the micromirror deflection model in Equation (4.71) occurs when an increase in micromirror deflection no longer requires an increase in applied voltage. Also shown in Figure 4.39 is measured deflection data for the micromirror in Figure 4.22. Micromirror deflection data was measured for low frequency operation (below 100 Hz), in air, at room temperature, and at one atmosphere. A Zygo interferometric microscope was used to measure deflection distances. Table 4.4 is a list of constants used in Equation (4.71) to generate the plot in Figure 4.39.

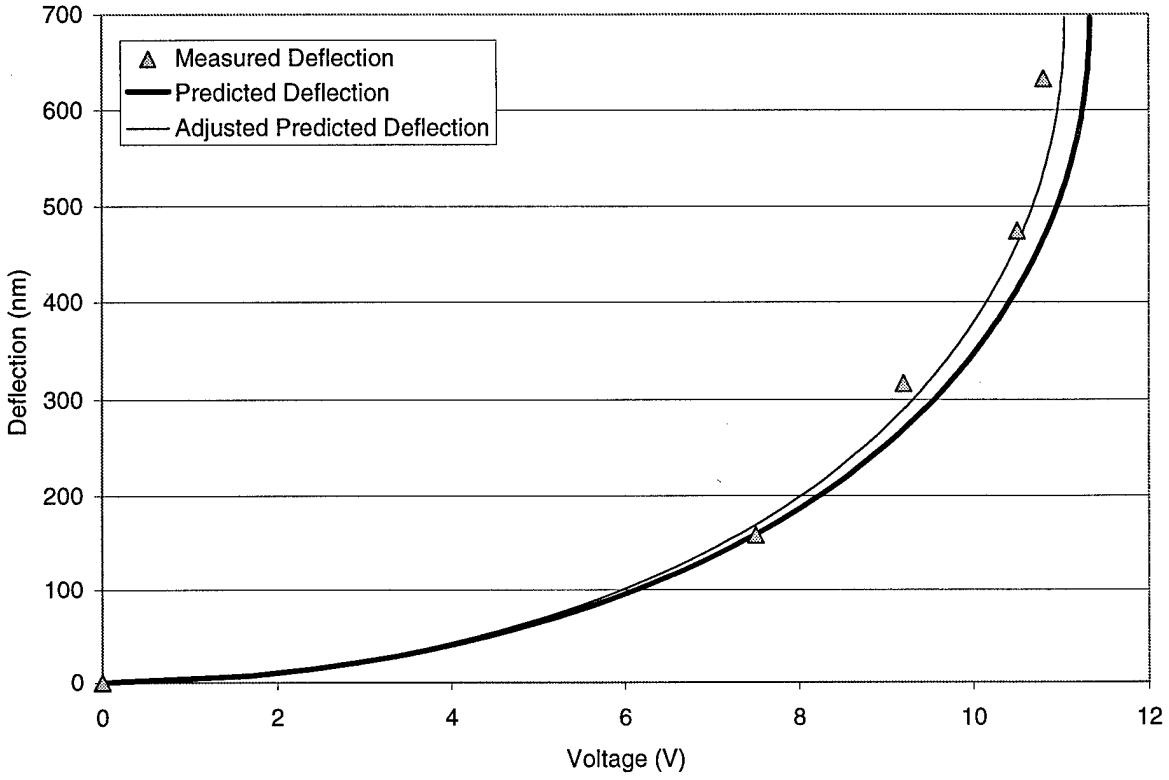

Figure 4.39. Deflection versus voltage plot for an electrostatically-actuated micromirror with linear force flexures (MUMPs 18).

The variance between the predicted and the measured deflections in Figure 4.39 was encountered often during the author's research. It was caused by fluctuations in the testing environment (humidity, temperature, and air pressure) and the manufacturing process. Each MUMPs run had small changes in both material properties and layer thicknesses. Appendix A lists some of the MUMPs material properties that changed each fabrication run. The "adjusted predicted deflection" plot in Figure 4.39 was created by evaluating Equation (4.71) with a flexure width (w) of 1.9 μm (instead of 2.0 μm). Thin width lines (less than 5 μm) are typically fabricated in MUMPs slightly narrower than the design width as a result of over-etching during the polysilicon patterning phase of construction. The adjusted predicted deflection plot demonstrates the effect of a 100 nm error in flexure width. A 100 nm flexure width error is within the error tolerances of MUMPs observed by the author during his research.

Table 4.4. Design and Material Constants Used to Model an Electrostatically Actuated Micromirror with Linear Flexures.

Item	Symbol	Value
Modulus of elasticity [26]	E	169 GPa
Number of Flexures	N	4
Flexure width	w	2.0 μm
Flexure thickness	t	1.5 μm (POLY-2)
Flexure length	L	120.0 μm
Flexure material stress [26]	σ	1.20 MPa
Flexure material Poisson ratio [26]	ν	0.22
Flexure spring constant (calculated)	k	0.6719 N/m
Initial electrode separation[a]	z_0	2.09 μm
Permittivity of free space	ε_0	8.854×10^{-14} F/cm
Electrode surface area	A	6,400 μm^2

[a] Effective electrode separation after accounting for the silicon nitride layer's dielectric effect

4.3 References

[1] R. W. Boyd, *Radiometry and the Detection of Optical Radiation*, New York, NY: John Wiley & Sons, 1983.

[2] J. Comtois, V. Bright, S. Gustafson, and M. Michalicek, "Implementation of hexagonal micromirror arrays as phase mostly spatial light modulators," *Proc. SPIE Microelectronic Structures and Microelectromechanical Devices for Optical Processing and Multimedia Applications*, vol. 2641, pp. 76-87, October 1995.

[3] E. Hecht, *Optics*, Second Edition, Reading, MA: Addison-Wesley Publishing, 1990.

[4] M. V. Klein and T. E. Furtak, *Optics*, New York, NY: John Wiley & Sons, 1986.

[5] E. A. Watson, "Analysis of beam steering with decentered microlens arrays," *Optical Engineering*, vol. 32, no. 11, pp. 2665-2670, 1993.

[6] W. Goltsos and M. Holz, "Agile beam steering using binary optics microlens arrays," *Optical Engineering*, vol. 29, no. 11, pp. 1392-1397, 1990.

[7] K. M. Flood, B. Cassarly, C. Sigg, and J. M. Finlan, "Continuous wide angle beam steering using translation of binary microlens arrays and a liquid crystal phased array," *Proc. SPIE*, vol. 1211, pp. 296-304, 1990.

[8] W. Goltsos and M. Holz, "Binary micro optics: an application to beam steering," *Proc. SPIE*, vol. 1052, pp. 131-141, 1989.

[9] Z. D. Popovic, R. A. Sprague, and G. A. Neville Connell, "Technique for monolithic fabrication of microlens arrays," *Applied Optics*, vol. 27, no. 7, pp. 1281-1284, 1988.

[10] J. T. Verdeyen, *Laser Electronics*, Englewood Cliffs, NJ: Prentice Hall, 1995.

[11] J. D. Gaskill, *Linear Systems, Fourier Transforms, and Optics*, New York, NY: John Wiley & Sons, 1978.

[12] P. M. Osterberg, R. K. Gupta, J. R. Gilbert, and S. D. Senturia, "Quantitative models for the measurement of residual stress, Poisson ratio and Young's modulus using electrostatic pull-in of beams and diaphragms," *Proc. Solid-State Sensor and Actuator Workshop*, Hilton Head Island, SC, pp. 184-188, June 13-16, 1994.

[13] M. H. Nayfeh and M. K. Brussel, *Electricity and Magnetism*, New York, NY: John Wiley & Sons, 1985.

[14] M. A. Michalicek, V. M. Bright, and J. H. Comtois, "Design, fabrication, modeling, and testing of a surface-micromachined micromirror device," *Proc. 1996 ASME Dynamic Systems and Control Division*, DSC-vol. 57-2, pp. 981-985, 1995.

[15] M. A. Michalicek, D. E. Sene, and V. M. Bright, "Advanced modeling of micromirror devices," *Proc. International Conference of Integrated Micro/Nanotechnology for Space Applications*, pp. 214-225, NASA & Aerospace Corp. Publications, October 30, 1995.

[16] J. L. Meriam, *Engineering Mechanics, Volume 1, Statics*, SI version, New York, NY: John Wiley & Sons, 1980.

[17] K. K. Stevens, *Statics & Strength of Materials*, 2nd ed., Englewood Cliffs, NJ: Prentice-Hall, 1987.

[18] T. H. Lin, "Implementation and characterization of a flexure-beam micromirror spatial light modulator," *Optical Engineering*, vol. 33, pp. 3643-3648, 1994.

[19] J. H. Comtois and V. M. Bright, "Surface micromachined polysilicon thermal actuator arrays and applications," *Proc. Solid-state Sensor and Actuator Workshop*, Hilton Head Island, SC, June 1996.

[20] D. A. Neamen, *Semiconductor Physics and Devices: Basic Principles*, Burr Ridge, IL: Irwin Inc., 1992.

[21] P. J. Ouseph, *Technical Physics*, New York, NY: John Wiley & Sons, Inc., 1986.

[22] S. Gartenhaus, *Physics: Basic Principles*, New York, NY: Holt, Rinehart, and Winston, 1977.

[23] MATLAB is a registered trademark of *The MathWorks, Inc.*, 24 Prime Park Way, Natick, MA 01760.

[24] J. W. Goodman, *Introduction to Fourier Optics*, New York, NY: McGraw-Hill Companies, Inc., 1996.

[25] R. G. Wilson, *Fourier Series and Optical Transform Techniques in Contemporary Optics*, New York, NY: John Wiley & Sons, Inc., 1995.

[26] W. N. Sharpe, Jr., B. Yuan, R. Vaidyanathan, and R. L. Edwards, "Measurements of Young's modulus, Poisson's ratio, and tensile strength of polysilicon," *Proc. 10th Annual IEEE MEMS Workshop*, Nagoya, Japan, pp. 424-429, 1997.

5 Optical Beam Steering for the Holographic Data Storage Initiative

The Holographic Data Storage Initiative (HDSI) is part of the DARPA/National Storage Industry Consortium (NSIC) holographic data storage project. The University of Dayton Research Institute (UDRI) sponsored the Air Force Institute of Technology to create both linear optical phased arrays and fast beam steering micromirror designs for directing a laser beam into a holographic data storage crystal. This chapter presents a description of a typical holographic data storage system and discusses the MEMS devices designed at AFIT for the HDSI program.

5.1 Background

Holographic data storage may be the next revolution in data storage. Holographic data storage devices with capacities of 63 Gbytes and a data transfer rate of 1.25 Gbytes/second have been proposed, and may be constructed within the next few years [1]. MEMS are an excellent fit for the HDSI program because micro-optical devices are typically cheap, reliable, fast, and rugged [2]. Also the size of micro-optical devices matches the scale of compact holographic data storage systems. Holographic data storage is a potential solution for the increasingly demanding Air Force data processing requirements, therefore AFIT is a logical choice for the development of MEMS optical devices for the HDSI program.

5.1.1 A Holographic Data Storage System

A simplified holographic data storage system is shown in Figure 5.1. To record data, a laser beam is passed through a Spatial Light Modulator (SLM) to form a two dimensional pattern (a data page) on the storage crystal. Because holographic data storage occurs in a volume, a reference laser beam is used to designate the address (or location) of the page in the storage medium. Often a photorefractive crystal is used as the storage medium. Holographic data storage systems read and write a page at a time. Liquid Crystal Displays (LCDs)

are often used as the SLM [3]; although MEMS SLMs are becoming available [4,5,6]. A stored page is read by inputting the reference beam in the same format that was used to store the data.

Three types of reference beam addressing have been proposed: angle multiplexing, phase code modulation, and wavelength modulation [1]. The author has designed micro-optical components for both angle multiplexing and phase code modulation addressing. Recently researchers at Cornell University announced they were close to completing the development of a micromachined tunable Vertical Cavity Surface Emitting Laser (VCSEL) [7]. A tunable VCSEL could be used to perform wavelength modulation in an HDSI system. Angle multiplexing is straight foreword: the reference beam is steered by a small scanning mirror so the angle of the reference beam's arrival at the storage crystal changes. The address of the page to be accessed in the storage crystal is given by the angle of the reference beam's arrival. Phase code modulation addressing will be discussed in the next section.

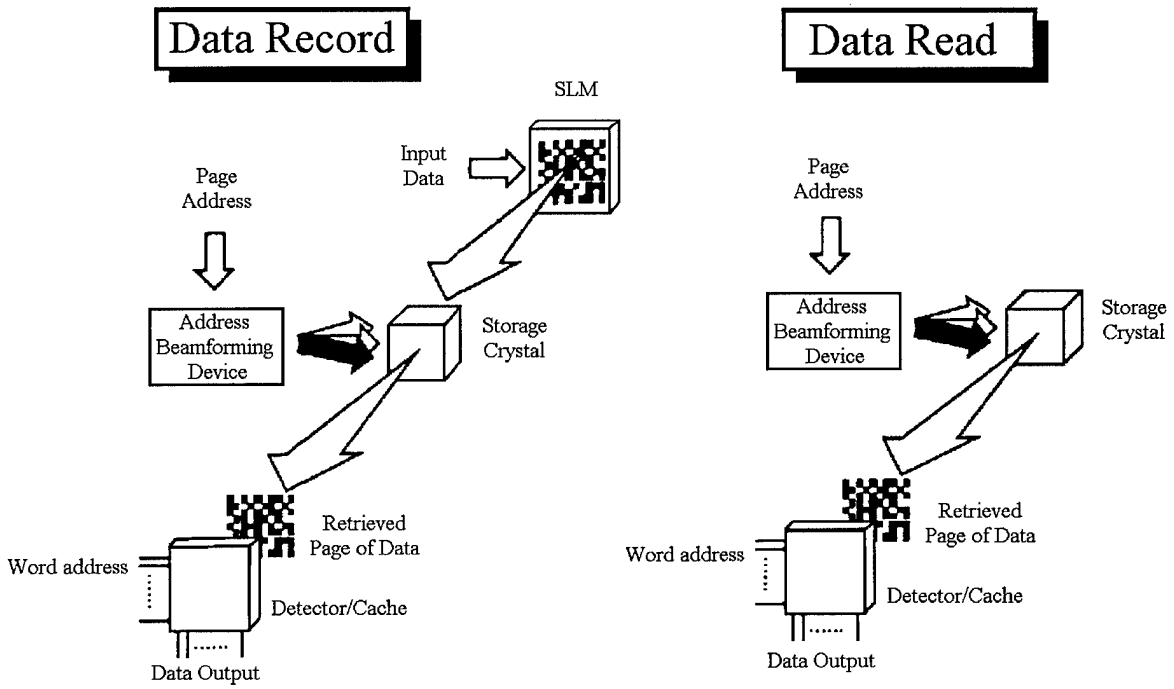

Figure 5.1. A holographic data storage system [1].

5.1.2 HDSI Linear Optical Phased Array System Overview

Linear optical phased arrays can be used to encode data in interference patterns and store the patterns in storage crystals. The interference patterns may be controlled using phase code multiplexing, in which all reference beams are employed simultaneously (at many angles) with a different phase pattern for each data record. Linear phased arrays may be particularly appropriate for phase code multiplexing if very low (e.g. less than 1%) systematic error in micromirror flatness and actuation displacement can be achieved [8]. Phase encoding is more challenging than angle multiplexing because optical noise and crosstalk are difficult to control using current state-of-the-art optical components [9].

A key advantage of phase encoding the reference beam is speed. Angle multiplexing requires both coarse and fine movements of the micromirror to achieve the high positional accuracies (±100 μrad) demanded by HDSI systems [10]. Linear optical phased arrays could be operated in a binary mode, eliminating the need for fine positional control. For binary operation, array elements are either up (zero phase change in reflected light) or down (the phase of the reflected light is increased by π radians). Binary mode operation for array elements fabricated in MUMPs relies on a fixed voltage to pull the array element down to rest on the silicon nitride layer. One of the proposed reference beam wavelengths for the HDSI project is 533 nm [11]. If the array elements are vertically displaced 2.0 μm, then the net phase change for normally incident light is 1.0094π (less than 1% error). A 2.0 μm displacement can be easily achieved in MUMPs because it is equal to the thickness of the first sacrificial oxide layer. Therefore most of the HDSI optical phased array element designs at AFIT have a 2.0 μm vertical displacement in the down position.

5.1.3 AFIT's Role in the Holographic Data Storage Initiative

The University of Dayton Research Institute sponsored the Air Force Institute of Technology to create three HDSI linear optical phased arrays prior to 1996; these arrays (designed by Comtois [12]) were designated as first, second, and third generation devices, respectively. Two more HDSI linear optical phased arrays were designed in 1996 and 1997 by the author and these arrays are designated as fourth and fifth generation devices.

Devices designed before 1996 are referred to as earlier generations; subsequent devices are referred to as later generations.

Primary differences between the generations are micromirror curvature tolerances and optical spacing requirements. Earlier generations were fabricated before test equipment (specifically the ZYGO Maxim-3D laser interferometer – see Appendix C for a description) was in place to evaluate the extent of micromirror curvature. The top electrode of all earlier generation designs consisted of a single POLY-2 plate covered by a layer of gold. Later generations used trapped-oxide or stacked-poly to reduce micromirror curvature. HDSI is an on-going project so optical requirements are continually being updated. After the fabrication of earlier generation designs was complete, the required array period was changed to 30 μm. Later generation designs all have an array period of 30 μm.

Under the sponsorship of the University of Dayton, the author designed, fabricated, released, and packaged the HDSI linear optical arrays. The author used MUMPs to fabricate the HDSI optical phased arrays; device release and packaging were done at AFIT and included wire-bonding all array elements to a Pin Grid Array (PGA) package. Figure 5.2 depicts a fourth generation linear optical phased array packaged by the author. The devices were scheduled to be shipped to Stanford University after packaging for optical testing. Unfortunately the linear optical phased array portion of the HDSI project was canceled before Stanford University could test the later generation devices. After the project was canceled, funding was not available for AFIT to test the devices in a holographic data storage system. Later generation devices were electrically and physically characterized and FFT modeling was used to predict optical performance. Previous researchers at AFIT have modeled and tested similar linear optical phased arrays with excellent results. Christensen used a 10 element MUMPs fabricated micromirror array to steer the output from a linear array of edge emitting semiconductor lasers [13].

5.1.4 State-of-the-Art Linear Optical Phased Arrays

Figure 5.3, Figure 5.4, and Figure 5.5 depict the first, second, and third generation linear optical phased arrays, respectively, designed by Comtois [12]. Physical and electrical characterizations of these arrays

were performed by the author and are listed in Table 5.1. Micromirror curvature and a requirements change for the array period compelled the author to design fourth and fifth generation devices. The third generation used a reduced gold layer size to minimize the effects of residual material stress induced curvature. An operational holographic data storage system using the array shown in Figure 5.5 would require a microlens array to create a useable fill factor.

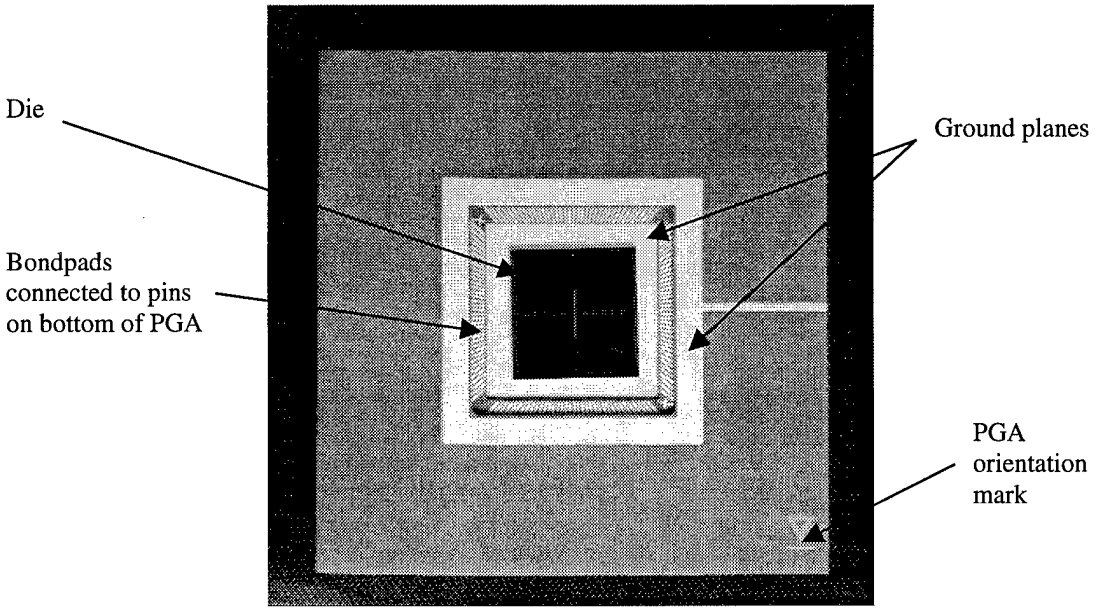

Figure 5.2. Fourth generation linear optical phased array in a 144 pin PGA package (fabricated by the author in MUMPs 15).

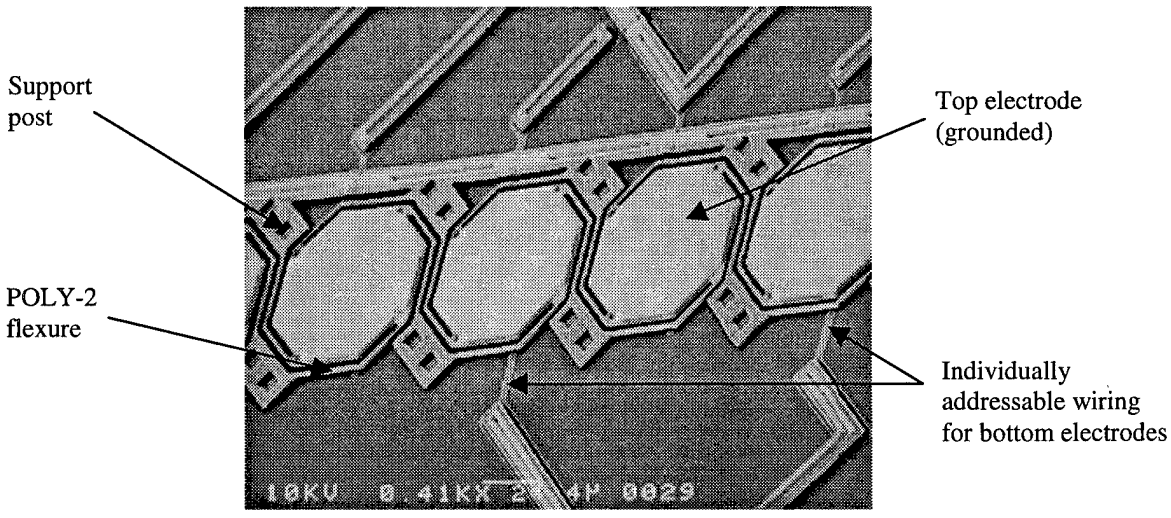

Figure 5.3. A first generation linear optical phased array (MUMPs 9).

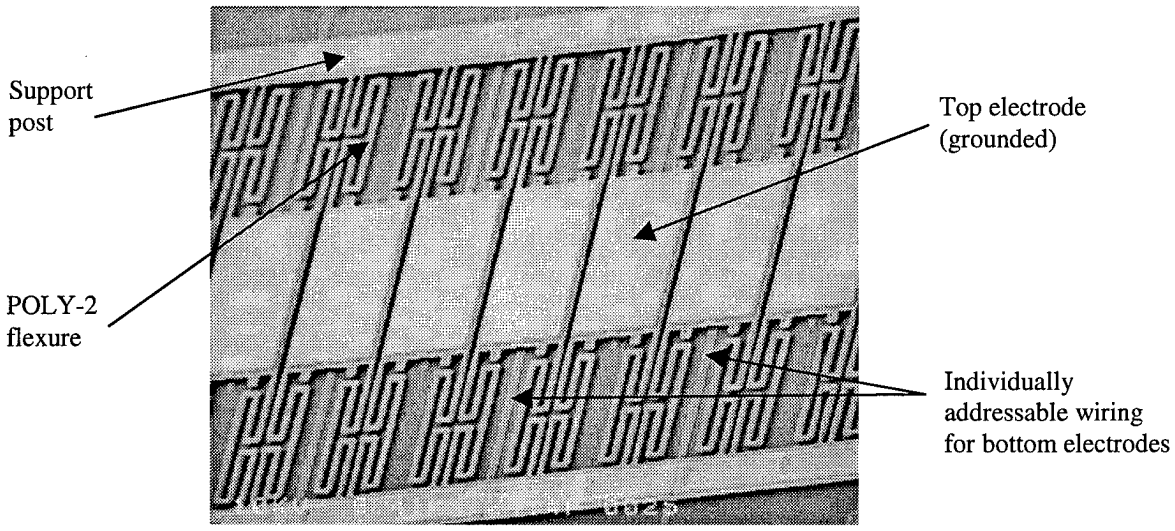

Figure 5.4. A second generation linear optical phased array (MUMPs 9)

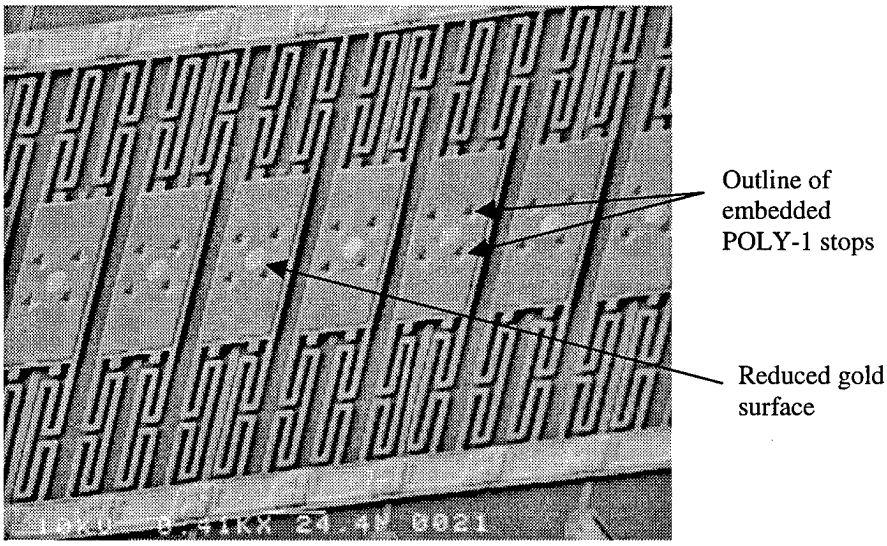

Figure 5.5. A third generation linear optical phased array (MUMPs 10).

The calculated pull down voltages in Table 5.1 were computed using Equation (4.71). The differences between the calculated and measured pull down voltages are due to variances in humidity (the devices were tested in air) and material stress (MUMPs material properties vary each production run). Values for the measured pull down voltages for the linear optical phased arrays were obtained using the ZYGO Maxim-3D laser interferometer and a Hewlett-Packard Digital Power Supply (both described in Appendix C). Because the

vertical displacement distance is small (2.0 μm or less), an ordinary microscope with a line-of-sight normal to the array element's top electrode is unable to show when an array element reaches snap-through. The ZYGO interferometer creates an interference pattern on the surface of the array element as a function of the array element's vertical position; deflections of a quarter wavelength are easily visible. The ZYGO interferometer uses a HeNe laser source operating at a wavelength of 632.8 nm [14] so deflections of 158.2 nm or more can be detected by the observer.

Table 5.1. Characteristics of Early Generation Linear Optical Arrays.

	1st Generation	2nd Generation	3rd Generation
MUMPs Fabrication Run	8*	9	10
Number of Elements	133	256	256
Vertical Range of Motion** (μm)	2.0	2.0	0.75
Array Period (μm)	92.37	53.50	53.50
Linear Fill Factor (%)	82.76	82.24	18.67
Number of Flexures	4	4	4
Flexure Length (μm)	65.0	185.0	185.0
Flexure Width (μm)	2.0	2.0	2.0
Surface Area Above Bottom Electrode (μm^2)	3,363.5	3,496.0	3,496.0
Width of Element's Gold Layer (μm)	76.37	44.0	10.0
Curvature Across Width (peak to valley) (nm)	270.3	67.4	16.1
Curvature Across Length (peak to valley) (nm)	270.3	228.6	16.1
Bottom Electrode Construction	POLY-0	POLY-0	POLY-0
Calculated Pull Down Voltage (V)	58.8	12.2	12.2
Measured Pull Down Voltage (V)	53.0	15.0	15.0

*Because of fabrication problems at MCNC, this design was resubmitted for MUMPS 9.

**Vertical range of motion has not been corrected for curvature.

The Hewlett-Packard digital power supply was used because of its fast response time (less than 750 μs) and minimal voltage overshoot (less than 1%) [15]. Voltage overshoot is defined as the difference between the peak voltage arriving at the device when the power supply's output is enabled and the average voltage arriving at the device after the power supply reaches steady state. The top electrode is in close proximity to the bottom electrode after snap-through so the amount of voltage required to hold the top electrode in this position is less than the snap-through voltage. This effect is sometimes called "latching". If a power supply with a significant voltage overshoot is used, a low snap-through voltage could be erroneously detected.

5.2 Fourth Generation HDSI Array

The design for the fourth generation linear optical phased array was submitted to MCNC in September 1996 (MUMPs 15). The author's primary objective in the fourth generation design was to minimize micromirror curvature. Trapped-oxide was used to create the flattest array element design possible with the MUMPs process. Another significant improvement over earlier generation devices is the use of the substrate as the bottom electrode. Earlier generation devices used POLY-0 bottom electrodes. Because MUMPs is a conformal surface micromachining process, the POLY-0 bottom electrodes unintentionally emboss all subsequent layers. To prevent unintentional embossing of the gold layer in earlier designs, the gold layer had to be inset farther from each edge of the array element so that it lay within the boundary of the bottom electrode. Insetting the gold layer farther from each edge of the element reduced the array's fill factor.

One of the innovations resulting from the author's research was the application of the substrate electrical contact technique developed by Comtois [12] to make the substrate the bottom electrode and eliminate the standard POLY-0 bottom electrode. In addition to improving the topology of the top electrode, the use of the substrate as the bottom electrode places the silicon nitride layer (an excellent electrical insulator) between the top and bottom electrodes. The silicon nitride layer prevents the destruction of the array element by excessive current flowing between the top and bottom electrodes after snap-through. The impact of using the substrate on a micromirror's stable deflection distance was discussed in Chapter 4. Earlier generations used grounded top electrodes and individually addressable bottom electrodes; later generations used a grounded substrate and individually addressable top electrodes.

5.2.1 Array Element Description

Figure 5.6 depicts a fourth generation linear optical phased array. A close-up view of the array in Figure 5.6 is shown in Figure 5.7. If the substrate is grounded, an array element can be pulled all the way down to the silicon nitride layer by applying 24.5 V to the top electrode. Stiction of the top electrode to the silicon nitride layer was not apparent; however the response time of the fourth generation array element (0.833 ms in nitrogen at a pressure of 20 mTorr) was slow. The slow response time is due to the large surface area of the array element (the entire lower surface area of the top electrode – 308 μm^2) in direct contact with the silicon nitride layer when the device is fully deflected.

No measurable inter-element crosstalk was observed between adjacent array elements using the ZYGO Maxim-3D interferometric microscope. However alternate array elements (every other array element) did exhibit crosstalk as a result of the array element address wiring. The wiring used to connect the top electrode of each array element to a bondpad at the edge of the die is visible in Figure 5.6. Every other array element is wired to the same side of the array. Address wires are constructed out of 15 μm wide POLY-0 busses separated by a distance of 45 μm. The wires are long (often over 5 mm) so inductive coupling caused alternate array elements on each side of the selected array element to be slightly deflected when voltage was applied on the address wire for the selected array element. Electrostatically actuated micromirrors require virtually zero current so even a small induced voltage from an adjacent address wire is capable of causing a deflection. When an array element in the middle of the array is pulled all the way down to the silicon nitride layer, an alternate array element may be pulled down as much as 150 nm. Alternate element crosstalk can be removed by placing grounded POLY-0 traces between the array element address wires; future array designs by the author with long address wires used grounded POLY-0 traces to eliminate alternate element crosstalk.

The array shown in Figure 5.6 had 128 elements, each separated by a gap of 3 μm. The gold layer was inset 4 μm from each edge of the top electrode. The vertical travel of the top electrode before it contacted the silicon nitride layer was 2.0 μm. The linear fill factor of the fourth generation linear optical phased array was 63.33%. The trapped-oxide design was very successful at reducing micromirror curvature; measured micromirror curvature across the width of this device was only 9.9 nm.

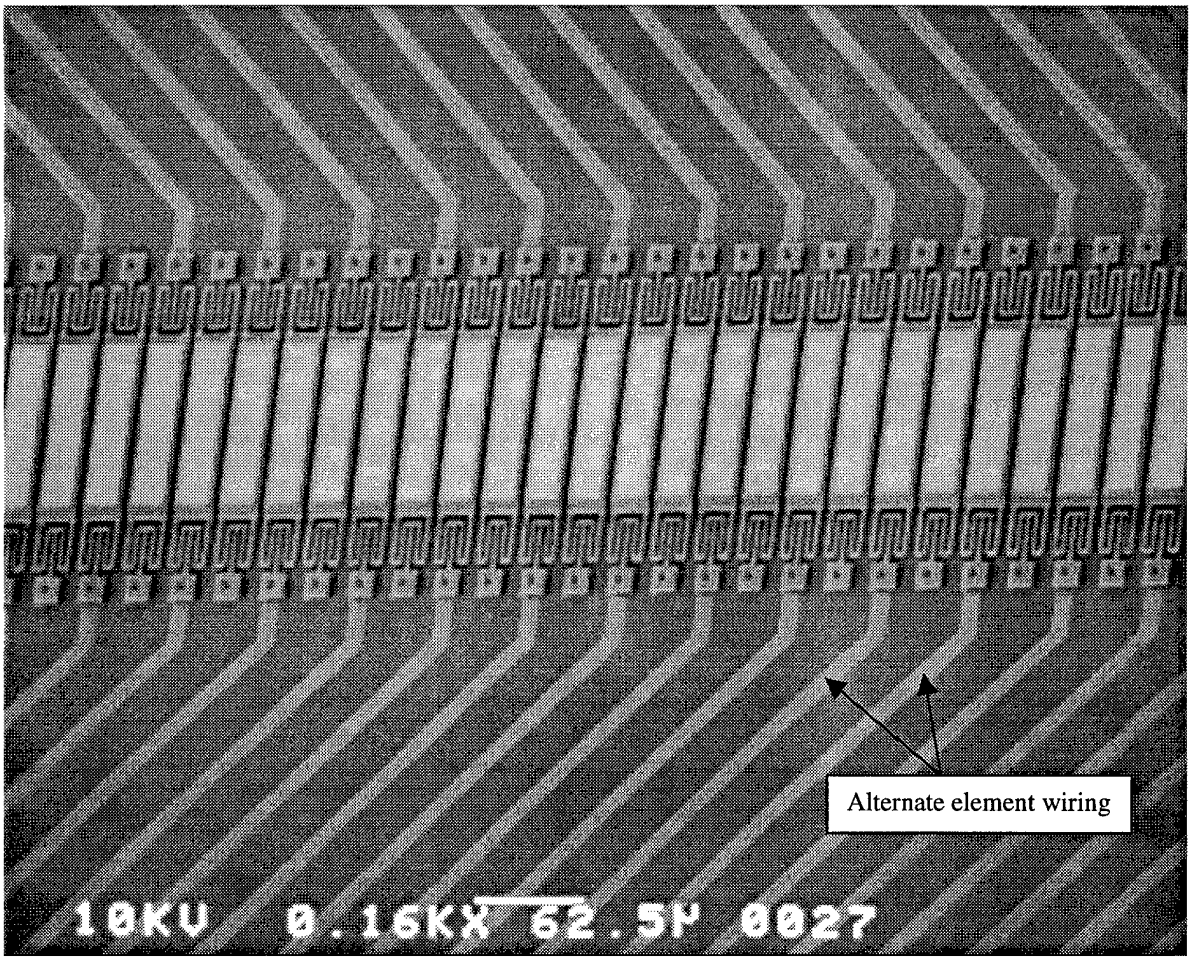

Figure 5.6. A fourth generation linear optical phased array (fabricated by the author in MUMPs 15).

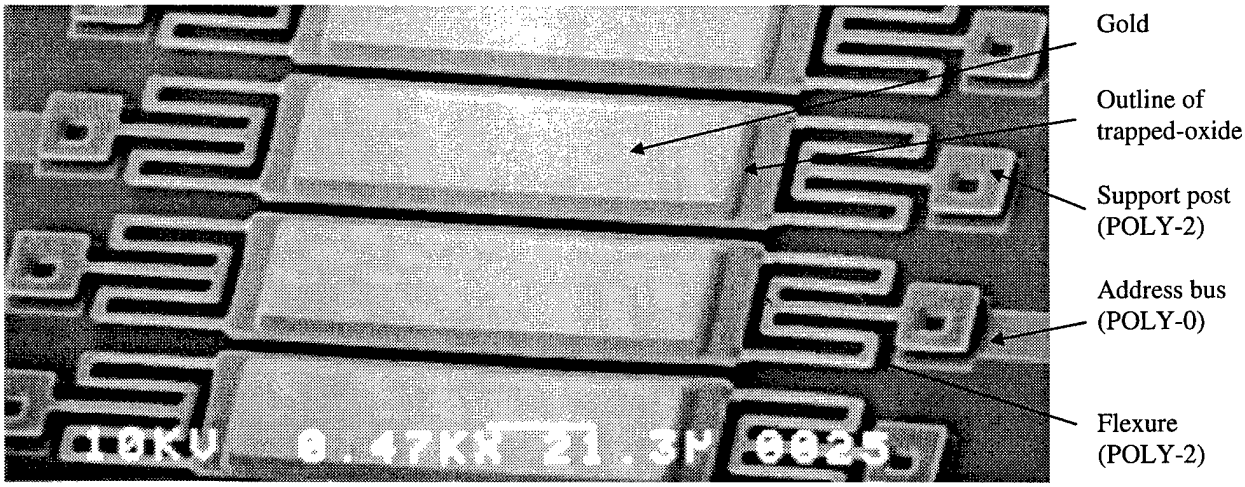

Figure 5.7. Close-up view of fourth generation linear optical phased array elements (fabricated by the author in MUMPs 15).

5.2.2 Predicted Array Performance

A 16,384 (2^{14}) point FFT simulation of the fourth generation linear optical phased array was conducted by the author. The objective of this FFT simulation was to model the optical efficiency (the ratio of the intensity of the light in the steered direction to the intensity of the source) as a function of the beam steering angle (measured from the axis normal to the face of the array). The illumination source was a normally incident HeNe laser with a wavelength of 632.8 nm. Because the phase encoding portion of the HDSI project was terminated, the FFT simulation was based on steering an optical beam (continuously adjustable array element vertical displacements). Many Air Force applications could benefit from continuous optical beam steering using a phased array [16,17,18]. In continuous mode operation, each array element is positioned so that the light reflected off all array elements creates a wavefront perpendicular to the desired beam steering direction. The FFT simulation sample size was 234.4 nm; no modeled features were less than 1 μm (well below the Nyquist interval [19]). The array elements were positioned to steer an optical beam over the range of ±0.604°. The results of the FFT simulation are shown in Figure 5.8. The beam steering angle was sampled 1,600 times so the beam steering angle interval was 7.55×10^{-4} degrees.

Optical efficiency for this linear array was relatively low because only 63.3% of the 30 μm array period was covered by the gold layer. The peak predicted optical efficiency was 38.2%. The "ringing" or output oscillation in Figure 5.8 was caused by the large width (compared to the wavelength of the source) of each array element. The positioning of each array element was calculated based on light reflected from the center of each element; however light is reflected from the entire width of the array element. If the beam steering angle was set to a nonzero value, then the light reflected off the center of the array element destructively interfered with the light reflected off other regions of the array element (such as near the edge of the gold layer). The degree of destructive interference changes as the beam steering angle was increased, causing oscillations. The magnitude of the oscillation could be greatly reduced if the array element's width was equal to half of the wavelength of the source; unfortunately current MEMS manufacturing processes do not support the construction of such a device.

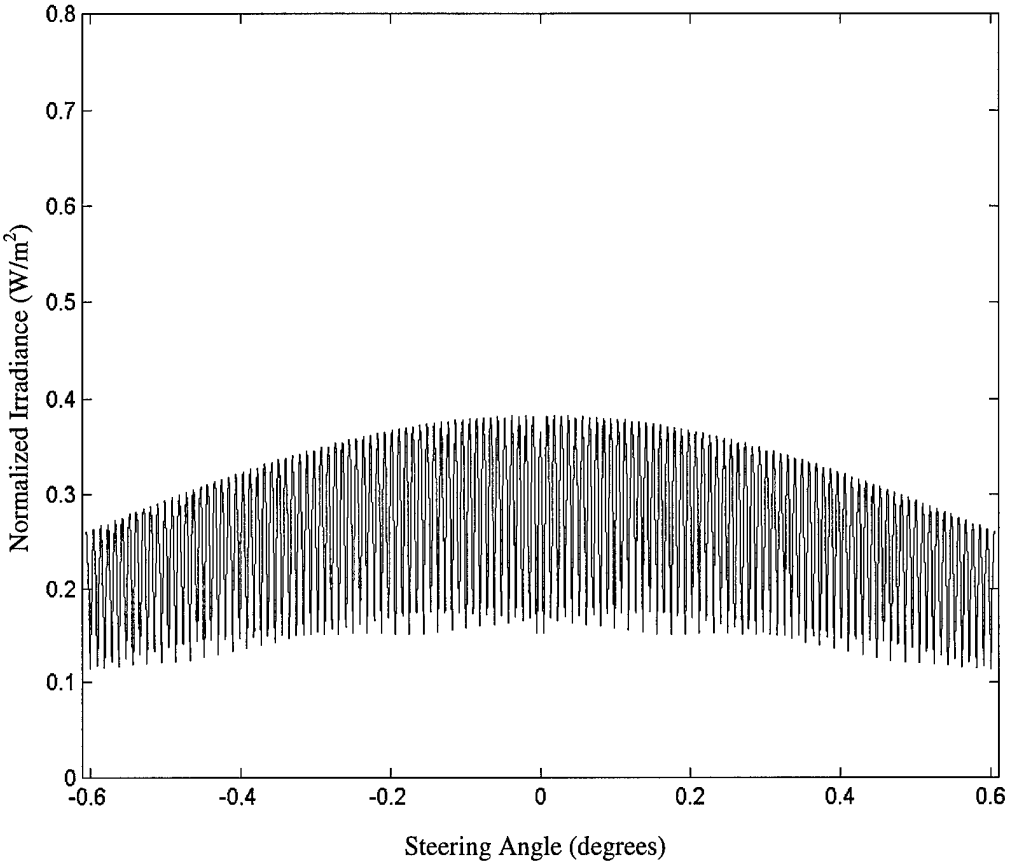

Figure 5.8. Fourth generation linear optical phased array predicted performance.

Interference also resulted from the 4 μm wide polysilicon border on each side of the gold layer which was 500 nm lower than the gold layer (the thickness of the gold layer). For a normally incident source with a wavelength of 632.8 nm, the light reflected from the polysilicon border was 1.16π radians out of phase with the light reflected from the gold layer. Much of the out of phase light reflected off the polysilicon border destructively interfered with the light reflected off the gold layer. Fortunately the measured reflectivity of the MUMPs POLY-2 layer at a source wavelength of 632.8 nm was only 34.9% compared to 91.5% for the gold layer.

The fourth generation array element design was one of the first applications of trapped-oxide to minimize micromirror curvature. The author created a number of test structures on subsequent MUMPs

fabrication runs and discovered that the HDSI array fill factor could be improved without sacrificing yield. Trapped-oxide designs with the gold layer inset 2 μm from each edge of the POLY-2 layer and a separation distance between adjacent array elements of 2 μm were determined by the author to be practical and were extensively used in subsequent variable blaze grating designs. Applying some of these lessons learned to the array element pictured in Figure 5.7 would result in a 24 μm wide gold layer with a 2 μm gap between adjacent array elements; the fill factor of the improved device would be 80%.

5.3 Fifth Generation HDSI Array

The effect of mirror curvature and array fill factor on array optical efficiency was investigated. The investigation evaluated the three basic top electrode designs (POLY-2 only, stacked-poly, and trapped-oxide) over array periods ranging from 20 μm to 100 μm. An FFT simulation was used to evaluate the maximum optical efficiencies of arrays constructed from each of the top electrode designs. Array elements were positioned to support a non-zero beam steering angle where the array optical efficiency was the highest; results of this FFT simulation are shown in Figure 5.9. The peak-to-valley residual material stress induced curvature increased for all top electrode designs as the array period increased; however the rate of curvature increase depended on the design of the top electrode. POLY-2 only and stacked-poly array elements had a gold layer that was inset 1 μm from each edge of the array element. Trapped-oxide array elements had a gold layer that was inset 2 μm from each edge of the array element. The gap between adjacent array elements was 2 μm for all array element designs. Based on Figure 5.9 and a required array period of 30 μm, the author decided to use a stacked-poly array element design for the fifth generation array. For array periods below 70 μm, the benefits of a higher array fill factor outweighed the costs associated with higher mirror curvature.

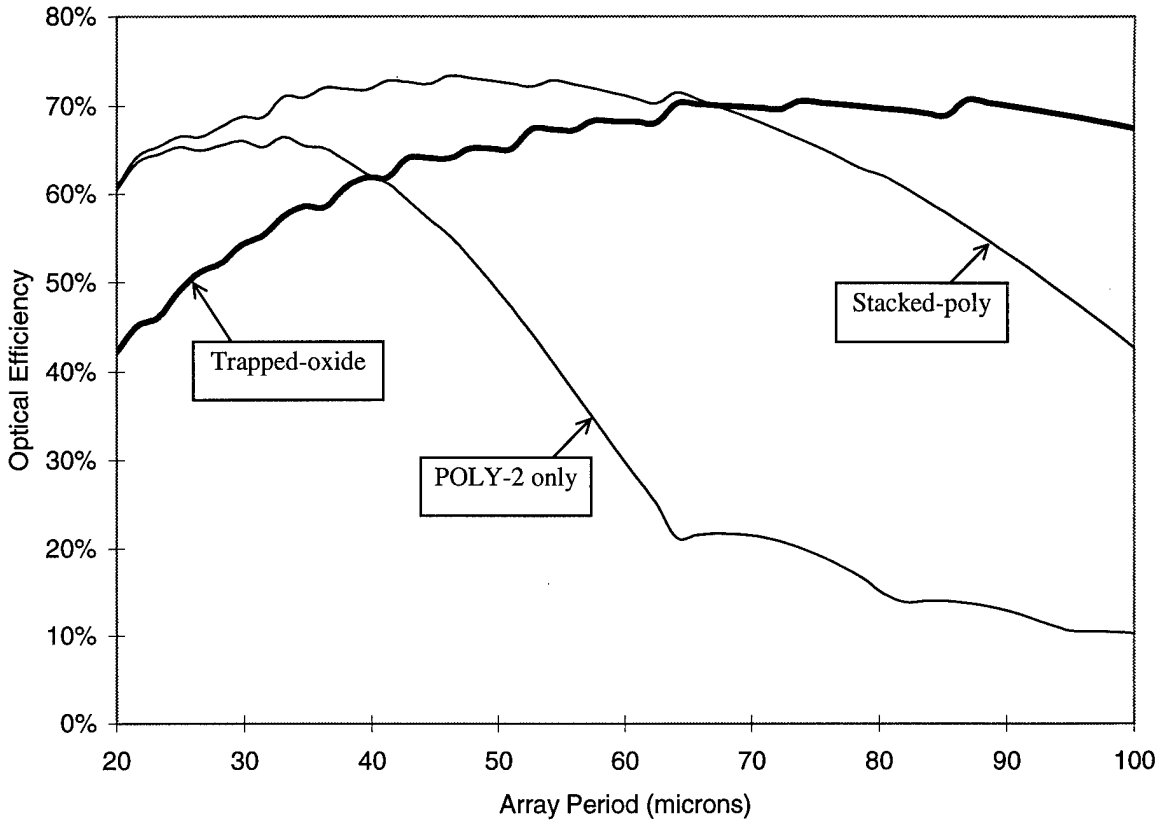

Figure 5.9. Predicted maximum optical efficiencies as a function of array period and element construction technique. Array elements were actuated to support the non-zero beam steering angle with the highest optical efficiency.

5.3.1 Array Element Description

The fifth generation linear optical phased array design is depicted in Figure 5.10. A close-up view of the array in Figure 5.10 is shown in Figure 5.11. The width of gold layer matched the width of the top electrode in this stacked-poly design. The gap between adjacent array elements was 2 μm. The yield for this device was 97.22% for each adjacent pair of array elements; 2.78% of the adjacent array element pairs had a gold bridge connecting the array elements. The gold bridge was a construction flaw created during fabrication; the 2 μm gap between adjacent gold layers was insufficient to guarantee that the patterning step would remove the gold between the array elements. If the gold layer was inset 1 μm from each edge of the top electrode, the yield was increased to 100%.

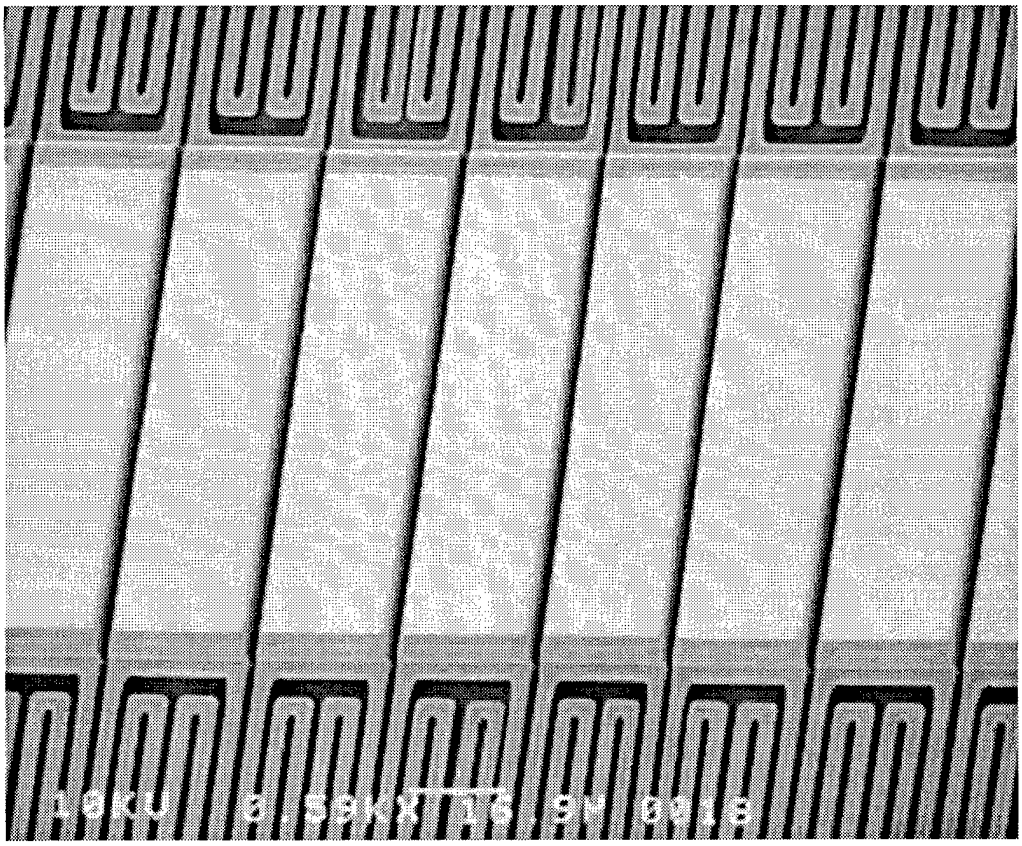

Figure 5.10. A fifth generation linear optical phased array (fabricated by the author in MUMPs 19).

The MUMPs process is continually improving [20] so it is very likely that the array elements pictured in Figure 5.10 will soon be commercially viable for large arrays. If a 100% yield with the MUMPs process is desired, then the array element in Figure 5.11 could be modified so that the gold layer is inset 1 μm from each edge of the array element. Table 5.2 lists the physical and electrical characteristics of the fourth and fifth generation linear optical phased arrays.

5.3.2 Predicted Array Performance

A 16,384 (2^{14}) point FFT simulation of the fifth generation linear optical phased array shown in Figure 5.10 was conducted for a normally incident laser source at a wavelength of 632.8 nm (HeNe). The objective of this FFT simulation was to model the array's optical efficiency as a function of the beam steering angle. The

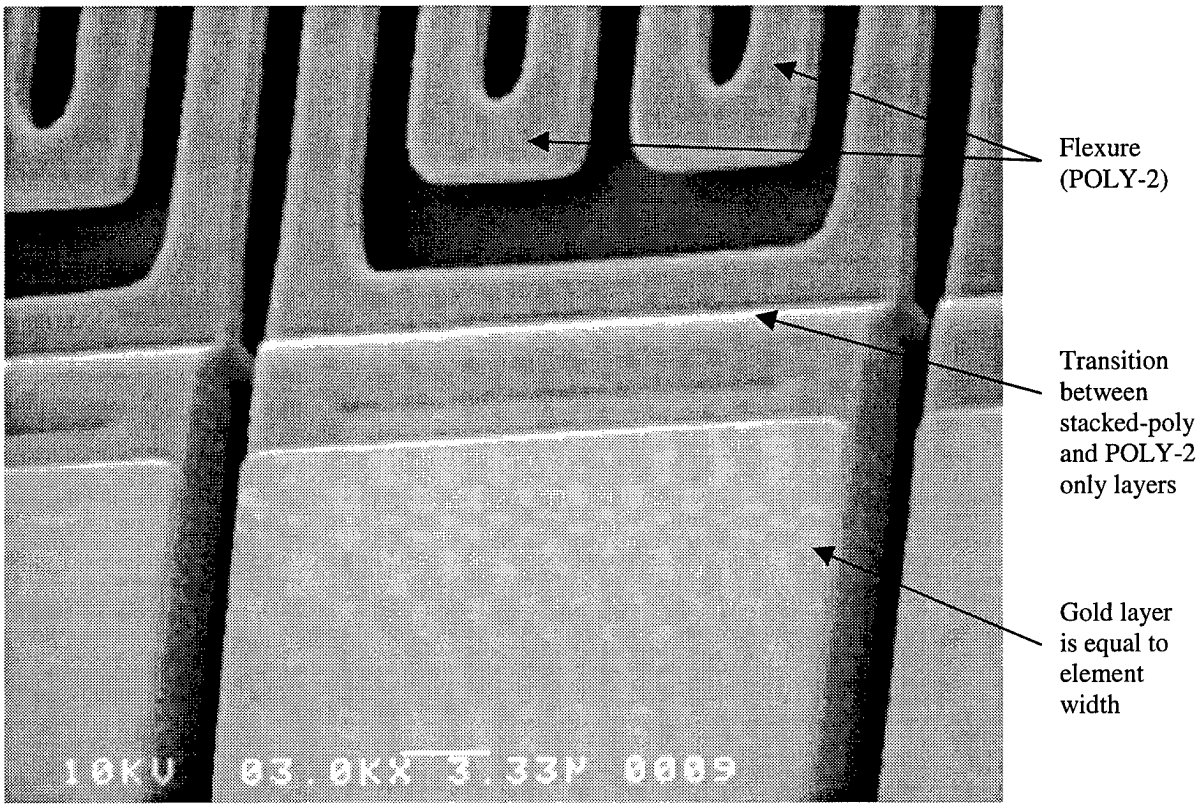

Figure 5.11. Close-up view of a fifth generation linear optical phased array element (fabricated by the author in MUMPs 19).

FFT simulation sample size was 234.4 nm; no modeled features had dimensions less than 1 μm. The array elements were positioned to steer an optical beam over the range of ±0.604°. The results of the FFT simulation are shown in Figure 5.12. The peak predicted optical efficiency for the fifth generation array was 78.7% . The predicted optical efficiency for the modified fifth generation array (includes a 1 μm polysilicon border on each side of the gold layer) is shown in Figure 5.13. The peak predicted optical efficiency of the modified fifth generation array element was 68.0%. The net result of adding the 1 μm border on each side of the fifth generation array element's gold layer was to reduce the magnitude of the oscillations in optical efficiency. However reducing the magnitude of the oscillations resulted in a 13.6% lower peak predicted optical efficiency for the modified fifth generation optical phased array. The beam steering angle was sampled 1,600 times to create Figure 5.12 and Figure 5.13; the beam steering angle interval was 7.55×10^{-4} degrees.

Table 5.2. Characteristics of Later Generation Linear Optical Arrays.

	4th Generation	5th Generation
MUMPs Fabrication Run	15	19
Number of Elements	128	10
Vertical Range of Motion* (μm)	2.0	2.0
Array Period (μm)	30.0	30.0
Linear Fill Factor (%)	63.33	93.33
Number of Flexures	4**	4
Flexure Length (μm)	85.0**	243.0
Flexure Width (μm)	1.75	2.0
Surface Area Above Bottom Electrode (μm^2)	3,294.0	2,912.0
Width of Element's Gold Layer (μm)	19.0	28.0
Curvature Across Width (peak to valley) (nm)	9.9	13.7
Curvature Across Length (peak to valley) (nm)	65.5	104.4
Bottom Electrode Construction	Substrate	Substrate
Calculated Pull Down Voltage (V)	23.1	6.3
Measured Pull Down Voltage (V)	24.5	5.5

*Vertical range of motion has not been corrected for curvature.

**Equivalent flexure after accounting for the yoke flexure design.

5.4 HDSI Scanning Micromirror

The HDSI project considered a fast beam steering micromirror as an alternative to the linear optical phased array. Specifications for the HDSI fast beam steering micromirror are listed in Table 5.3. The author was sponsored by UDRI to investigate the feasibility of a MEMS HDSI fast beam steering micromirror [10]. The author created the micromirror shown in Figure 5.14 specifically to meet the HDSI fast beam steering micromirror's requirements. The electrostatically actuated micromirror in Figure 5.14 was submitted for fabrication in May 1996 (MUMPs 13). The capabilities of the micromirror in Figure 5.14 are listed in Table 5.3.

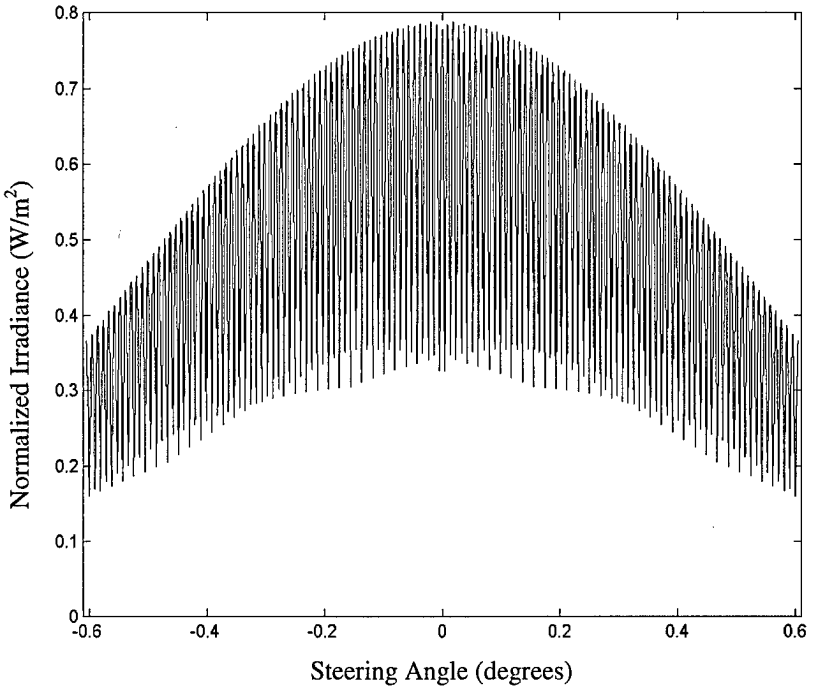

Figure 5.12. Fifth generation linear optical phased array predicted performance.

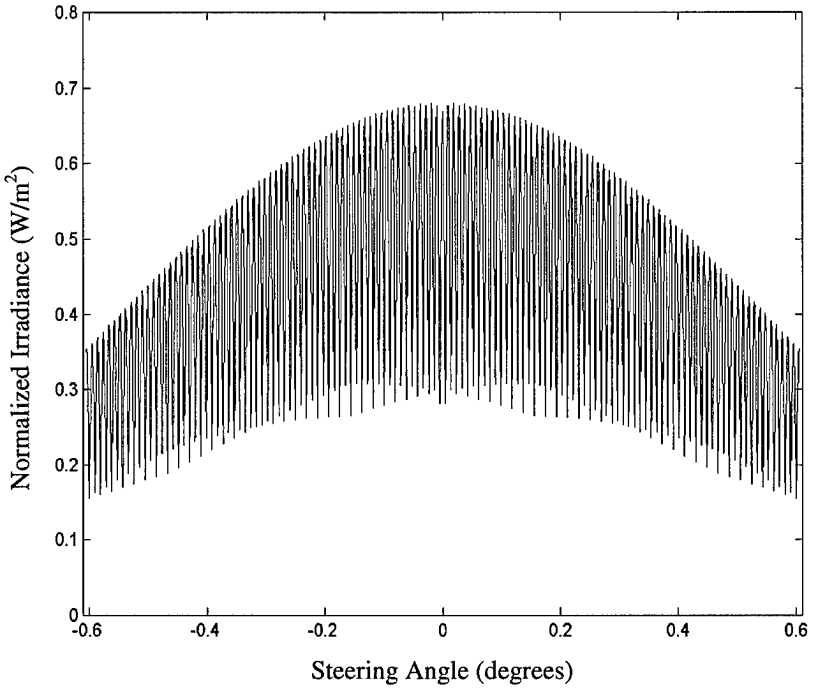

Figure 5.13. Modified (high yield) fifth generation linear optical phased array predicted performance. The gold layer is inset 1 μm from each edge of the array element.

Table 5.3. Specifications for the HDSI Fast Beam Steering Micromirror[10].

Specification	Requirement	Author's Design
Size	100 μm diameter	100 μm diameter
Maximum stable tilt angle	±20 mrad	±15.8 mrad
Positional accuracy (with feedback control)	±100 μrad	unknown
Speed (time required to scan over full range)	100 μsec	< 40 μsec
Power handling	1 W	1.46 W*

*predicted value for operation in Helium at a pressure of one atmosphere

The positional accuracy was not measured because the HDSI scanning micromirror project was restructured into a linear optical phased array with a 30 μm period (later generation HDSI phased array designs) before the micromirror could be tested at Stanford University. The micromirror's speed is a conservative estimate based on the performance of similar micromirrors tested at AFIT [21]. The calculations for the micromirror's power handing capability are given in Chapter 9.

The author used a polysilicon former to raise the height of the micromirrors in Figure 5.14 and increase the maximum stable tilt angle. A typical MUMPs micromirror is constructed out of POLY-2 and gold. The separation distance between the top electrode and the bottom electrode (POLY-0) is the thickness of the first and second sacrificial oxide layers. An edge of the micromirror supported by linear restorative force flexures can travel a third of the initial separation distance between the top and bottom electrodes before becoming unstable [22]. For a tilting micromirror with a width w and an initial separation distance of h, the maximum stable tilt angle θ before snap-through is given by Equation (5.1):

$$\theta = \tan^{-1}\left(\frac{h}{3w}\right) \tag{5.1}$$

A typical 100 μm diameter micromirror without a polysilicon former has an initial separation distance of 2.75 μm; the maximum stable tilt angle of this micromirror is ±9.17 mrad (calculated using Equation (5.1)). If a POLY-1 former is used to raise the height of the micromirror during fabrication, the initial separation distance between the top and bottom electrodes can be increased to 4.75 μm. The increased separation height resulting from a POLY-1 former was used to get the maximum stable tilt angle shown in Table 5.3. A

disadvantage of using a POLY-1 former is that the micromirror's top electrode can not be fabricated out of stacked-poly or trapped-oxide (because the POLY-1 layer must be removable). Curvature can still be minimized if the micromirror is fabricated without the gold layer. A thin layer of gold (approximately 150 nm) can then be evaporated onto the die at AFIT.

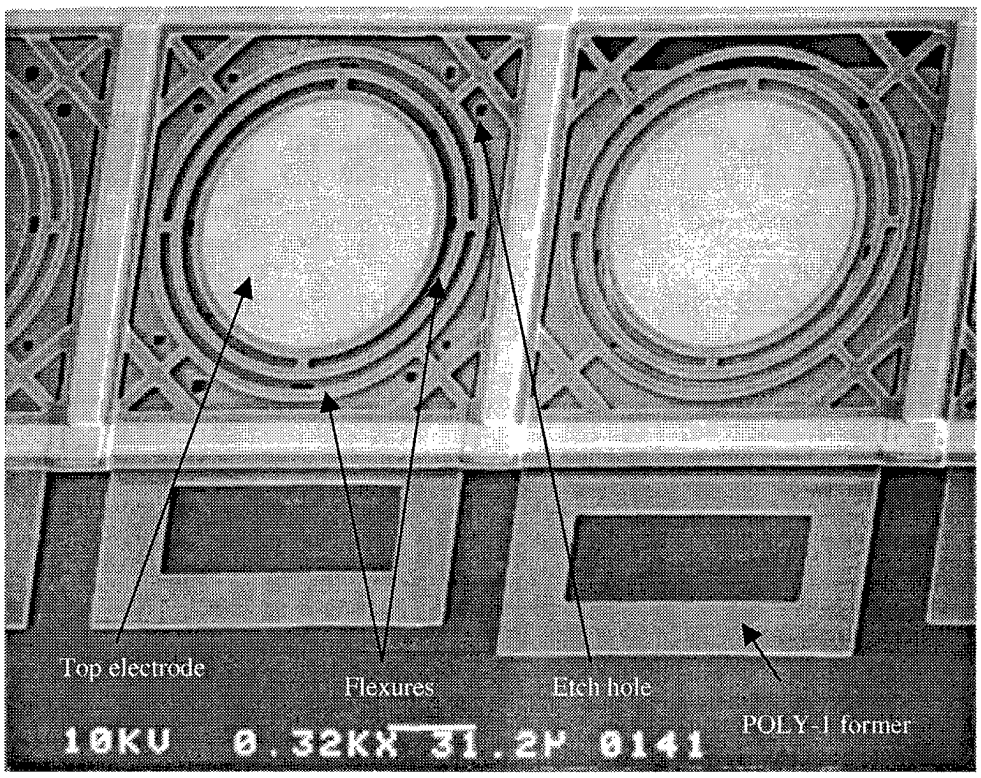

Figure 5.14. A pair of HDSI fast beam steering micromirrors (100 μm diameter). The POLY-1 former has been partially removed from the micromirror on the right (fabricated by the author in MUMPs 14).

5.4.1 Automated Removal of Polysilicon Former

The micromirror in Figure 5.14 had a polysilicon former that had to be manually removed from under the micromirror's top electrode with a probe tip after the device was released. The author created a new single-use micromotor to remove the polysilicon former without the use of a manual probe station; the use of automated assembly improves yield and greatly reduces cost by decreasing the manual labor required to fabricate MEMS. Figure 5.15 shows the HDSI fast beam steering micromirror after the polysilicon former was automatically removed with a single-use micromotor. The double hot arm thermal actuators (described in

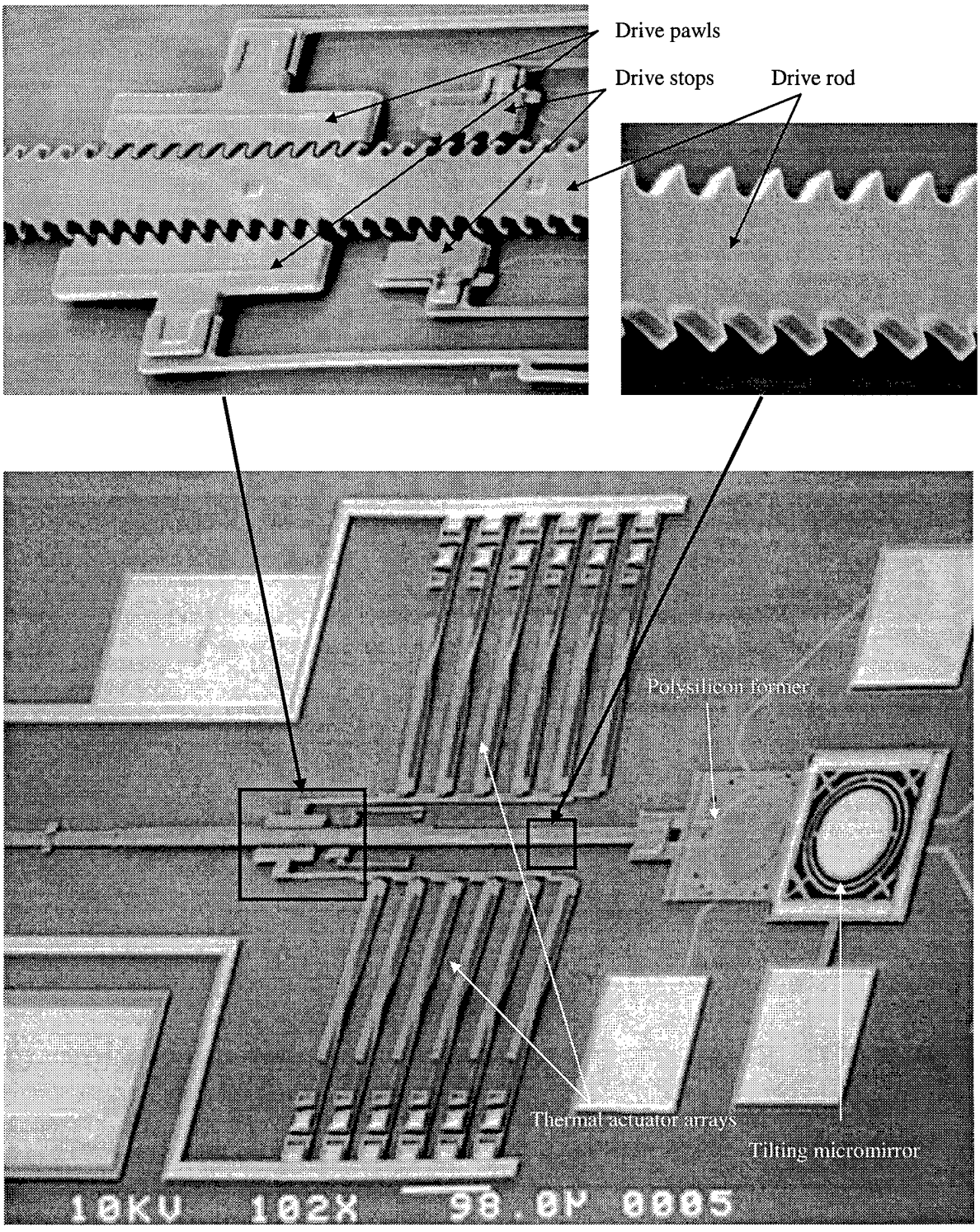

Figure 5.15. A 100 μm diameter tilting micromirror after the polysilicon former was removed with a single-use linear micromotor (fabricated by the author in MUMPs 18).

Chapter 9) used to power the single-use motor are a new design by the author and have 80% more force than traditional thermal actuators.

The micromotor in Figure 5.15 requires a 13.5 volt square wave drive signal. When the drive voltage is "on", the thermal actuator array pushes the drive pawls away from the micromirror and pulls the POLY-1 former out from under the micromirror. When the drive voltage is "off" (zero volts), the drive pawls return to their starting positions. The teeth of the drive rod and drive pawls are angled so that they engage when the drive voltage is on and slide over each other when the drive voltage is off. Drive stops are used to prevent the drive rod from slipping back towards the micromirror when the drive voltage is switched off. Close-up views of the micromirror after the POLY-1 former was partially and then completely removed are shown in Figure 5.17. and Figure 5.17, respectively.

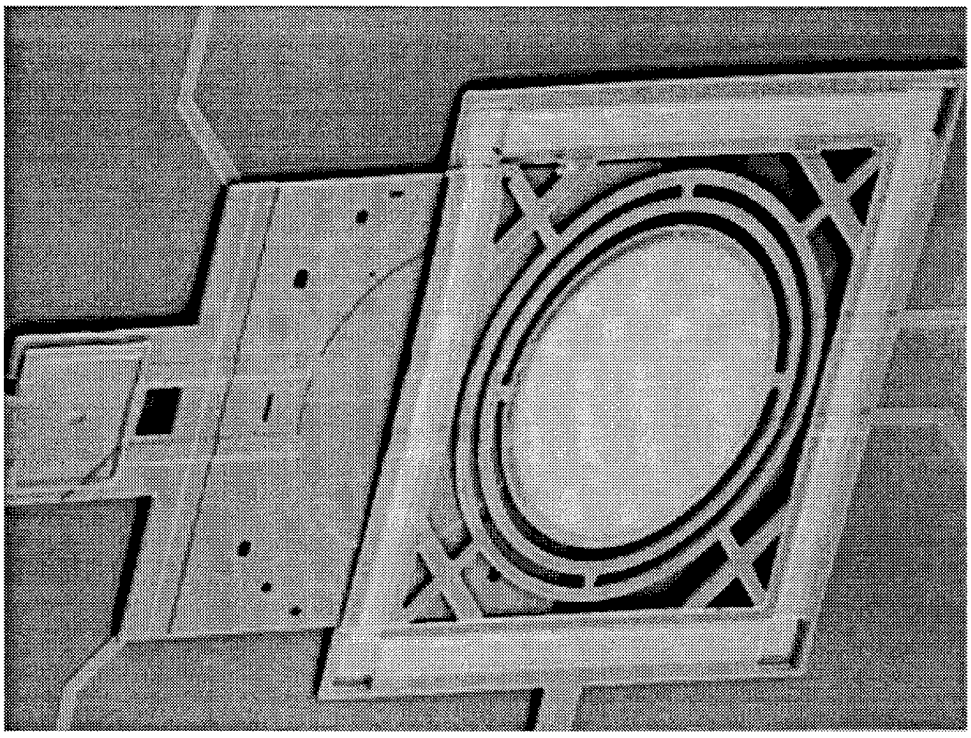

Figure 5.16. Close-up view of the polysilicon former after it was partially removed from under the tilting micromirror (fabricated by the author in MUMPs 18).

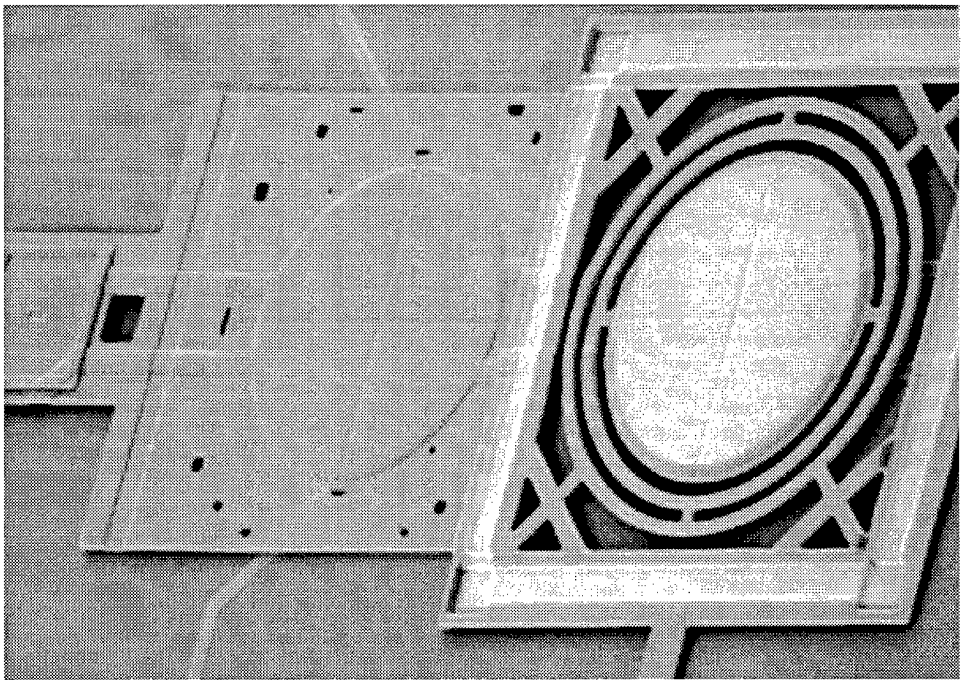

Figure 5.17. Close-up view of the polysilicon former after it was completely removed from under the tilting micromirror (fabricated by the author in MUMPs 18).

5.4.2 Lift and Slide Method for Increasing the Maximum Stable Tilt Angle

The micromirrors in Figure 5.14 met or exceeded every requirement in Table 5.3 except for the maximum stable tilt angle; although the single-use micromotor helps with assembly, it does not increase the maximum stable tilt angle. The author invented a new method of increasing the electrode separation distance: lift and slide micromirrors. A schematic diagram of a HDSI fast beam steering micromirror coupled to a lift and slide mechanism is shown in Figure 5.18. The mechanism was designed to be manually assembled, although the single-use micromotor shown in Figure 5.15 could be adapted for automated assembly.

The lift and slide mechanism in Figure 5.18 was assembled by pushing the slide mechanism towards the raised platforms until the micromirror's surface was centered over the bottom electrodes. When the micromirror's surface was centered over the bottom electrodes, the guide stops engage and prevent further motion. The lifting jacks raise the front edge of the top electrode over and onto the elevated platforms as the top electrode is slid into position. Figure 5.19 depicts the HDSI fast beam steering micromirror before assembly and Figure 5.20 shows the micromirror after assembly. The elevated platforms were constructed out

of anchored POLY-1, POLY-2, and gold. The electrode separation distance is 7.25 μm after the top electrode is in position over the bottom electrodes. Using Equation(5.1), the maximum stable tilt angle for the HDSI fast beam steering micromirror coupled to a lift and slide mechanism is ±24.2 mrad. The author was able to meet all of the HDSI fast beam steering micromirror requirements in Table 5.3 using the lift and slide mechanism.

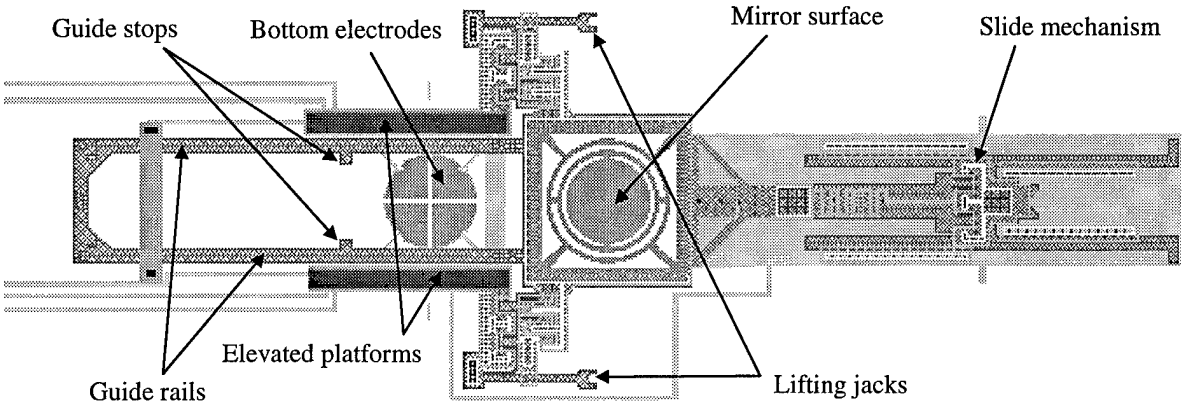

Figure 5.18. A schematic diagram of the HDSI fast beam steering micromirror coupled to a lift and slide mechanism (fabricated by the author in MUMPs 13).

5.5 Summary

Two techniques for steering an optical beam were reported in this chapter: linear optical phased arrays and a fast beam steering micromirror. Both techniques have applications beyond the holographic data storage project. Other applications include laser radar systems, laser target designators, and optical communications. However both techniques have limitations. The optical efficiency of the linear optical phased array oscillates in continuous mode operation, making the linear optical phased array a poor choice for systems requiring a uniform output amplitude. As MEMS technology improves, the width of the array elements may approach half the source wavelength; at this point optical efficiency oscillations will be greatly reduced and more applications will be able to use linear optical phased arrays. A key design trade-off for array element design is fill factor versus micromirror curvature. For a given array period, the magnitude of the optical efficiency oscillations can be reduced if the fill factor is reduced; the cost of reducing the fill factor is a lower optical

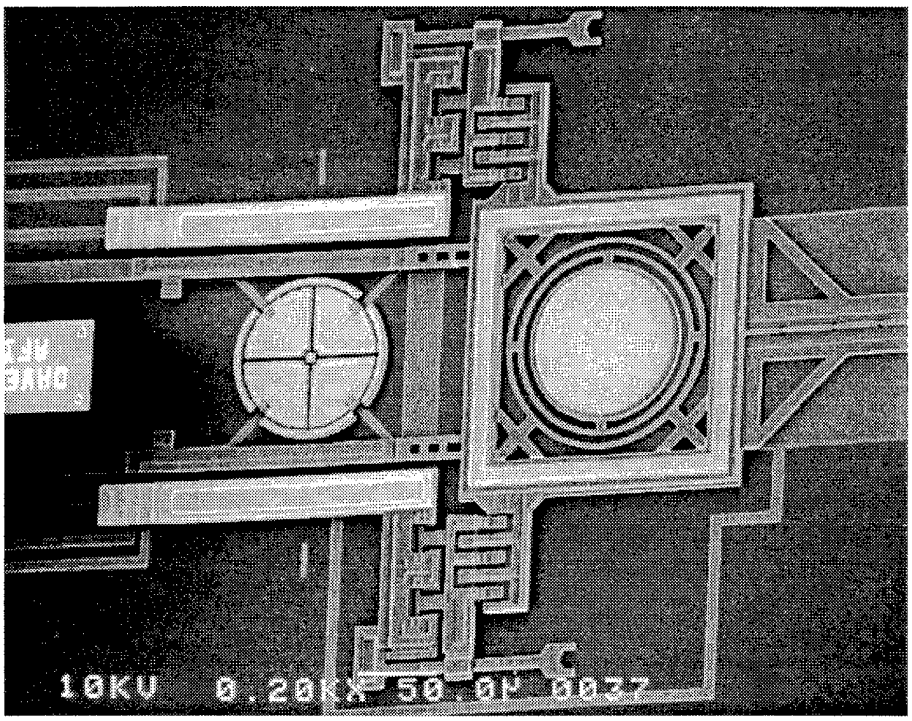

Figure 5.19. Lift and slide mechanism before assembly (fabricated by the author in MUMPs 13).

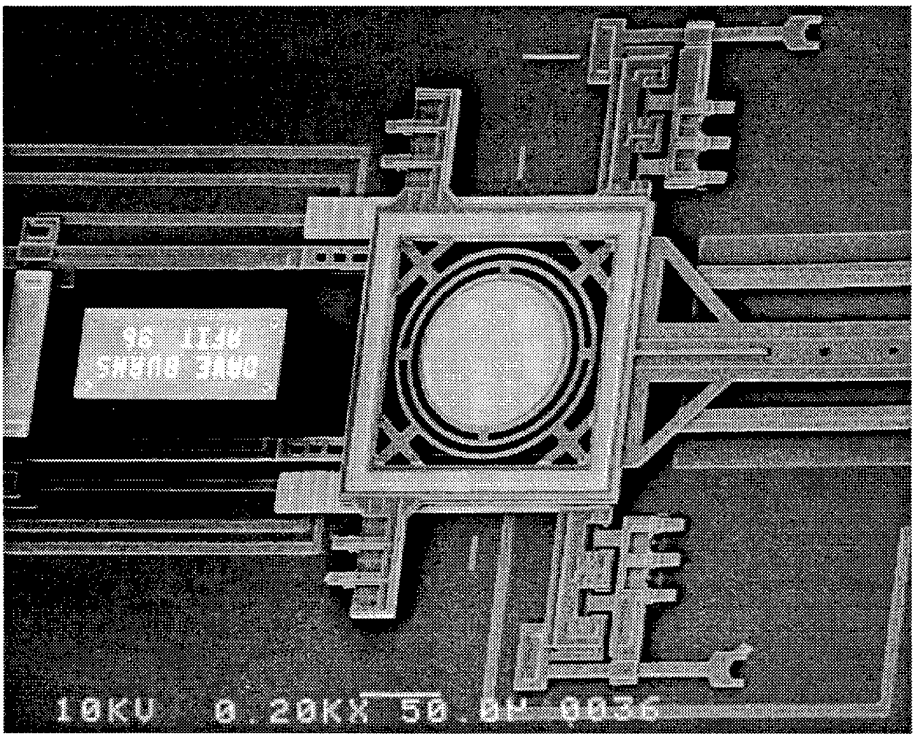

Figure 5.20. Lift and slide mechanism after assembly (fabricated by the author in MUMPs 13).

efficiency. Micromirror curvature also reduces optical efficiency. The flattest possible array elements were constructed out of trapped-oxide. A drawback of using trapped-oxide is a lower fill factor.

Electrostatically actuated fast beam steering micromirrors also have limitations. The small diameter (100 μm) causes a higher divergence angle than larger mirrors constructed out of traditional materials. Also the maximum tilt angle of the micromirror is limited to a maximum of ±24.2 mrad (using the lift and slide mechanism). However three key benefits of using fast beam steering micromirrors are extremely quick response times, almost negligible current supply requirements, and low cost.

5.6 References

[1] J. H. Hong, I. McMichael, T. Y. Chang, W. Christian, and E. G. Paek, "Volume holographic memory systems: techniques and architectures," *Optical Engineering*, vol. 34, no. 8, pp. 2193-2203, August 1995.

[2] R. P. Feynman, "There's plenty of room at the bottom," *Journal of Microelectromechanical Systems*, vol. 1, no. 1, pp. 60-66, March 1992.

[3] B. J. Goertzen and P. A. Mitkas, "Volume holographic storage for large relational databases," *Optical Engineering*, vol. 35, no. 7, pp. 1847-1853, July 1996.

[4] G. Perregaux, P. Weiss, B. Kloeck, H. Vuilliomenet, and J.-P. Thiebaud, "High-speed micro-electromechanical light modulation arrays," *Proc. 1997 International Conference on Solid-State Sensors and Actuators (Transducers-97)*, Chicago, IL, pp. 71-74, June 1997.

[5] J. Comtois, V. Bright, S. Gustafson, and M. Michalicek, "Implementation of hexagonal micromirror arrays as phase mostly spatial light modulators," *Proc. SPIE Microelectronic Structures and Microelectromechanical Devices for Optical Processing and Multimedia Applications*, vol. 2641, pp. 76-87, October 1995.

[6] L. J. Hornbeck, "Deformable-mirror spatial light modulators," *SPIE Critical Reviews of Optical Science and Technology*, vol. 1150, pp. 86-102, August 1989.

[7] G. L. Christenson, A. T. T. D. Tran, Z. H. Zhu, Y. H. Lo, M. Hong, J. P. Mannaerts, and R. Bhat, "Surface micromachined long wavelength LED/photodetector with a continuous tuning range of 75 nm," *IEEE MEMS-97 Workshop*, Nagoya, Japan, pp. 61-65, January 1997.

[8] P. B. Catrysse, M. C. Bashaw, J. F. Heanue, and L. Hesselink, "Systems issues in digital phase code multiplexed holographic data storage," *OSA Annual Meeting,* Rochester, NY, October 1996.

[9] C. Denz, G. Pauliat, G. Roosen, and T. Tshudi, "Potentialities and limitations of hologram multiplexing by using the phase-encoding technique," *Applied Optics*, vol. 31, no. 26, pp. 5700-5705, September 1992.

[10] Letter from S. Gustafson, University of Dayton Research Institute, to Dr. L. Hesselink, Stanford University, "Tentative specifications for a fast micromirror for angle multiplexing," April 19, 1996.

[11] S. C. Gustafson, G. R. Little, W. A. Bernard, V. M. Bright, J. H. Comtois, and D. M. Burns, "Micromirrors for multiplexing in holographic data storage systems," *OSA Annual Meeting*, paper MI3, Rochester, NY, October 21, 1996.

[12] J. H. Comtois, "Structures and techniques for implementing and packaging complex, large scale microelectromechanical systems using foundry fabrication processes," *Doctoral Dissertation*, Air Force Institute of Technology, Wright-Patterson AFB, OH, AFIT/DS/ENG/96-04, May 1996.

[13] C. J. Christensen, V. M. Bright, J. W. Grantham, and J. H. Comtois, "Control of a phase-locked laser diode array using piston micromirrors," *Proc. SPIE*, vol. 2881, pp. 26-34, 1996.

[14] ZYGO model Maxim-3D laser interferometer operation and maintenance manual, part number: OMP-0256, *ZYGO Corporation*, Laurel brook road, Middlefield, CT 06255, May 1988.

[15] Hewlett Packard model 6624A system DC power supply operating manual, part number: 5957-6377, *Hewlett Packard Company*, 150 Green pond road, Rockaway, NJ 07866, January 1993.

[16] P. F. McManamon, E. A. Watson, T. A. Dorschner, L. J. Barnes, "Applications look at the use of liquid crystal writable gratings for steering passive radiation," *Optical Engineering*, vol. 32, no. 11, pp. 2657-2664, November 1993.

[17] S. C. Gustafson, G. R. Little, V. M. Bright, J. H. Comtois, and E. A. Watson, "Micromirror arrays for coherent beam steering and phase control," *Proc. SPIE*, vol. 2881, pp. 65-74, 1996.

[18] E. A. Watson and A. R. Miller, "Analysis of optical beam steering using phased micromirror arrays," *Proc. SPIE*, vol. 2687, pp. 60-67, 1996.

[19] J. D. Gaskill, *Linear Systems, Fourier Transforms, and Optics*, New York, NY: John Wiley & Sons, 1978.

[20] D. Koester, R. Mahedevan, A. Shishkoff, and K. Marcus, *Multi-User MEMS Processes (MUMPS) Introduction and Design Rules*, rev. 4, July 15, 1996, MCNC MEMS Technology Applications Center, 3021 Cornwallis Road, Research Triangle Park, NC, 27709.

[21] M. A. Michalicek, V. M. Bright, and J. H. Comtois, "Design, fabrication, modeling, and testing of a surface-micromachined micromirror device," *Proc. 1996 ASME Dynamic Systems and Control Division*, DSC-vol. 57-2, pp. 981-985, 1995.

[22] P. M. Osterberg, R. K. Gupta, J. R. Gilbert, and S. D. Senturia, "Quantitative models for the measurement of residual stress, Poison ration and Young's modulus using electrostatic pull-in of beams and diaphragms," *Proc. Solid-State Sensor and Actuator Workshop*, Hilton Head Island, SC, pp. 184-188, June 13-16, 1994.

6 Variable Blaze Gratings

Microelectromechanical Variable Blaze Gratings (VBGs) can be used to steer incident light if the blaze angle of each slat is adjusted so that specular reflection of the incident light matches a particular grating diffraction order. The VBG blaze angle is adjustable with either electrostatic or thermal actuators. VBGs direct incident light in discrete directions and are useful for steering light with beam diameters greater than 5 mm and power levels greater than 1 watt. This chapter is organized into four sections. The first section is an introduction. The second section describes ten VBG designs that are representative of the author's research. The second section also presents modeling and experimental data for each design. The third section discusses the optical modeling used to optimize the diffraction efficiency of VBGs. The last section is a summary of the author's VBG research.

6.1 Introduction to VBGs

Reflection gratings are often used to disperse incident light into angular directions corresponding to the incident light's wavelength and the construction properties of the grating. Blazing, or contouring individual grating elements, can be used to improve the ratio of light diffracted in a specific direction to the incident light (defined as the diffraction efficiency). Traditional blazed gratings have a blaze angle that is fixed at the time of construction. Variable blaze gratings have adjustable blaze angles that can be set with a fast time response (less than 10 ms) as often as required after construction.

Many applications of microelectromechanical systems include optical beam scanning or optical spectral analysis. Often optical beam scanning systems require beam diameters that are too large to fit on a single surface micromachined micromirror. Previously reported micromirror arrays and gratings have low diffraction efficiencies, which may render them unsuitable for directing high power optical beams [1,2,3]. Some optical beam scanning applications (such as optical switching) may benefit from an optical beam steering system that directs nearly monochromatic light into discrete directions. VBGs have a high fill factor (up to 100% for non-normally incident light) and direct the majority of the diffracted light in a specific direction.

Micromachined spectral analyzers using transmission gratings and Fabry-Perot interferometers have also been reported. A bulk micromachined spectrum analyzer with an integrated transmission grating and photodetector array has recently been constructed and demonstrated [4]. This device used a transmission grating to spread incident light so that diffracted light was separated into bands corresponding to the incident light's wavelength. The diffracted light was then reflected on to a photodetector array. The output of each element in the photodetector array directly corresponded to an optical frequency band. Bulk and surface micromachined Fabry-Perot interferometers have also been demonstrated [5,6]. Electrostatic force was used to adjust the width of Fabry-Perot cavity, creating a tunable optical band pass filter.

Micromachined VBGs could be used to improve the frequency sensitivity of these spectral analyzers. VBGs with higher diffraction efficiencies than typical micromachined transmission gratings have been demonstrated by the author; a higher diffraction efficiency increases the strength of the desired diffracted light on photodetector array elements. A VBG could be combined with a Fabry-Perot interferometer design to increase the device's resolving power. VBGs are also suitable for spectrum analyzers requiring multiple diffraction orders [7]. Multiple diffraction orders would allow an intelligent spectrum analyzer to trade receiver signal strength for frequency resolution in real time. Other potential applications for VBGs include airborne laser radar systems, micro laser radars for small robots, and astronomy.

6.2 VBG Design Categories

The author designed and tested more than 90 complete VBGs systems. Ten of the most significant VBG designs are listed in Table 6.1 and will be described in this section. The presentation of each VBG design begins with an overview of the design, followed by description of the flexures used to support each VBG slat. Calculated and measured diffraction efficiencies are then discussed for all operational VBGs. VBG design numbers 1 through 5 proved the VBG device concept. VBG design numbers 6 through 8 were used to evaluate VBG diffraction efficiency as a function of slat construction. VBG design numbers 9 and 10 were used to explore methods of increasing the number of selectable diffraction orders and the VBG footprint. The test set-up used to evaluate all VBGs is depicted in Appendix C.

Table 6.1. Summary of Significant VBG Design Characteristics. Diffraction Efficiency is for the First Diffraction Order (632.8 nm Source Wavelength).

VBG Design Number	MUMPs Run	Actuator Type *	Slat Construction **	Gold Width (μm)	Slat Width (μm)	Grating Period (μm)	Slat Peak to Valley Curvature (nm)	Diffraction Efficiency		Measured Number of Orders	Length of Slats (mm)	Number of Slats
								Predicted	Measured			
1	11	E	P	6	10	12	12.2	7.2 %	N/A	N/A	0.2	48
2	13	E	P	40	42	44	185.7	22.9 %	8.9 %	3	1.2	16
3	15	D	P	36	42	44	111.2	30.1 %	13.6 %	7	2.3	50
4	15	T	P	80	82	84	499.9	8.3 %	< 5%	5	2.5	36
5	15	S	S	15.5	17.5	20	9.0	47.2 %	32.1 %	3	2.9	140
6	15	S	P	54	58	60	303.4	5.8 %	6.7 %	3	2.4	36
7	15	S	S	54	58	60	63.5	58.8 %	40.5 %	3	2.4	36
8	15	S	T	54	58	60	31.5	64.9 %	48.8 %	3	2.4	36
9	17	S	T	74	78	80	79.1	59.0 %	51.9 %	5	3.0	36
10	21	S	T	75	78	80	72.1	61.2 %	56.1 %	3	9.4	119

* **E**: Electrostatic (single-sided), **D**: Double-sided electrostatic, **T**: Thermal, and **S**: Electrostatically actuated through the substrate

** **P**: POLY-2 only, **S**: stacked-poly, and **T**: trapped-oxide

N/A Not Available (device is not functional)

6.2.1 VBG Design Number 1

VBG design number 1 is depicted in Figure 6.1. This design was the first attempt by the author to create a VBG (design submitted in January, 1996). Each slat was supported by torsion flexures at the ends. VBG design number 1 was not wired for operational use (note that no wire traces connect the grating in Figure 6.1 to a bondpad). Instead this VBG was intended to be a study of how long and narrow slats are fabricated in MUMPs. The slats fabricated cleanly. The width of the gap used in this VBG (2 μm) became the standard gap size used for almost all of the author's subsequent VBG designs. From studying VBG design number 1, the author learned that interim support was needed under each slat as well as at the ends of the slat. The interim support flexures under each slat increased the slat's width (and the period) for future VBG designs. Also the torsion flexures at the ends of the slats were too stiff; subsequent VBG designs used a folded flexure at each slat end. The low predicted diffraction efficiency for this VBG is primarily caused by the low gold fill factor of this grating.

6.2.2 VBG Design Number 2

VBG design number 2 is depicted in Figure 6.2 and was fabricated in the 13th MUMPs fabrication run. The ZYGO interferometric microscope was not in place at AFIT until after the designs were submitted for MUMPs 13 so the author was unable to determine the extent of the residual material stress induced curvature problem. Consequently the author did not start using stacked-poly and trapped-oxide slat designs until MUMPs 15 (when the ZYGO microscope was in place). VBG design number 2 was significant because it was the first operational high fill factor VBG ever constructed.

A schematic diagram of the supporting flexure under each slat is shown in Figure 6.3. Each 1.2 mm long slat in VBG design number 2 had six embedded support flexures along its length. The top of the slat (POLY-2 and gold layers) was only connected to the POLY-1 support flexure at the via. The dimple was used to prevent stiction. When a voltage was placed between the top of the slat and the POLY-0 bottom electrode, the POLY-1 flexures would twist and bend so that the edge of the slat next to the via was displaced towards the substrate. This VBG is referred to as "single-sided" because only one side of the slat can be tilted towards the

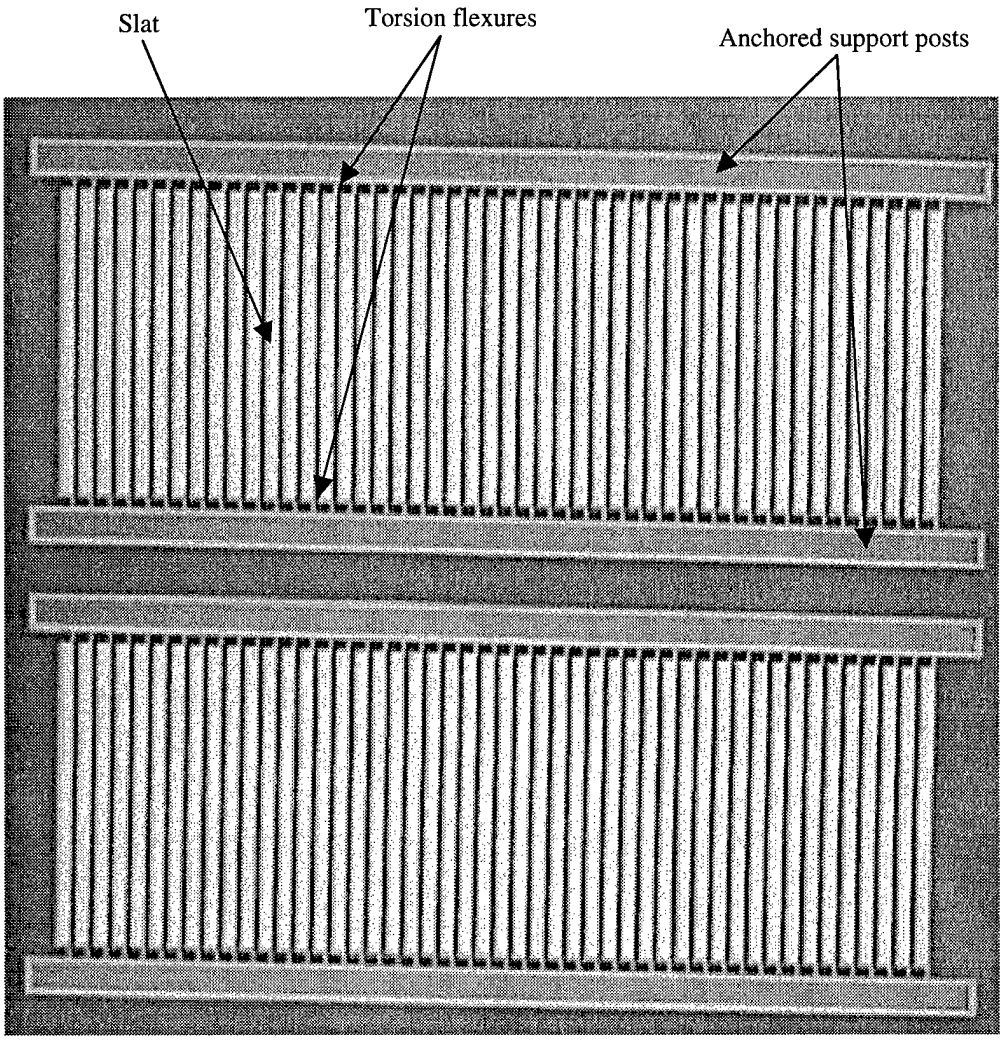

Figure 6.1. Scanning electron micrograph of VBG design number 1. Each slat is 10 μm wide (fabricated by the author in MUMPs 11).

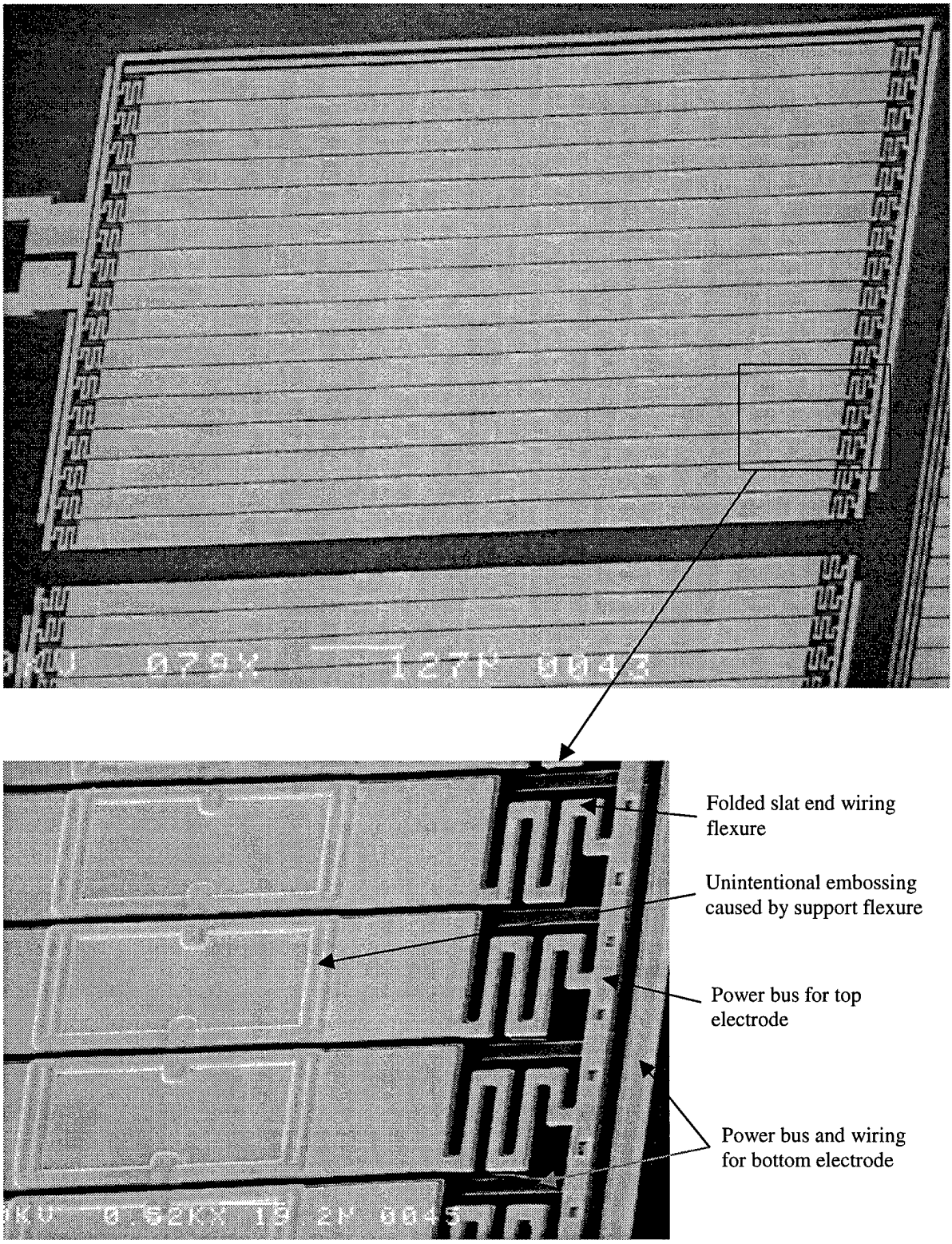

Figure 6.2. Scanning electron micrograph of VBG design number 2. Each slat is 42 μm wide. The lower picture is a close-up view of the support flexure and folded wiring flexure (fabricated by the author in MUMPs 13).

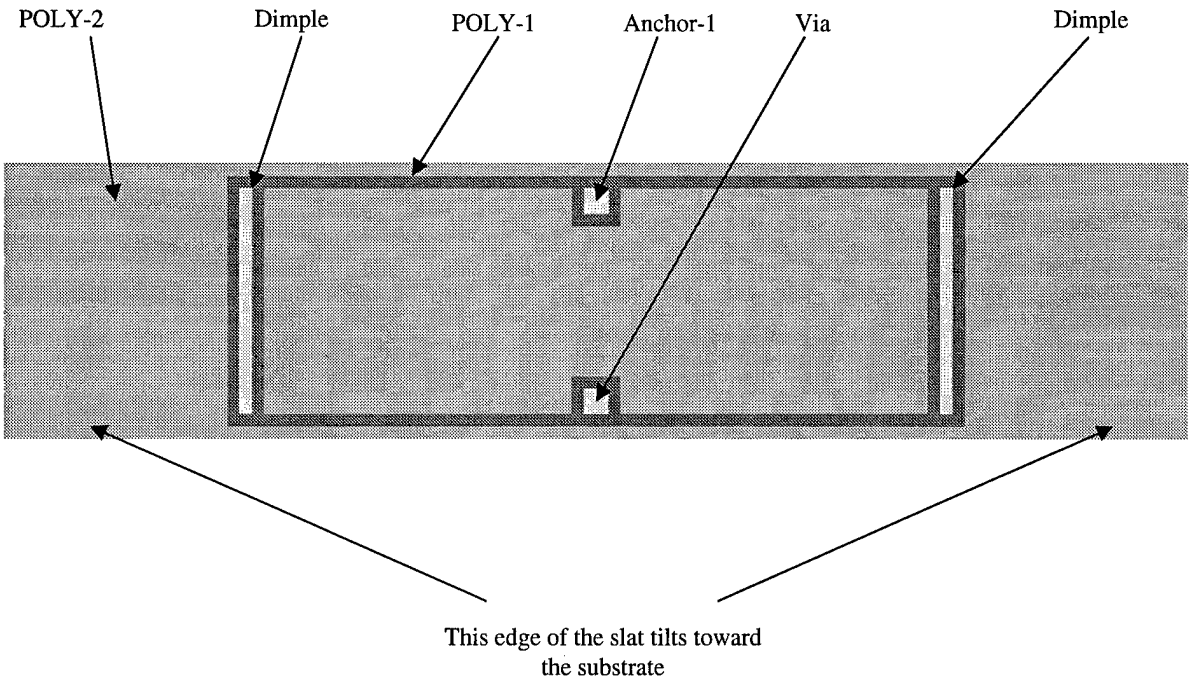

Figure 6.3. Diagram of the supporting flexure used in VBG design number 2. The bottom POLY-0 electrode is not shown.

substrate. The folded wiring flexures used at the ends of each slat in VBG design number 2 were adopted as the standard slat wiring flexure for most of the author's subsequent VBG designs.

Test measurements for VBG design number 2 are in Table 6.2. The voltage measurements for this VBG were made with a 1 KΩ resistor in series with the bottom electrode (to prevent excessive current from destroying the grating if snap-through occurred). All of the electrostatically actuated VBG designs required virtually no current (not measurable). The far field intensity pattern for VBG design number 2 had nearly equal intensities in the first and second diffraction orders when the blaze angle was set to favor the first diffraction order; the equal diffraction order intensities are a result of the low diffraction efficiency. This VBG is unsuitable for beam steering, although it may have other applications.

Table 6.2. VBG Design Number 2 Test Data.

Diffraction order	Blaze angle	Steering angle	Drive voltage (V)
0	0°	0°	0
1	0.453°	0.907°	10.5
2	0.907°	1.814°	14.0

6.2.3 VBG Design Number 3

VBG design number 3 is shown in Figure 6.4. This electrostatically actuated VBG was designed to tilt on either side of a center support flexure. The grating has 50 slats, each 42 μm wide and 1.6 mm long. Two underlying POLY-0 electrodes were used to tilt the top POLY-2 slat on either side of its center torsion support spring. The purpose of a double-sided slat was to increase the blaze angle range, therefore increasing the number of selectable diffraction orders. VBG design number 3 supported 7 diffraction orders.

Figure 6.5 is a diagram of the double-sided VBG. When the top electrode was grounded and a voltage was placed on one of the two bottom electrodes, the torsion flexure would twist; this motion caused the edge of the slat on the side of the selected bottom electrode to tilt towards the substrate. Because the slat was tilted on a center flexure instead of an edge mounted flexure (such as the support flexure used in VBG design number 2), the maximum tilt angle before snap through was increased. The increased tilt angle is demonstrated in Figure 6.6. A draw-back of the double-sided slat is the unintentional embossing down the center of the slat from the embedded support flexure. The unintentional embossing and the residual material stress induced curvature (the peak-to-valley curvature in Table 6.1 is for each side of the slat) lowered both the predicted and measured diffraction efficiencies for this grating.

Because the top electrode of the double-sided slat touched a bottom electrode at snap-through, a current-limiting resistor was required to be in series with the electrodes to prevent destruction of the device. Table 6.3 lists the orders that the double-sided VBG could direct light into and the voltage required. The voltage measurements for the double-sided VBG included the effects of a 1 KΩ resistor in series with the top electrode.

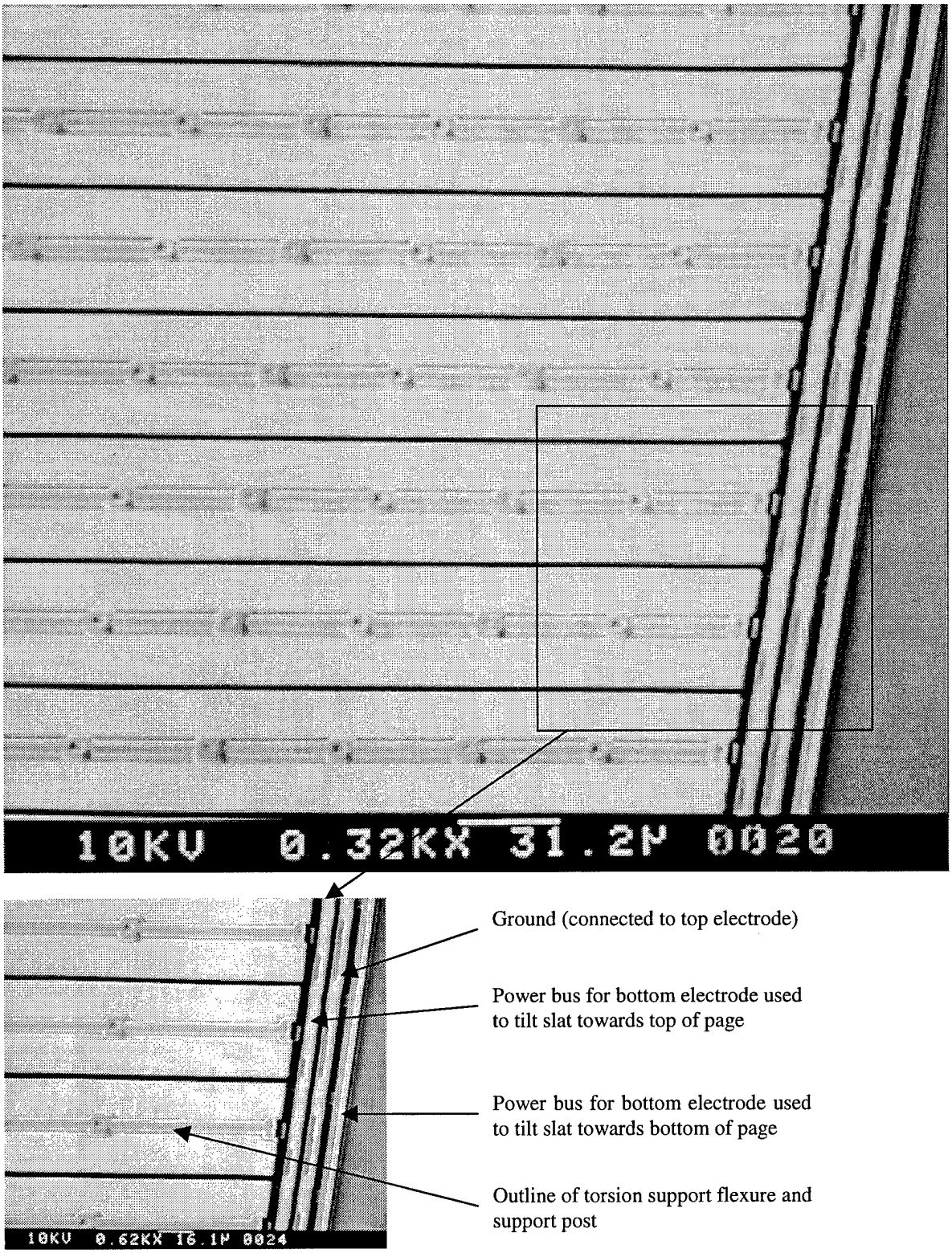

Figure 6.4. Scanning electron micrograph of VBG design number 3. Each slat is 42 μm wide. The lower picture is a close-up view of the support flexure and electrode wiring (fabricated by the author in MUMPs 15).

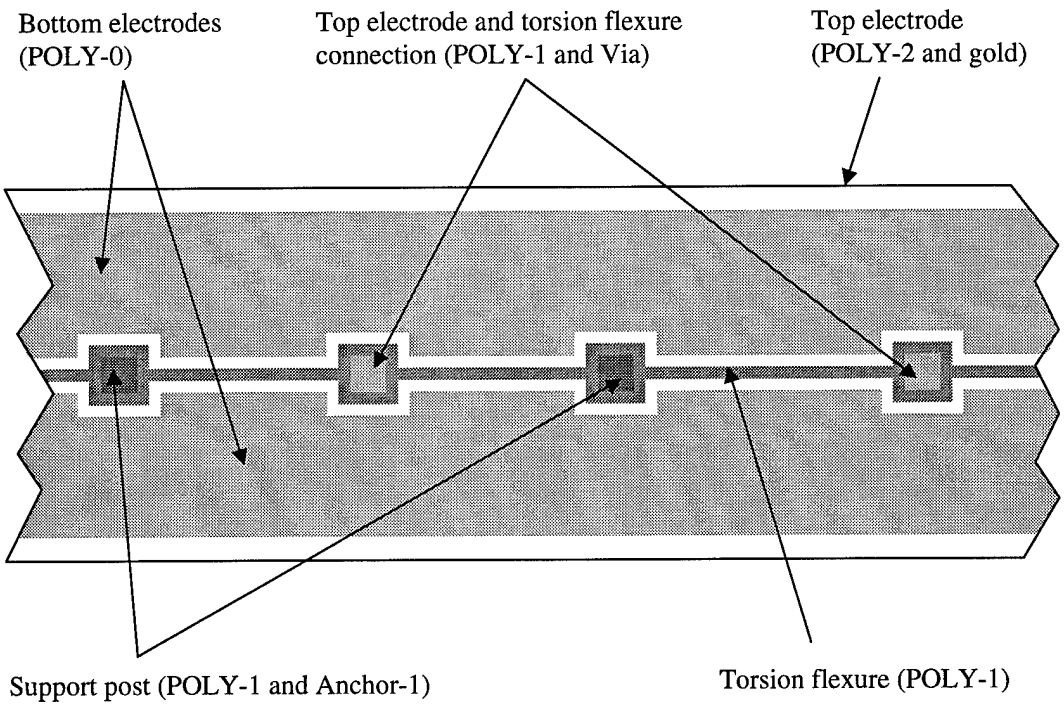

Figure 6.5. Diagram of the slat support post and center torsion support flexure used in the double-sided VBG (VBG design number 3). The top electrode was made transparent in order to shown the underlying structure.

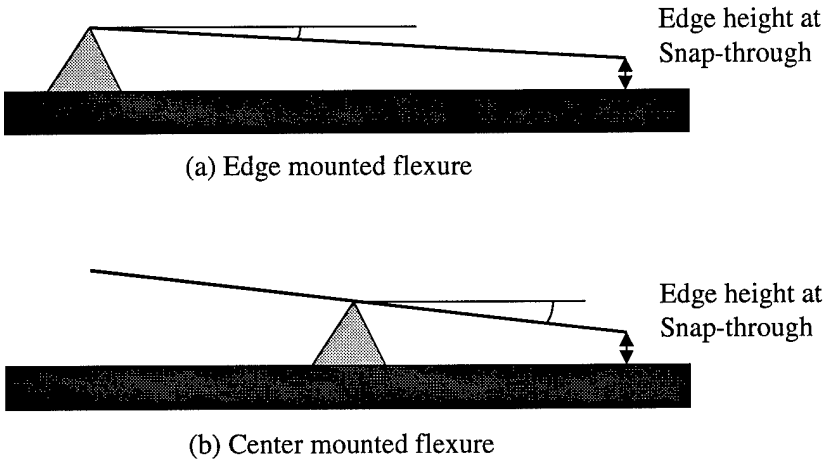

Figure 6.6. Comparison of (a) edge and (b) center mounted flexures. Edge height at snap-through is the same for both designs and is equal to two thirds of the initial electrode height.

Table 6.3. VBG Design Number 3 Test Data.

Diffraction order	Blaze angle	Steering angle	Drive voltage (V)
-3	-1.3°	-2.5°	61.2
-2	-0.8°	-1.6°	48.5
-1	-0.4°	-.08°	29.6
0	0°	0°	0
1	0.4°	0.8°	29.9
2	0.8°	1.6°	48.9
3	1.3°	2.5°	61.5

6.2.4 VBG Design Number 4

VBG design number 4 was significant because it was thermally driven and had 5 selectable diffraction orders. The large number of selectable diffraction orders (compared to single sided electrostatic VBGs) convinced the author to widen his investigation of thermally driven VBGs. Unfortunately it was not possible to construct an operational thermally driven VBG out of stacked-poly or trapped-oxide. As a result, all of the author's thermally driven VBGs had low diffraction efficiencies as a result of high slat curvature. Figure 6.7 is a picture of VBG design number 4.

Figure 6.8 is a diagram of the thermally actuated VBG with transparent POLY-2 and gold layers to show the underlying structure. Each 2.5 mm long slat had 17 identical embedded thermal actuators. The slats were tilted by heating underlying 1.5 μm wide POLY-1 actuator arms with electric current. The increase in temperature caused each actuator arm to expand and lift an edge of the slat off the substrate. The fill-factor of the device was improved by using the gold layer on each slat as the electrical contact to and from the underlying thermal actuators, eliminating the need for additional wiring between slats. The slats were wired together in pairs using POLY-0 connectors between slats. Current traveled out on one slat and returned on the adjacent

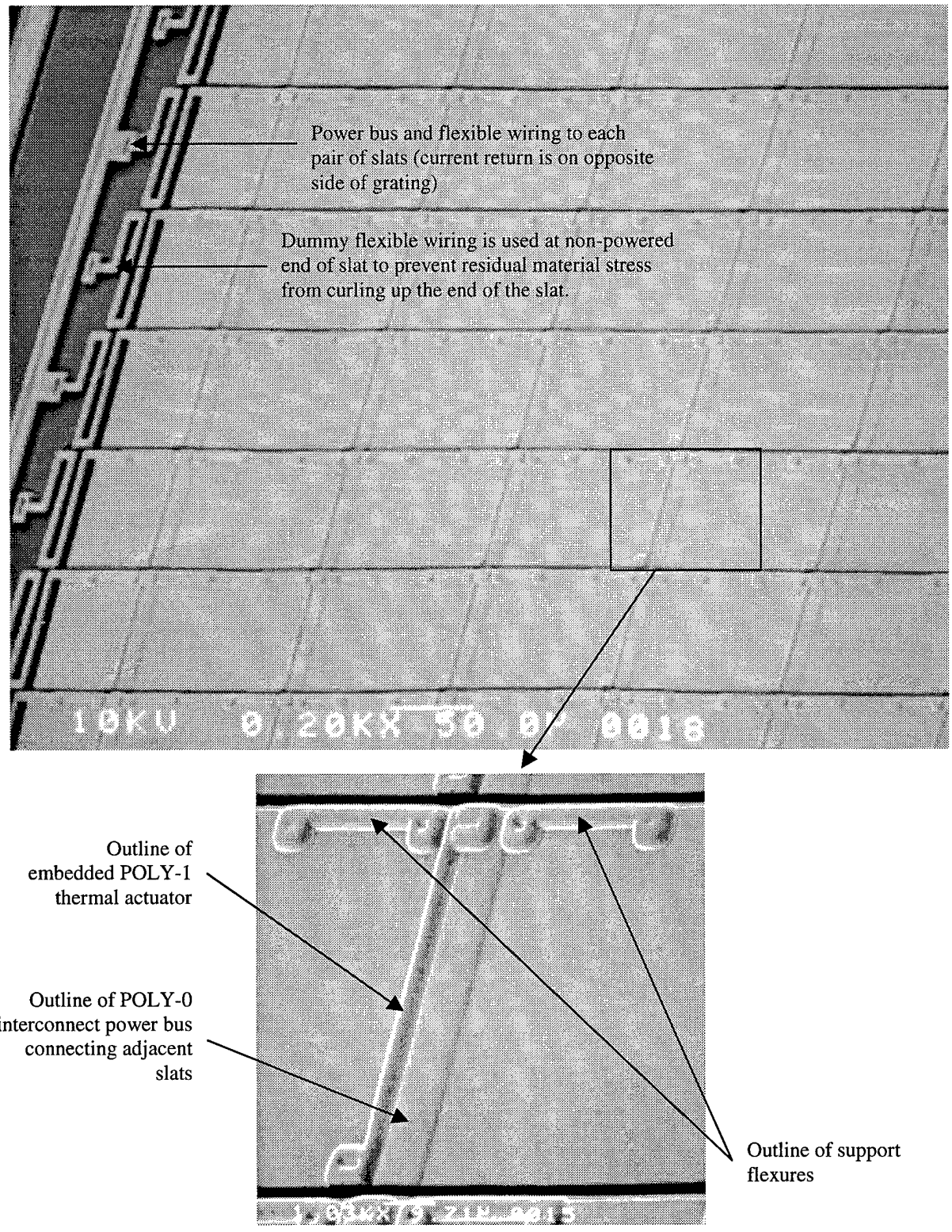

Figure 6.7. Scanning electron micrograph of VBG design number 4. Each slat is 42 μm wide. The lower picture is a close-up view of the thermal actuator and support flexures (fabricated by the author in MUMPs 15).

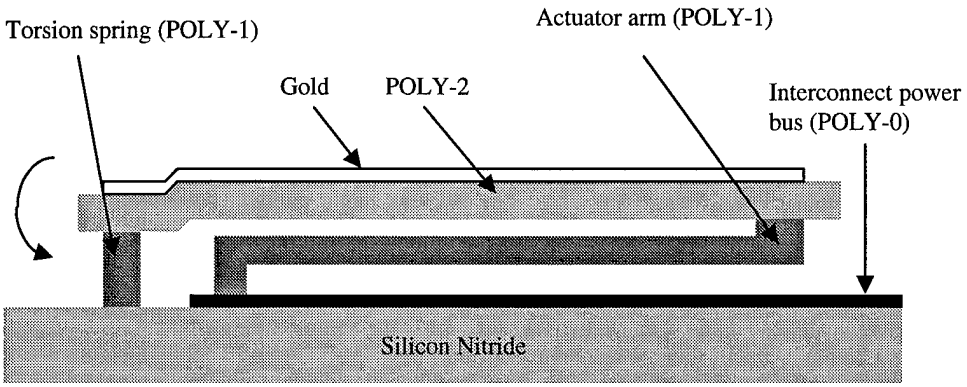

(a) Cross-sectional view of a thermally actuated slat.

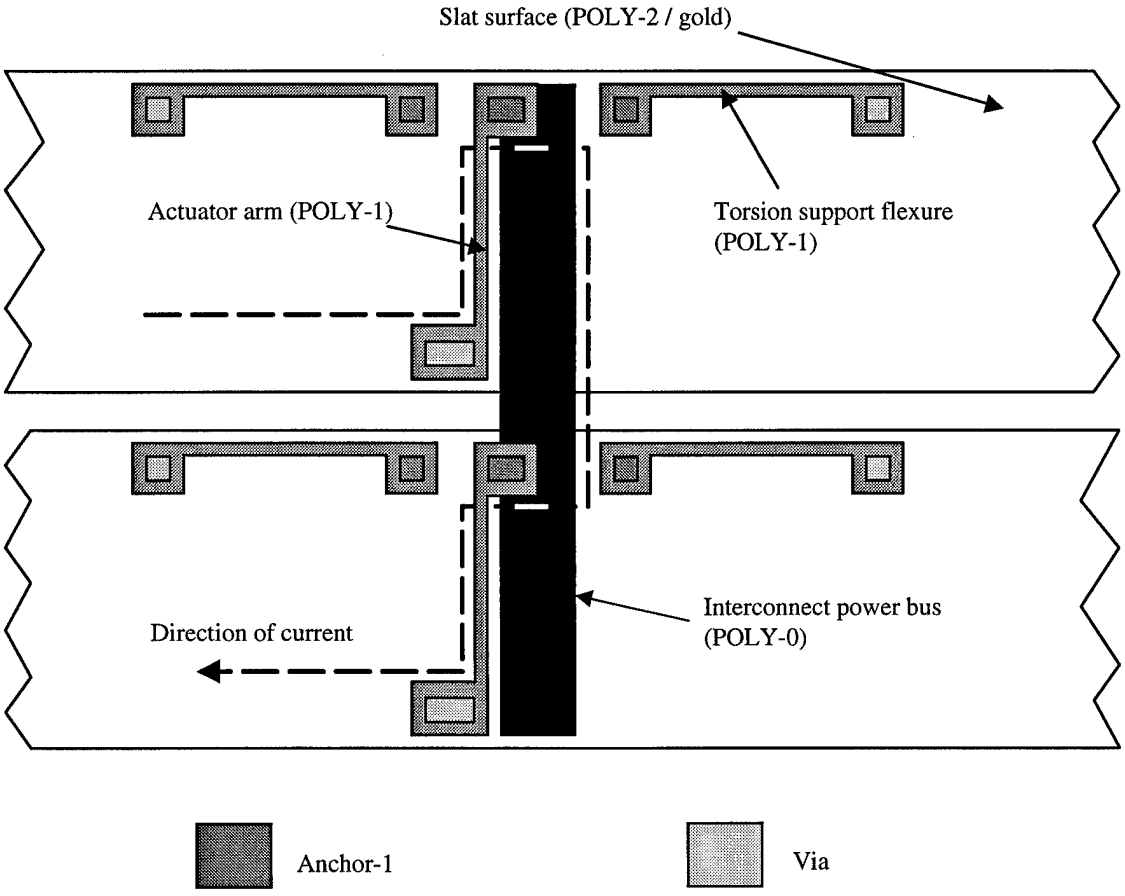

(b) Top view of a pair of thermally actuated slats.

Figure 6.8. Schematic diagrams of the thermally actuated VBG (VBG design number 4).

slat after passing through thermal actuators under both slats. The measured electrical resistance of the entire VBG was 103.4 Ω.

Test measurements for VBG design number 4 are in Table 6.4. The power consumption for this thermally driven VBG was high; the fourth diffraction order required 17.1 watts of continuous power. A large scale thermally driven VBG would require a maximum of 273.0 watts/cm^2. The POLY-2 and gold slat used in VBG design number 4 had nearly equal curvature both across the width and in the length between thermal actuators. The predicted far field irradiance pattern for VBG design number 4 is shown in Figure 6.9 and was created using the VBG model presented in Chapter 4. Note that the irradiance predicted in Figure 6.9 when the first diffraction order was selected (using the blaze angle) is actually less than the irradiance in two other diffraction orders (m=-2 and m=4) as a result of slat curvature. Figure 6.10 shows the observed far field irradiance pattern for VBG design number 4; the effects of extreme slat curvature across both the width and length of each slat are visible.

Table 6.4. VBG Design Number 4 Test Data.

Diffraction order	Blaze angle	Steering angle	Drive voltage (V)
0	0°	0°	0
1	0.22°	0.43°	6.1
2	0.43°	0.86°	17.8
3	0.65°	1.30°	30.2
4	0.87°	1.73°	42.0

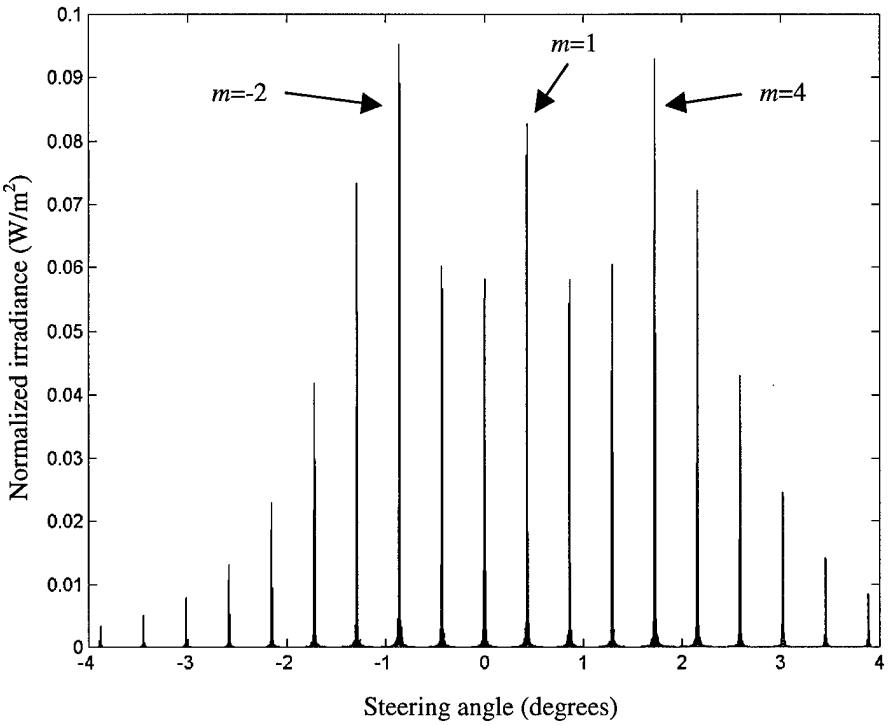

Figure 6.9. Predicted far field irradiance pattern for the thermally driven VBG (VBG design number 4) with a blaze angle favoring the first (m=1) diffraction order (located at +0.43°).

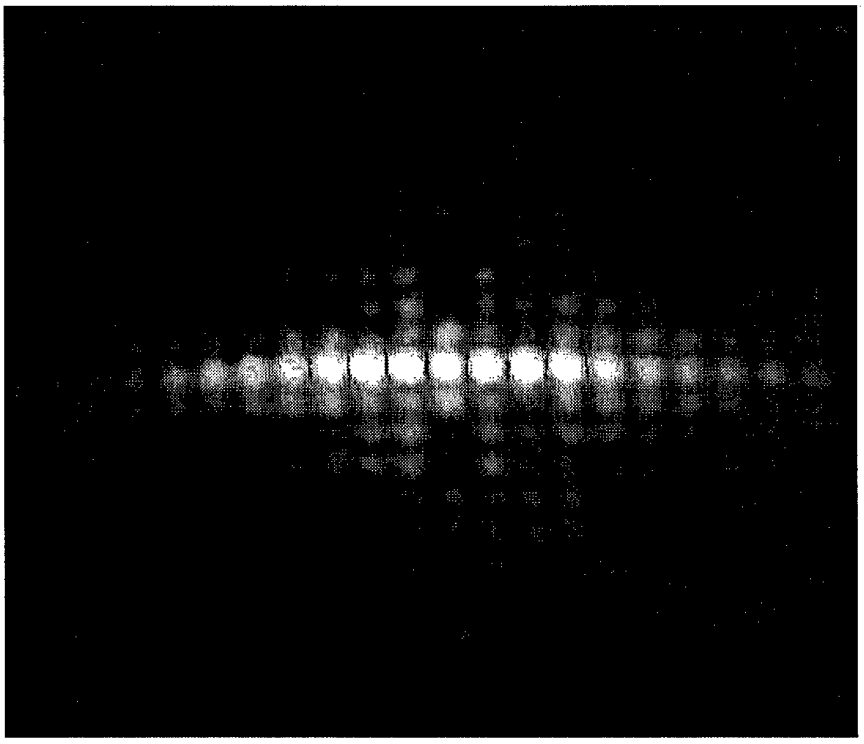

Figure 6.10. Observed far field irradiance pattern for the thermally driven VBG (VBG design number 4) with a blaze angle supporting the first diffraction order. The center row (most intense) corresponds to the region modeled in Figure 6.9. The irradiance scattered above and below the center row is caused by curvature along the length of each slat between the thermal actuators.

6.2.5 VBG Design Number 5

VBG design number 5 shown in Figure 6.11 was the smallest period (20 μm) functional VBG constructed by the author. This design was constructed with a stacked-poly slat and an exposed support post and torsion flexure. Stacked-poly was used to increase the strength of the slat along its length and increase the separation distance between support posts and flexures on the same slat. The exposed POLY-2 support post and flexure was used instead of an embedded POLY-1 support post and flexure to ensure that the support post and flexure was not bonded to the overlying POLY-2 layer; a POLY-1 support post or flexure could be bonded accidentally to the POLY-2 layer if the via oxide etch positional error was 2 μm or more. The exposed POLY-2 support post and flexure required a 2.5 μm separation from the edge of the adjacent slat's stacked-poly edge. Consequently VBG design number 5 had a gap of 2.5 μm between slats. VBG design number 5 was the first electrostatically actuated VBG designed with no bottom POLY-0 electrode; instead the author used the substrate as the bottom electrode.

Test data for VBG design number 5 is listed in Table 6.5. The far field irradiance patterns for this VBG are shown in Figure 6.12. VBG design number 5 supported 3 diffraction orders with an average diffraction efficiency of 35%. The support post and flexure used in VBG design number 5 was required because of the narrow slat width (17.5 μm). This support post and flexure design was not robust and the slat tilt angle error was high (see Section 6.2.2) resulting in the scattered light visible in Figure 6.12. The driving design requirements for the support post and flexure were minimum anchor-1 dimensions (4 μm on each side), minimum POLY-1 flexure width (2 μm), and minimum POLY-1 gap widths used between the flexure and the stacked-poly slat (2 μm).

Table 6.5. VBG Design Number 5 Test Data.

Diffraction order	Blaze angle	Steering angle	Drive voltage (V)
0	0°	0°	0
1	0.91°	1.81°	27.1
2	1.81°	3.63°	30.6

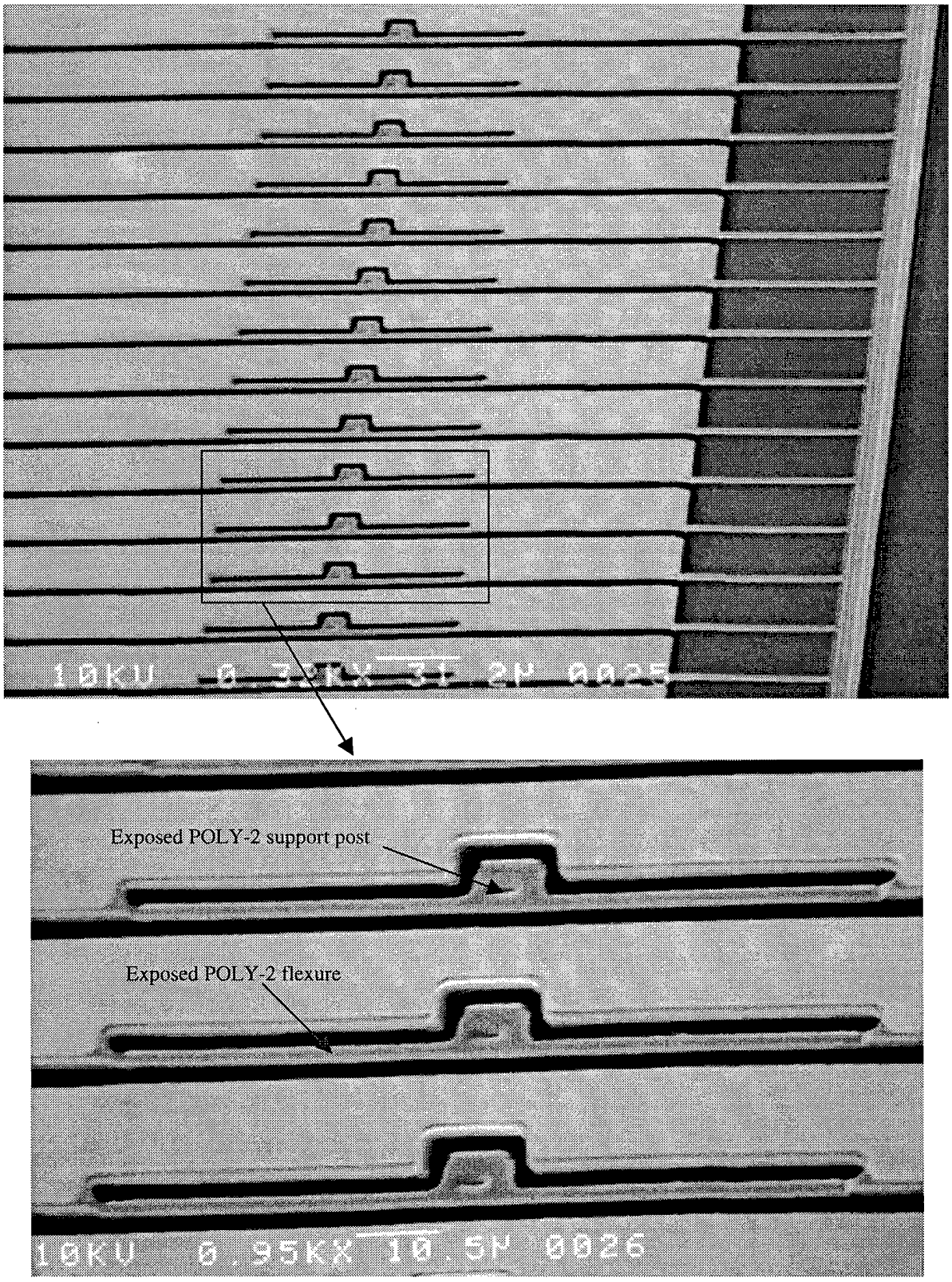

Figure 6.11. Scanning electron micrograph of VBG design number 5. Grating period is 20 μm (fabricated by the author in MUMPs 15).

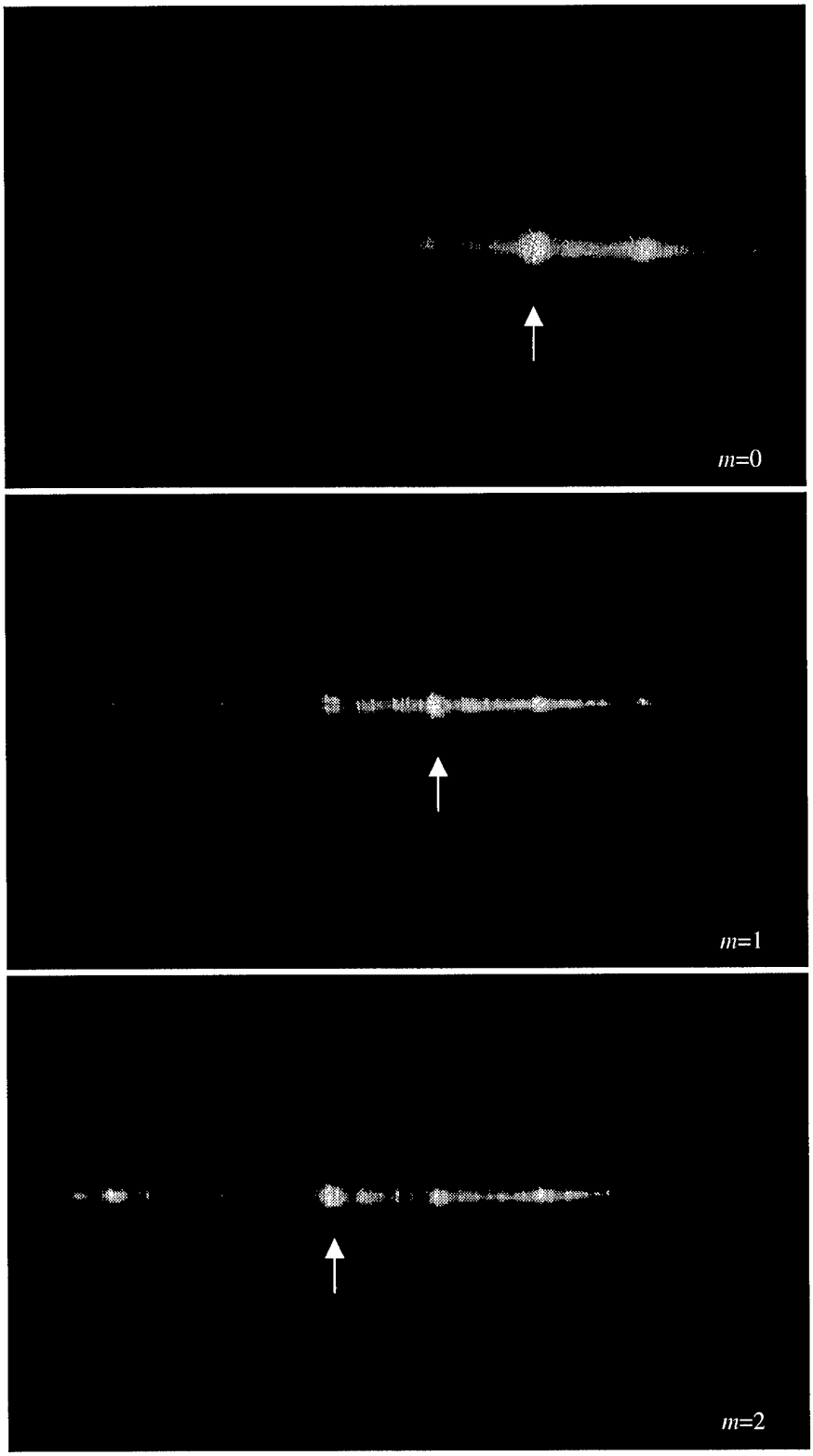

Figure 6.12. Far field irradiance patterns for VBG design number 5. The irradiance patterns correspond to each of the diffraction orders in Table 6.5. The light scattered to the left of the main lobe in the second diffraction order (m=2) is caused by a small number of slats that have already snapped down to the substrate.

6.2.6 VBG Design Numbers 6, 7, and 8

VBG design numbers 6, 7, and 8 were used to evaluate the effect of different slat construction methods on diffraction efficiency. These electrostatically actuated devices used the substrate as the bottom electrode. All three VBGs had the same period (60 μm) and supporting flexure design; however the three VBGs had slats constructed using POLY-2 only, stacked-poly, and trapped-oxide, respectively. As a result the peak-to-valley curvatures for VBG design numbers 6, 7, and 8 were 303.4 nm, 63.5 nm, and 31.5 nm, respectively. The gold layer was inset 2 μm from each edge of all three slat designs. Normally the author used a 1 μm gold layer inset from each edge of POLY-2 only and stacked-poly slats. Trapped-oxide slats had a gold layer that was typically inset 2 μm from each edge of the slat; the extra inset distance on the trapped-oxide slat was required to allow space for a via at the edge of the slat to seal in the second oxide layer. However to allow the three designs to be directly compared, a 2 μm inset for the gold layer was used on all three designs.

Figure 6.13 depicts VBG design number 8 (trapped-oxide slat). With the exception of the via around the edge of each slat (trapping the second oxide), VBG design numbers 6 and 7 are visually indistinguishable from Figure 6.13. A diagram of the torsion support flexure used in all three VBG designs is shown in Figure 6.14. Because the three designs were similar except for the peak-to-valley curvature, the effects of curvature on diffraction efficiency could be determined. Figure 6.15 is a plot of the first order diffraction efficiency for the slat design used in VBG design numbers 6, 7, and 8 as a function of peak-to-valley curvature. Measured diffraction efficiencies for VBG design numbers 6, 7, and 8 are also shown in Figure 6.15. The steering angles and drive voltages for VBG design number 8 listed in Table 6.6 are representative of all three VBG designs. Figure 6.16 is the far field irradiance patterns for VBG design number 8 with a blaze angle supporting each of the first 3 diffraction orders.

Table 6.6. VBG Design Number 8 Test Data.

Diffraction order	Blaze angle	Steering angle	Drive voltage (V)
0	0°	0°	0
1	0.3°	0.6°	13.9
2	0.6°	1.2°	22.9

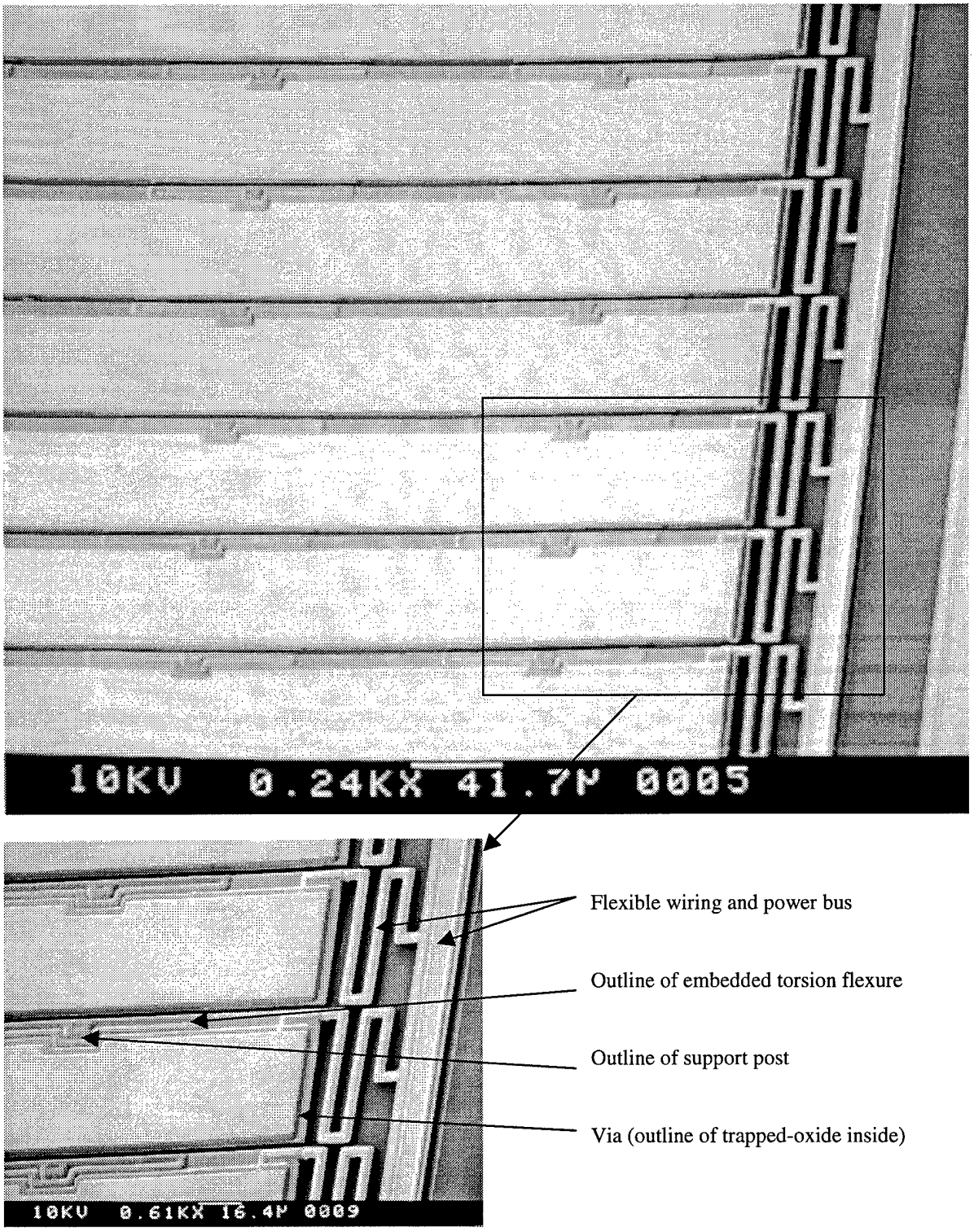

Figure 6.13. Scanning electron micrograph of VBG design number 8 (fabricated by the author in MUMPs 15).

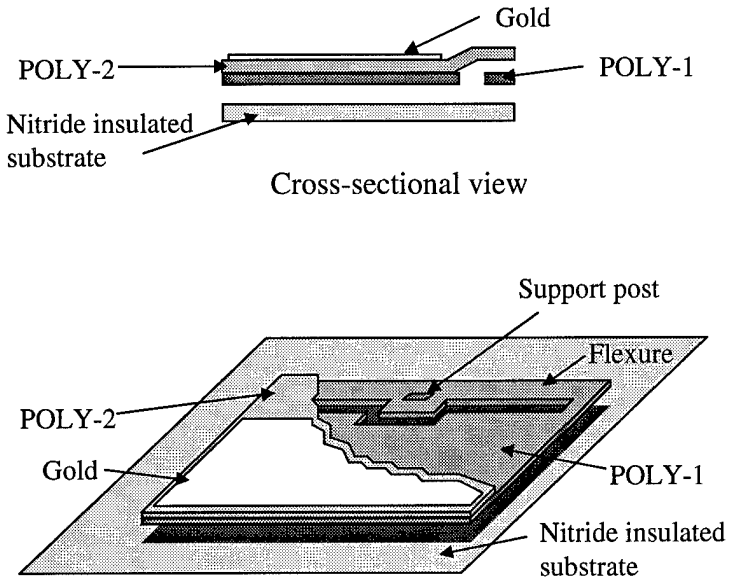

Figure 6.14. Schematic diagram of the torsion flexure used in VBG design numbers 6, 7, and 8. The slat design in this diagram is for a stacked-poly slat (VBG design number 7).

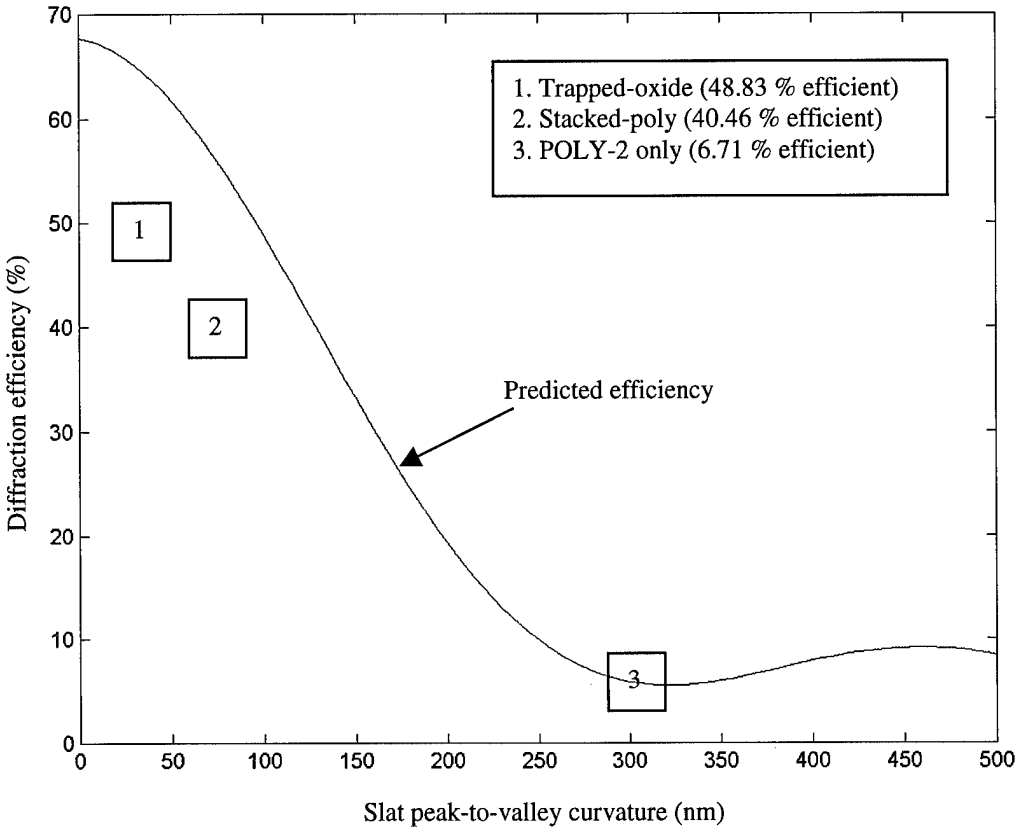

Figure 6.15. First order diffraction efficiency for the slat used VBG design numbers 6, 7, and 8 as a function of slat curvature.

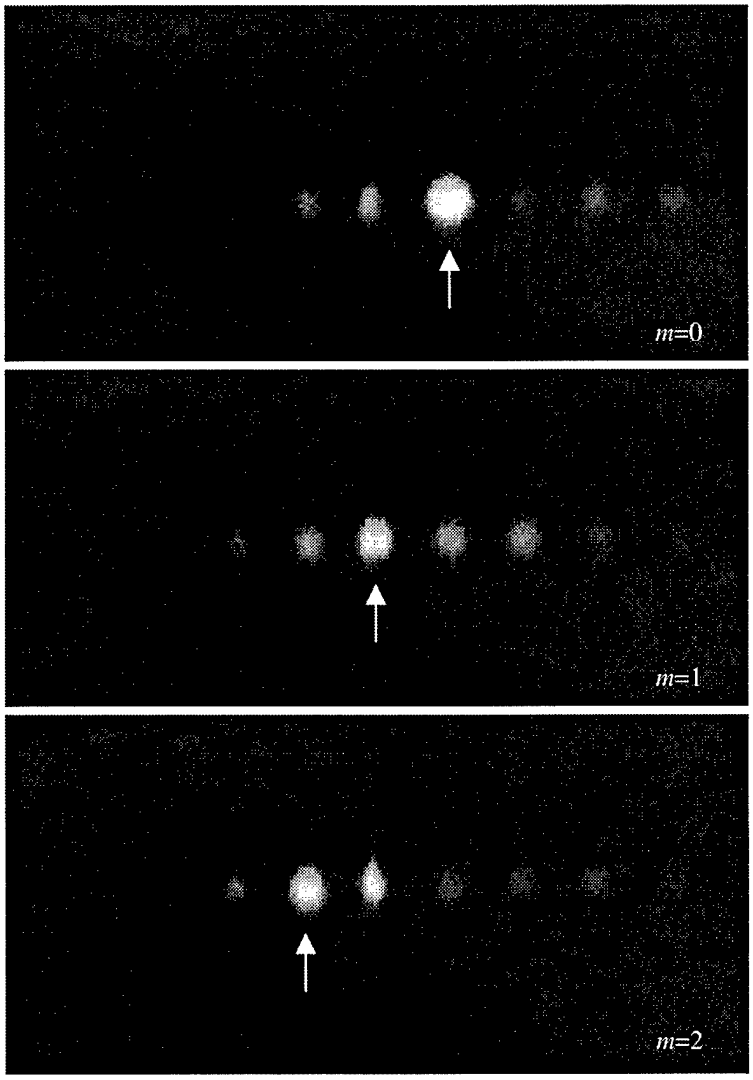

Figure 6.16. Far field irradiance patterns of VBG design number 8. The irradiance patterns correspond to each of the diffraction orders listed in Table 6.6.

6.2.7 VBG Design Number 9

VBG design number 9 was the first VBG with a measured diffraction efficiency greater than 50%. Figure 6.17 depicts VBG design number 9. This VBG had 78 μm wide trapped-oxide slats. The grating had 36 slats, each 3.0 mm long, and a separation between support posts on the same slat of 380 μm. The gold layer on each slat was 74 μm wide and a 2 μm polysilicon border separated the gold layer from each edge of the slat.

VBG design number 9 was also the first single-sided electrostatically actuated VBG with more than 3 selectable diffraction orders. The key to increasing the number of selectable diffraction orders was the incorporation of a nonlinear flexure design into the slat. Figure 6.18 is a diagram of the nonlinear support flexure used in VBG design number 9. Slats supported by linear force flexures exhibited snap-through after the edge of the slat traveled one-third of the initial separation distance, limiting the number of diffraction orders that could be supported by the grating to three (independent of the slat's width). The nonlinear flexure used in VBG design number 9 increased the maximum stable deflection distance for the slat's edge as it was tilted towards the substrate.

When a voltage was initially placed between the slat and the substrate, electrostatic force pulled the edge of the slat opposite the flexure towards the substrate. If the voltage was increased, the slat would snap down to rest on the top of the support post. Higher voltages resulted in the slat rotating on top of the support post until the edge of the slat eventually rested on the substrate. The slat did not exhibit snap through until the edge of the slat was less than 300 nm above the silicon nitride layer. The slat's flexure exhibited two distinct spring constants: one value before the slat rested on the support post and a higher value after the slat rested on the support post. The second spring constant was caused by changing the direction and amount of force on the flexure. The flexure bent to counter the electrostatic force before the slat rested on the support post. After the slat rested on the support post, the flexure continued to bend and the edge of the flexure opposite the support post was lifted up.

The nonlinear force flexure grating supported blaze angles for five diffraction orders. The first additional diffraction order was a result of increasing the range of stable tilt angles. The second additional diffraction order was a result of moving the support post under the slat; after snap-through, the mirror's position on the silicon nitride layer and support post matched the blaze angle for the highest selectable diffraction order. The steering angles and drive voltages for VBG design number 9 are listed in Table 6.7. Figure 6.19 is the far field irradiance patterns for VBG design number 9 with a blaze angle supporting each of the first 5 diffraction orders.

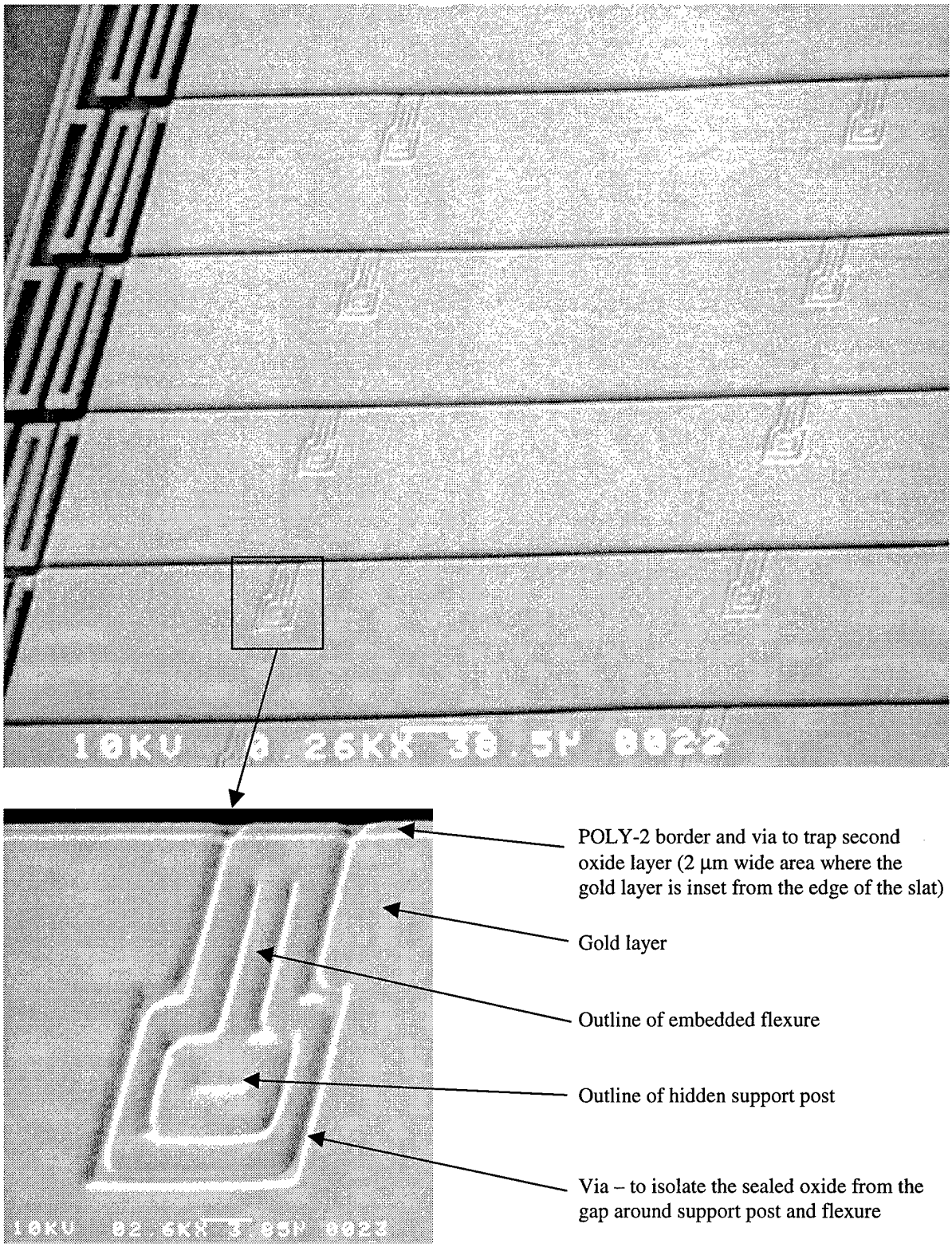

Figure 6.17. Scanning electron micrograph of VBG design number 9 (fabricated by the author in MUMPs 17).

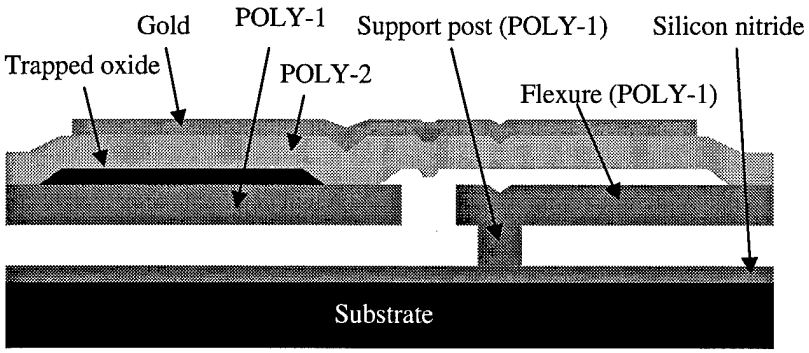

Cross-sectional view of a VBG slat.

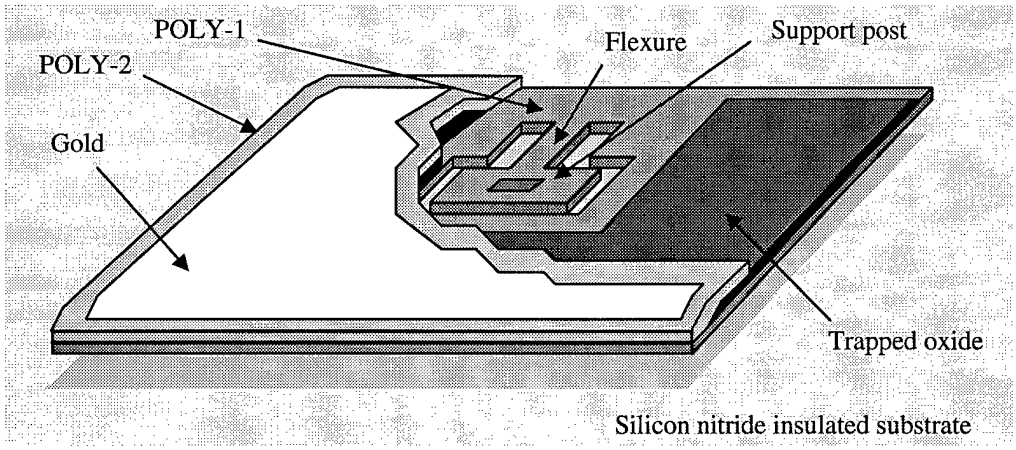

Figure 6.18. Diagram of the slat support post and flexure used in VBG design number 9. A cross-sectional view of the slat across the flexure is shown at the top. The embossing present in the cross-sectional view of the gold layer is visible in Figure 6.14.

Table 6.7. VBG Design Number 9 Test Data.

Diffraction order	Blaze angle	Steering angle	Drive voltage
0	0°	0°	0
1	0.23°	0.45°	13.4
2	0.46°	0.91°	22.9
3	0.68°	1.36°	26.6
4	0.91°	1.81°	29.4

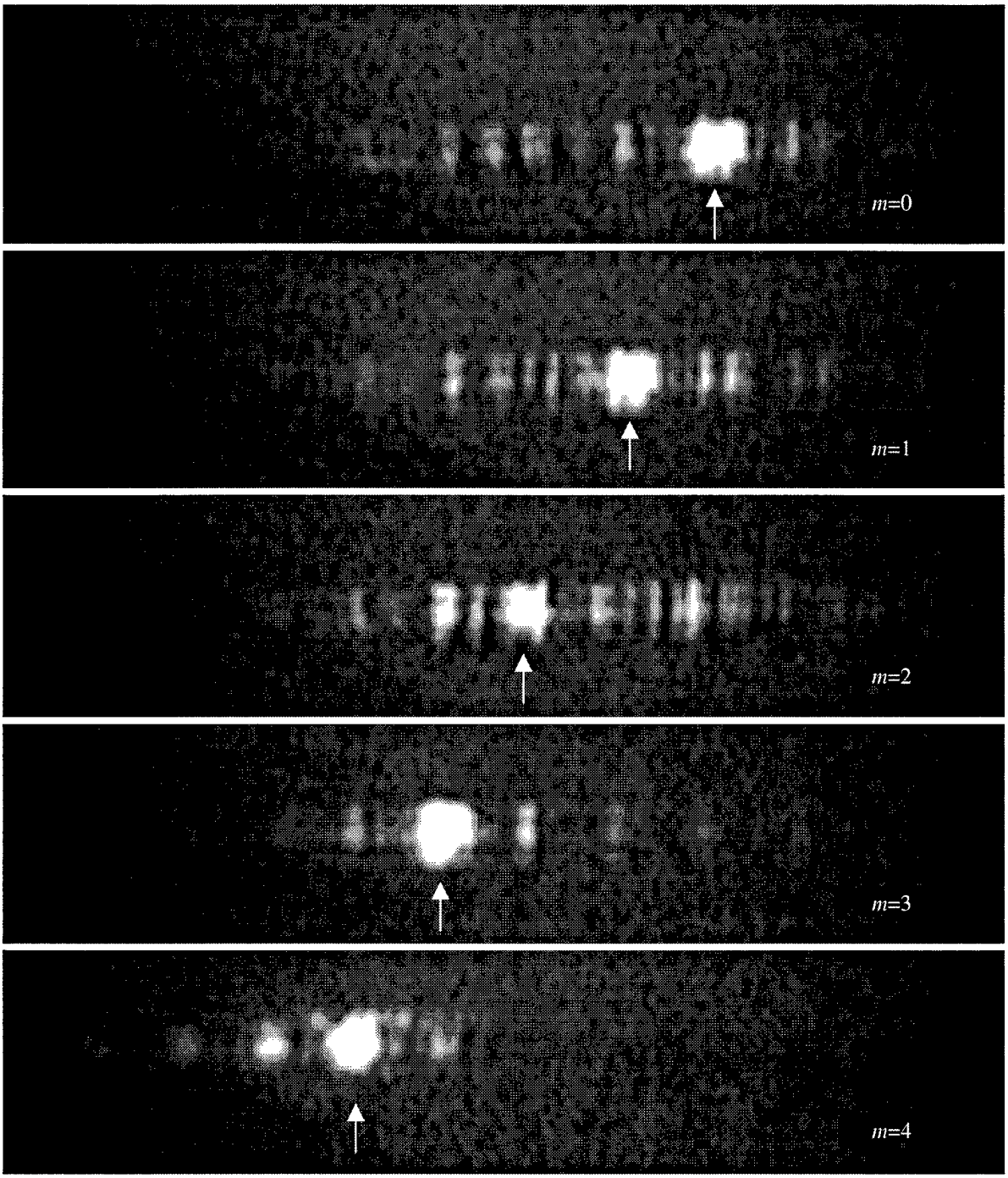

Figure 6.19. Far field irradiance patterns of VBG design number 9. The irradiance patterns correspond to each of the diffraction orders listed in Table 6.7.

6.2.8 VBG Design Number 10

VBG design number 10 was the largest VBG created by the author. Figure 6.20 is a picture of VBG design number 10 packaged in a 144 PGA. The surface area of VBG design number 10 was almost 1 cm^2 and the design filled an entire MUMPs die. The objective of VBG design number 10 was to prove that the author's VBG designs could be extended to large scale optical structures. The surface area of the largest VBG previously constructed and successfully tested by the author was 0.25 cm^2, although the author had successfully tested 0.950 cm long individual slats. The slat design used in VBG design number 10 was derived from VBG design number 9; VBG design number 9 had the highest measured diffraction efficiency at the time VBG design number 10 was created. Two slight modifications to the VBG design number 9 slat were made for VBG design number 10: increased gold width and support post position.

The width of the gold layer on VBG design number 10 was 3 μm less than the slat width (compared to 4 μm on VBG design number 9). The author used the extra gold layer width as a result of studying trapped-oxide test structures; 1.5 μm was determined to be the minimum gold layer inset from each side of a trapped-oxide slat. The support post was moved 1 μm away from the side of the slat connected to the support flexure (see Figure 6.18). The support post move was an attempt to increase the diffraction efficiency of the second diffraction order (m=2). The blaze angle for the second diffraction order occurred when the slat rested on the support post. Predicted and measured grating performance for VBG design number 10 were similar to VBG design number 9.

6.3 VBG Optical Modeling

The author investigated three optical modeling topics in addition to predicting VBG far fields: optimizing slat construction for a specific VBG period, slat tilt angle error, and slat reflectivity sensitivity. Optimizing slat construction for a specific VBG period was a method for selecting the slat construction technique with the highest diffraction efficiency. Slat tilt angle error was a potential cause of the variance between the predicted and measured diffraction efficiencies presented in Section 6.2. Slat reflectivity sensitivity modeling evaluated the effect of reflectivity on diffraction efficiency; the reflectivity of gold varies from 35% to over 90% as a function of wavelength in the visible spectrum.

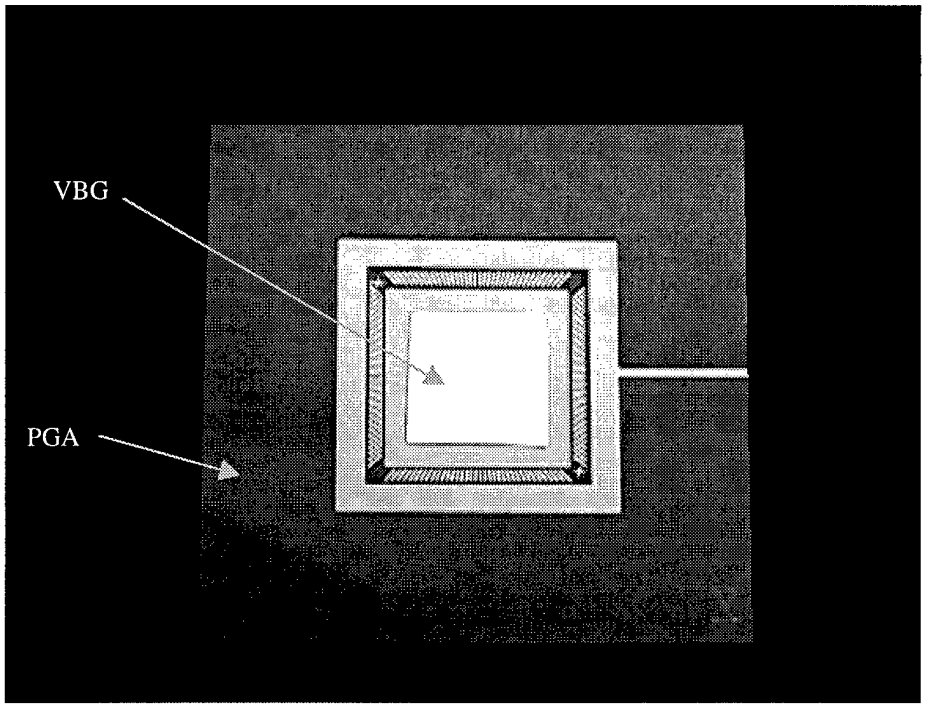

Figure 6.20. VBG design number 10 in a 144 PGA. Individual VBG slats are too small to be seen; even close inspection with the naked eye gives the impression of a single sheet of gold (fabricated by the author in MUMPs 21).

6.3.1 Slat Curvature

Diffraction efficiency depends both on slat curvature and the fill factor of the reflective region on each slat. Figure 6.21 is a plot of first diffraction order efficiencies for each slat construction technique based on a finite element Fourier transform analysis of each grating for normally incident light at a wavelength of 632.8 nm. Slat curvature for the three construction techniques was based on curvature measurements from MUMPs 19; measured curvatures for slats designed using the three construction techniques fabricated in MUMPs 19 was presented in Chapter 4. All of the VBGs used in Figure 6.21 had 36 slats tilted to support the first diffraction order.

Slat curvature increases quadratically as a function of slat width for each slat construction design; consequently all designs lose diffraction efficiency as slat width increases. Smaller periods have lower diffraction efficiencies because the gap between adjacent slats is fixed at 2 μm. The fixed gap width causes the ratio of the slat width to grating period (fill factor) to decrease as the size of the grating period is reduced. VBGs with periods of 20 μm to 100 μm have been successfully fabricated and tested. Gratings with periods

below 55 μm had higher diffraction efficiencies if their slats were constructed with-stacked-poly. Gratings with periods above 55 μm had higher diffraction efficiencies if they are constructed using trapped-oxide slats.

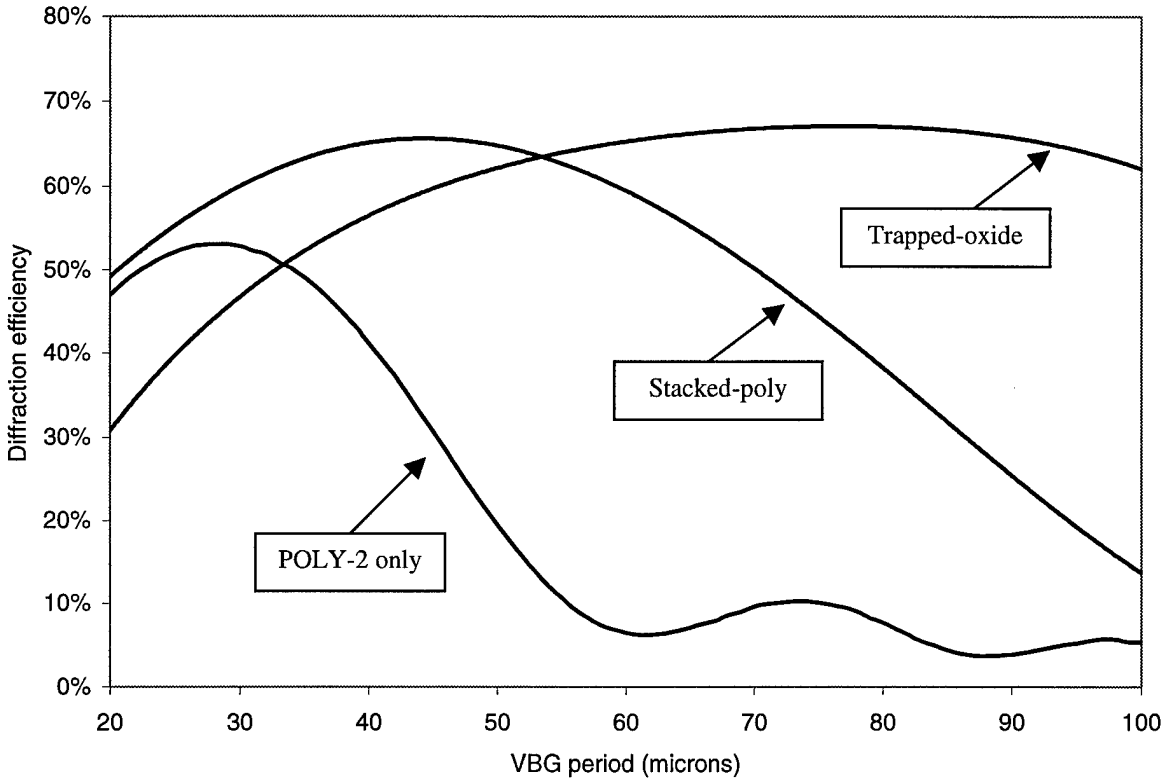

Figure 6.21. Predicted first diffraction order efficiencies for VBG slats constructed out of POLY-2 only, stacked-poly, and trapped-oxide. The width of each slat is 2 μm less than the period. The width of gold region on POLY-2 only and stacked-poly slats is 2 μm less than the slat width and 4 μm less than the slat width on trapped-oxide slats.

6.3.2 Slat Tilt Angle Error

Diffraction efficiency can also be reduced by slat tilt angle error. The tilt angle for each slat was modeled as a normal distribution with mean γ_m (the desired blaze angle). Figure 6.22 shows the effect of increasing the slat tilt angle variance (as a percentage of γ_m) on VBG design number 9. Figure 6.22 was created by randomly tilting each slat in the grating so that tilt angles for all of the slats in the grating form the intended normal distribution. The mean slat tilt angle favored the first diffraction order. The continuous line in Figure 6.22 was the best-fit fifth order polynomial approximation to the statistical diffraction efficiencies

simulation samples. The actual slat tilt angle distribution was not measured because the variance of individual slat tilt angles was too small to accurately observe.

Not all of the losses in diffraction efficiency between the VBG model and measured VBG data are due to slat curvature and slat tilt angle error; further losses in diffraction efficiency are caused by the embedded actuators and torsion springs. Each layer in MUMPs conforms to the surface topology of underlying layers. The actuators and torsion springs cause the slat's reflective surface to be unintentionally embossed. However, the effect of unintentional embossing on diffraction efficiency is small because all slat designs had less than 3 percent of the top reflective surface embossed.

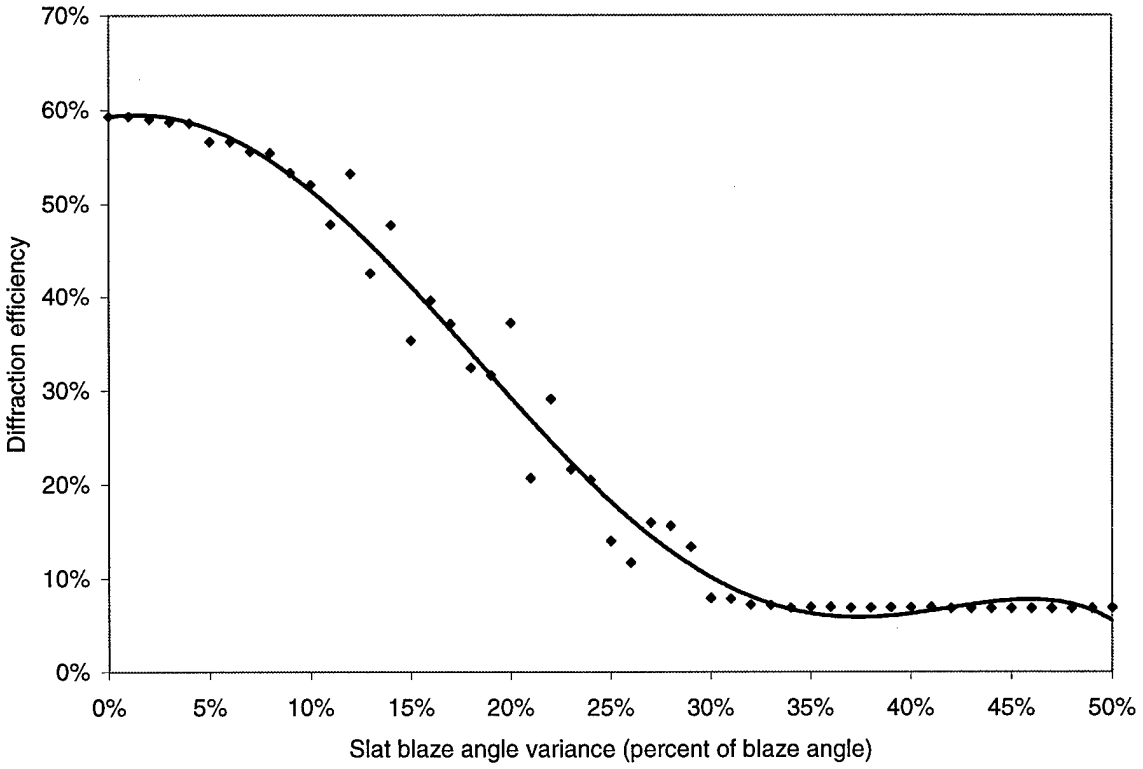

Figure 6.22. Effect of slat blaze angle error on first order diffraction efficiency (based on the slat design used in VBG design number 9).

6.3.3 Slat Reflectivity Sensitivity

The power reflectivity of gold varies from 35% in the blue region of the visible spectrum to over 90% in the red region of the visible spectrum (see Appendix A for a plot of the reflectivity of gold as a function of

wavelength). Figure 6.23 is a plot of the first order diffraction efficiency for VBG design number 9 as the reflectivity of the gold is varied from 30% to 100% (reflectivities of the other layers were held constant). The diffraction efficiency decreased linearly as the reflectivity was reduced. Alternate materials, such as silver and aluminum may be required for practical VBGs operating at shorter visible wavelengths (such as the blue region). Gold is excellent for VBGs operating in the infrared spectrum; for wavelengths above 12 μm, the reflectivity of gold is greater than 98%.

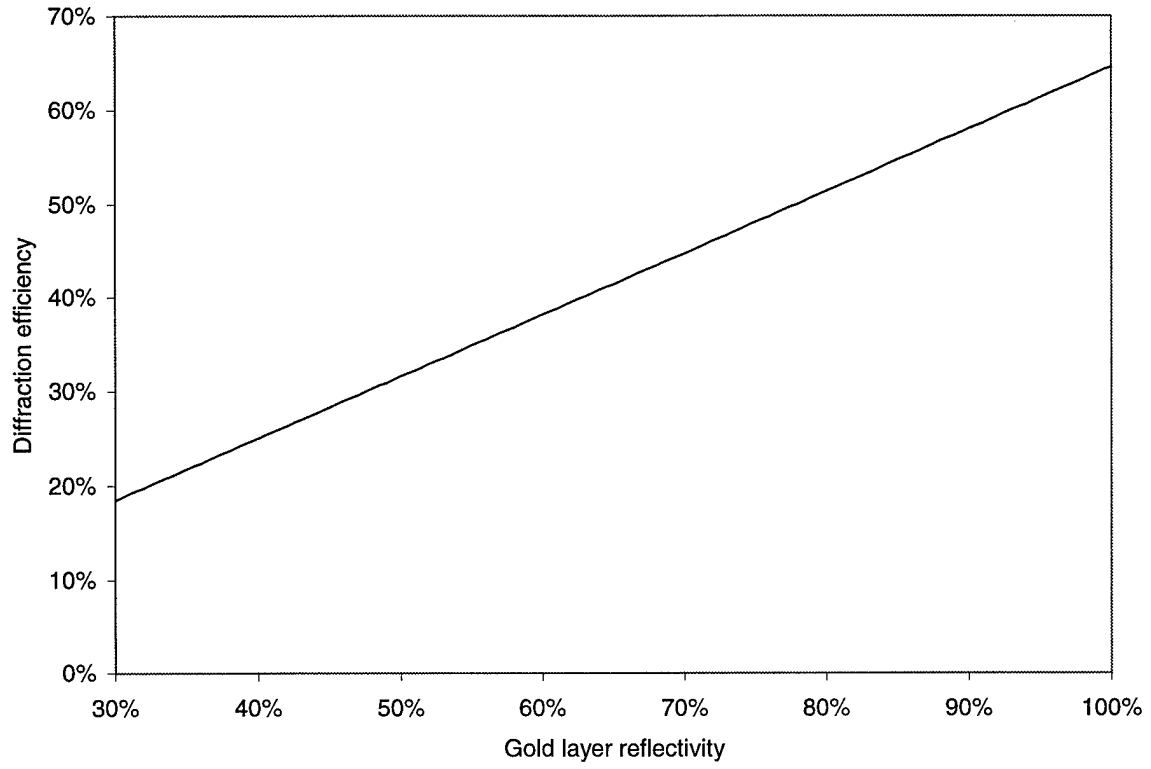

Figure 6.23. First diffraction order efficiency for VBG design number 9 as the power reflectivity of the gold layer is varied from 30% to 100%.

6.4 Summary

Variable blaze gratings with thermal and electrostatic actuators have been developed and tested. The diffraction efficiency was simulated, measured, and found to be a direct function of residual material stress-induced slat curvature. Slat curvature was reduced by stacking polysilicon layers and retaining the second

oxide layer to counter the tensile stress in the gold layer. Variations in slat tilt angle contributed to individual VBG diffraction orders having slightly different diffraction efficiencies. The diffraction efficiencies of all tested VBGs can be improved by using a more reflective surface and extending the width of the reflective region closer to the length of the period.

6.5 References

[1] J. H. Comtois, V. M. Bright, S. Gustafson, and M. A. Michalicek, "Implementation of hexagonal micromirror arrays as phase-mostly spatial light modulators," *Proc. SPIE*, vol. 2641, pp. 76-87, October 1995.

[2] D. E. Sene, J. W. Grantham, V. M. Bright, and J. H. Comtois, "Development and characterization of micro-mechanical grating for optical modulation," *Proc. IEEE MEMS-96 Workshop*, San Diego, CA, pp. 222-227, February 11-15, 1996.

[3] R. B. Apte, F. S. A. Sandejas, W. C. Banyai, and D. M. Bloom, "Deformable grating light valves for high resolution displays," *Proc. Solid-State Sensor and Actuator Workshop*, Hilton Head Island, SC, pp. 1-6, June 13-16, 1996.

[4] T. A. Kwa and R. F. Wolffenbuttel, "Integrated grating/detector array fabricated in silicon using micromachining techniques," *Sensors and Actuators A*, vol. 31, pp. 259-266, 1992.

[5] J. H. Jerman and D. J. Clift, "Miniature Fabry-Perot interferometers micromachined in silicon for use in optical fiber WDM," *Technical Digest IEEE International Solid-State Sensors and Actuators (Transducers-91)*, San Francisco, CA, pp. 372-375, June 24-27, 1991.

[6] K. Aratani, P. J. French, P. M. Sarro, D. Poenar, and R. F. Wolffenbuttel, "Surface micromachined tuneable interferometer array," *Sensors and Actuators A*, vol. 43, pp. 17-23, 1994.

[7] G. M. Yee, N. I. Maluf, P. A. Hing, M. Albin, and G. T. A. Kovacs, "Miniature spectrometers for biochemical analysis," *Proc. SPIE*, vol. 2978, pp. 75-81, February 1997.

7 Optical Beam Steering Using Decentered Microlenses

This chapter reports the author's investigation into optical beam steering using decentered microlenses. The theoretical basis for steering an optical beam using decentered microlenses was presented in Chapter 4; optical beam steering using decentered microlenses requires the lateral movement (with respect to the microlens' optical axis) of one or more microlenses. The decentered microlens beam steering systems discussed in this chapter fall into two categories: double and triple lens configurations. The author is the only researcher to ever report on these categories of micromachined decentered lens beam steering systems.

Previous researchers have reported a variety of surface micromachined thermal and electrostatic actuators capable of providing lateral movement [1,2,3]. Considerable research has also been directed towards the construction of microlenses. Relevant portions of previously reported microlens construction methods and lateral actuators are reviewed in Section 7.1. Section 7.2 presents the techniques evaluated by the author for the construction of microlenses. Section 7.3 presents a triple microlens beam steering design. Section 7.4 presents double microlens beam steering designs. The author's decentered microlens beam steering investigation is summarized in Section 7.5.

7.1 Background

Optical beam steering using decentered lenses requires the application of two technologies to surface micromachining: microlens fabrication and lateral actuators. This section reviews previously reported methods for constructing microlenses and providing lateral movement to surface micromachined micro-optical devices.

7.1.1 Previously Reported Methods for Constructing Microlenses

The two principle techniques for constructing micromachined lenses are stamping and photoresist. Stamping uses a bulk micromachined silicon wafer to shape a plastic lens blank. The bulk micromachined

wafer can be used again after imprinting. A variety of methods have been reported for shaping microlens molds out of silicon wafers including: direct electron-beam lithography [4], Reactive-Ion Etching (RIE) [5,6], electroforming photoresist (similar in some ways to LIGA) [7], and a combination of direct laser writing with RIE [8]. Stamping is well suited to high volume production of microlenses; however the stamping process is not compatible with the construction of surface micromachined optical beam steering systems.

The second well-documented technique for constructing microlenses is melting photoresist into the shape of a microlens. In this process, a photoresist pattern is formed using conventional lithography; the photoresist pattern is often a cylinder, however it may be pre-shaped into a more complex structure [9]. The photoresist is then melted by baking, resulting in a microlens compatible with the construction of surface micromachined optical beam steering systems [10]. Figure 7.1 depicts a microlens array formed using this technique. Note that this technique results in the formation of a half-sided lens; the bottom of the microlens is flat. Researchers at UCLA combined the construction of a photoresist microlens with surface micromachined flip-up plates; this technique can be used to construct microlenses perpendicular to the substrate as shown in Figure 7.2. Light is refracted at both the spherical top side and the flat bottom side, which may result in a slight defocusing of the image [11]. Another drawback of using photoresist microlenses is transmissivity: photoresist microlenses absorb significant energy at non-infrared wavelengths [12].

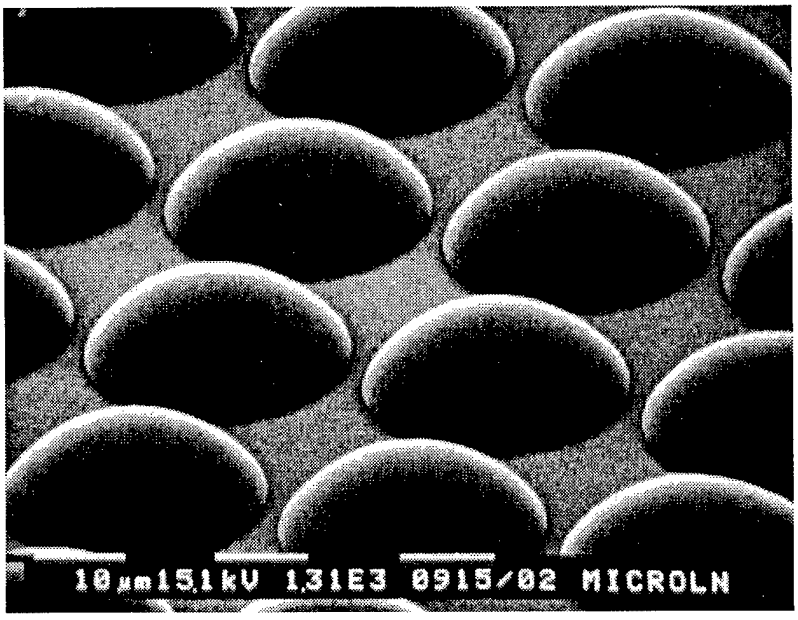

Figure 7.1. A section of a microlens array formed out of melted photoresist [10].

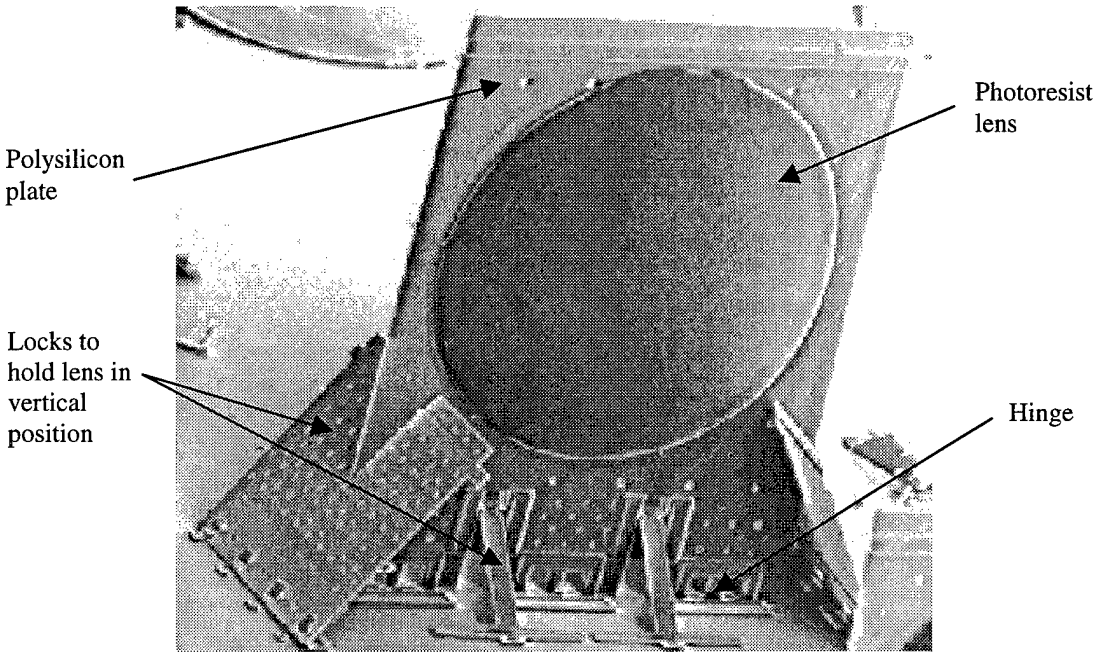

Figure 7.2. A flip-up photoresist lens constructed using surface micromachining [13].

Both of these techniques have been extensively documented and many researchers are still investigating them. The author chose to investigate a new method for constructing double-sided microlenses for operation in the visible spectrum: polyurethane droplets. The use of polyurethane to construct microlenses will be discussed in section 7.3. Because the construction of polyurethane droplet microlenses was unproven in surface micromachined systems, the author also used Fresnel lenses in many of his designs. Fresnel microlenses have been fabricated by Sene [14], Reid [15], and Bouchard [16] at AFIT. Figure 7.3 depicts a flip-up array of Fresnel microlenses constructed by Sene using MUMPs.

7.1.2 Lateral Actuation Methods Compatible with Surface Micromachining

Both thermally driven and electrostatically driven lateral actuators can be constructed using MUMPs. Thermally driven actuators rely on the thermal expansion of a polysilicon beam to rotate the tip of the actuator around a flexure. The temperature increase required for thermal expansion is typically induced by resistive heating due to electric current flowing through the polysilicon beam.

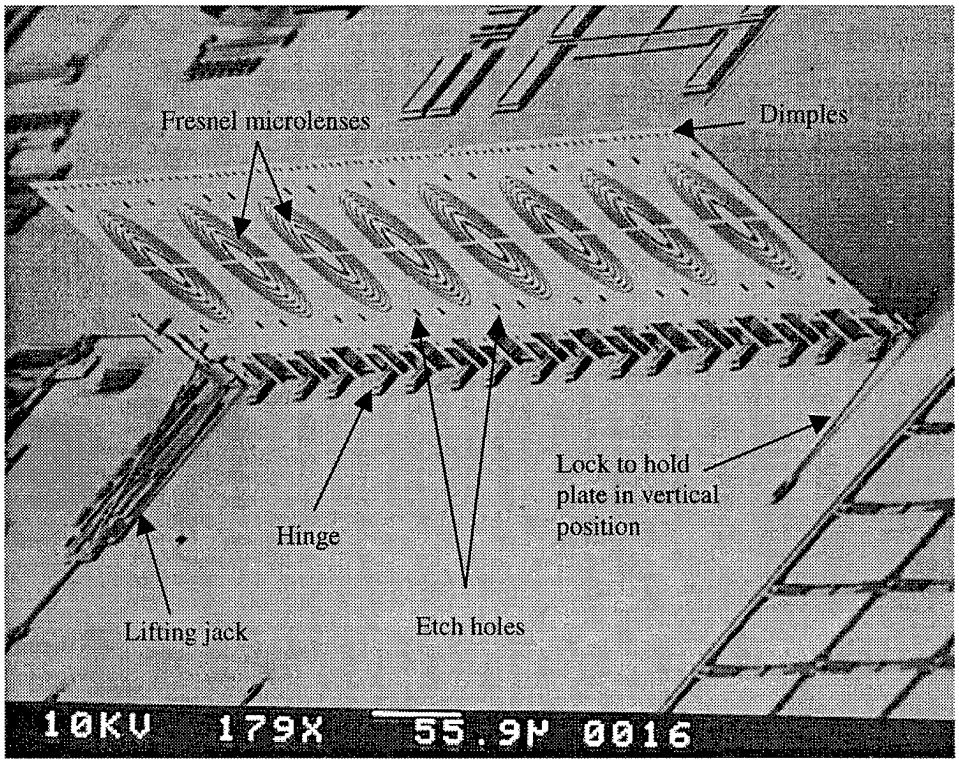

Figure 7.3. Scanning electron micrograph of an 8 element Fresnel lens array designed by Sene [14]. Diameter and focal length of each lens are 133 μm and 500 μm, respectively (MUMPs 9).

Scratch Drive Actuators (SDAs) are electrostatically driven lateral actuators. SDAs use a tilted "L" shaped top electrode to convert vertical motion resulting from the electrostatic attraction of the top electrode to the substrate to a horizontal motion. Large arrays of thermal actuators can require a relatively high operating current (and power) compared to other MEMS devices; SDAs require almost no power but do require high voltages (often 90 volts or higher) and a more complex drive signal.

7.1.2.1 Lateral Single Hot Arm Thermal Actuators

A traditional lateral single hot arm (abbreviated as "1-H") thermal actuator is shown in Figure 7.4. A schematic diagram of the 1-H actuator is shown in Figure 7.5. The cross-sectional areas of the hot and cold arms (perpendicular to current flow) are 5 μm^2 and 28 μm^2, respectively. The actuator is 200 μm long. When electric current passes through the actuator, the hot arm is resistively heated to a higher temperature than the

cold arm. As the hot arm is heated, it expands in length more than the cold arm. The difference in length between the hot arm and the cold arm causes the actuator to rotate around the flexure at the base of the cold arm. The electrical and mechanical properties of similar polysilicon thermal actuators have been extensively evaluated [1,17,18]. The tip of the actuator shown in Figure 7.4 moves 10 μm (towards the bottom of the page) when a current of 5.12 mA is applied. This rotational movement can be used in single actuator designs or in actuator array designs [2,19,20]. Thermally driven actuators are often tested in air because they tolerate humidity and microscopic dust better than electrostatic actuators.

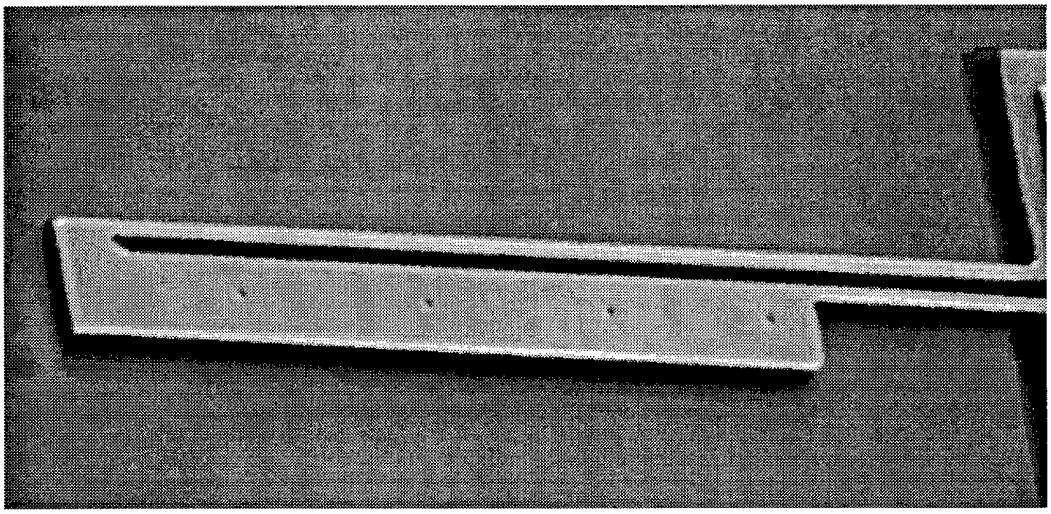

Figure 7.4. Micrograph of a traditional polysilicon thermal actuator (1-H actuator). The actuator is 200 μm long. The other dimensions of this actuator are discussed in Chapter 9 and listed in Table 9.2 (fabricated by the author in MUMPs 17).

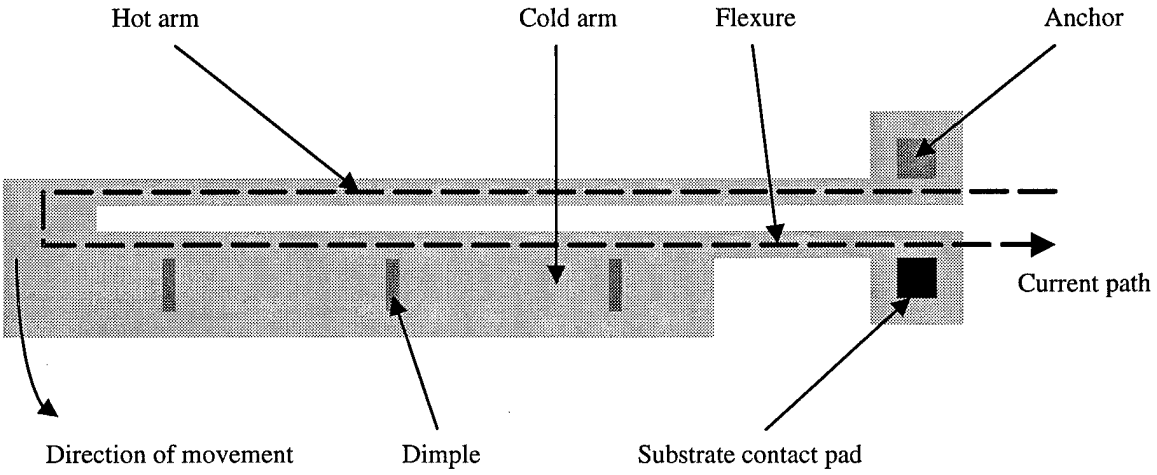

Figure 7.5. Schematic diagram of current flow in a 1-H actuator.

The design of the flexure used in the thermal actuator depicted in Figure 7.4 is important. Ideally the flexure should be as thin as possible. Thin flexures allow more of the force generated by the expansion of the hot arm to translate into movement at the tip of the actuator. However electric current passes through the flexure. If the flexure is thinner than the hot arm, then the temperature of the flexure will be higher than the hot arm and the flexure could be destroyed by excessive heat. Also the flexure has to be long enough so that it can be elastically bent by the hot arm. If the flexure is too long, then movement of the actuator's tip will be significantly reduced; long flexures expand when current is applied, countering the intended rotational movement. The flexure and cold arm contribute to the actuator's overall electrical resistance because they complete the electrical circuit for current passing through the hot arm. Power dissipated in the flexure and cold arm does not contribute to the desired movement of the actuator. Only the power dissipated in the hot arm directly translates into the intended movement of the actuator. The flexure and cold arm account for 23% of the electrical resistance of the actuator shown in Figure 7.4.

If the actuator is driven to within approximately 10% of it maximum current limit (before failure), the hot arm will shrink below its original length. This phenomenon is called "back-bending" [2]. Back-bending can be used to relocate the resting (zero current) position of thermal actuators.

7.1.2.2 Scratch Drive Actuators

A scratch drive actuator consists of a flat polysilicon plate with a bushing on one edge. Figure 7.6 is a cross-sectional view of a POLY-2 SDA fabricated using MUMPs. The bushing is 2 μm deep (the thickness of the 1st sacrificial oxide layer). The SDA is driven by a sinusoidal voltage source [21]. Figure 7.7 depicts the operation of an SDA. Figure 7.7(a) shows the SDA at rest (before voltage is applied). Figure 7.7(b) shows the SDA when the peak (positive) voltage is applied; the voltage is high enough to deform the plate and push the bushing forward. Friction from the large surface area of the plate resting on the silicon nitride layer prevents the SDA from moving when the bushing is pushed forward. In Figure 7.7(c) the polarity of the applied voltage is reversed and the electrostatic force on the plate is reduced so that the bushing bends back towards it original position. This movement from the bushing pulls the SDA forward. Figure 7.7(d) shows the SDA as the applied

voltage reaches its minimum (negative) value; the electrostatic force on the SDA is identical to the force on the SDA in Figure 7.7(b) and the bushing is again pushed forward.

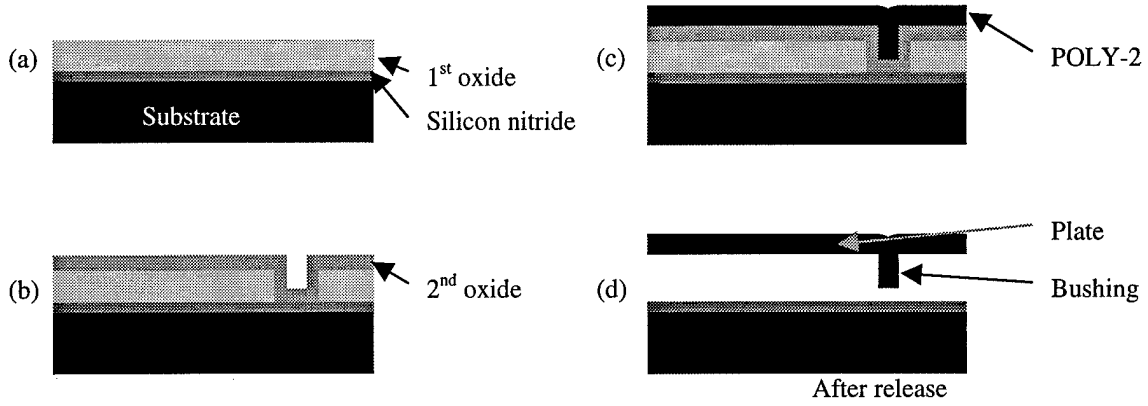

Figure 7.6. Cross-sectional schematic diagram of the SDA construction process [21].

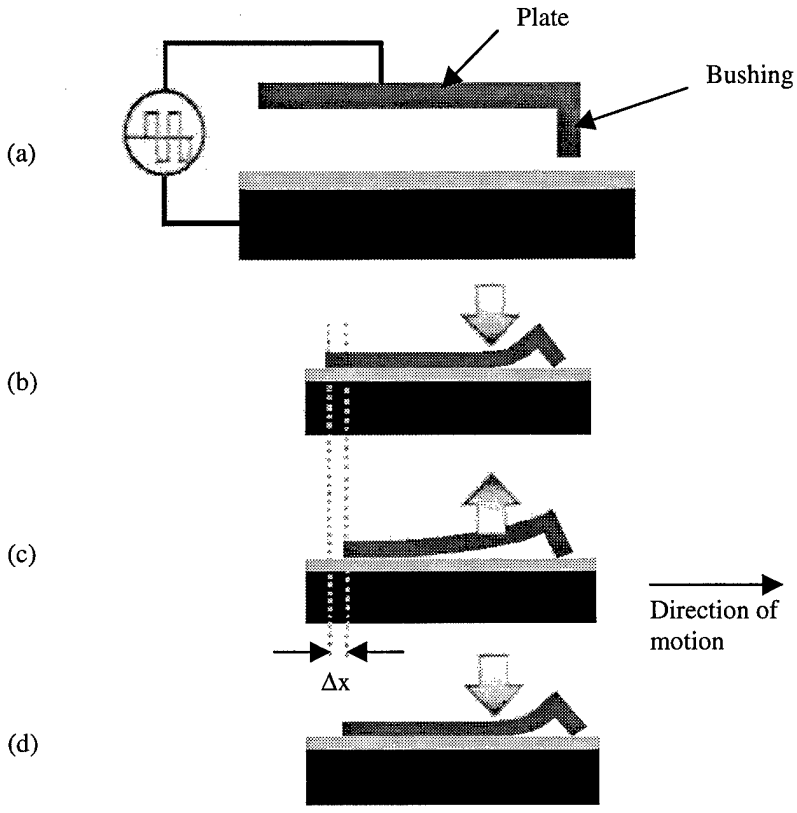

Figure 7.7. SDA operation [21].

SDAs can be used to position optical components with high accuracy; lateral movement resolution is equal to the step size (Δx in Figure 7.7). The step size is typically 11 nm for an SDA fabricated using MUMPs [3]. SDA operating frequencies of 50 kHz have been reported [21]. Typical lifetime for an SDA is 30 million cycles [22]. Average lateral velocity for an SDA is 2.5 mm/second (at an operating frequency of 50 kHz) [21].

Figure 7.8 depicts a flip-up focusing Fresnel lens constructed at UCLA using MUMPs [3]. This focusing lens can be positioned along its optical axis using SDAs. A row of four SDAs is located at each side of the lens baseplate. Note the springs on each side of the Fresnel lens' base; SDAs work in one direction only. The springs are used to restore the lens' position after actuation. The springs require the actuation voltage to be held on the device when it reaches its final position to prevent the springs from inadvertently pulling the lens back to its starting position.

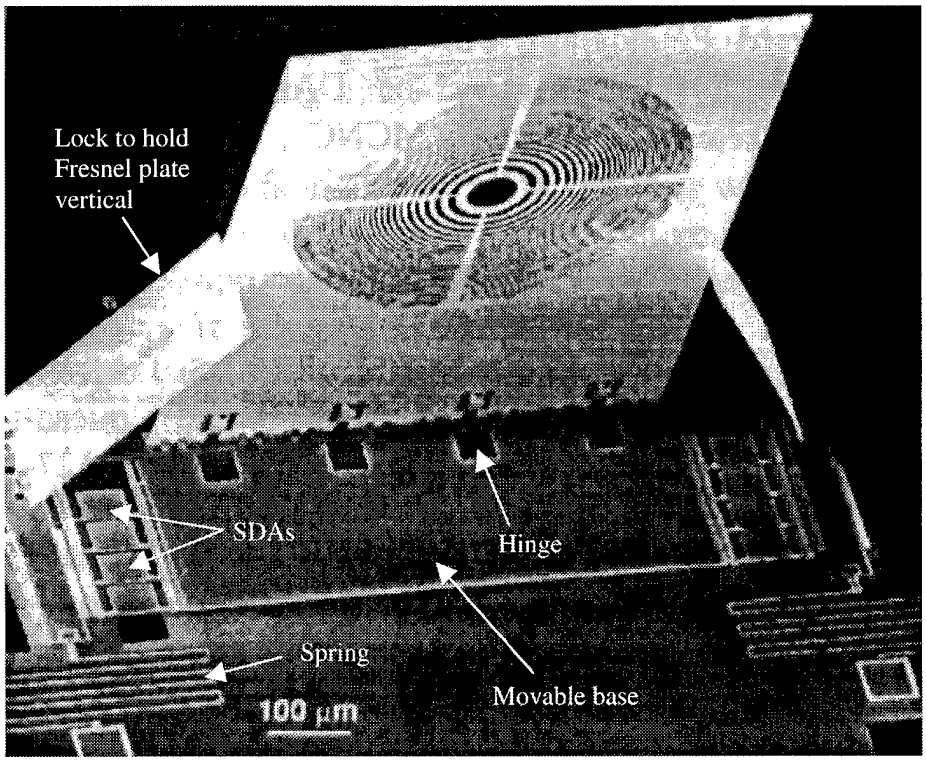

Figure 7.8. A flip-up Fresnel lens designed to be positioned with SDAs [3].

7.2 Investigated Techniques for Constructing Microlenses

This section presents the surface micromachining techniques used by the author for constructing microlenses. Because of the large number of researchers currently investigating photoresist microlenses, the author decided not to pursue developing photoresist microlenses. Instead the author evaluated two techniques for constructing microlenses: polyurethane and Fresnel microlenses. Each of these techniques has strengths and weaknesses. Polyurethane lenses have a transmissivity approaching 100% for visible wavelengths, however fabricating multiple polyurethane lenses with identical and predictable focal lengths is difficult. Fresnel lenses have a focal length that is fixed during fabrication, however at most only 50% of the incident light is passed through the lens (half the Fresnel zones).

7.2.1 Polyurethane Microlenses

The author constructed polyurethane microlenses by first fabricating and erecting a flip-up polysilicon plate with a circular hole in the middle and then placing a small drop of polyurethane in the hole. Capillary forces formed the polyurethane droplet into the shape of a double-sided spherical lens with an excellent transmissivity in the visible spectrum. Figure 7.9 is a cross-sectional view of the construction process developed by the author to construct a polyurethane microlens. Factors determining the quality of the lens include: size of the droplet, index of refraction, drying time, and capillary force. The author investigated 5 different polyurethane compounds.

A significant design challenge for the construction of polyurethane lenses in a surface micromachining system was the design of the flip-up polysilicon plate. The polysilicon plate had to be strong enough to hold a mass of polyurethane many times the weight of the polysilicon plate and rigid enough to survive the application of the polyurethane drop. The author used microprobes to place a droplet of polyurethane in the hole in the polysilicon plate. Capillary forces held the droplet to both the plate and the probe tip; when the probe was withdrawn after depositing the droplet, the plate was pulled towards the probe. The author used a stacked-poly plate with reinforcement ribs of trapped-oxide and double side mounted locks (similar to the micromirror in

Figure 3.1); this plate design was sufficient to survive approximately 95% of the plate positionings (flipping the plate up to a vertical position) but only 5% of the polyurethane droplet applications.

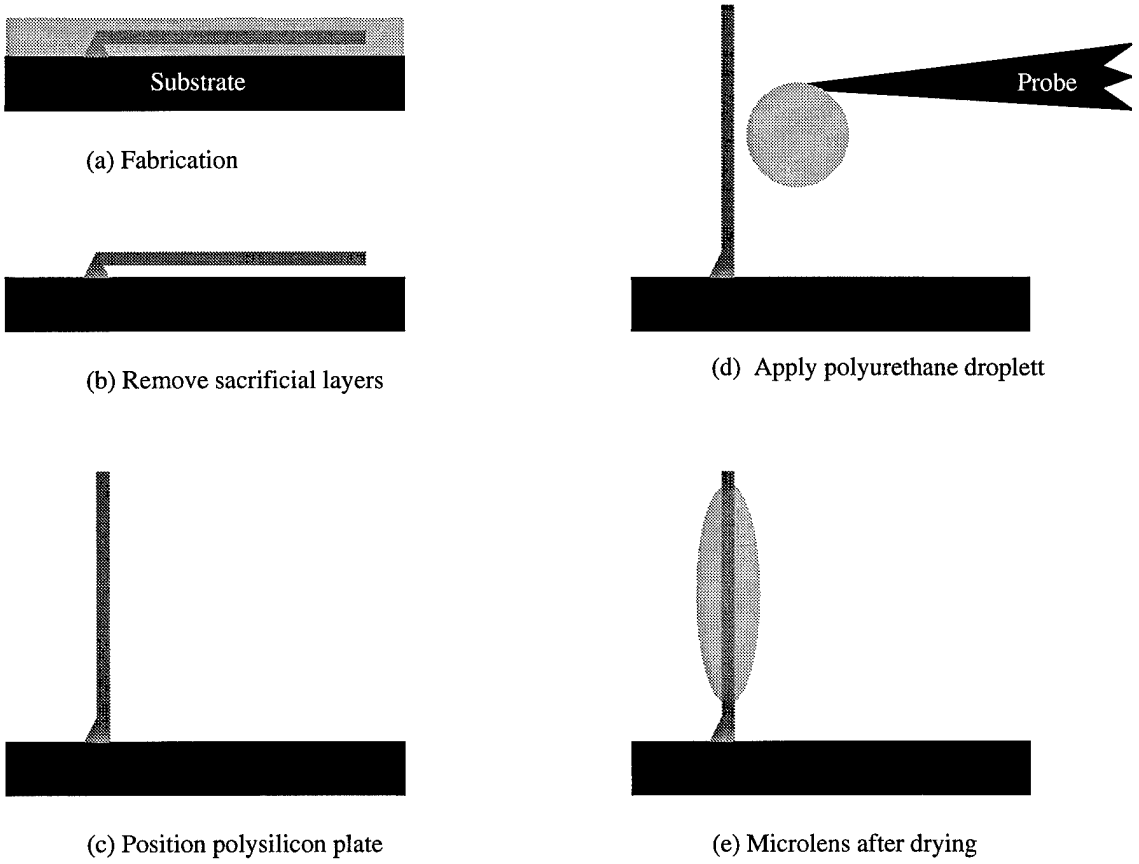

Figure 7.9. Cross-section view of the construction process used to create a polyurethane microlens.

The author experimented with the construction of polyurethane microlenses using the five compounds listed in Table 7.1. The five compounds had varying drying times, bases, and active chemicals. The author was able to construct microlenses using only the fifth compound, *Minwax Oil-based Polyurethane Finish*. The other compounds adhered to both the probe and polysilicon plate, destroying the device when the probe was removed. Figure 7.10 depicts a 300 μm diameter microlens constructed by the author. The thickness at the center of the microlens is 70 μm. The index of refraction for acrylic based polyurethane is 1.49 [23,24]; using the lens maker equation (Equation (4.22)) and the equation for the radius of curvature (Equation (4.29)), the predicted focal length for the microlens in Figure 7.10 is 345.8 μm.

Table 7.1. Compounds Used to Construct Polyurethane Microlenses.

	Name	Base
1	Valspar (Enterprise) Polyurethane Varnish [25]	Water
2	Valspar (Enterprise) Duramax Latex Gloss Finish [26]	Water
3	Minwax Polycrylic [27]	Water
4	Valspar Polyurethane Varnish [28]	Oil
5	Minwax Polyurethane [29]	Oil

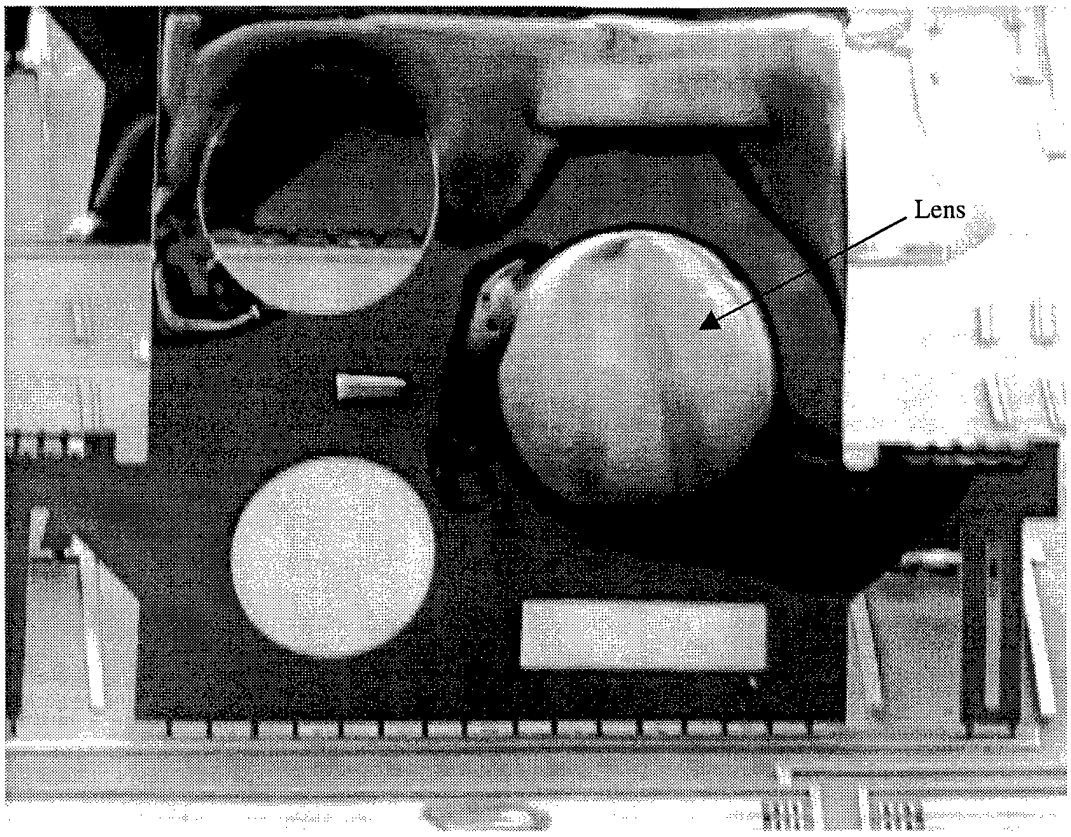

Figure 7.10. Scanning electron micrograph of a vertical 300 μm diameter polyurethane lens constructed by the author. The apparent discoloration in the lens is actually an image of the surrounding structure formed by the electron beam (fabricated by the author in MUMPs 19).

All of the compounds in Table 7.1 had a drying time sufficiency long enough to permit positioning of a droplet in the polysilicon aperture. The best method for creating a droplet was to place a large drop of polyurethane on an unused portion of the die using a syringe and hypodermic needle and then dipping a probe tip into the drop. When the probe tip was removed from the large drop, a droplet would typically remain at the end of the probe tip. The size of the polyurethane droplet could be controlled by changing the distance the probe tip was dipped into the drop (larger droplets resulted when the probe was dipped further into the drop). Based on the minimum practical size of the droplets produced using this method, the author estimated that microlenses diameters as small as 50 μm could be fabricated. However the technique shown in Figure 7.9 may be better suited to bulk micromachining; the majority of microlenses constructed by the author were destroyed when the probe was removed (including many fabricated with the fifth compound in Table 7.1). Polyurethane microlens clarity and shape appeared to be good.

7.2.2 Fresnel Microlenses

Fresnel microlenses constructed by previous researchers were not specifically designed for decentered lens beam steering; the author made a number of improvements to the basic MUMPs Fresnel microlens design to optimize the design for decentered lens beam steering. These improvements include: improved zone blocking, larger size, higher fill factor, and cylindrical lenses. Improved zone blocking resulted from using a stacked-poly Fresnel microlens. Sene had reported that the optical performance of his Fresnel microlenses may have been impaired by an incomplete blocking of alternate Fresnel zones [30]. Sene had used a single POLY-2 layer to block the alternate zone. The author improved the zone blocking design by using stacked-poly Fresnel microlenses; the additional polysilicon layer (POLY-1) more than doubled the thickness of each microlens.

The author also improved the size of the Fresnel microlens by using stacked-poly with tapped-oxide reinforcement ribs for the Fresnel microlenses support plate. Constructing large devices in a surface micromachining process such as MUMPs is challenging because each layer thickness is constant. Large thin plates are similar to a sheet of paper and can bend very easily. By increasing the plate thickness (using stacked-

poly or trapped-oxide), the author was able to construct larger plates. The author increased the diameter of the Fresnel microlens to 250 μm and the focal length to 500 μm. The author also moved the microlenses closer together (laterally) to improve the fill factor. Figure 7.11 depicts an array of 10 stacked-poly Fresnel microlenses; this structure is large enough to be seen by the naked eye. Cylindrical Fresnel microlenses were designed to further improve the fill factor. Because the author's flip-up decentered microlens beam steering designs directed light over only one axis, the standard Fresnel microlens could be replaced by a Fresnel cylindrical lens. Figure 7.12 depicts an array of 10 stacked-poly cylindrical Fresnel microlenses. A close-up view of this array is shown in Figure 7.13. The focal length of each cylindrical microlens is 500 μm, the width of each microlens is 250 μm, and the height of each microlens is 400 μm.

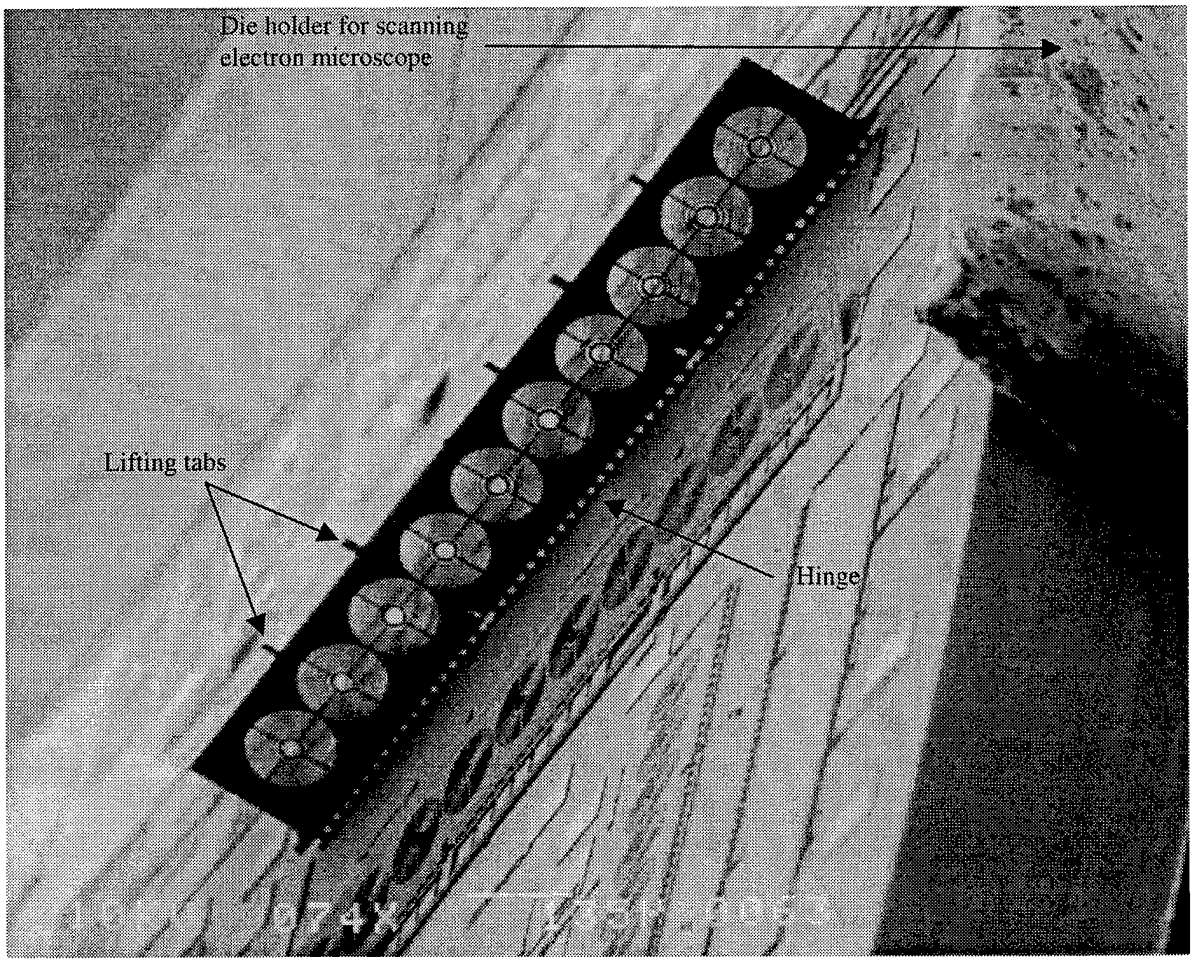

Figure 7.11. Micrograph of an array of ten 250 μm diameter Fresnel lenses. The dark shapes on the Fresnel lenses are objects on the other side of the array. The bottom edge of the die can be seen in the lower right of the micrograph (fabricated by the author in MUMPs 20).

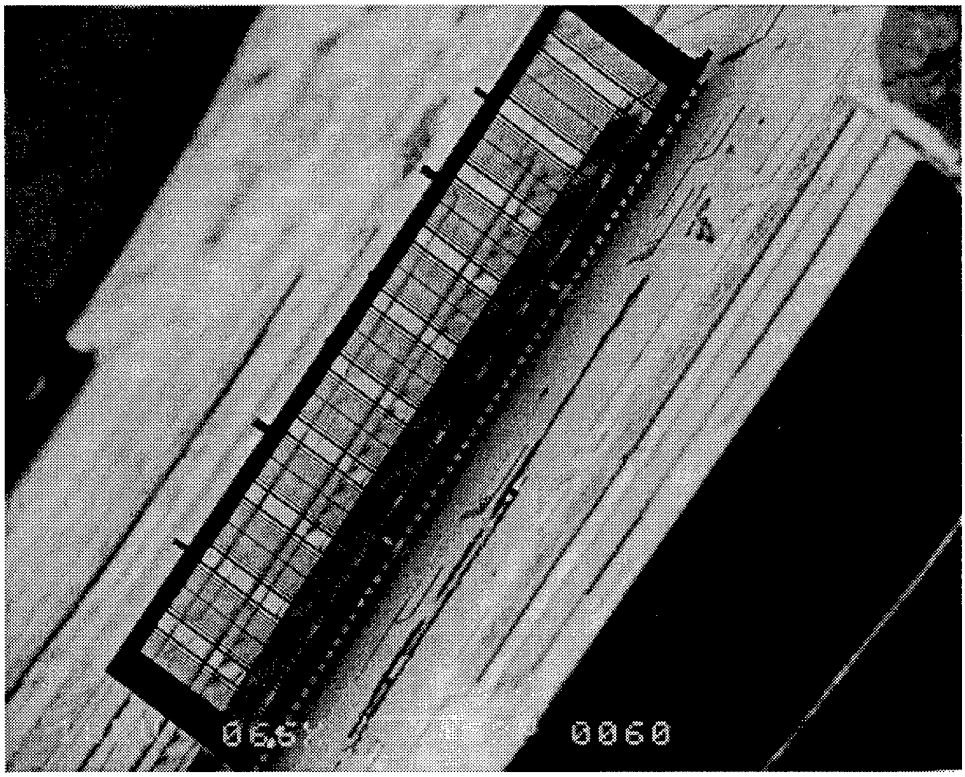

Figure 7.12. Scanning electron micrograph of a movable (left to right) array of cylindrical Fresnel microlenses (fabricated by the author in MUMPs 20).

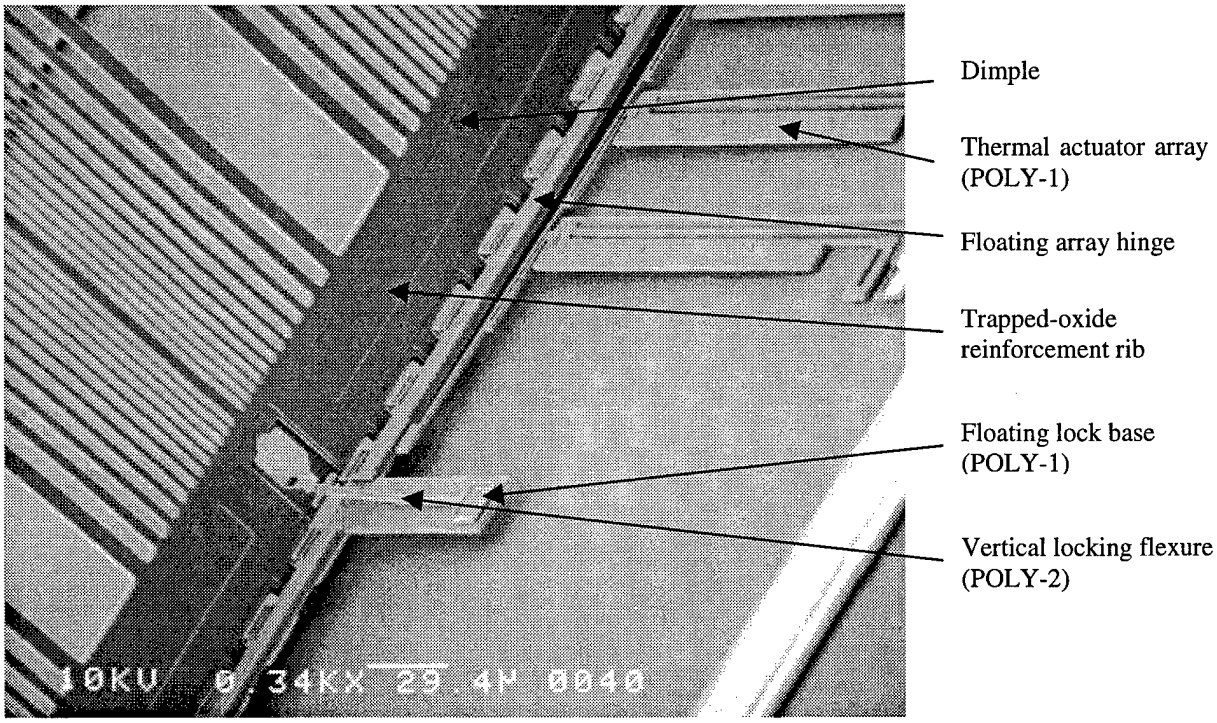

Figure 7.13. Close-up of the locking mechanism and connection to the thermal actuator array used in the cylindrical Fresnel microlens array. Note that this picture is on the other side of the array in Figure 7.12 (fabricated by the author in MUMPs 20).

7.3 Triple Microlens Beam Steering System

A triple microlens, single aperture beam steering system is shown in Figure 7.14. This system was designed to be used with polyurethane droplet lenses. The microlenses in Figure 7.14 were to be constructed with a diameter of 150 μm and a focal length of 500 μm. Only the microlens on the left (the drive microlens) was designed to move; the other two microlenses were fixed. Two arrays of thermal actuators were used to position the drive microlens. The tip of each thermal actuator moves in an arc around its flexure. By using two coupled arrays, the author was able to convert the arcing movement into a linear movement and avoid changing the separation distance between microlenses as the drive microlens was moved laterally.

Although the thermal actuators were able to move the drive microlens aperture over a range of 8 μm, the author was unable to construct polyurethane microlenses without damaging the polysilicon plates. If polyurethane microlenses with a focal length of 500 μm (equal to the separation distance between the polysilicon plates) were constructed in this system, the predicted beam steering range (full angle) would be 16.0 mrad (from Equation (4.17)). The author discontinued his research into triple microlens beam steering systems after experiencing difficulty with constructing polyurethane microlenses in vertical surface micromachined polysilicon plates.

Fresnel microlenses are not suitable for triple microlens beam steering systems because the light passing through the system is focused to its minimum waist size at the center microlens (refer to Figure 4.10 in Chapter 4); if a Fresnel microlens is used as the center microlens, only one or two zones will be illuminated. Other Fresnel zones will not be illuminated and the center microlens will be very inefficient at refocusing the light for the next stage. Also a zone blocking Fresnel lens passes only 50% of the incident light. For the best optical efficiency, decentered microlens beam steering systems should have as few Fresnel lens stages as possible. In Section 7.4, arrays of Fresnel microlenses were constructed in a double microlens system and successfully used to steer optical beams.

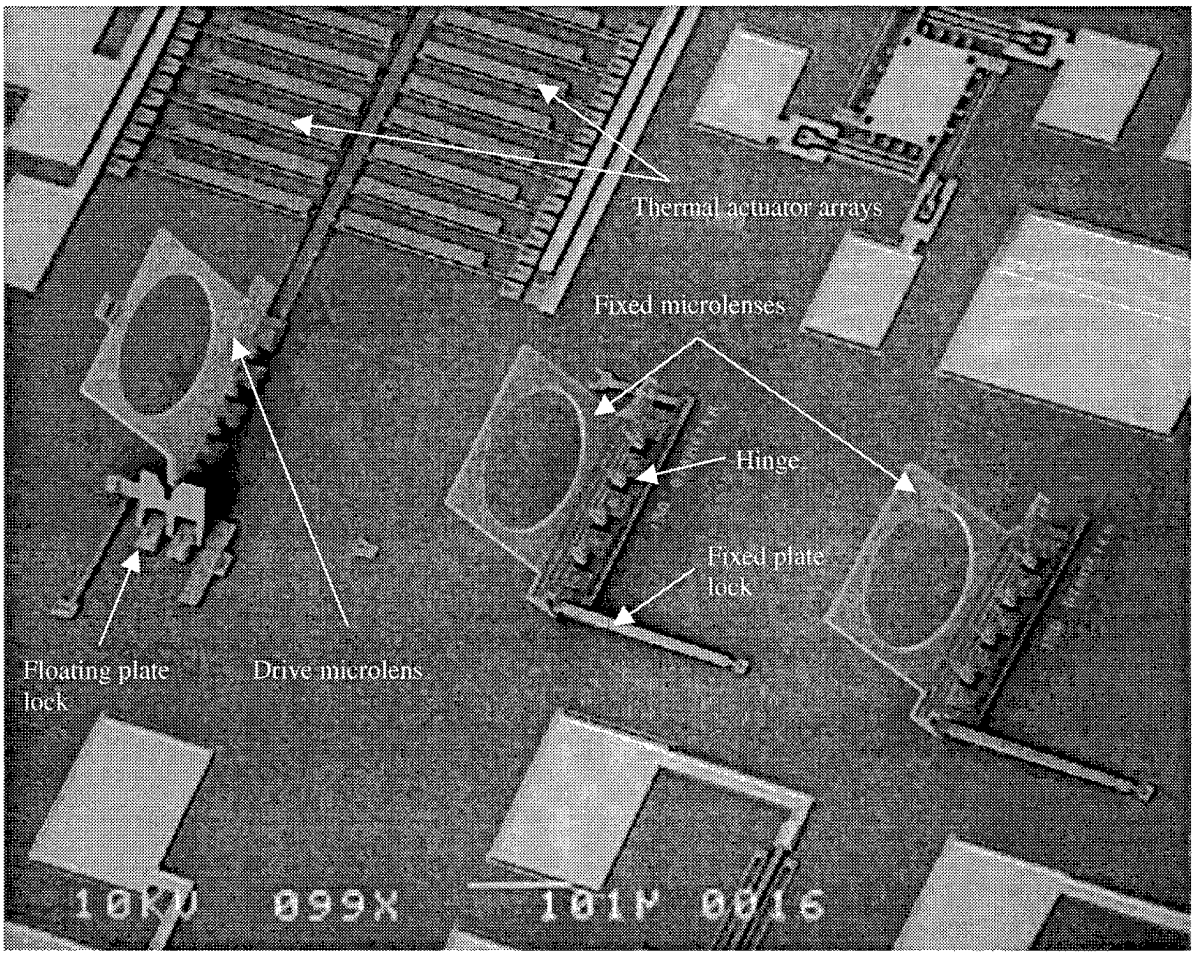

Figure 7.14. Scanning electron micrograph of a triple microlens, single aperture beam steering system (fabricated by the author in MUMPs 14).

7.4 Double Microlens Beam Steering System

The author constructed decentered microlens beam steering systems using the Fresnel microlens arrays shown in Figure 7.11 and Figure 7.12 and driven with both thermal actuators and SDAs. The most successful design was the Fresnel circular microlens array shown in Figure 7.11 coupled to four arrays of thermal actuators. Figure 7.15 is a schematic diagram of the complete system. The microlens arrays and the 45° mirror are all 2.7 mm long. The large length of the 45° mirror resulted in a divergence of the steered optical beam exiting the fixed microlens array (the trapped-oxide mirror was curved by residual material stress). The centers of the steered circular beams were 260 μm apart at the fixed array; the center to center separation distance

increased to 5 cm at a distance of 2 meters. The purpose of the 45° mirror was to reduce the size of the incident beam so that the only irradiance on a target in the far field of the system (to the right of Figure 7.15) is from the steered optical beams. The 45° mirror allowed the author to test the system with a collimated normally incident beam flooding the entire surface of the die; unfortunately this method of illuminating the die made it impossible to accurately measure the optical efficiency of this beam steering system. Based on the irradiance calculated for the surface of the 45° mirror, the author estimated the optical efficiency at 4% (the sum of the optical power in all of the steered beams equaled 4% of the optical power falling on the 45° mirror).

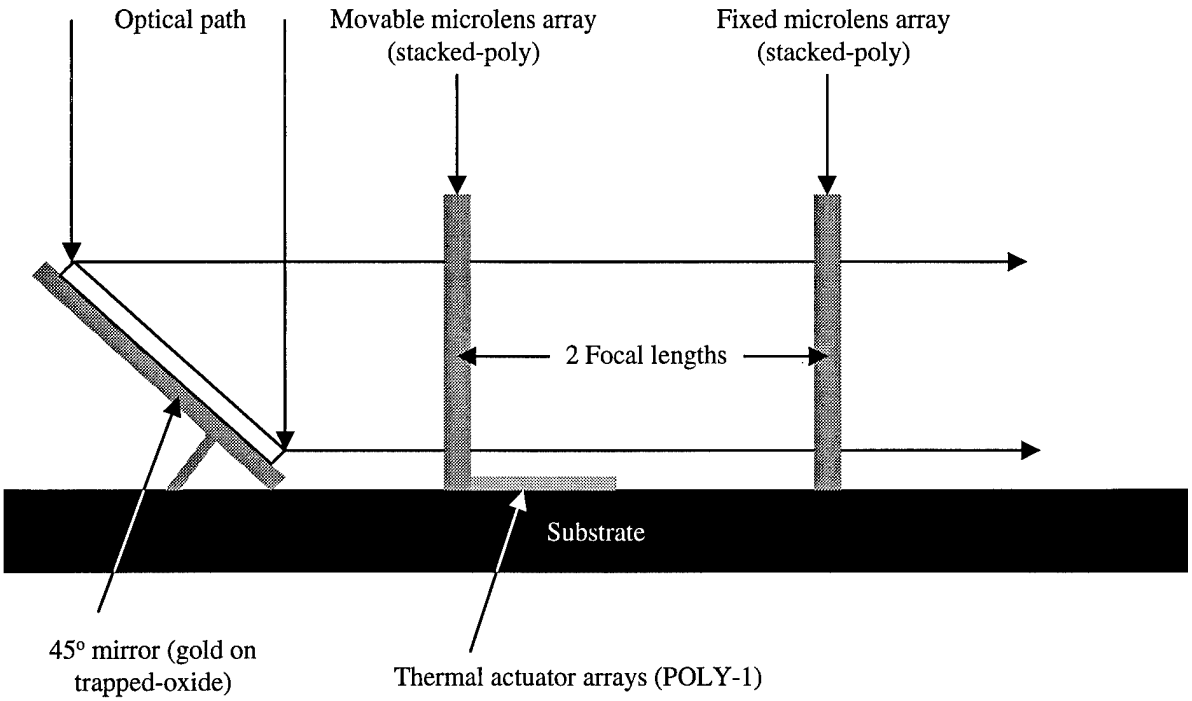

Figure 7.15. Cross-sectional schematic diagram of the decentered microlens array beam steering system designed by the author. The focal length of both microlens arrays is 500 μm. The system was illuminated by a perpendicular source; the steered beam was parallel to the substrate.

Figure 7.16 is a picture of the far field irradiance created by the decentered microlens array beam steering system depicted in Figure 7.15. The measured beam steering range for this device was 20 mrad; a predicted beam steering range of 20 mrad (using Equation (4.13)) requires a lateral displacement of 10 μm (well within the measured range of the author's lateral thermal actuators). The author used four thermal actuator arrays for a total of 32 thermal actuators; this provided more than enough motive force and required a maximum

of 600 mA at 9.1 V. The microlens array could have been driven with a quarter of this electrical power if the number of thermal actuators was reduced by a factor of four.

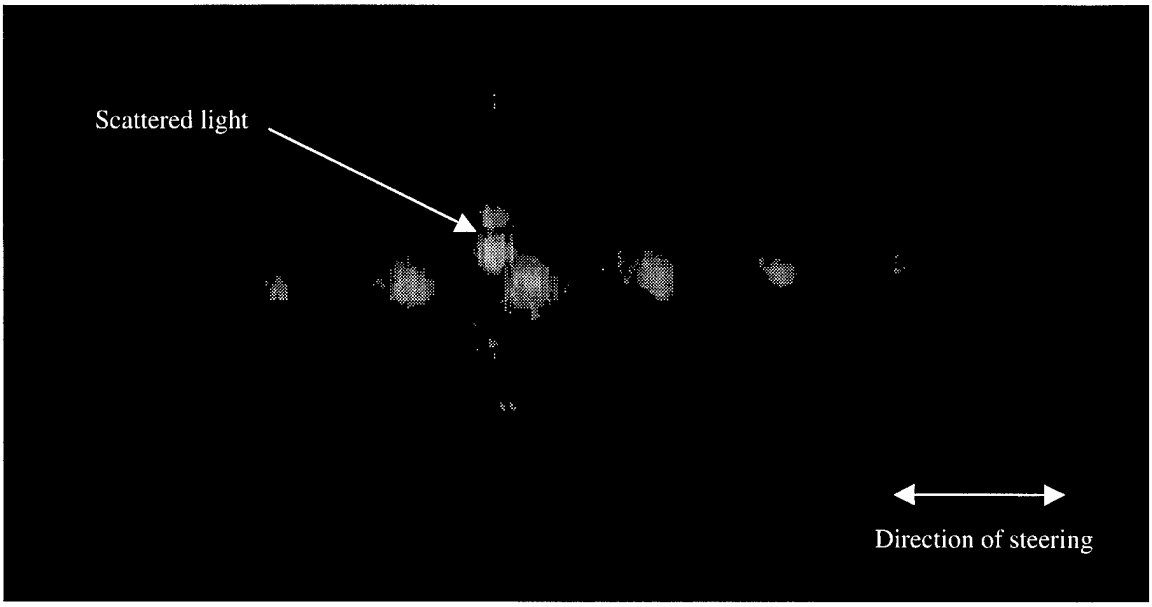

Figure 7.16. Far field picture of steered optical beams from the decentered microlens beam steering system described in Figure 7.15. The scattered light above the center most intense row of steered beams is reflected from another region of the die or chip carrier; this scattered light was fixed and did not move when the steered beams were driven over their full range. Circular Fresnel microlenses were used in this beam steering system.

Attempts to move microlens arrays coupled to SDAs were unsuccessful. Test devices may have failed due to the hinge design used to raise the microlens array. Because MUMPs has only two releasable layers (POLY-1 and POLY-2), a floating hinge such as the one in Figure 7.13 drags against the underlying layers (POLY-0 for microlens arrays driven by SDAs). The hinge also lifts up an edge of the actuator (visible in Figure 7.13). Thermal actuators can function if the active end is lifted up, but lifting one side of an SDAs reduces the efficiency of the actuator because it decreases the SDAs contact with the silicon nitride layer. Figure 7.17 and Figure 7.18 show pictures of a microlens array connected to SDAs.

Other possible causes of the failure of SDA driven microlenses include drive voltage risetime. The author was restricted by available power supplies to a 60 Hz sine wave (drive voltage often exceeded 100 V). Previously reported SDAs were driven at frequencies above 10 kHz. It is possible that the slow frequency used by the author allowed the SDA to slip backwards each cycle so that no net motion resulted.

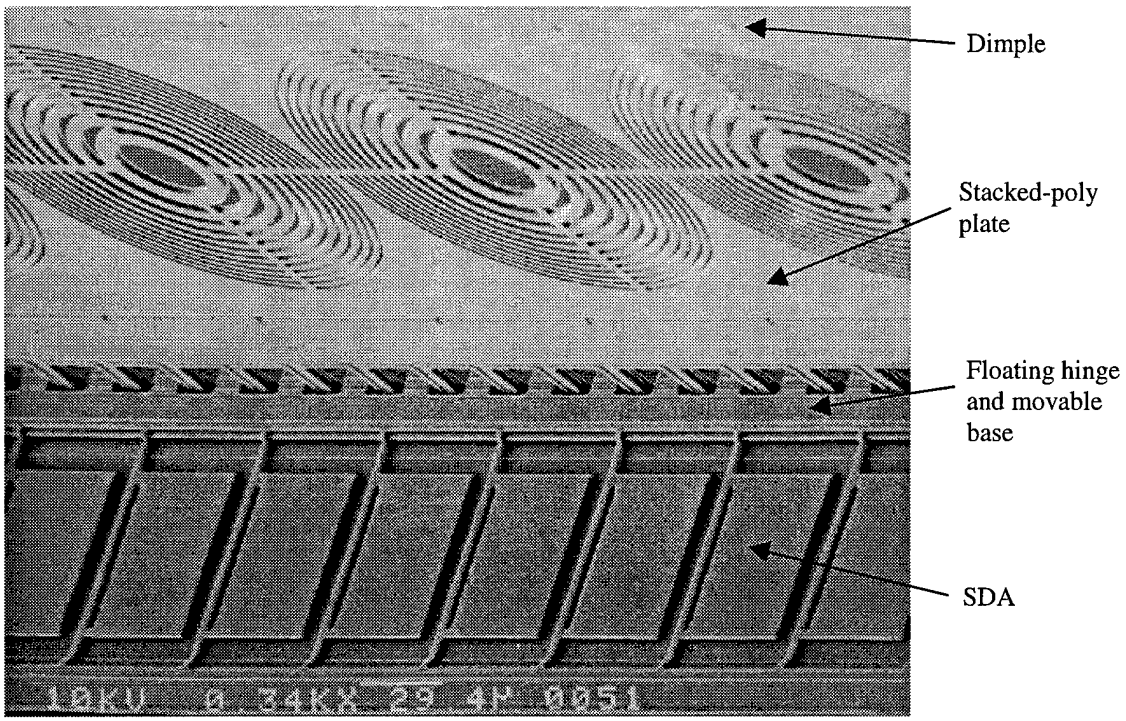

Figure 7.17. Scanning electron micrograph of a Fresnel microlens array coupled to SDAs (fabricated by the author in MUMPs 20).

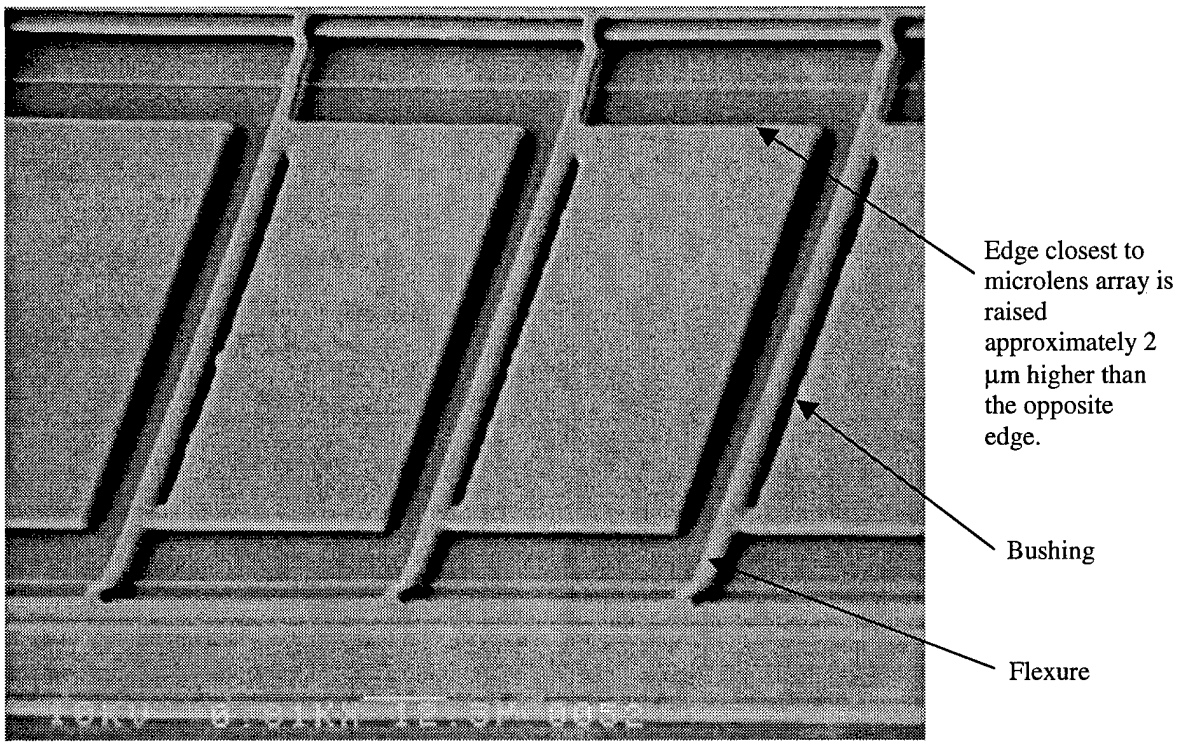

Figure 7.18. Close-up view of the SDAs in Figure 7.17 (fabricated by the author in MUMPs 20).

7.5 Summary

The author designed both triple microlens and double microlens beam steering systems. Triple polyurethane microlens systems could not be constructed without damaging the polysilicon plates and hinges. Triple Fresnel microlens systems were not practical because only a small region of the center Fresnel microlens would be illuminated. Double Fresnel microlens systems functioned well and the author was able to demonstrate a 20 mrad beam steering angle using a thermally actuated 10 microlens array. The author was able to construct oil-based polyurethane microlenses, however the fabrication of these microlenses may be better suited to a bulk or LIGA micromachining process.

7.6 References

[1] J. R. Reid, V. M. Bright, and J. H. Comtois, "Force measurements of polysilicon thermal micro-actuators," *Proc. SPIE*, vol. 2882, pp. 296-306, 1996.

[2] J. H. Comtois and V. M. Bright, "Surface micromachined polysilicon thermal actuator arrays and applications," *Technical Digest, Solid State Sensor and Actuator Workshop*, Hilton Head, SC, pp. 174-177, 1996.

[3] L. Y. Lin, J. L. Shen, S. S. Lee, G. D. Su, and M. C. Wu, "Microactuated micro-XYZ stages for free-space micro-optical bench," *Proc. IEEE Microelectromechanical Systems Workshop MEMS-97*, pp. 43-48, Nagoya, Japan, January 26, 1997.

[4] H. Zarschizky, Al Stemmer, F. Mayerhofer, G. Lefranc, and W. Gramann, "Binary and multilevel diffractive lenses with submicrometer feature sizes," *Optical Engineering*, vol. 33, no. 11, pp. 3527-3536, November 1994.

[5] M. Eisner and J. Schwider, "Transferring resist microlenses into silicon by reactive ion etching," *Optical Engineering*, vol. 35, no. 10, pp. 2979-2982, October 1996.

[6] M. B. Stern and T. R. Jay, "Dry etching for coherent refractive microlens arrays," *Optical Engineering*, vol. 33, no. 11, pp. 3547-3551, November 1994.

[7] M. T. Gale, M. Rossi, J. Pedersen, and H. Schutz, "Fabrication of continuous-relief micro-optical elements by direct laser writing in photoresists," *Optical Engineering*, vol. 33, no. 11, pp. 3556-3566, November 1994.

[8] T. R. Jay and M. B. Stern, "Preshaping photoresist for refractive microlens fabrication, *Optical Engineering*, vol. 33, no. 11, pp. 3552-3555, November 1994.

[9] D. Daly, R. F. Stevens, M. C. Hutley, and N. Davies, "The manufacture of microlenses by melting photoresist," *Measurement Science Technology (Journal)*, vol. 1, no. 4, pp. 759-766, April 1990.

[10] Z. D. Popovic, R. A. Sprague, and G. A. Neville-Connell, "Technique for monolithic fabrication of microlens arrays," *Applied Optics*, vol. 27, no. 7, pp. 1281-1284, April 1988.

[11] M. V. Klein and T. E. Furtak, *Optics 2nd Edition*, New York, NY: John Wiley & Sons, 1986.

[12] Private conversation with M.-H. Kiang of Berkeley, University of California, on June 5, 1996.

[13] C. R. King, L. Y. Lin, and M. C. Wu, "Monolithically integrated refractive microlens standing perpendicular to the substrate," *Proc. SPIE*, vol. 2687, pp. 123-130, 1996.

[14] D. E. Sene, "Design, fabrication, and characterization of micro opto-electro-mechanical systems," *Master's Thesis*, Air Force Institute of Technology, Wright-Patterson AFB, OH, AFIT/GEO/ENG/95D-03, December 1995.

[15] J. R. Reid, Jr., "Microelectromechanical isolation of acoustic wave resonators," *Doctorate Dissertation*, Air Force Institute of Technology, Wright-Patterson AFB, OH, AFIT/DS/ENG/96-12, December 1996.

[16] J. G. Bouchard, "Microelectromechanical scanner using a vertical cavity surface emitting laser," *Master's Thesis*, Air Force Institute of Technology, Wright-Patterson AFB, OH, AFIT/GCS/ENG/97D-04, December 1997.

[17] J. T. Butler, V. M. Bright, and W. D. Cowan, "SPICE modeling of polysilicon thermal actuators," *Proc. SPIE*, vol. 3224, pp. 284-293, Austin, TX, September 29-30, 1997.

[18] P. Lerch, C. K. Slimane, B. Romanowicz, and P. Renaud, "Modelization and characterization of asymmetrical thermal micro-actuators," *Journal of Micromechanics and Microengineering*, vol. 6, no. 1, pp. 134-137, 1996.

[19] J. R. Reid, V. M. Bright, and J. H. Comtois, "Arrays of thermal micro-actuators coupled to micro-optical components," *Proc. SPIE*, vol. 2865, pp. 74-82, 1996.

[20] J. H. Comtois, V. M. Bright, and M. W. Phipps, "Thermal microactuators for surface-micromachining processes," *Proc. SPIE*, vol. 2642, pp. 10-21, 1995.

[21] S.-S. Lee, E. Motamedi, and M. C. Wu, "G-performance characterization of surface-micromachined FDDI optical bypass switches," *Proc. SPIE*, vol. 3226, pp. 94-101, September 29, 1997.

[22] Private conversation with S. S. Lee of UCLA on September 30, 1997.

[23] S. Musikant, *Optical Materials: An Introduction to Selection and Application*, New York, NY: Marcel Dekker, Inc., 1985.

[24] M. Laikin, *Lens Design*, New York, NY: Marcel Dekker, Inc., 1991.

[25] Lot number: 73W5460, Product number: 96389 (Gloss), The Valspar Corporation, Wheeling, IL 60090.

[26] Lot number: 783906361, Product number: 930 (Gloss), Enterprise Paint Co. (a division of the Valspar Corporation), Wheeling, IL 60090.

[27] Lot number: W017975-04832, Product description: Clear gloss, Minwax Co., Upper Saddle River, NJ 07458

[28] Lot number: 68R5402, Product number: 48329 (Gloss), The Valspar Corporation, Wheeling, IL 60090.

[29] Lot number: W028304-00817, Product description: Clear gloss, Minwax Co., Upper Saddle River, NJ 07458

[30] D. E. Sene, "Design, fabrication, and characterization of micro opto-electro-mechanical systems," *Master's Defense*, Air Force Institute of Technology, Wright-Patterson AFB, OH, AFIT/GEO/ENG/95D-03, December 1995.

8 Optical Power Induced Damage to Micromirrors

This chapter presents results of the author's investigation into optical power induced damage to surface-micromachined mirrors. A mathematical model was developed and used to predict the minimum incident optical power that would permanently damage the reflective surface of a micromirror. The model was based upon a heat flow analysis of a micro-electro-mechanical device in thermal equilibrium under continuous direct illumination and was validated using a variety of micromirror designs with both thermal simulation and direct laser illumination. This chapter is organized into five sections. Section 8.1 introduces a typical electrostatically-actuated micromirror design. Section 8.2 presents the underlying theory and develops the micromirror thermal model. Section 8.3 describes the thermal testing used to obtain device failure temperature thresholds for the thermal model. Section 8.4 details the optical power testing set-up used to validate the thermal model and compares optical power test results with predicted values. Section 8.5 summarizes the investigation.

8.1 Introduction

Applications of surface-micromachined mirrors range from full color video projection systems [1] to wavefront correction for improving telescope imagery [2]. The micromirrors are often electrostatically-actuated, requiring virtually zero power. Micromirrors are a perfect fit for many systems because of their high optical efficiency and small pixel size. Also a micromirror's low mass and small deflection distance results in a fast response time. Figure 8.1 depicts a surface-micromachined micromirror that can be tilted and pistoned. The micromirror in Figure 8.1 is a slight modification of an earlier micromirror design by Comtois [2]. Figure 8.2 is a diagram of the micromirror in Figure 8.1 after a portion of the top surface was removed. The micromirror can be tilted simultaneously on two axis by grounding the top electrode and placing a voltage on one or more of the bottom electrodes. Single micromirrors can be tilted to steer an incident beam. Elements in micromirror arrays are tilted to modulate the amplitude of the light diffracted into a specific direction. If the same voltage is placed on all the bottom electrodes, then the micromirror will be pistoned down, lengthening

the optical path of light reflected off the micromirror. Pistoning is used for phase modulation in coherent systems.

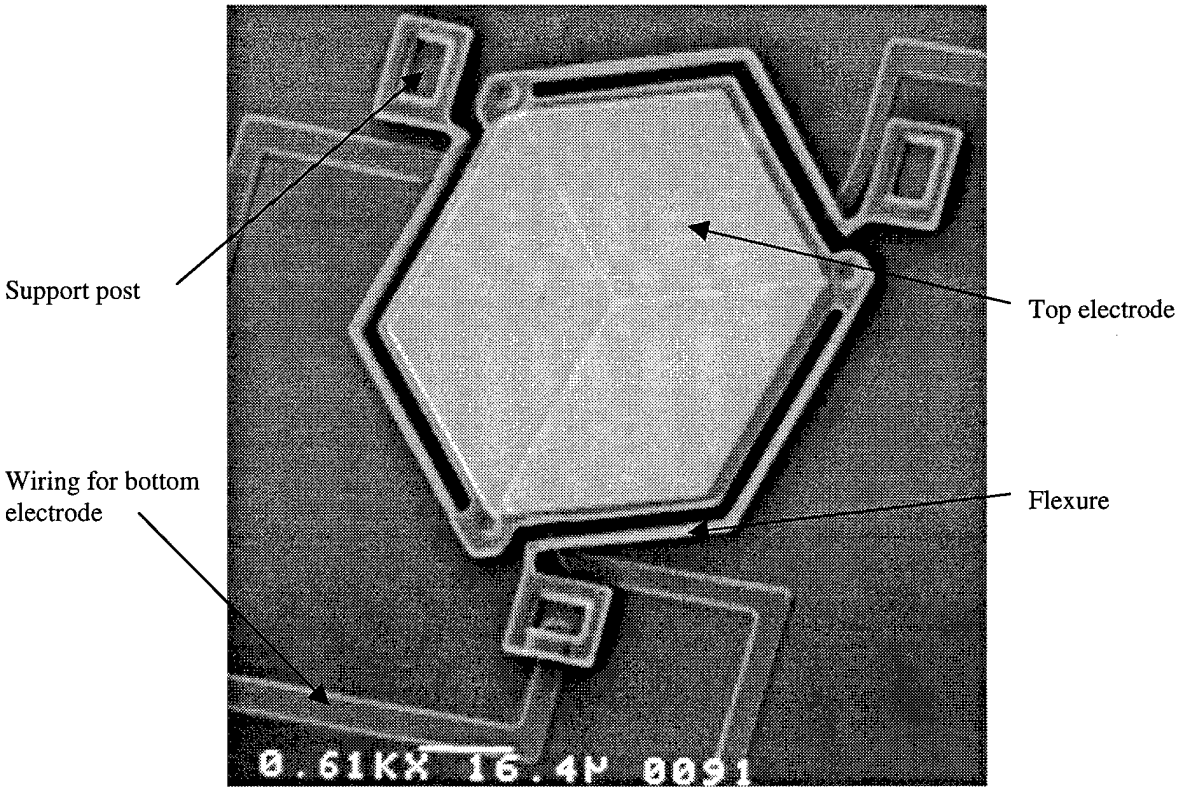

Figure 8.1. Baseline micromirror for thermal and optical power evaluation. Note the unintentional embossing of the top electrode caused by the underlying three bottom POLY-0 electrodes (fabricated by the author in MUMPs 13).

Many applications of micro-electro-mechanical systems require optical power levels that are large in comparison to the size of the micro-optical structures [3,4]. High optical power levels can ablate micromirror surfaces and melt supporting flexures. Lower optical power levels can distort reflective surfaces and reduce the optical efficiency of the system. This chapter presents a thermal model that can be used to predict when optical power induced damage will occur. The model is a function of the device's construction materials and geometry, and has been validated with a variety of surface-micromachined micromirrors under continuous direct laser illumination.

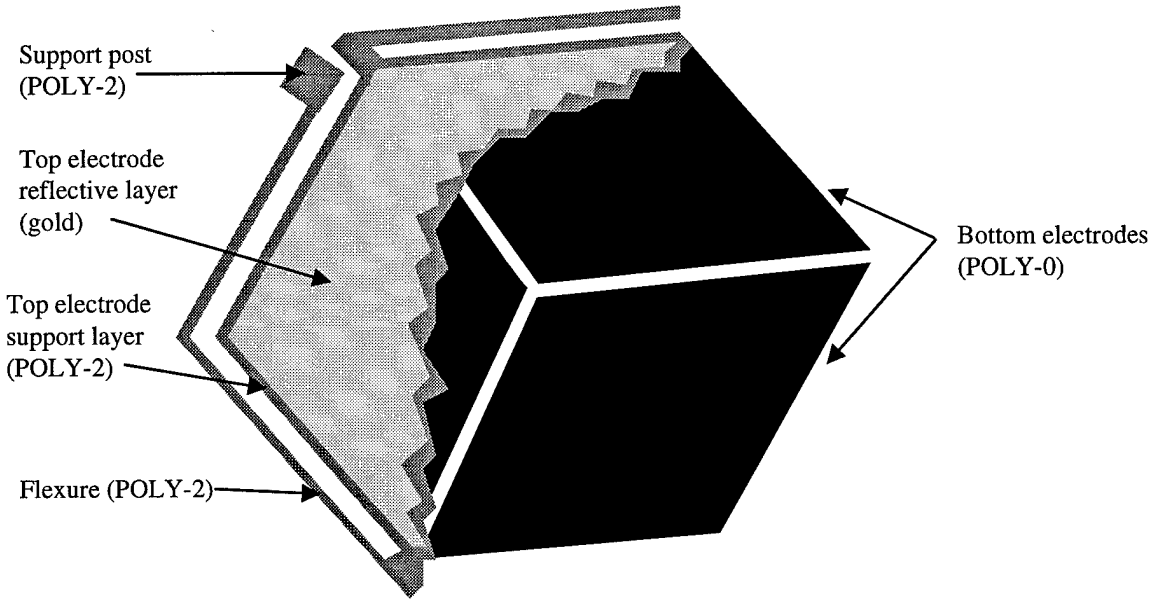

Figure 8.2. Diagram of the micromirror in Figure 8.1 after a portion of the top electrode was removed to show the underlying bottom electrodes.

Micromirrors used to validate the model were fabricated through the 13th MUMPs production run. A top layer of gold was used as the reflective surface for each micromirror. The reflectivities and layer thickness for each of the films used in MUMPs are listed in Appendix A. The reflectivities were measured by the author using the VBG test set-up, a 20 mW HeNe laser, and the Newport optical power meter (all described in Appendix C). The micromirror in Figure 8.1 consists of a top electrode formed out of POLY-2 and gold suspended 2.75 μm (the thickness of the two sacrificial oxide layers) above three bottom POLY-0 electrodes.

8.2 Theory

All modeling and optical power testing in this chapter was based on the assumption that the micromirror is in thermal equilibrium; only continuous time-invariant illumination on a stationary micromirror is considered. A stationary micromirror implies that the only source of thermal energy is the illuminating source. When a micromirror is in thermal equilibrium, the thermal power absorbed from an illuminating source, P_a, is equal to the thermal power directly dissipated by the top electrode, P_t, and conducted out of the top electrode through each of the flexures, P_f, as shown in Equation (8.1):

$$P_a = P_t + NP_f \tag{8.1}$$

where N is the number of flexures used to support the top electrode.

Because the micromirror is in thermal equilibrium, temperature is a function of position on the micromirror and is not time dependent. Primary thermal dissipation mechanisms are radiation, conduction to the surrounding gas, and conduction through the support flexures to the substrate. Micromirrors are usually hermetically sealed in chip carriers to prevent dust and moisture contamination. External forced gas convection is typically not practical. Free convection can be neglected due to the small scale of the micromirrors [5].

8.2.1 Absorbed power

If only the gold region of the micromirror in Figure 8.1 is illuminated, the absorbed optical power is proportional to the incident power. Equation (8.2) calculates the absorbed power, P_a, as a function of the incident power, P, and the reflectivity of gold, $R_g(\lambda)$.

$$P_a = \left[1 - R_g(\lambda)\right] P \tag{8.2}$$

Reflectivity is a function of the wavelength of the source, λ. All unreflected power is absorbed by the gold and underlying polysilicon layers.

8.2.2 Power dissipated by top electrode

The thermal conductivity of gold is excellent (κ = 317 W/m-K at 300°K [6]) and the polysilicon structural layer in the top electrode is thin, so temperature variances across the top electrode are negligible. Thermal dissipation mechanisms for the top electrode are radiation and conduction through the surrounding gas to the substrate. Thermal power dissipated by radiation, P_{tb}, is given by Equation (8.3), where ε_p and ε_g are the emissivities of polysilicon and gold, respectively, S_p is the surface area of the polysilicon, S_g is the surface area of the gold, and σ is Boltzmann's constant [7].

$$P_{tb} = (\varepsilon_p S_p + \varepsilon_g S_g)\sigma (T_d^4 - T_s^4) \tag{8.3}$$

T_d is the temperature of the top electrode. T_s is the temperature of the substrate, the bottom electrodes, and the micromirror package, including external lenses (if any).

Thermal conduction through the surrounding gas is dependent both on the composition and pressure of the gas. Equation (8.4) calculates the thermal power dissipated by the top electrode through the surrounding gas to the bottom electrodes and substrate, P_{tc} [5,8]:

$$P_{tc} = S_t \frac{\kappa_g \rho}{h \rho_0} (T_d - T_s) \tag{8.4}$$

where S_t is the surface area of the top electrode normal to the substrate, κ_g is the thermal conductivity of the surrounding gas at a reference pressure ρ_0, h is the top electrode's height above the bottom electrode, and ρ is the pressure of the surrounding gas. Thermal conduction of the top and sides of the top electrode through the surrounding gas to the micromirror package also dissipates energy; however the separation distance between the top and bottom electrodes (h=2.75 μm for the micromirror in Figure 8.1) is much less than the distance between the top electrode and the micromirror package (typically > 1 mm for micro-optical device packaging). Thermal conduction through the surrounding gas to the micromirror package is more than 2 orders of magnitude less than the value predicted by Equation (8.4), so it can be neglected with only a minimal impact on the model's accuracy. Equation (8.4) is valid only for microstructures at low pressure or when $\rho = \rho_0$; for a discussion of thermal conduction through gas at intermediate or high pressures, see [5,8].

8.2.3 Power dissipated through flexures

Flexure temperature varies as a function of position, so Equations (8.3) and (8.4) can not be directly applied to calculate the thermal power dissipated by each flexure. In addition to radiation and conduction through the surrounding gas, flexures also directly conduct thermal power to the substrate. Figure 8.3 is a cross-sectional schematic diagram of a flexure. The total length of the flexure is L and the distance from the top electrode to the differential volume shown in the inset to Figure 8.3 is x. The thermal energy conducted into the differential volume is q_{in} and the thermal energy conducted out of the differential volume is q_{out}. The thermal energy radiated out of the exposed surface area of the differential volume is q_{rad} and the thermal energy conducted out of the differential volume to the surrounding gas is q_{gas}. The temperature of the differential volume is T.

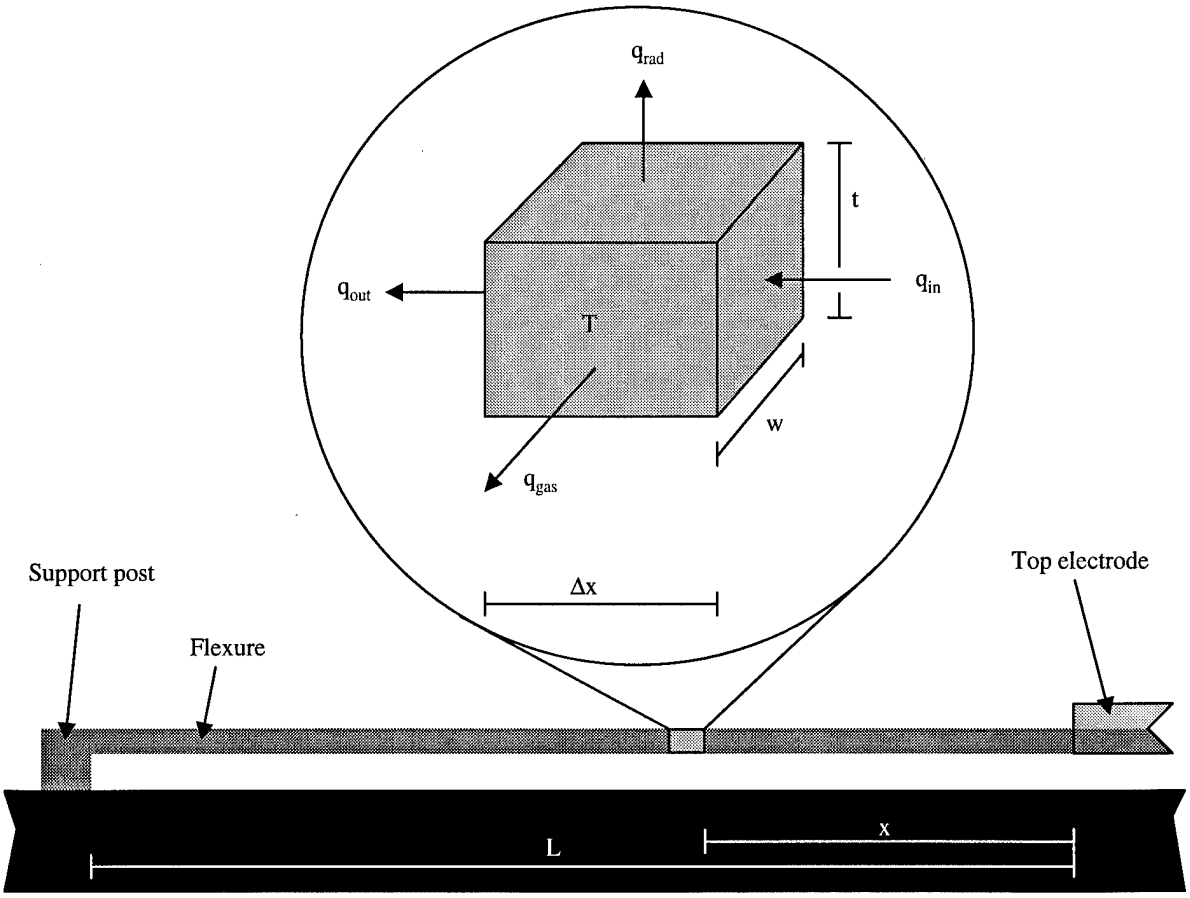

Figure 8.3. A cross-sectional schematic diagram of power dissipation mechanisms for a micromirror flexure.

Under the condition of thermal equilibrium in the flexure depicted in Figure 8.3:

$$q_{in} = q_{out} + q_{rad} + q_{gas} \tag{8.5}$$

Thermal energy conducted across an infinitesimally thin slice of the flexure is given by Equation (8.6) [9]:

$$q = -\kappa_p A_p \frac{dT}{dx} \tag{8.6}$$

where A_p is the cross-sectional area of the flexure (assumed to be constant along the length of the flexure), κ_p is the thermal conductivity of the polysilicon, and dT/dx is the change in temperature across the thickness of the slice. The energies conducted in and out of the differential volume can be calculated by evaluating Equation (8.6) at the boundaries of the differential volume shown in Figure 8.3, and are given by Equation (8.7) and Equation (8.8), respectively:

$$q_{in} = q\big|_x = -\kappa_p A_p \left.\frac{dT}{dx}\right|_x \tag{8.7}$$

$$q_{out} = q\big|_{x+\Delta x} = -\kappa_p A_p \left.\frac{dT}{dx}\right|_{x+\Delta x} \tag{8.8}$$

Thermal energy radiated out of the differential volume is given by Equation (8.9):

$$q_{rad} = 2\varepsilon_p \Delta x (w + t)\sigma (T^4 - T_s^4) \tag{8.9}$$

where w is the width of the flexure and t is the thickness of the flexure. Equation (8.9) can be derived from Equation (8.3) by replacing S_p with $2\,(w+t)\Delta x$ (the exposed surface area of the differential volume), eliminating S_g, and replacing the temperature of the top electrode T_d with the temperature of the differential volume T. Equation (8.10) calculates the energy conducted from the bottom side of the flexure through the surrounding gas to the substrate. Equation (8.10) results from applying Equation (8.4) to the geometry of the differential volume in Figure 8.3:

$$q_{gas} = w\Delta x(T - T_s)\frac{\kappa_g \rho}{h\rho_0} \tag{8.10}$$

Equation (8.10) is an approximation based on a straight flexure; micromirrors are often supported by curved or folded flexures. Examples of micromirrors with curved and folded flexures are shown in Figures 8.4 and 8.5, respectively. The micromirror in Figure 8.5 is a derivative of an earlier design by Comtois [2]. The micromirror flexures depicted in Figures 8.4 and 8.5 conduct energy through the surrounding gas back to different regions in the same flexure. The net energy conducted out of the folded or curved flexures is marginally higher than the energy calculated by Equation (8.9) and may be neglected provided $\kappa_g << \kappa_p$.

Substituting Equations (8.7) through (8.10) into Equation (8.5) and dividing by Δx yields Equation (8.11):

$$\frac{\kappa_p A_p}{\Delta x}\left(\left.\frac{dT}{dx}\right|_{x+\Delta x} - \left.\frac{dT}{dx}\right|_x\right) = 2\varepsilon_p (w+t)\sigma(T^4 - T_s^4) + w(T - T_s)\frac{\kappa_g \rho}{h\rho_0} \tag{8.11}$$

If we define $\Psi(x) = dT/dx$, Equation (8.11) can be simplified to:

$$\frac{\Psi(x+\Delta x) - \Psi(x)}{\Delta x} = \frac{2\varepsilon_p (w+t)\sigma(T^4 - T_s^4)}{\kappa_p A_p} + \frac{w(T - T_s)\kappa_g \rho}{\kappa_p A_p h\rho_0} \tag{8.12}$$

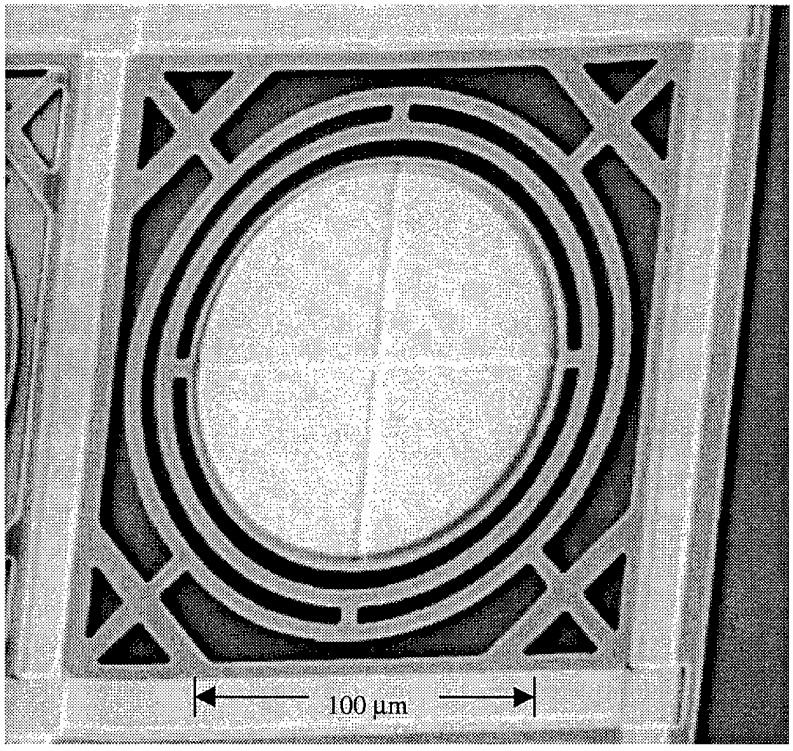

Figure 8.4. A round micromirror with curved flexures (fabricated by the author in MUMPs 13).

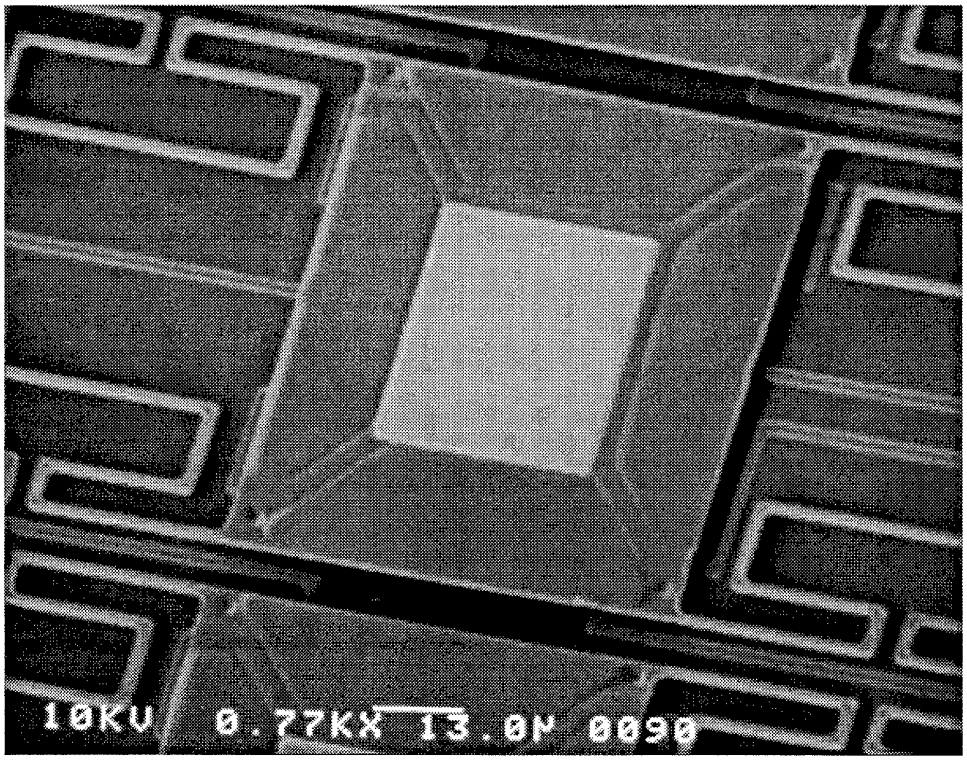

Figure 8.5. A square micromirror with folded flexures (fabricated by the author in MUMPs 13).

Taking the limit of Equation (8.12) as $\Delta x \rightarrow 0$ yields Equation (8.13):

$$\frac{d\Psi(x)}{dx} = \frac{2\varepsilon_p (w+t)\sigma(T^4 - T_s^4)}{\kappa_p A_p} + \frac{w(T - T_s)\kappa_g \rho}{\kappa_p A_p h \rho_0} \tag{8.13}$$

After substituting $\Psi(x) = dT/dx$, Equation (8.13) becomes:

$$\frac{d^2T}{dx^2} - \frac{2\varepsilon_p (w+t)\sigma(T^4 - T_s^4)}{\kappa_p A_p} - \frac{w(T - T_s)\kappa_g \rho}{\kappa_p A_p h \rho_0} = 0 \tag{8.14}$$

Equation (8.14) can not be directly solved by analytic techniques; it must be numerically solved using computational methods. The boundary conditions for Equation (8.14) are given by Equations (8.15) and (8.16); these boundary conditions are required to join the flexure to the top electrode and substrate, respectively.

$$T\big|_{x=0} = T_d \quad \textit{at the edge of the top electrode} \tag{8.15}$$

$$T\big|_{x=L} = T_s \quad \textit{at the support post} \tag{8.16}$$

Temperature decreases as the location of the differential volume moves from the edge of the top electrode towards the support post; thermal radiation is a strong (4^{th} order) function of temperature so the amount of energy dissipated by thermal radiation quickly diminishes. Equation (8.14) can be simplified by noting that the surface areas of the top electrode of the micromirrors in Figures 8.1, 8.4, and 8.5 are much larger than the surface areas of the flexures; the amount of energy dissipated by thermal radiation out of the flexures is small compared to the thermal energy radiated out of the top electrode. Equation (8.17) results from neglecting the thermal radiation term in Equation (8.14) and substituting the product of the flexure width (w) and thickness (t) for the flexure cross-sectional area (A_p):

$$\frac{d^2T}{dx^2} - \frac{\kappa_g \rho}{\kappa_p th\ \rho_0}(T - T_s) = 0 \tag{8.17}$$

Equation (8.17) is a second order differential equation and can be solved using classical techniques. Using substitution of variables ($\theta(x) = T(x) - T_s$) and the boundary conditions given in Equations (8.15) and (8.16), the solution to Equation (8.17) is:

$$\theta(x) = (T_d - T_s)\frac{\sinh[n(L-x)]}{\sinh(nL)} \tag{8.18}$$

where n is given by:

$$n = \sqrt{\frac{\kappa_g \rho}{\kappa_p th\ \rho_0}} \tag{8.19}$$

An expression for temperature as a function of position on the flexure can be derived by substituting ($T(x)$ = $\theta(x) + T_s$) back into Equation (8.18):

$$T(x) = (T_d - T_s)\frac{\sinh[n(L-x)]}{\sinh(nL)} + T_s \tag{8.20}$$

If Equation (8.20) is substituted back into Equation (8.6) and the result is evaluated at x=0, then the thermal power flowing into the flexure from the top electrode can be calculated:

$$P_f = n\kappa_p wt(T_d - T_s)\coth(nL) \tag{8.21}$$

Equation (8.21) can be used to determine the amount of thermal power dissipated by each of the flexures when the micromirror is in thermal equilibrium.

8.2.4 Thermal model

By substituting Equations (8.2), (8.3), (8.4), and (8.21) into Equation (8.1), a relationship between incident power, P, and the temperature of the top electrode, T_d, can be found:

$$P = \frac{(\varepsilon_p S_p + \varepsilon_g S_g)\sigma(T_d^4 - T_s^4) + (T_d - T_s)\left(\frac{S_t \kappa_g \rho}{h\rho_0} + Nwtn\kappa_p \coth(nL)\right)}{1 - R_g(\lambda)} \tag{8.22}$$

Under direct illumination, the highest temperature in the micromirror is the temperature of the top electrode. If device failure occurs when the temperature of the top electrode, T_d, exceeds a threshold value, then Equation (8.22) can be used to calculate the incident optical power that will raise the temperature of the device to this threshold temperature. The device failure threshold temperature is a function of the construction materials used to fabricate the mirror and is independent of device geometry. The device failure threshold temperature can be empirically determined by baking a representative device for an extended period of time in an oven. After the device failure threshold temperature is known, the predicted optical power required to damage a device is a sole function of the device's geometry.

8.3 Thermal Testing

The micromirrors shown in Figures 8.1, 8.4, and 8.5 were baked in nitrogen (to avoid oxide formation) at temperatures ranging from 200°C to 700°C for one hour. The electronic oven used for thermal testing is described in Appendix C. All devices baked at temperatures of 250°C or more had visible damage to the gold reflective region. Figures 8.6 and 8.7 show the effects of baking micromirrors for one hour in nitrogen at one atmosphere of pressure. Initial mirror reflectivity at a laser wavelength of 632.8 nm was measured as 91.5%.

Baking devices at 225°C or lower temperatures resulted in no apparent damage (or significant loss of reflectivity). After baking devices at 250°C for one hour, mirror reflectivity at 632.8 nm dropped to 67.9%. Micromirror reflectivity continued to decrease when the device temperature was increased to 300°C. Micromirror reflectivity actually improved when the micromirror's temperature was increased above 300°C (see Figures 8.6(d) and 8.7(a)). However close examination of micromirrors baked at temperatures above 325°C indicated that the gold layer was no longer planar; large areas of the gold layer delaminated enough to cause significant phase distortion in the reflected light. Micromirror reflectivity after thermal stress is a function of small fluctuations in the fabrication process and it varied to some degree on each of the MUMPs fabrication runs; for example, MUMPs 15 die could withstand 275°C with no significant loss of reflectivity.

The thermal damage was likely due to a widening of the eutectic bond under the gold layer, release of the phosphorous (which boils at 280°C) in the polysilicon under the gold, or a combination of these effects. The thermal damage visually appeared as a discoloration and a loss of planarity (appearance of small bumps) in the gold layer. Polysilicon and silicon nitride layers suffered no visible damage. Figure 8.8 is a close-up view of a damaged gold layer resulting from baking a micromirror at 300°C for one hour. Two types of damage are visible in Figure 8.8; in addition to the many approximately 500 nm wide pits is a broad swath of discoloration. The author noted no reduction in residual material stress induced curvature after baking the micromirrors at temperatures up to 700°C for one hour.

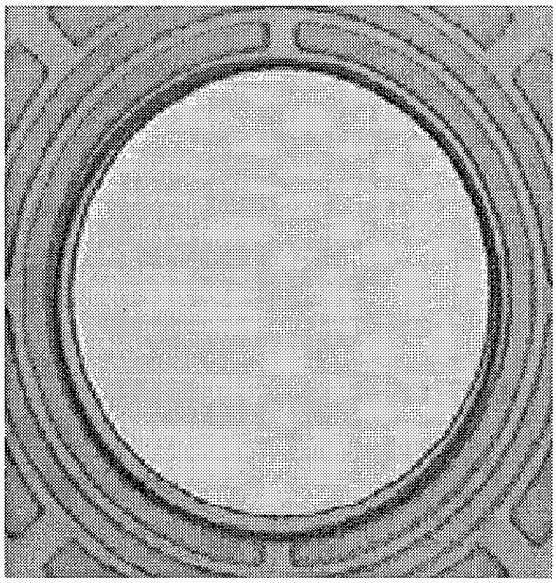

(a) 225°C

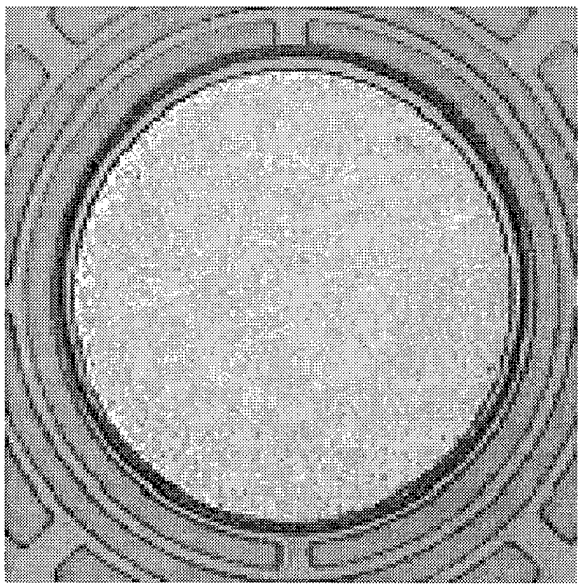

(b) 250°C

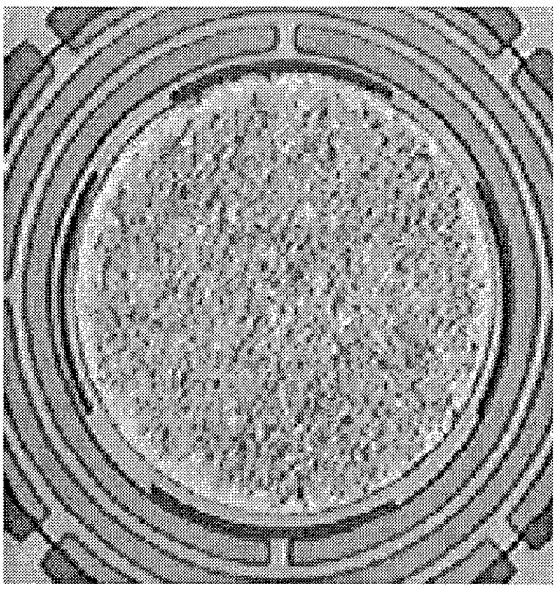

(c) 300°C

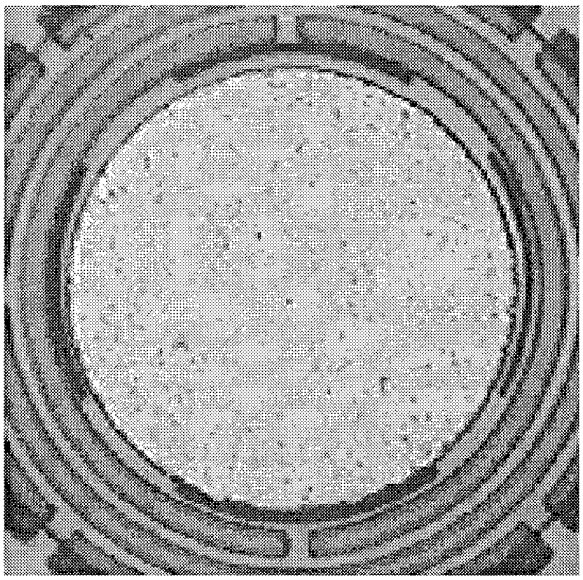

(d) 340°C

Figure 8.6. Effects of thermal stress on micromirrors baked for one hour in nitrogen at one atmosphere (fabricated by the author in MUMPs 13).

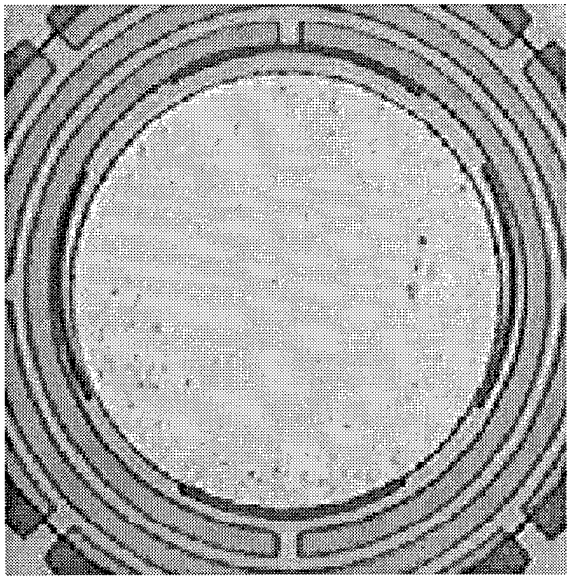

(a) 360°C

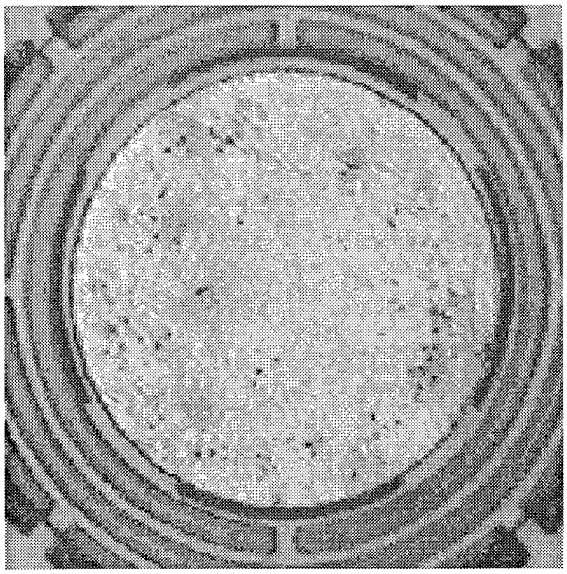

(b) 400°C

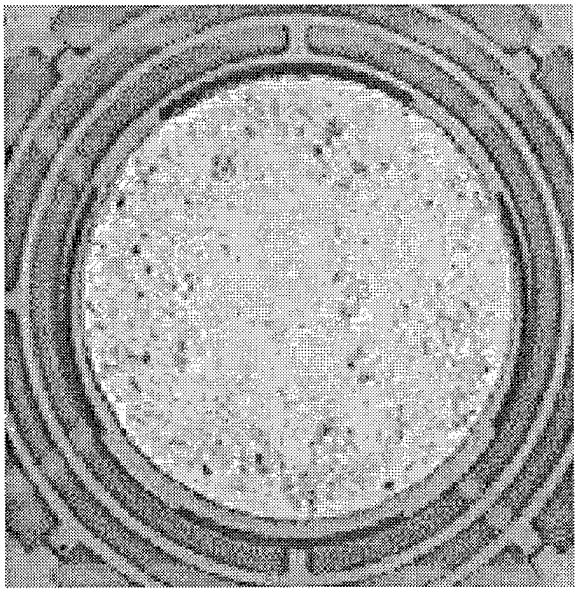

(c) 500°C

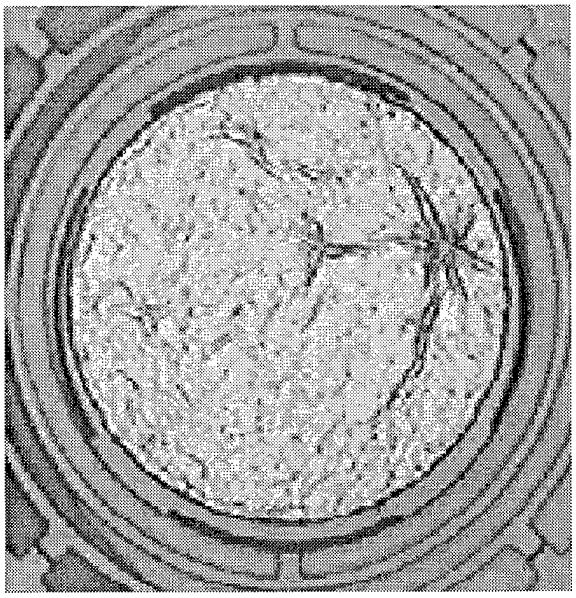

(d) 700°C

Figure 8.7. Effects of thermal stress on micromirrors baked for one hour in nitrogen at one atmosphere (fabricated by the author in MUMPs 13).

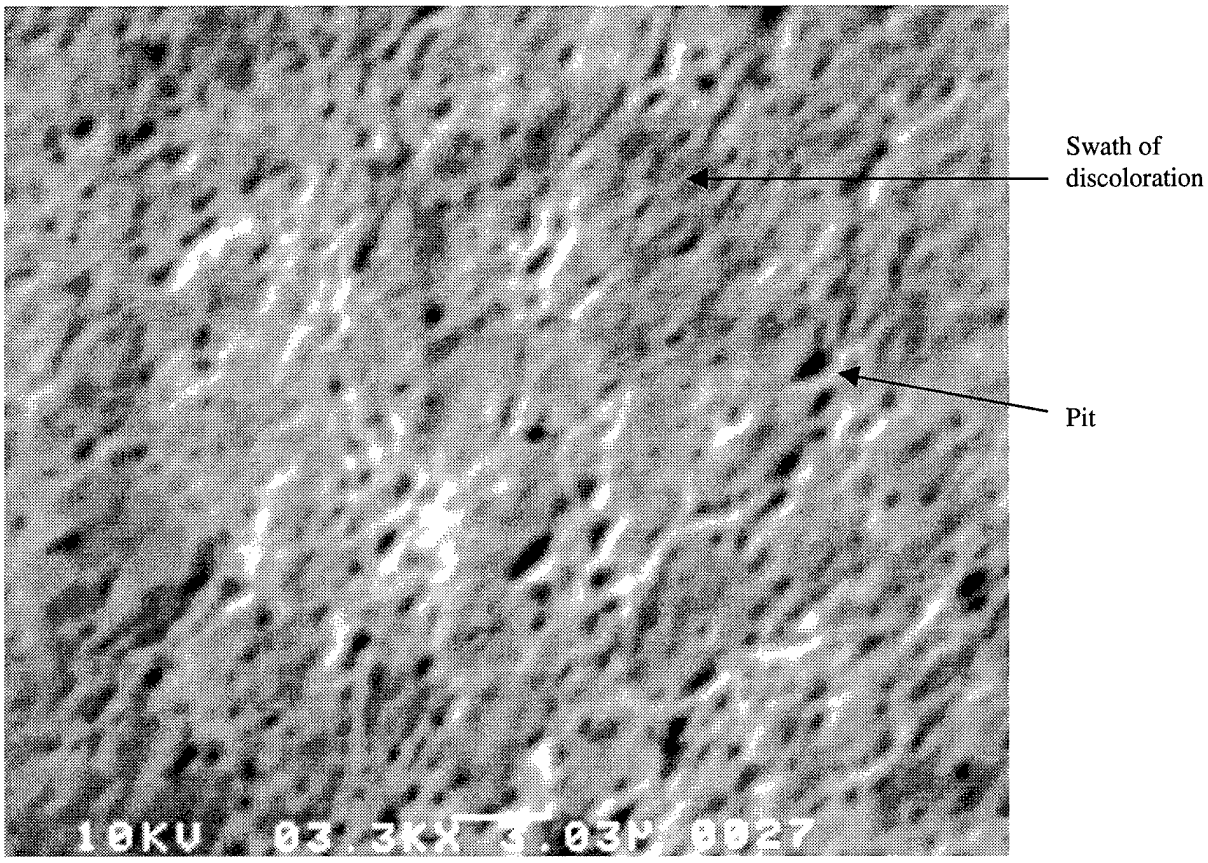

Figure 8.8. Scanning electron micrograph of the damage caused to a micromirror by baking the micromirror at 300°C for one hour (fabricated by the author in MUMPs 13).

8.4 Optical Power Testing

The optical power testing section contains four subsections: optical power predictions, optical power test results, power dissipation mechanisms, and surrounding gas calculations.

8.4.1 Optical Power Predictions

Using a device failure threshold temperature of 250°C, the amount of optical power required to damage the reflective layer was calculated for each of the micromirrors shown in Figures 8.1, 8.4, and 8.5 using Equation (8.22). Table 8.1 lists the device geometry independent variables used in Equation (8.22). The temperature of the top electrode, T_d, was set equal to the device failure threshold temperature. The reflectivity of the MUMPs gold layer was measured in air at room temperature and is in good agreement with the

reflectivity of bulk gold [10]. Table 8.2 lists device specific data and the predicted optical power required to damage each of the micromirrors.

Table 8.1. Device Independent Variables for Calculating the Optical Power Rating.

Boltzmann's Constant (σ) W/m^2K^4 [9]	5.67×10^{-8}
Maximum Allowable Device Temperature (T_d) °K	498
Temperature of Substrate and Surrounding Environment (T_s) °K	295
Measured Reflectance of Gold at 632.8 nm (R_g) %	91.5
Estimated Emissivity of Polysilicon (ε_p) % [5]	20
Emissivity of Gold (ε_g) % [9]	3
Thermal Conductivity of Phosphorus-doped Polysilicon (κ_p) W/m-K [11]	29
Thermal Conductivity of Nitrogen at 295°K (κ_g) W/m-K Interpolated From [6]	0.0258
Pressure in Test Chamber (ρ) Torr	0.020
Reference pressure (ρ_0) Torr (one atmosphere)	760

8.4.2 Optical Power Test Results

The minimum optical power resulting in damage for each of the micromirrors in Figures 8.1, 8.4, and 8.5 was measured using a NEC model GLG5734 continuous wave 50 mW HeNe (632.8 nm) laser for a duration of one hour with the devices in low pressure (20 mTorr) dry nitrogen. A picture of the vacuum chamber and focusing lens used in the optical power testing is shown in Figure 8.9. A schematic diagram of the complete optical power test set-up is shown in Figure 8.10. The shutter, variable attenuator, and laser source are outside the field of view of Figure 8.9 (to the right side). The test procedures used to determine the minimum optical power resulting in damage are listed in Appendix D. A complete list of the equipment used by the author for optical power testing (including the model numbers) is given in Appendix C.

Table 8.2. Device Specific Data and Predicted Optical Power Rating.

	Mirror 1 Figure 8.1	**Mirror 2** Figure 8.4	**Mirror 3** Figure 8.5
Number of Flexures (N)	3	4	4
Flexure Length (L) μm	100.0	170.8	203.0
Flexure width (w) μm	2.0	3.0	1.75
Flexure thickness (t) μm	1.5	1.5	1.5
Surface Area of Polysilicon (S_p) μm^2	11,234	11,671	12,340.0
Surface Area of Gold (S_g) μm^2	9,216	7,854	1,600.0
Top Electrode's Surface Area Normal to Substrate (S_t) μm^2	10,000	9,503	6,724
Micromirror Height Above Substrate and Bottom Electrodes (h) μm	2.75	2.75	2.75
Predicted Optical Power Resulting in Damage (T_d=250°C) mW	7.12	8.35	4.14
Lowest Observed Optical Power Resulting in Damage, mW	7.5	9.0	4.5

The laser's output was focused so that the laser's spot filled the gold reflective surface but did not fall on the polysilicon border. Losses in the beam splitter and microscope objective reduced the optical power incident on the micromirror to 33.86% of the optical power exiting the variable attenuator. The substrate and surrounding environment were held at room temperature (T_s=22°C) during the test. Table 8.2 lists the test results for each micromirror design. Optical power damage was determined by measuring the reflectivity of the micromirror after laser illumination. A new micromirror was used for each test and each micromirror was continuously illuminated for one hour. Damaged devices had a minimum reflectivity decrease of 25%. The optical power level for each test was attenuated in 500 μW increments.

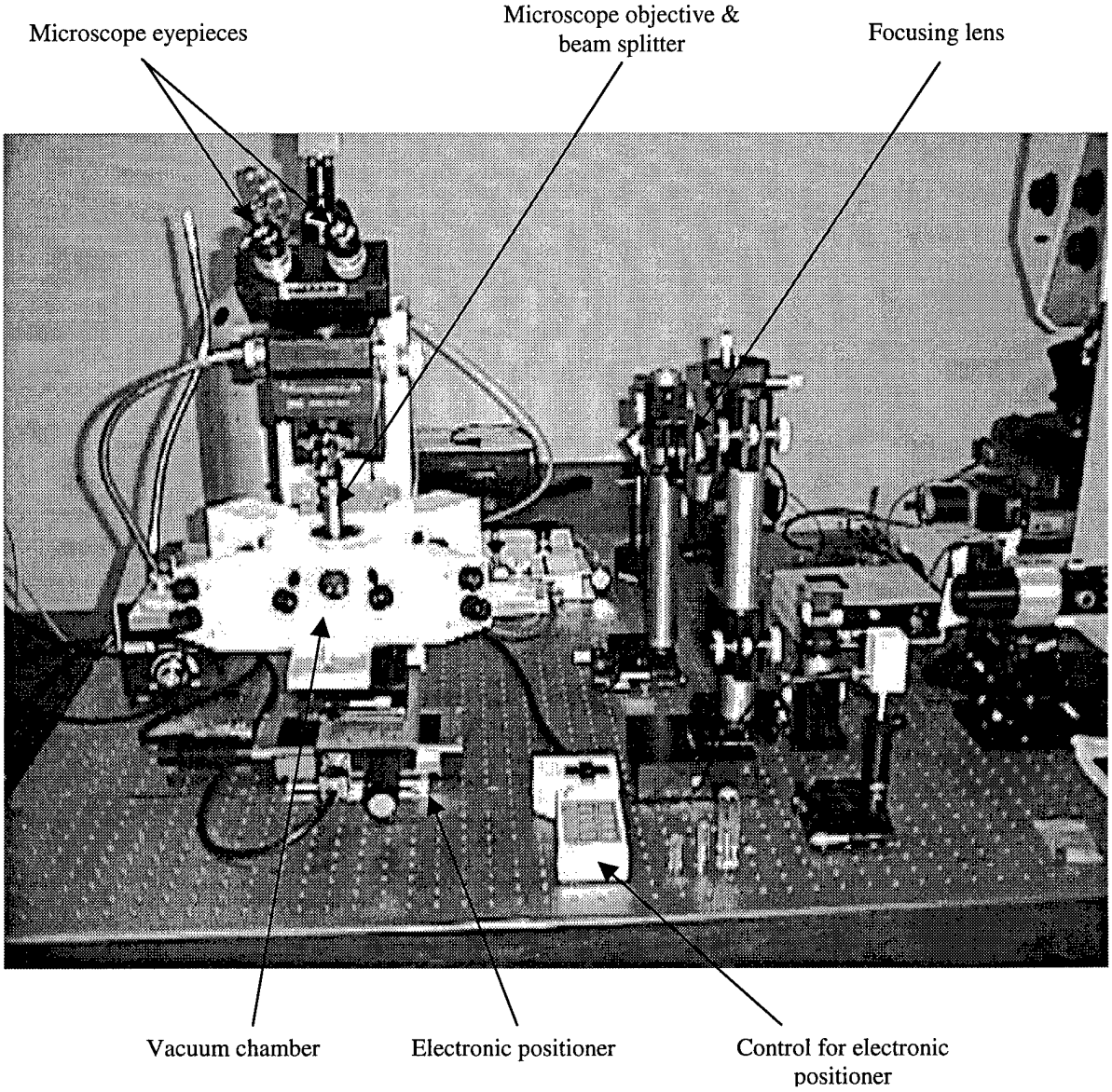

Figure 8.9. Vacuum chamber and focusing lens for optical power testing.

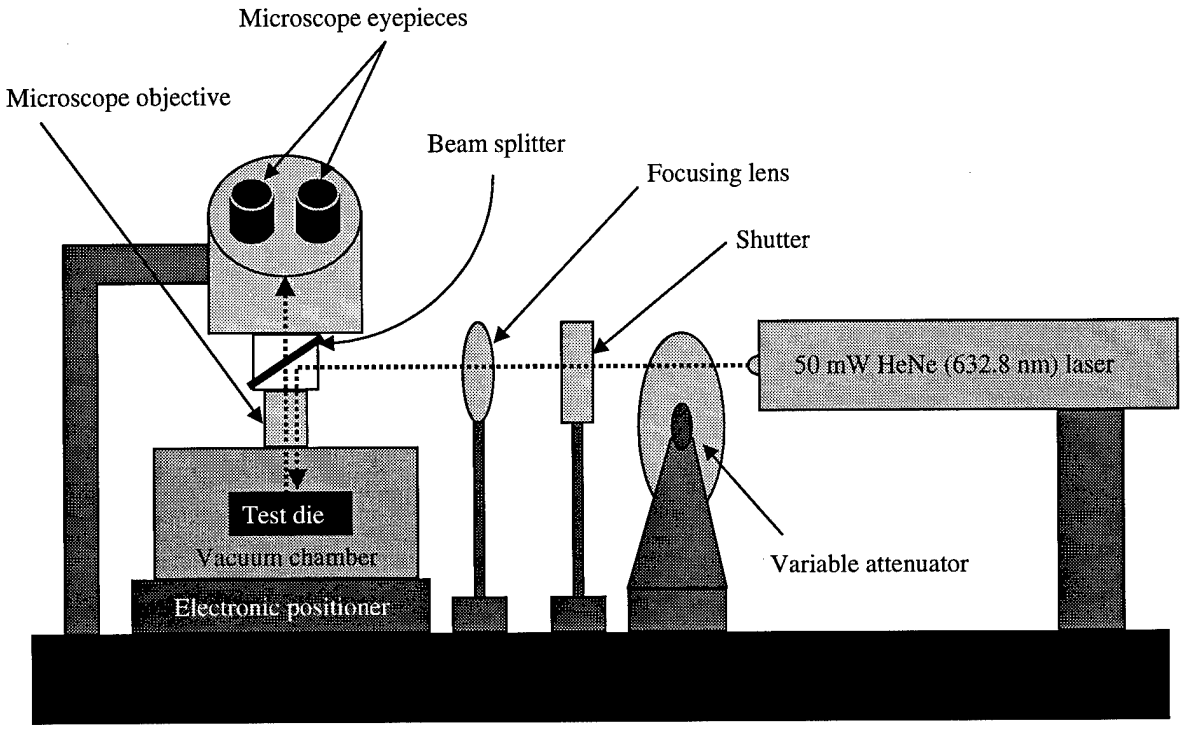

Figure 8.10. Schematic diagram of the optical power test setup.

The lowest observed optical power resulting in damage was higher than the predicted value in all cases. All optical power measurements that resulted in damage were less than 9% higher than the predicted values. Variations between the predicted and observed values may be due to an increase in the thermal radiation between the bottom of the top electrode and the substrate. Thermal radiation has been reported as increasing sharply above the value given by Equation (8.3) when the separation distance between the source and the sink is very small (less than the wavelength of the largest magnitude radiation frequency) [12]. The emissivity of the polysilicon is an estimate; published emissivity measurements of MUMPs polysilicon were not found. A comparison of the predicted and measured incident optical power levels required to damage the micromirrors in Figures 8.1, 8.4, and 8.5 (mirrors 1, 2, and 3, respectively) is shown in Figure 8.11.

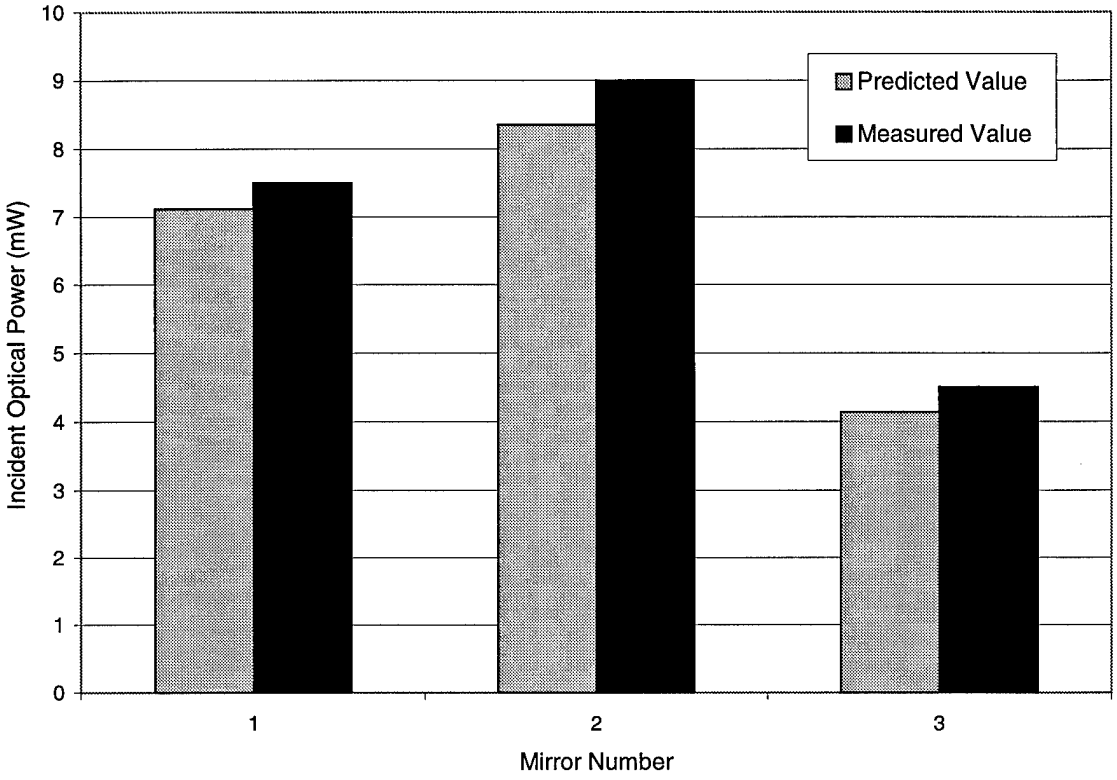

Figure 8.11. Comparison of the predicted and measured incident optical power levels required to damage the micromirrors in Figures 8.1, 8.4, and 8.5.

Variations between the predicted and observed values may also result from an inaccurate estimate for the thermal conductivity of the polysilicon. The thermal conductivity of the polysilicon used in the MUMPs process may be higher than the value reported in Table 8.1. The actual width of the support flexures varies slightly from design values, depending upon fabrication etch rates and times. Also each MUMPs production run has small variances in the polysilicon layer thickness (see Appendix A). Although Equation (8.22) included only the bottom surface area of the micromirror for thermal conduction to the surrounding gas, additional simulations indicate that the contribution of the sides and top of the top electrode and flexures is less than one percent of the dissipated power to the surrounding gas. The predicted optical power resulting in damage given by Equation (8.22) is in general conservative.

If the incident optical power exceeds the predicted value in Table 8.2 by a significant amount, the micromirror can suffer structural damage. Figures 8.12 and 8.13 show two micromirrors damaged by higher optical power levels. The structural damage resulted from a cascade effect: the reflectivity of the gold

decreased resulting in the absorption of more optical power, which in turn further decreased the micromirror's reflectivity. The gold and top polysilicon layer have been completely ablated in the damaged region of each micromirror. No damage was observed in the bottom electrode (Poly-0) or silicon nitride layer. The ablated region in the micromirror in Figure 8.12 is not typical; most high optical power tests for this micromirror yielded similar damage to the top gold layer but no gap was formed. The ablated region in the micromirror in Figure 8.13 was consistently formed during every high optical power test.

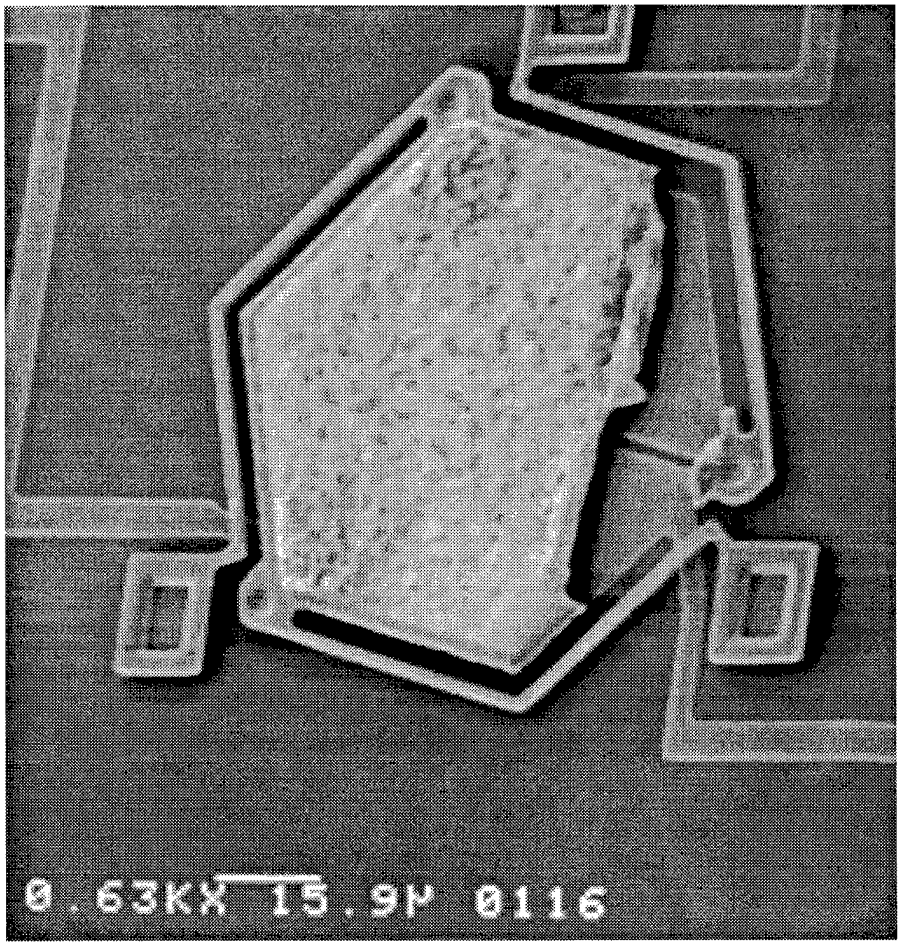

Figure 8.12. Rapid micromirror failure resulting from 12.65 mW continuously applied for 3 seconds (fabricated by the author in MUMPs 13).

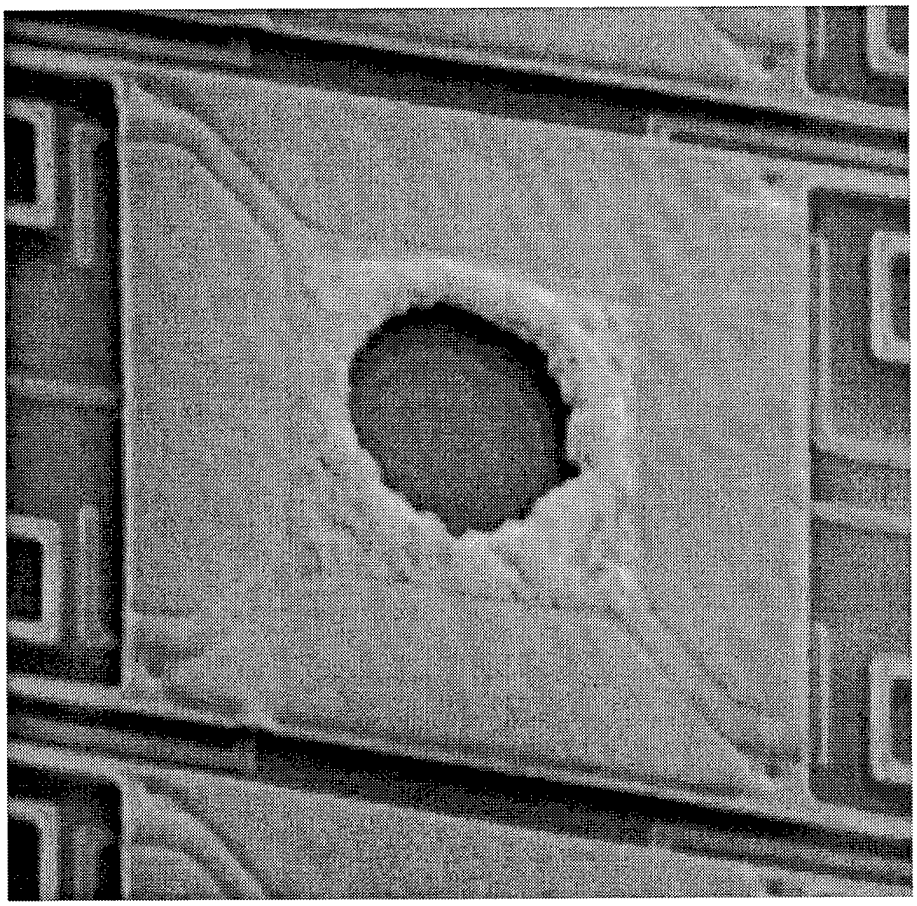

Figure 8.13. Rapid micromirror failure resulting from 9.35 mW continuously applied for 3 seconds (fabricated by the author in MUMPs 13).

8.4.3 Power Dissipation Mechanisms

Most of the thermal power dissipated by the micromirrors in Section 8.4.2 was through thermal conduction. Figure 8.14 shows the percentage of thermal power dissipated by thermal radiation for micromirror device temperatures ranging from 200°C to 1000°C for the micromirrors shown in Figures 8.1, 8.4, and 8.5 (referred to as mirrors 1, 2, and 3, respectively). Figure 8.14 was created by iteratively evaluating Equation (8.22) over the range of device temperatures. The incident optical power predicted by Equation (8.22) is a strong function of thermal conduction for all of the micromirrors until the device temperature exceeds 650°C. Thermal conduction is a linear function of device temperature (for the case of a low pressure surrounding gas) so the incident optical power predicted by Equation (8.22) can be approximated by a linear function for device temperatures below 650°C.

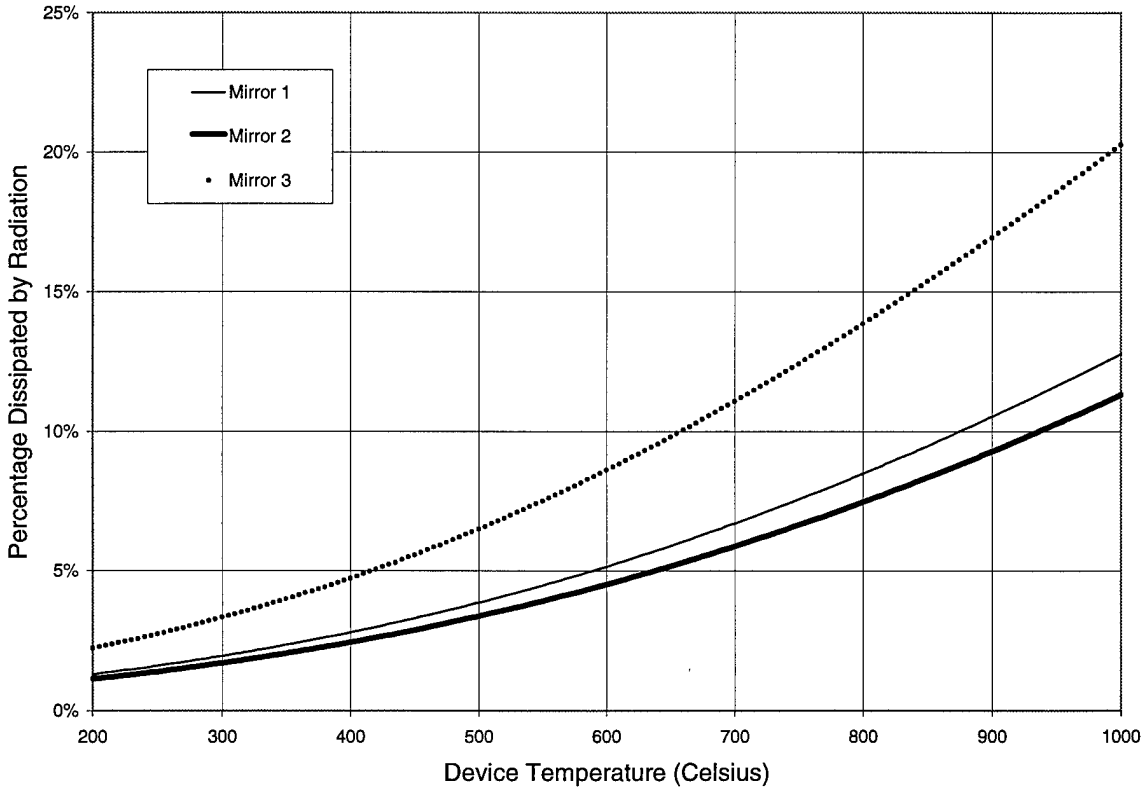

Figure 8.14. Percentage of thermal power dissipated by thermal radiation as a function of device temperature (T_d).

Incident optical power as a function of device temperature is shown in Figure 8.15 for each of the three micromirror designs tested by the author. A single incident optical power level (10 mW for example) will heat the three micromirrors to three different temperatures (340°C, 300°C, and 540°C, respectively). Since the primary thermal power dissipation mechanism is thermal conduction, an arbitrary micromirror's tolerance for incident optical power can be improved by increasing the number of flexures, thickening the flexures, and decreasing the length of the flexures. These design trade-offs all increase the actuation voltage for electrostatically actuated micromirrors. The actuation voltage could be reduced for the improved optical power micromirror by increasing the surface area of the top electrode normal to the bottom electrode or decreasing the separation distance between electrodes.

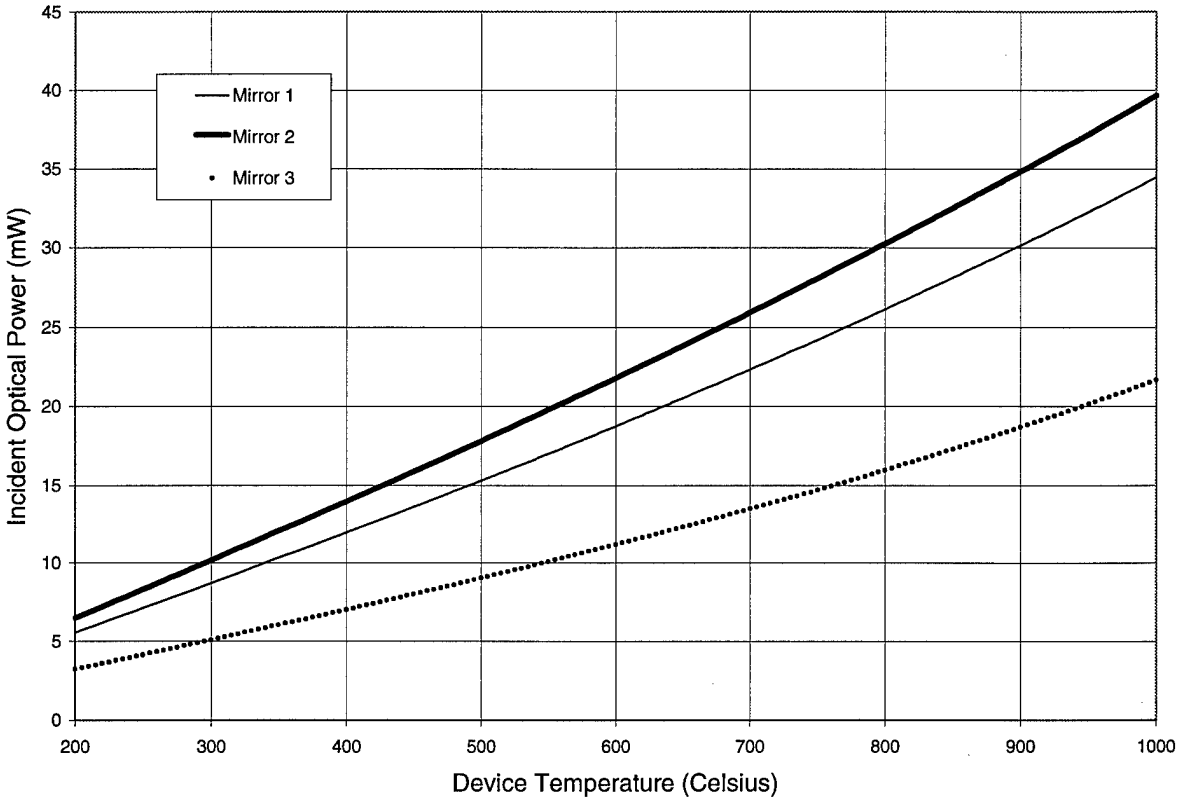

Figure 8.15. Incident optical power as a function of device temperature (T_d).

8.4.4 Thermal Dissipation Through a Surrounding Gas

Optical power predictions based on Equation (8.22) can be greatly increased if the pressure of the surrounding gas is higher than the pressure used to create Table 8.2 (nitrogen at 20 mTorr). Table 8.3 predicts the optical power required to damage the micromirror in Figure 8.1 for several different gasses at one atmosphere of pressure. The large increase in the predicted optical power for gasses at one atmosphere of pressure is due to the large micromirror surface area normal to the substrate and the small separation distance (h) between the top and bottom electrodes; the thermal model indicates that heat can be easily transported across this gap in the presence of a surrounding gas at one atmosphere of pressure. The optical power predictions for hydrogen and helium are probably unrealistically high; Equation (8.22) is based on holding the substrate and chip carrier at a constant temperature. The large optical power predictions listed in Table 8.3 for hydrogen and helium would make it difficult to hold the bottom electrodes, the substrate, and the chip carrier to

a uniform temperature. A drawback of using a higher pressure surrounding gas is that micromirror movement will be dampened by the gas resulting in a slower micromirror response time. Each time the micromirror's top electrode is pulled down towards the bottom electrodes, the intervening gas is either compressed or forced out of the micromirror.

Table 8.3. Effect of Common Gasses on Optical Power Predictions ($T_s = 22°C$).

Gas	Pressure (Torr)	Thermal Conductivity (κ_g) at One Atmosphere (W/m-K) Interpolated from [6]	Predicted Optical Power Resulting in Damage to Mirror 1 (T_d =250°C) (mW)
Nitrogen (baseline pressure)	0.020	0.0258	7.12
Air (one atmosphere pressure)	760	0.0262	267
Nitrogen	760	0.0258	263
Helium	760	0.152	1,508
Hydrogen	760	0.182	1,803

The author was unable to verify the predictions listed in Table 8.3 because the power levels were high enough to damage the optical equipment. One of the microscope eyepieces was burned by the author's high optical power experiment resulting in Figure 8.12. A replacement microscope eyepiece was found and used in the remaining tests. The test equipment shown in Figure 8.9 was used by other researchers as part of a laser interferometer system so the author was careful to avoid damaging equipment and delaying their research.

8.5 Summary

A model of a MEMS device in thermal equilibrium and under continuous optical illumination has been developed and validated. The thermal model is flexible enough to accommodate a wide variety of micromirror designs. If the pressure of the surrounding gas for the micromirrors in Figures 8.1, 8.4, and 8.5 is very low, then the dominant thermal energy dissipation mechanism is thermal conduction through the flexures. Thermal

conduction through the surrounding gas to the bottom electrodes and substrate is predicted to be the dominant thermal energy mechanism for gas pressures at or above one atmosphere. If the micromirror is not at rest, then forced convection may be induced by the top electrode's movement in the gas located between the top and bottom electrodes. The forced convection will improve the micromirror's ability to tolerate high optical power levels. However exploiting this improvement may be difficult from a system engineering perspective because it requires the micromirror to be almost continually in motion; a micromirror can be quickly heated due to it's low mass (as was shown in Figures 8.12 and 8.13). It is possible that microbellows could be developed and used around each micromirror to assist in forced convection.

8.6 References

[1] T.-H. Lin, "Implementation and characterization of a flexure-beam micromechanical spatial light modulator," *Optical Engineering*, vol. 33, no. 11, pp. 3643-3648, 1994.

[2] J. H. Comtois, V. M. Bright, S. Gustafson, and M. A. Michalicek, "Implementation of hexagonal micromirror arrays as phase-mostly spatial light modulators," *Proc. SPIE*, vol. 2641, pp. 76-87, 1995.

[3] R. A. Miller, G. W. Burr, Y. Tai, and D. Psaltis, "Electromagnetic MEMS scanning mirrors for holographic data storage," *Proc. Solid-State Sensor and Actuator Workshop*, Hilton Head Island, pp. 183-186, 1996.

[4] V. P. Jaecklin, C. Linder, J. Brugger, N. F. de Rooij, J.-M. Moret, and R. Vuilleumier, "Mechanical and optical properties of surface micromachined torsional mirrors in silicon, polysilicon and aluminum," *Sensors and Actuators A*, vol. 43, pp. 269-275, 1994.

[5] S. M. Sze, *Semiconductor Sensors*, New York, NY: John Wiley & Sons, Inc., 1994.

[6] F. P. Incropera and D. P. DeWitt, *Fundamentals of Heat Transfer*, New York, NY: John Wiley & Sons, 1981.

[7] R. W. Boyd, *Radiometry and the Detection of Optical Radiation*, New York, NY: John Wiley & Sons, 1983.

[8] A. W. van Herwaarden and P. M. Sarro, "Performance of integrated thermopile vacuum sensors," *Journal of Physics E*, vol. 21, pp. 1162-1167, 1988.

[9] R. Siegel and J. R. Howell, *Thermal Radiation Heat Transfer, 2nd Edition*, New York, NY: McGraw-Hill Book Company, 1981.

[10] W. G. Driscoll and W. Vaughan, *Handbook of Optics*, New York, NY: McGraw-Hill Book Company, 1978.

[11] F. Volklein and H. Baltes, "A microstructure for measurement of thermal conductivity of polysilicon thin films," *Journal of Microelectromechanical Systems*, vol. 1, no. 4, 1992.

[12] D. Polder and M. Van Hove, "Theory of radiative heat transfer between closely spaced bodies," *Physical Review B*, vol. 4, no. 10, pp. 3303-3314, 1971.

9 Other Microdevices Resulting From the Author's Research

The author designed many other MEMS devices in addition to the micro-optical devices described in the previous chapters. This chapter presents these other microdevices. The microdevices are: focusing mirrors, double hot arm thermal actuators, nonlinear flexures, improved single use micromotors, variable blaze phased arrays, and integrated VCSEL beam steering systems.

9.1 Focusing Mirrors

Micromachined gold and polysilicon layers can be used to create curved reflective surfaces. Residual internal material stresses in gold and polysilicon layers are typically tensile and compressive, respectively. The stress imbalance causes mirrors constructed out of gold on polysilicon to become concave after fabrication. Although residual internal material stress induced curvature is usually undesirable, it was exploited in this work to create micromachined focusing mirrors. This section presents two types of focusing mirrors: four arm and eight arm focusing mirrors. All of the focusing mirrors presented in this section are thermally driven. Each focusing mirror approximates a spherical mirror with an adjustable radius of curvature. The net effect of each mirror ring curling as a result of residual internal material stress causes the height of the mirror's surface above the substrate to increase exponentially as a function of distance from the center of the mirror.

9.1.1 Focusing Mirror Theory

A cross-sectional view of a spherically curved mirror is depicted in Figure 9.1. L is the length of the mirror, R is the radius of curvature for the mirror, θ is the divergence angle for normally incident light reflected off the mirror, and f is the mirror's focal length. The dashed lines in Figure 9.1 represent normally incident rays of light; these rays intersect at the focal point of the mirror located a distance f from the center of the mirror. The focal length for the mirror in Figure 9.1 is given by Equation (9.1) [1].

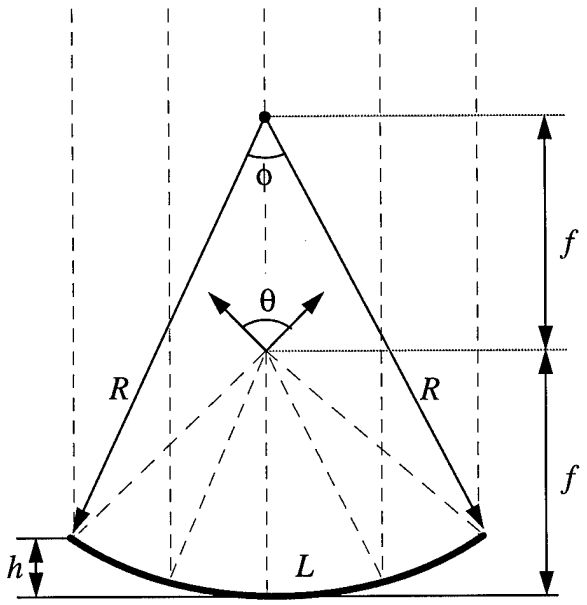

Figure 9.1. Schematic diagram of a focusing mirror.

$$f = \frac{R}{2} \tag{9.1}$$

The length of the mirror, L, is equal to the length of the arc defined by ϕ (measured in radians) on a circle with radius R. Given L and ϕ, R can be calculated by:

$$R = \frac{L}{\phi} \tag{9.2}$$

The angles θ and ϕ are related by Equation (9.3):

$$\tan\left(\frac{\theta}{2}\right) = \frac{\sin\left(\frac{\phi}{2}\right)}{\cos\left(\frac{\phi}{2}\right) - \frac{1}{2}} \tag{9.3}$$

The distance h in Figure 9.1 is the difference in height between the center of the mirror and the outer edge of the mirror. If the condition $R>>h$ is valid, then a solution to Equation (9.3) for ϕ can be approximated as:

$$\phi \cong 2\tan^{-1}\left(\frac{\tan(\theta/2)}{2}\right) \tag{9.4}$$

Combining Equations (9.1), (9.2), and (9.4) gives an approximation for the focal length:

$$f \cong \frac{L}{4\tan^{-1}\left(\frac{\tan(\theta/2)}{2}\right)} \tag{9.5}$$

The mirror length is a design value and is determined before fabrication. The divergence angle can be directly measured.

9.1.2 Four Arm Focusing Mirrors

A four arm focusing mirror with a diameter of 1 mm is depicted in Figure 9.2. The width of each ring in the focusing mirror is 30 μm and the gap between adjacent rings is 2 μm. The focusing mirror in Figure 9.2 is constructed out of a 500 nm thick layer of gold deposited on a stacked-poly layer. After fabrication, the sacrificial oxide layer is removed and the mirror immediately curls into a concave spherical shape. The design of each ring is similar to the slat design in variable blaze gratings.

The four arm focusing mirror is actuated by passing electric current into the outer ring through two of the polysilicon thermal actuators. The current returns to ground on the opposite two thermal actuators. The thermal actuators are resistively heated by the current and expand in length. When the thermal actuators expand, residual material stress in the polysilicon and gold mirror lifts the outer rings and decreases the mirror's focal length. The thermal actuators in Figure 9.2 are each 200 μm long, 10 μm wide, and 2 μm thick.

The electrical resistance of the focusing mirror in Figure 9.2 is 133.3 Ω. The minimum focal length in air is achieved with a drive current of 60.0 mA (8 volts). In nitrogen at 40 mTorr, the drive current is reduced by a factor of two because less thermal power is dissipated to the surrounding gas. The maximum operating frequency for mirror travel over the full focusing range is greater than 120 Hz in air at one atmosphere.

Pictures of an image plane illuminated by reflection from the mirror in Figure 9.2 are shown in Figure 9.3 for a 632.8 nm source (a HeNe laser). The image plane in Figure 9.3 was located 2 meters from the mirror (far field). The drive voltage for each image in Figure 9.3 was measured in air and is listed in Table 9.1. The focal lengths in Table 9.1 were calculated from measured far field divergence angles using Equation (9.5). The divergence angle for normally incident light reflected off the mirror in Figure 9.2 could be adjusted over the range of 83.3 mrad (zero volts applied) to 135.1 mrad (8 volts applied).

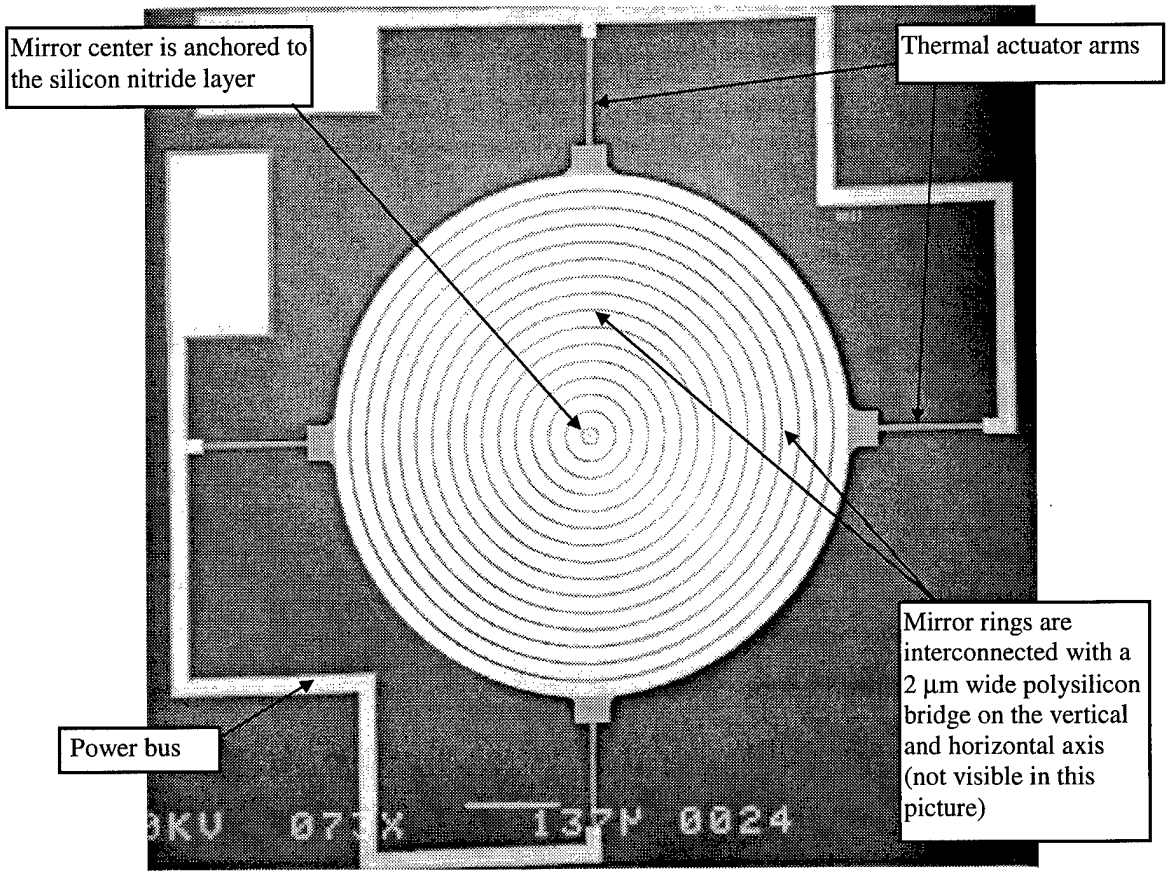

Figure 9.2. Scanning electron micrograph of a four arm focusing mirror (fabricated by the author in MUMPs 19).

The circles in the images in Figure 9.3 are caused by interference resulting from the periodic design of the mirror (equal width rings) and the coherent source (a HeNe laser). The circles can be eliminated if the mirror is illuminated by white light.

If the mirror in Figure 9.2 is over-driven by applying 8.6 volts for 5 seconds, then the thermal actuator arms will contract when power is removed. This phenomenon is called "back-bending" [5] and it permanently distorts the mirror's shape. Figure 9.4 shows two far field images of the four arm focusing mirror in Figure 9.2 after the actuator arms were backbent. Figure 9.4(a) has pincushion distortion (elongated corners) and Figure 9.4(b) has barrel distortion (elongated top, bottom, and sides). These optical aberrations are caused by the placement of the four thermal actuator arms. It may be possible to use the distortion in Figure 9.4 to correct aberrations in an imaging system. For example if an optical system had a variable amount of barrel distortion, the four arm focusing mirror could be used to correct the wavefront by supplying a equivalent amount of pincushion distortion.

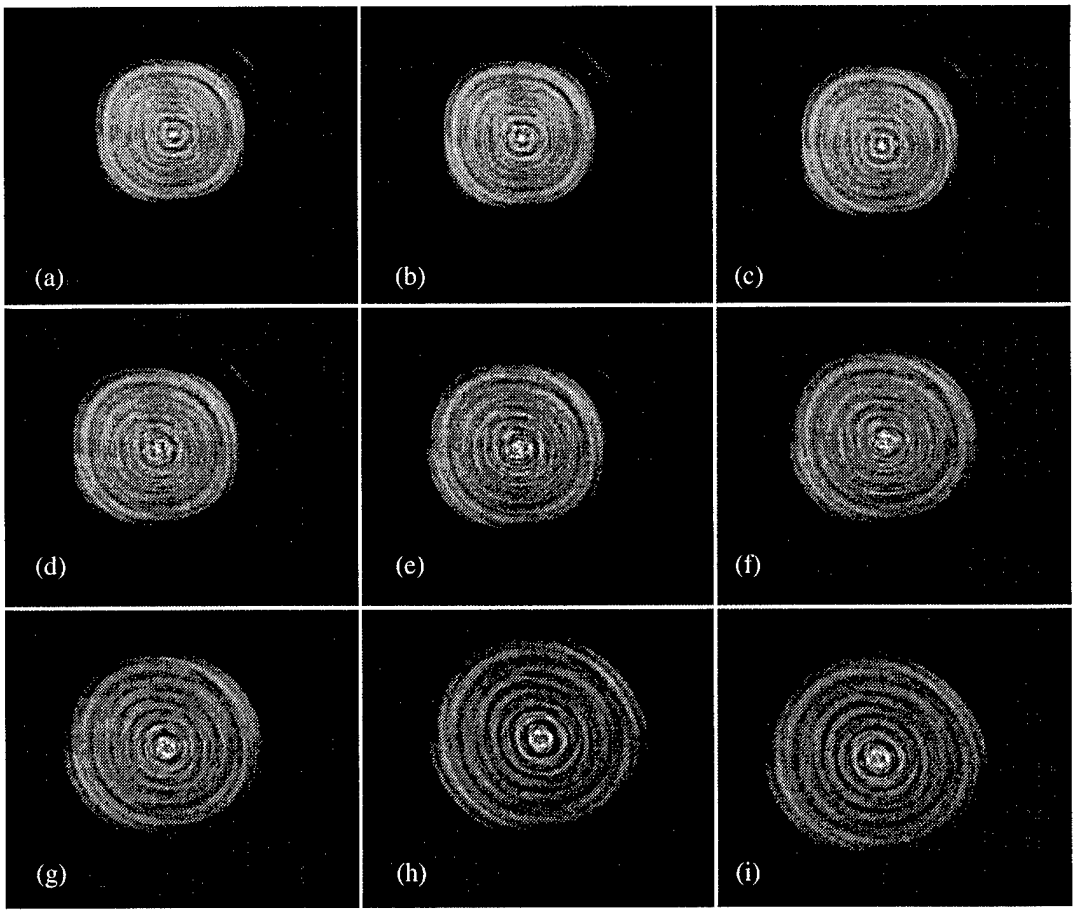

Figure 9.3. Pictures of an image plane illuminated by light reflected from the four arm focusing mirror in Figure 9.2. The upper left picture (a) was created by the mirror at rest (zero drive voltage). Other pictures were created by the mirror as the drive voltage was increased in one volt increments.

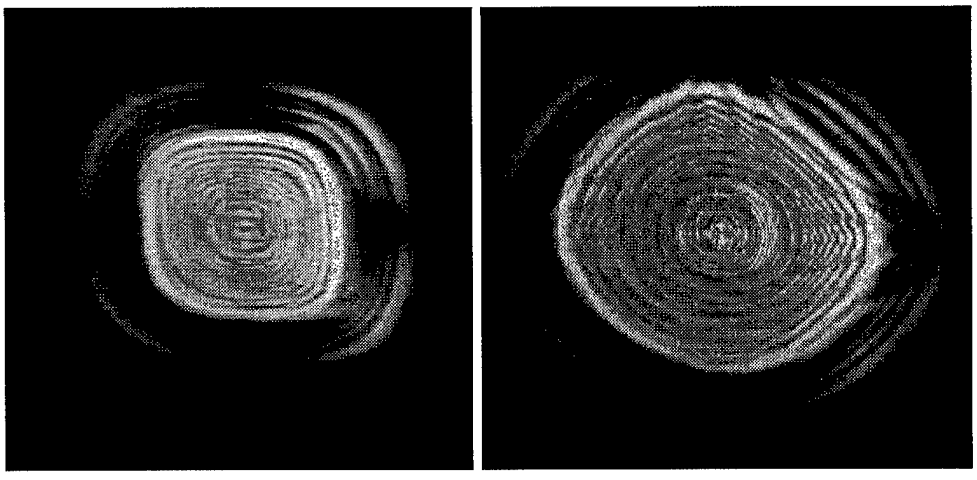

(a) Mirror at rest (zero volts) (b) Mirror at full drive voltage (9.1 volts)

Figure 9.4. Pictures of an image plane illuminated by light reflected from the four arm focusing mirror after the thermal actuator arms were backbent.

Table 9.1. Experimental Results for the Four Arm Mirror in Figure 9.2.

Image	Drive voltage (volts)	θ (mrad)	Focal length (mm)
(a)	0.0	83.3	12.0
(b)	1.0	85.3	11.7
(c)	2.0	87.3	11.4
(d)	3.0	92.8	10.8
(e)	4.0	99.0	10.1
(f)	5.0	104.6	9.6
(g)	6.0	111.6	9.0
(h)	7.0	128.9	7.8
(i)	8.0	135.1	7.4

9.1.3 Eight Arm Focusing Mirrors

An eight arm focusing mirror is shown in Figure 9.5. The rings in this 1 mm diameter mirror are identical in form to the rings in the four arm mirror depicted in Figure 9.2. The thermal actuator arms in Figure 9.5 are each 325 μm long, 14 μm wide, and 2 μm thick. Drive current enters the eight arm focusing mirror on source thermal actuator arms and returns on the alternately spaced sink thermal actuator arms. The mirror in Figure 9.5 used holes in the silicon nitride layer to connect the sink thermal actuator arms to the grounded substrate. The holes in the silicon nitride layer were etched before the final polysilicon layer was deposited on the die [2]. A close-up view of the center of the mirror in Figure 9.5 is shown in Figure 9.6.

Pictures of an image plane illuminated by reflection from the mirror in Figure 9.5 (632.8 nm source wavelength) are shown in Figure 9.7. The image plane in Figure 9.7 was located 2 meters from the mirror. The drive voltage for each image in Figure 9.7 was measured in air and is listed in Table 9.2. The focal lengths in Table 9.2 were calculated from measured far field divergence angles using Equation (5). The divergence angle

for normally incident light reflected off the mirror in Figure 9.5 could be adjusted over the range of 69.6 mrad (at rest) to 87.9 mrad (5 volts applied).

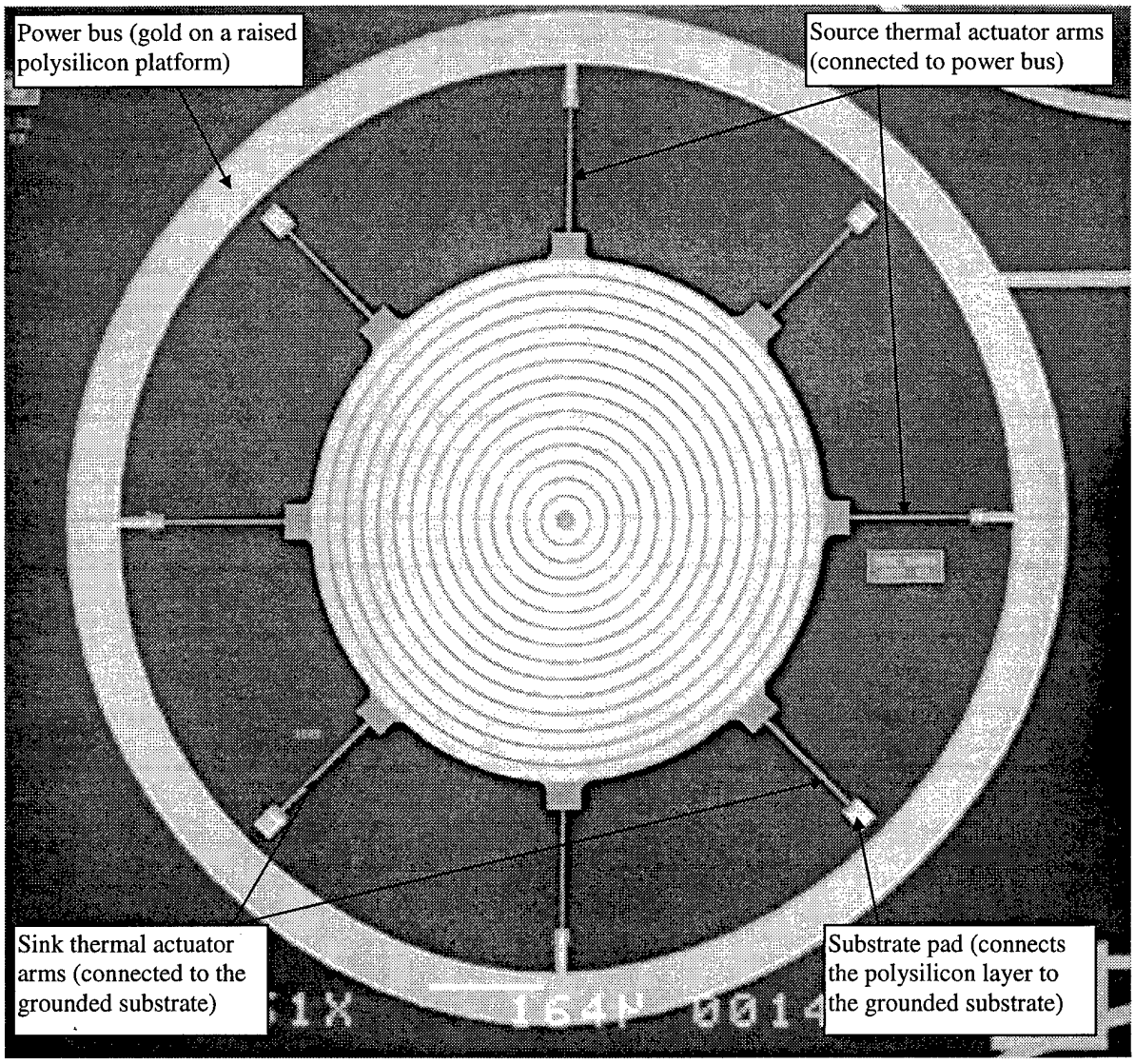

Figure 9.5. Scanning electron micrograph of an eight arm focusing mirror. Diameter of the mirror is 1 mm (fabricated by the author in MUMPs 21).

The maximum selectable focal length was larger for the eight arm focusing mirror than for the four arm focusing mirror. The increased focal length for the eight arm focusing mirror resulted from offsetting the residual internal material stress induced curvature in the eight arm focusing mirror with the tension from eight thermal actuator arms. As a result of the additional four thermal actuator arms, the eight arm focusing mirror

was not as concave as the four arm focusing mirror. The electrical resistance of the eight arm focusing mirror in Figure 9.5 was 104.7 Ω. The maximum operating frequency for mirror travel over the full focusing range was greater than 120 Hz in air at one atmosphere.

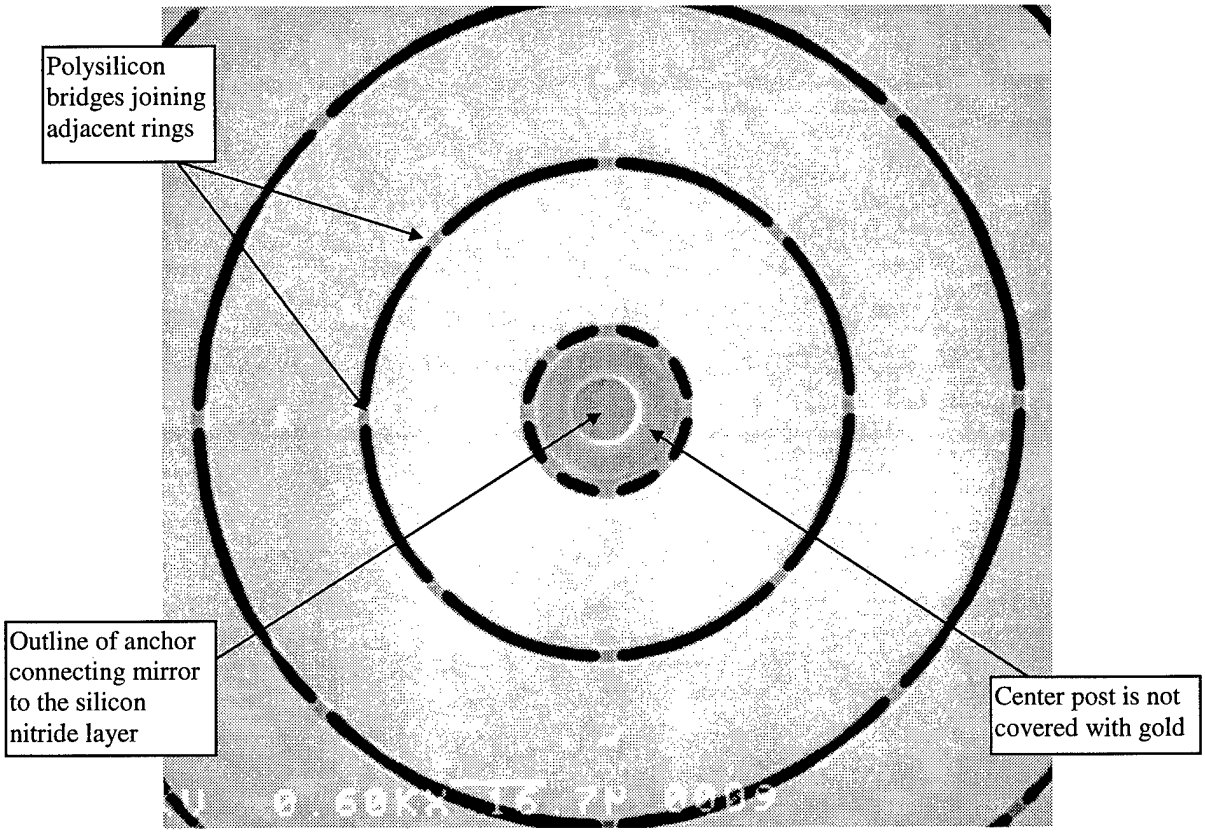

Figure 9.6. Scanning electron micrograph of the center of an eight arm focusing mirror (fabricated by the author in MUMPs 21).

9.1.4 Focusing Mirror Applications

The thermally driven focusing mirror could be used for shaping laser spots for small laser mapping systems and holographic data storage devices. Other applications include focusing light onto a photodetector or optical fiber for communications and collimating the output of a fiber optical cable for transmission in free space.

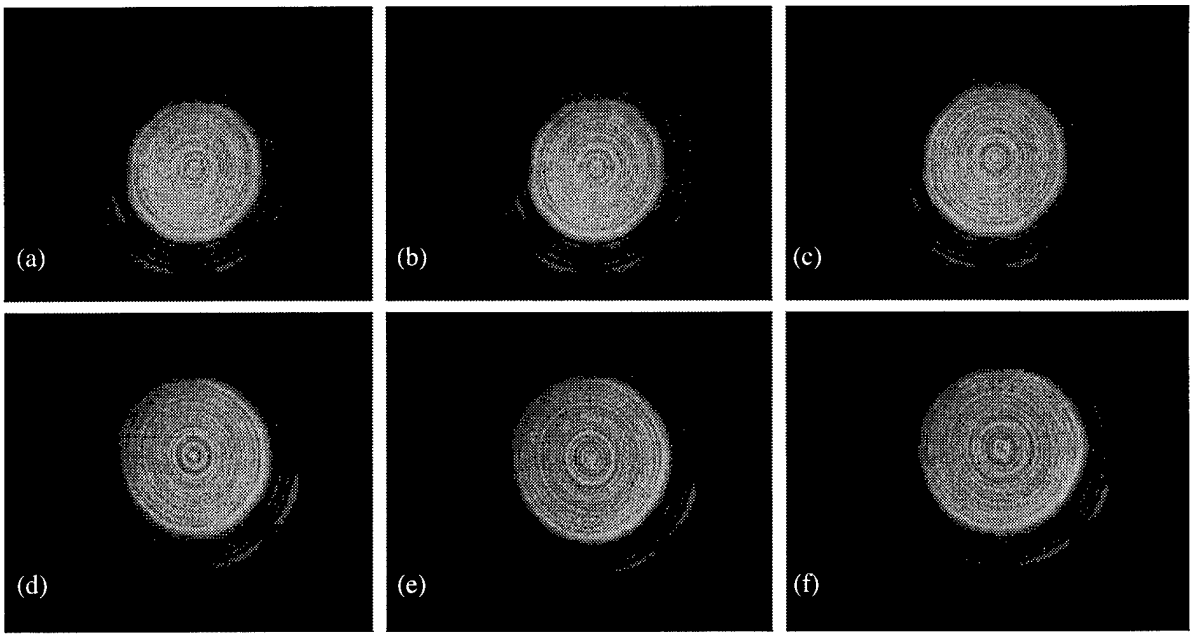

Figure 9.7. Pictures of an image plane illuminated by light reflected from the eight arm focusing mirror in Figure 9.5. The upper left picture (a) was created by the mirror at rest (zero drive voltage). Other pictures were created by the mirror as the drive voltage was increased in one volt increments.

Table 9.2. Experimental Results for the Eight Arm Mirror in Figure 9.5.

Image	Drive voltage (volts)	θ (mrad)	Focal length (mm)
(a)	0.0	69.9	14.4
(b)	1.0	72.3	13.8
(c)	2.0	74.9	13.4
(d)	3.0	79.6	12.6
(e)	4.0	83.9	11.9
(f)	5.0	87.9	11.4

9.1.5 Focusing Mirror Summary

Both four arm and eight arm focusing mirrors were fabricated and characterized. Four arm focusing mirrors had shorter focal lengths and required less electrical power than eight arm focusing mirrors. Four arm

focusing mirrors may be capable of correcting pincushion or barrel distortion. The mirrors in Figures 9.2 and 9.5 were capable of reflecting 17.3 mW of continuous optical power (HeNe laser operating at 632.8 nm) in air with no observed change in focal length. The optical efficiency for both four and eight arm focusing mirrors was measured as 74.9% for a HeNe laser operating at 632.8 nm.

9.2 Double Hot Arm Thermal Actuators

A typical lateral thermal (1-H) actuator was shown in Figure 7.4 (Chapter 7). The author improved the design of this actuator by creating a new class of thermal actuators: the double hot arm thermal actuator (2-H actuator). The author's new thermal actuator design is shown in Figure 9.8. Electric current enters a 2-H actuator on one hot arm and returns on the other hot arm, eliminating the requirement for the flexure and cold arm to form a section of the circuit. Figure 9.9 is a schematic diagram of current flow in a 1-H actuator and a 2-H actuator. The 2-H actuator outer hot arm is longer than the inner hot arm because the outer hot arm must expand more than the inner hot arm as the actuator is rotated towards the cold arm. The thickness of the 2-H actuator flexure can be less than traditional thermal actuator flexure because the 2-H actuator flexure does not carry current. The width of the 2-H actuator cold arm is identical to the width of the 1-H actuator cold arm; the 2-H actuator cold arm's width was not reduced because a stiff cold arm forces the flexure at the base of the actuator to bend and offset the expansion of the hot arms. The tip of the actuator moves more if the flexure bends and the cold arm stays rigid. The 2-H actuator pictured in Figure 9.8 is formed out of POLY-1 and had an outer hot arm that was 252 μm long. The inner hot arm was 221 μm long and both hot arms were 2.5 μm wide. The 2-H actuator flexure was 2 μm wide. Other design details are listed in Table 9.3.

Both 1-H and 2-H thermal actuators used a substrate contact pad to sink current flowing through the actuator into the grounded substrate. The 1-H actuator's cold arm flexure and the 2-H actuator's inner hot arm were attached to substrate contact pads. The substrate contact pad simplified wiring for both actuators; only a single connection to the supply power bus was needed on the surface of the die for each actuator. Current entered each device on a hot arm and returned through the grounded substrate. The substrate contact pad was formed during fabrication by removing a portion of the silicon nitride layer and depositing a layer of POLY-2 directly onto the exposed substrate [2]. Dimples were used on the cold arms of both actuator designs to reduce

the amount of polysilicon in direct contact with the silicon nitride layer. Dimples reduced friction and prevented the polysilicon layer from sticking to the silicon nitride layer.

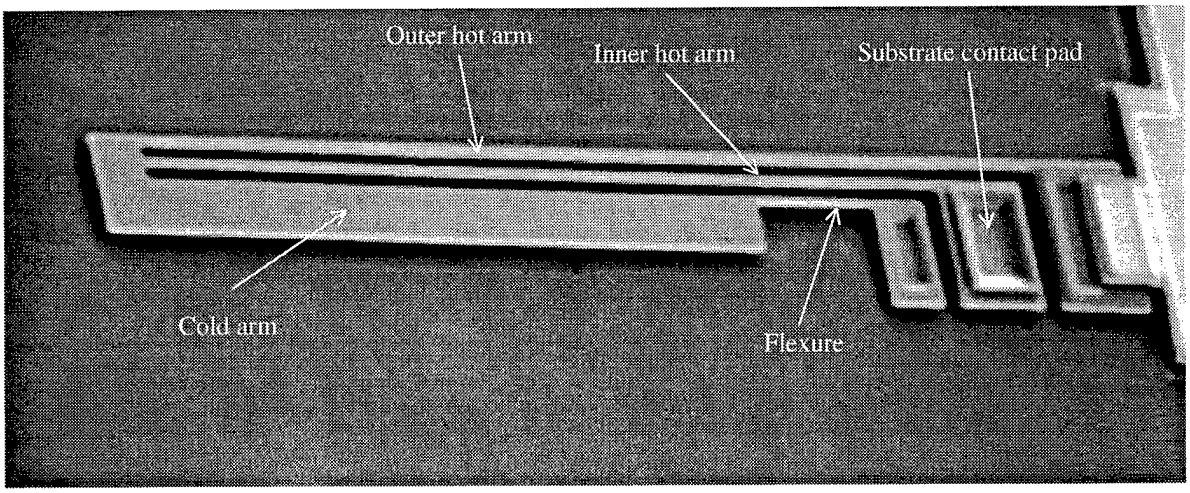

Figure 9.8. Scanning electron micrograph of a double hot arm thermal actuator (2-H actuator) fabricated by the author in MUMPs 17.

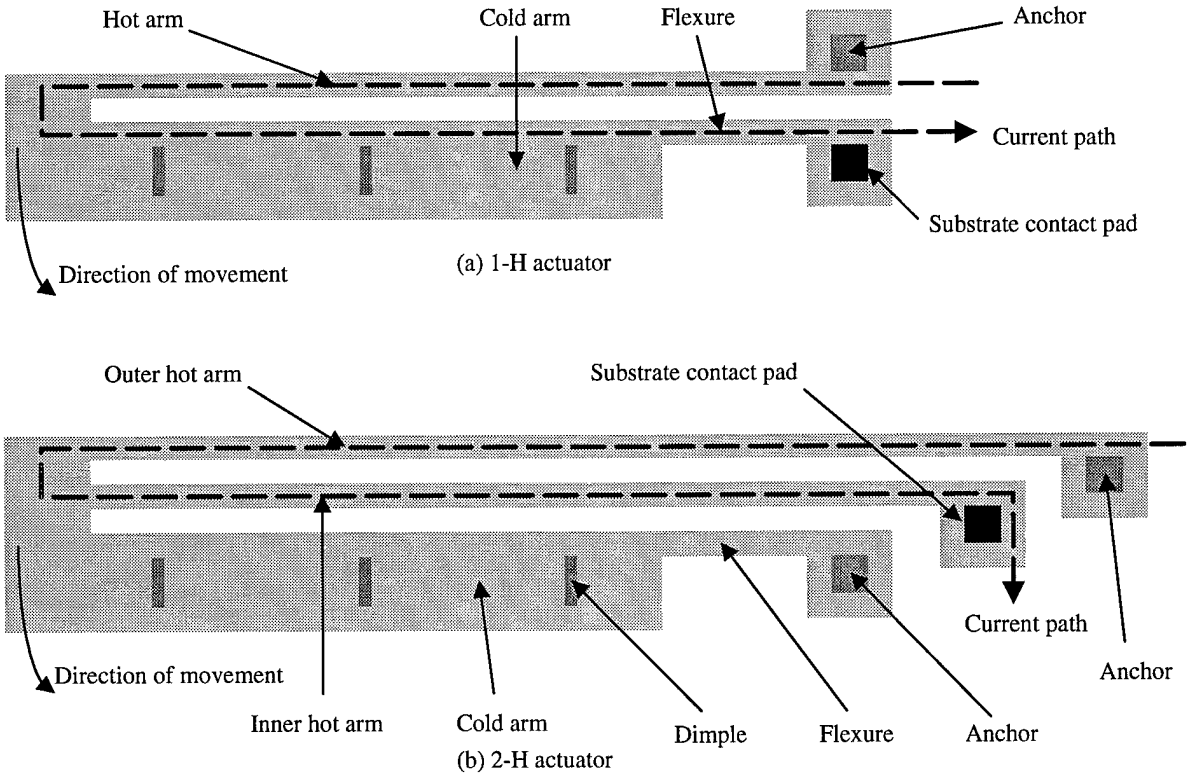

Figure 9.9. Schematic diagram of current flow in (a) 1-H actuator and (b) 2-H actuator.

Table 9.3. Design Measurements for Thermal Actuators.

	1-H actuator (Figure 7.4)	2-H actuator (Figure 9.8)
Cold arm length	162 μm	162 μm
Cold arm width	14 μm	14 μm
Flexure length	38 μm	38 μm
Flexure width	2.5 μm	2.0 μm
Inner hot arm length	200 μm	221 μm
Outer hot arm length	not applicable	252 μm
Hot arm width	2.5 μm	2.5 μm
Separation between inner hot arm and cold arm	3 μm	3 μm
Separation between hot arms	not applicable	3 μm

A 2-H actuator was more electrically efficient than a traditional single hot arm actuator because no electrical power was wasted in the flexure and cold arm. As a result more of the applied power was used to heat the hot arms and rotate the actuator on its flexure. The actuation voltage for a 2-H actuator was higher than a similarly-sized traditional thermal actuator because the actuator circuit contained two hot arms instead of one. The resistance of the thermal actuator shown in Figure 7.4 was 1.510 KΩ and the resistance of the 2-H actuator shown in Figure 9.8 was 2.413 KΩ (both fabricated in MUMPs 17). The width of the hot arms in the actuators shown in Figure 7.4 and Figure 9.8 was the same (2.5 μm) so the actuation current density was similar for both devices. The 2-H actuator flexure shown in Figure 9.8 was 20% thinner than the flexure in the thermal actuator shown in Figure 7.4. Thinner flexures allowed more of the force generated by the expanding hot arms to translate into rotational movement, because less force was required to bend the flexure. Also two hot arms were countered by the bending force generated by one flexure instead of the one hot arm to one flexure ratio in a traditional 1-H actuator.

Arrays of the new thermal actuator design were smaller than equivalent force 1-H actuator arrays. 2-H actuator elements were longer than 1-H actuator elements because of the additional hot arm length. However an array of double hot arm actuators had half as many cold arms per hot arm as a similar 1-H actuator array so the new design permitted more hot arms in a given area. A typical 2-H actuator array is shown in Figure 9.10. The linear separation between adjacent actuators was the same for both 1-H actuator and 2-H actuator arrays (21 μm). The 2-H actuator array shown in Figure 9.10 required 31.4% less area than a 1-H actuator array with the same number of hot arms.

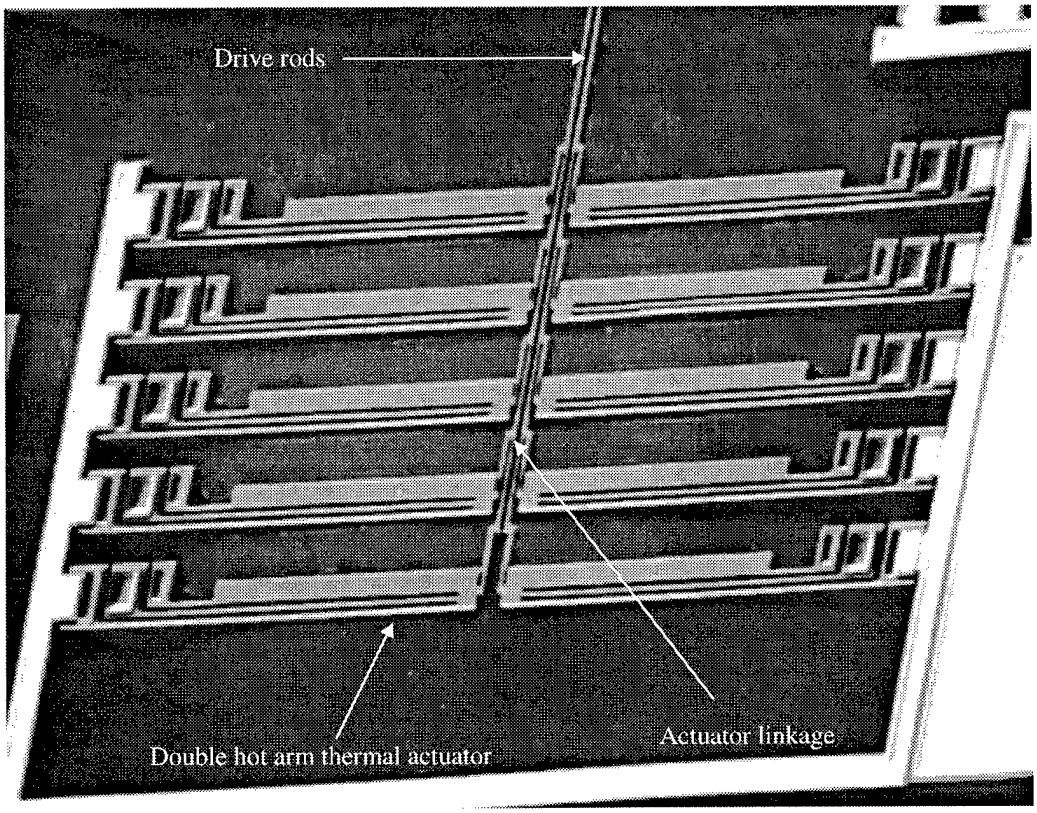

Figure 9.10. Scanning electron micrograph of a typical double hot arm thermal actuator array (fabricated by the author in MUMPs 17).

The author characterized the deflection and force of thermal actuators shown in Figure 7.4 and Figure 9.8 as a function of applied current. All measurements were obtained in air, at room temperature, and at one atmosphere of pressure. Deflection measurements were made with no load. Deflection is the distance the tip of the actuator moves along an arc centered at the middle of the flexure. If excessive current (within 10% of the maximum current rating for the device) was applied to a thermal actuator, the hot arm would shrink below its

original length when the current was removed. Shrinkage of the hot arm resulted in backbending of the actuator (as discussed in Chapter 7). For the actuators in Figures 7.4 and 9.8, positive deflection measurements were obtained at current levels below the backbending current threshold.

Force measurements were calculated based on the distance a POLY-1 cantilever was bent by the tip of the thermal actuator. Figure 9.11 depicts the force measurement set-up used to determine actuator force. This method was first used by Reid [3]. As force was applied from the thermal actuator, the cantilever's flexure bends. As the flexure bends, the tip of the cantilever was moved along the gauge. The device was initially separated from the thermal actuator by a gap of 2 μm. The period of the teeth in the gauge was 4 μm and the amount of force required to move the indicator from one tooth to the next tooth was approximately 2.28 μN.

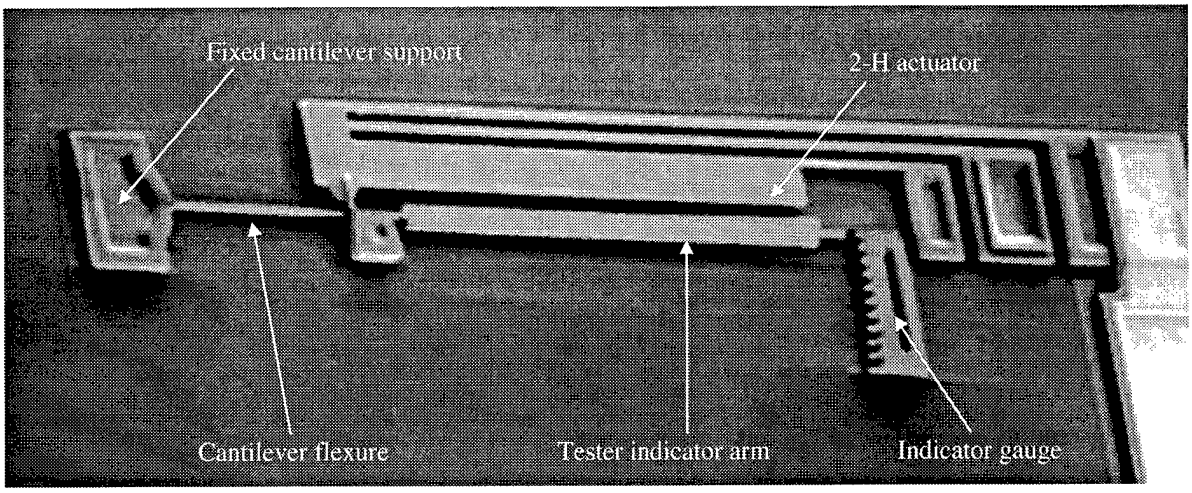

Figure 9.11. A cantilever force measurement device coupled to a thermal actuator (fabricated by the author in MUMPs 17).

Figure 9.12 is a plot of deflection versus applied current for the thermal actuators shown in Figure 7.4 and Figure 9.8. The data in Figure 9.12 was an average of data collected from three sets of 1-H actuator and 2-H actuator test devices in air. All test devices had 200 μm long cold arms (including flexures) and were fabricated in the 18th MUMPs production run. All thermal actuators provided very repeatable data during any given test session, however actuator power varied from day to day. Daily actuator power variations were probably a function of the humidity level at the test station. Humidity levels were not controlled in the test laboratory during thermal actuator testing.

Test 2-H actuators deflected 40% more than the 1-H actuators. At large deflections (above 10 μm), the inner and outer 2-H actuator hot arms touched. The native oxide in the polysilicon hot arms prevented the hot arm contact from passing a measurable current; however the contact did appear to limit the maximum deflection of the 2-H actuator. The thermal actuators shown in Figure 7.4 and Figure 9.8 could be backbent by applying 6.30 mA and 5.97 mA, respectively, for 5 seconds. The tip of the 1-H actuator after backbending was 8 μm below its original position. The tip of the 2-H actuator after backbending was 12.0 μm below its original position, a 50% improvement over the traditional 1-H actuator design.

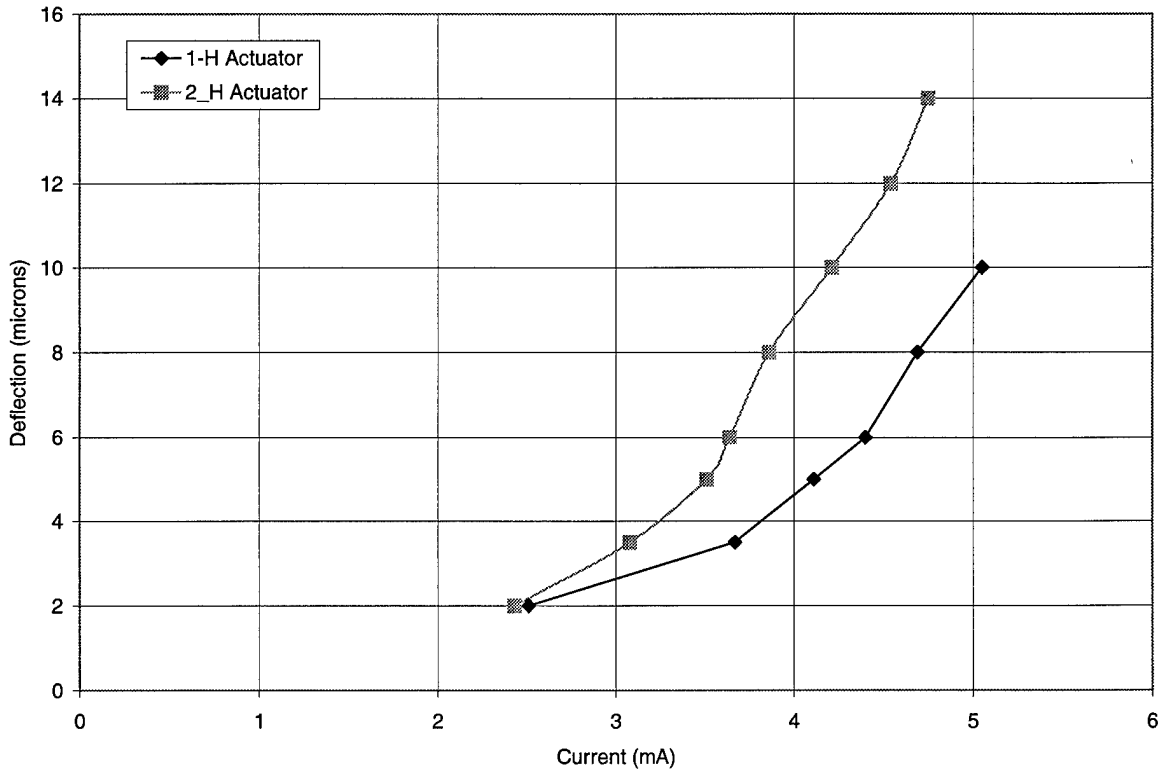

Figure 9.12. Deflection versus applied current plots for single and double hot arm thermal actuators.

Figure 9.13 is a plot of actuator force versus applied current for the thermal actuators shown in Figure 7.4 and Figure 9.8. The average maximum force of the 2-H actuator was 80% higher than the 1-H actuator. Note that the current measurements in Figure 9.13 for both actuators were slightly higher than the current measurements in Figure 9.12. The force measuring system shown in Figure 9.11 may have dissipated heat from

both actuators during force testing. The slight increase in current in Figure 9.13 may have been required to provide additional heating to the actuators to offset the losses in the force measuring system Although the force of a backbent 2-H actuator was not measured, observations of backbent 2-H actuator arrays suggest a backbent 2-H actuator had substantially more force than a backbent 1-H actuator. 2-H actuator hot arms did not touch each other during force testing or after backbending.

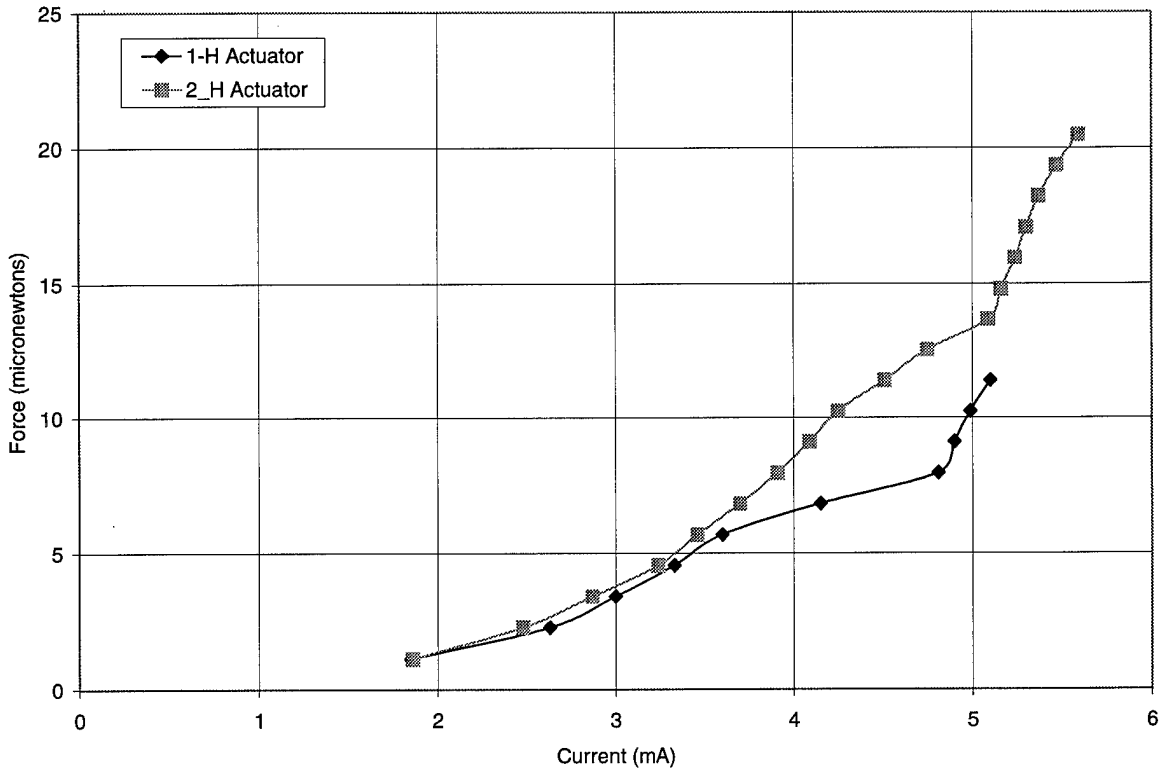

Figure 9.13. Force versus applied current plots for single and double hot arm thermal actuators.

The maximum operating frequency was measured using a laser interferometer. All frequency measurements were made with no load present. The maximum operating frequency was determined by positioning the laser spot in the laser interferometer at the center of the path in which the thermal actuator moves. The maximum operating frequency was defined as the highest drive signal frequency where the thermal actuator was still able to move back and forth across the laser's spot. Maximum operating frequencies of the thermal actuators in Figures 7.4 and 9.8 were 12 kHz and 17 kHz, respectively (measured in air, at room

temperature, and one atmosphere of pressure). Some of the increase in maximum operating frequency is probably a result of improving the actuation force versus mass ratio. Increasing the actuation force versus mass ratio decreases the actuator's deflection time constant. The active mass of a 2-H actuator is 23.6% higher than a 1-H actuator; however a 2-H actuator has 80% more peak force than a 1-H actuator.

Maximum operating frequencies in nitrogen at 40 mTorr for a 1-H actuator and a 2-H actuator were measured as 4 kHz and 27 kHz, respectively. The decrease in the 1-H actuator's maximum operating frequency was probably a result of the hot arm taking more time to dissipate heat after current is removed. The longer cooling time slowed the contraction of the 1-H actuator's hot arm. Also current flowed through the 1-H actuator's cold arm, so the cold arm and flexure both warmed and lengthened in a near vacuum [4]. The improvement in the 2-H actuator's maximum operating frequency probably results from reduced air damping. The 2-H actuator's hot arms have more surface area to radiate heat and two base pads to conduct heat to the substrate; a 2-H actuator dissipates heat more effectively than a 1-H actuator at 40 mTorr. Also no current travels through the 2-H actuator's cold arm, so it does not lengthen significantly during actuation.

Practically any MEMS device that works with traditional 1-H actuators can be improved by using 2-H actuators. Figure 9.14 shows a micromotor driven by a 2-H actuator array; this micromotor was based on a design by Comtois [5]. The micromotor is driven by two 2-H actuator arrays. The pusher array pushed the drive pawl against the drive gear when the drive array was moving the drive pawl away from the drive array. The drive pawl then rotated the drive gear in a counter-clockwise direction. If the drive pawl was pushed against the drive gear when the drive array was contracting, then the drive gear would rotate in a clockwise direction. 2-H actuator arrays have approximately 80% more force than 1-H actuator arrays so the improved micromotor should have more torque than previous designs (however the author was unable to directly measure this).

Figure 9.15 is a fan micromirror driven by a 2-H actuator array; this fan micromirror was based on a design by Reid [6]. Twin vertical thermal actuators were used to lift the micromirror off the substrate, and lock the micromirror to the 2-H actuator array pushrod. As the 2-H actuator array deflected, the fan micromirror rotated on an axis parallel to the surface of the substrate.

Figure 9.16 is a vertical thermal actuator based on the 2-H actuator design. The vertical 2-H actuator design relied on backbending to shorten the hot arms and lift the tip of the actuator off the substrate. When 14.2

volts (5.2 mA) was applied for 5 seconds to the vertical thermal actuator and then removed, backbending caused the tip of the actuator to rise approximately 20 μm off the substrate.

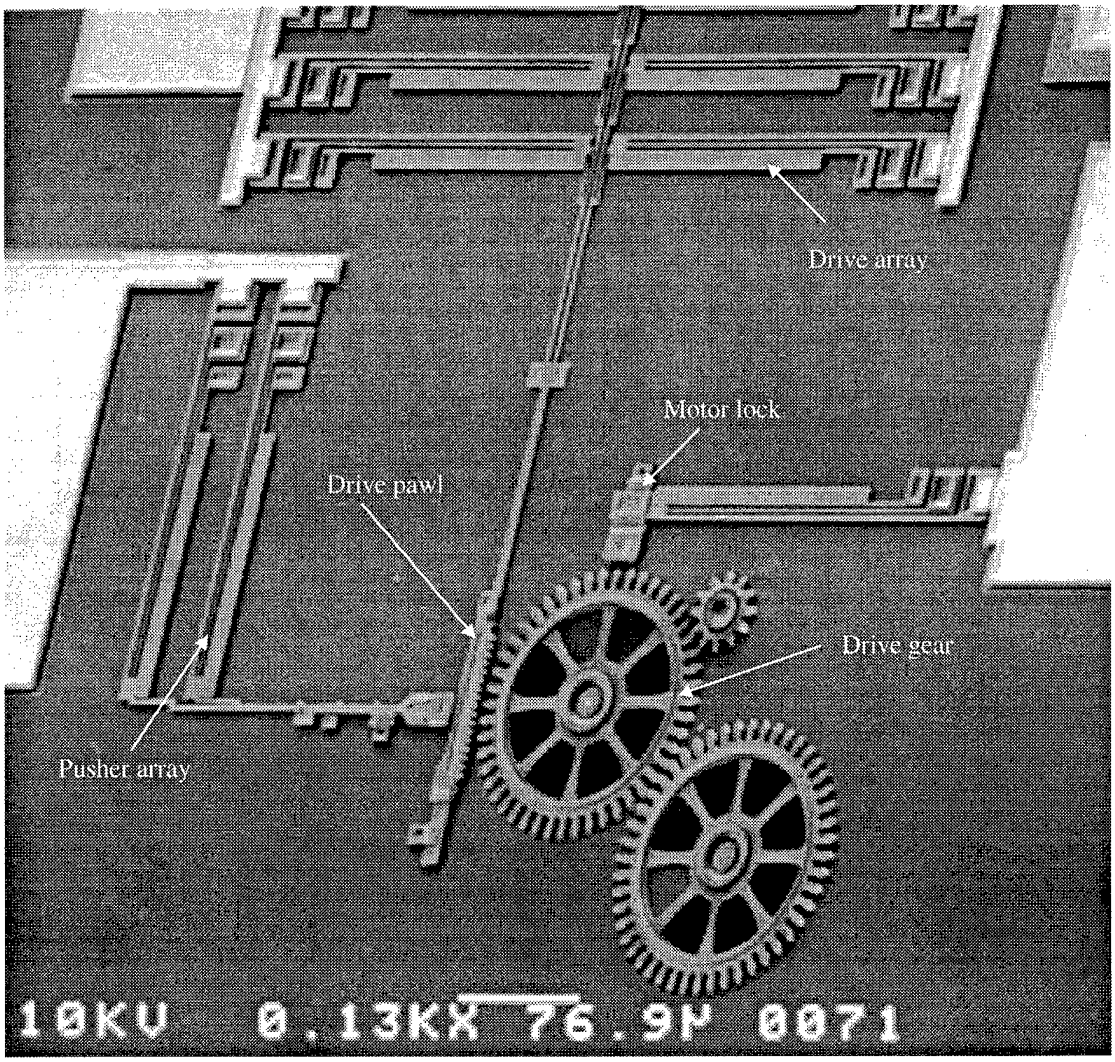

Figure 9.14. A micromotor driven by a 2-H actuator array (fabricated by the author in MUMPs 17).

Table 9.4 summarizes the properties of lateral single and double hot arm thermal actuators. A 2-H actuator can not replace a 1-H actuator in all applications; drive voltage is higher for a 2-H actuator than a 1-H actuator. However many applications can benefit from the lower actuator response time and the smaller layout area of 2-H actuator arrays. The 2-H actuator shown in Figure 9.8 is a first generation device, whereas the 1-H actuator in Figure 7.4 is at least a third generation device.

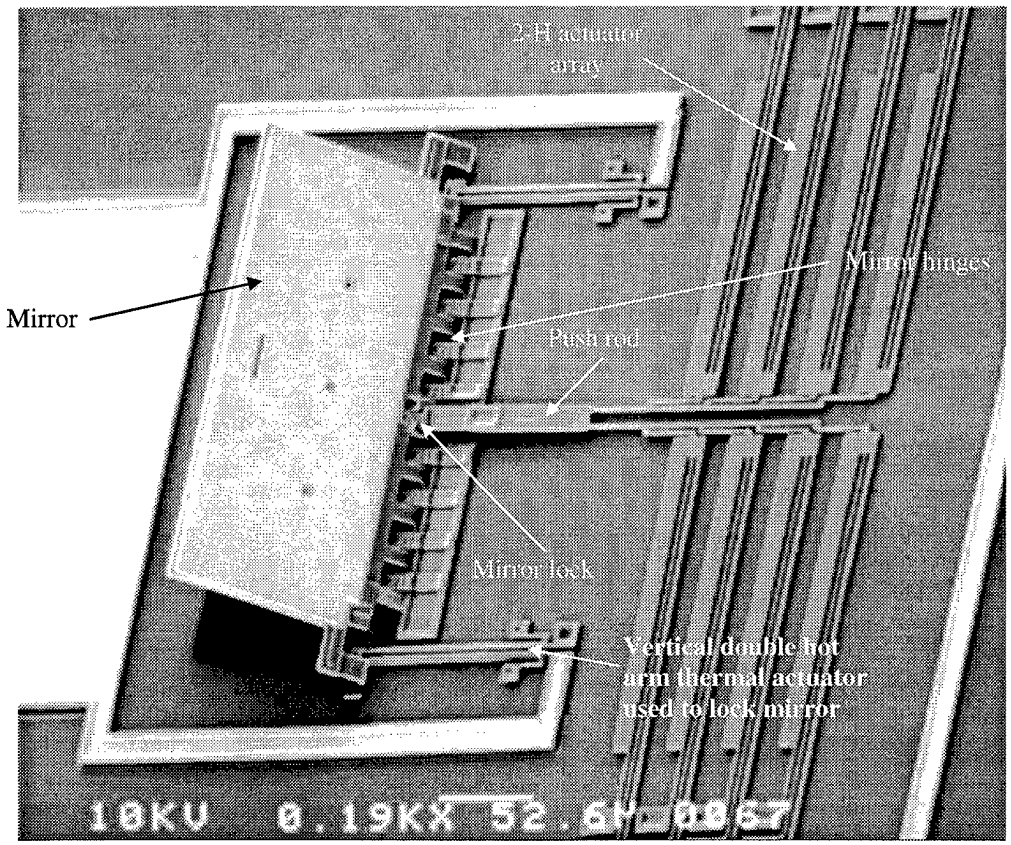

Figure 9.15. A fan micromirror driven by a double hot arm thermal actuator array (fabricated by the author in MUMPs 17).

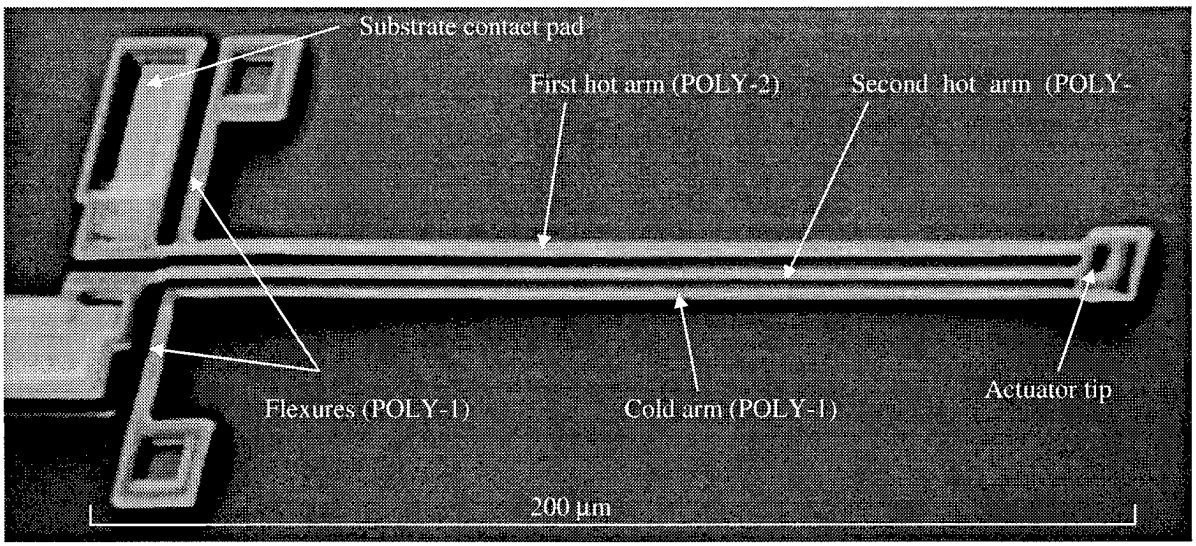

Figure 9.16. A vertical double hot arm thermal actuator (fabricated by the author in MUMPs 17).

Table 9.4. Comparison of 1-H Actuator (Figure 7.4) and 2-H Actuator (Figure 9.8) Operating Properties.

	1-H actuator	2-H actuator
Electrical resistance	1.510 KΩ	2.413 KΩ
Maximum deflection (positive)	10 μm	14 μm
Maximum deflection (backbending)	8 μm	12 μm
Maximum force	11.4 μN	20.5 μN
Maximum current before backbending (under load)	5.12 mA	5.59 mA
Maximum operating frequency (air)	12 kHz	17 kHz
Maximum operating frequency (nitrogen at 40 mTorr)	4 kHz	27 kHz

9.3 Nonlinear Flexures

One drawback of electrostatic actuation is that electrostatic force is a nonlinear function of distance; electrostatic force increases exponentially as the distance between electrodes decreases. Supporting flexures typically provide a restorative force that is a linear function of distance. After the separation distance between the electrodes in a device with linear force flexures decreases by one-third, the positions of the electrodes become unstable and they quickly travel the remaining separation distance (snap-through). Snap-through limits the useful range of motion in an electrostatic device with linear force flexures to one-third of the initial separation distance between electrodes. This section reviews a variety of nonlinear flexures designed by the author to increase the distance electrodes in an electrostatically actuated micromirror can travel before snap-through.

Two nonlinear flexure designs from the macro-world are shown in Figure 9.17. The truck suspension in Figure 9.17(a) relied on a main spring for support under most load and driving conditions. If a heavy load or excessively bumpy road was encountered, the axle would be depressed upward so that the auxiliary spring contacted the bearing plates. The auxiliary spring increased the system spring constant and provided additional

restorative force to counter the axle's upward motion [7]. This suspension concept applied to micromirrors is called an "auxiliary flexure design."

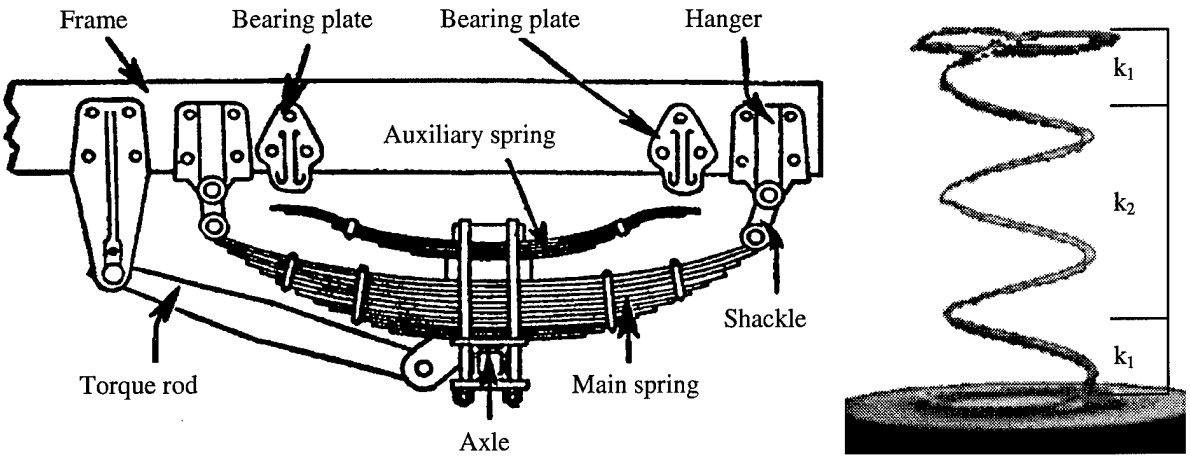

(a)Truck suspension [7] (b) Mattress spring [8]

Figure 9.17. Examples of nonlinear flexures. The image of the mattress spring has been copyrighted by the Sealy corporation[8]. The design of the mattress spring has been patented by the Sealy corporation [8].

Another nonlinear flexure design is illustrated by the mattress spring shown in Figure 9.17(b). The mattress spring has two different spring constants, k_1 and k_2. The spring constant for the outer portion of the spring, k_1, is substantially less than the spring constant for the inner portion of the spring, k_2. The outer spring regions depress first as the spring is contracted by the weight of the sleeper. If additional weight is placed on the spring, the inner portion of the spring will begin to compress [8]. Thus the single spring has two different spring constants and the system's spring constant depends on the distance the spring is depressed. Although micromirror flexures designed with dual spring constants are mechanically quite different than the spring shown in Figure 9.17(b), the micromirror's spring constant is functionally similar. Micromirrors flexures with two spring constants are called "dual spring constant flexure designs."

9.3.1 Auxiliary Flexure Designs

The maximum stable deflection distance for a micromirror can be increased using auxiliary flexures. Figure 9.18 shows two electrostatically actuated piston micromirrors similar to the micromirror in Figure 4.22 (Chapter 4) except for flexure modifications. The initial separation between the top electrode and the silicon nitride layer was 2 μm for both micromirrors. The micromirror depicted in Figure 9.18(a) used a conventional POLY-2 flexure at each corner of the micromirror. The POLY-2 flexure was always engaged to resist electrostatic force and is called the main flexure. An auxiliary POLY-1 flexure passed under two POLY-2 overhangs connected to the micromirror's top electrode. The POLY-2 overhangs were similar in function to the bearing plates in Figure 9.17(a). The gap between the top of the auxiliary flexure and the bottom of the POLY-2 overhang was initially the thickness of the second sacrificial oxide layer: 750 nm. After the micromirror in Figure 9.18(a) was deflected 666.6 nm, the top electrode snapped down 84 nm to rest on the auxiliary flexure for a total deflection of 750 nm. The micromirror could then be deflected an additional 475 nm before snap-through. The micromirror in Figure 9.18(a) had a stable deflection region that was 71% larger than the micromirror in Figure 4.22.

A schematic diagram of the micromirror flexure used in Figure 9.18(b) is presented in Figure 9.19. The POLY-2 tip of the auxiliary flexure was fabricated 750 nm above the POLY-1 auxiliary support post. When a voltage was first applied to the micromirror in Figure 9.18(b), the main flexure bent until the auxiliary flexure rested on the auxiliary support post. The micromirror did not exhibit snap-through on the main flexure because the auxiliary flexure added support before the micromirror was displaced two-thirds of a micron. The tip of the auxiliary flexure contacted the auxiliary support post before snap-through because the auxiliary flexure is angled down as a result of the main flexure bending to accommodate electrostatic force. As the applied voltage increased, both the main and auxiliary flexures continued to resist the electrostatic force, until snap-through was reached at a displacement of 950 nm. The micromirror in Figure 9.18(b) was limited by snap-through because the combined flexure resistance was still a linear function of deflection (after the auxiliary flexure rests on the auxiliary support post). However the use of auxiliary flexures increased the maximum stable deflection distance by 50%. Figure 9.20 is a plot of measured deflection versus voltage data for both micromirrors pictured in Figure 9.18.

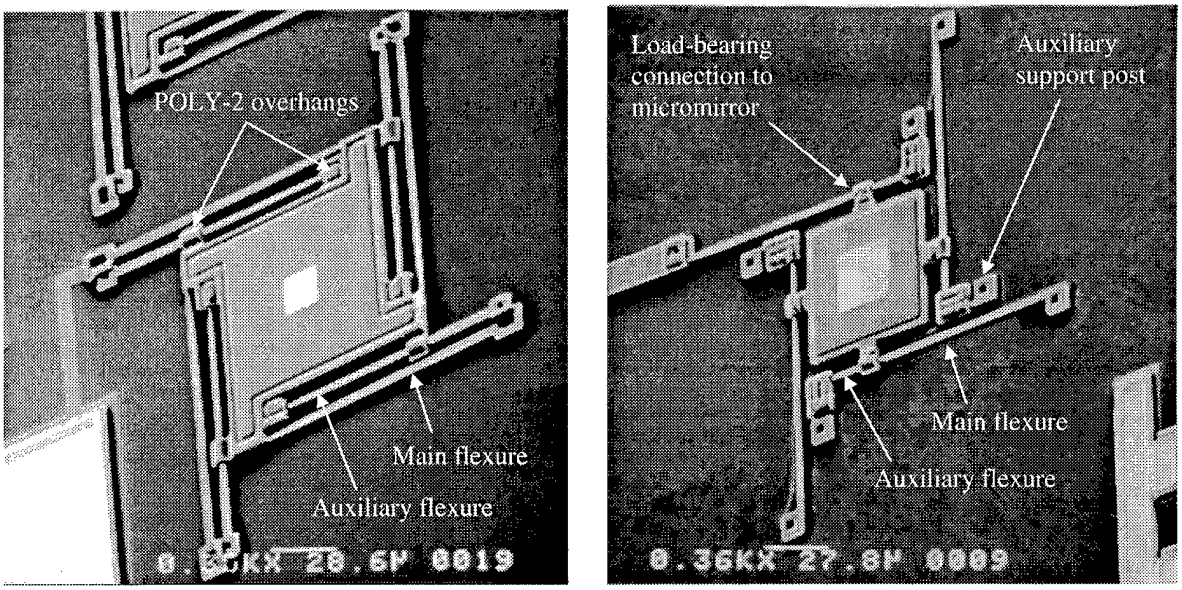

(a) Dual flexures (MUMPs 16) (b) Dual support posts (MUMPs 18)

Figure 9.18. Electrostatically actuated micromirrors with auxiliary flexures fabricated by the author.

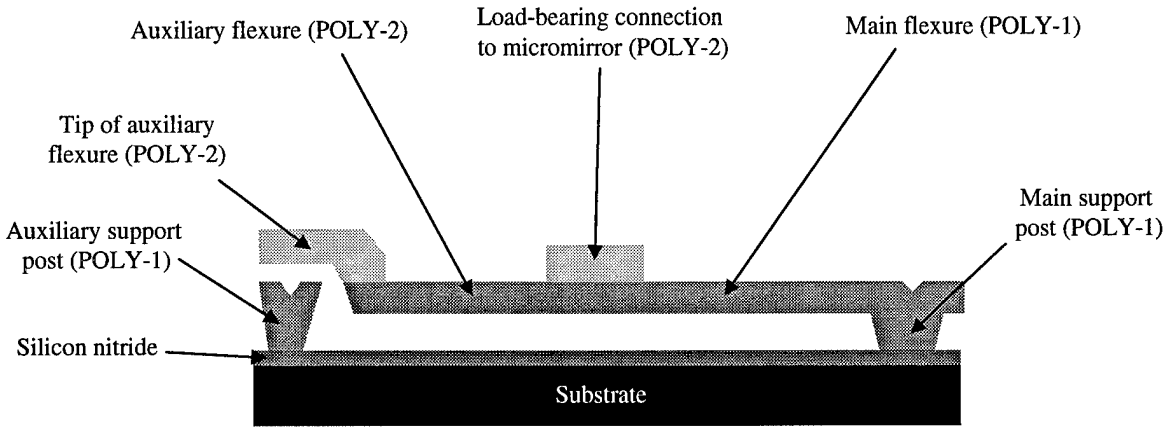

Figure 9.19. Cross-sectional schematic diagram of a dual support post auxiliary flexure micromirror.

9.3.2 Dual Spring Constant Flexure Designs

Unlike auxiliary flexure designs, dual spring constant flexure designs rely on a single flexure that provides two or more different spring constants depending on the deflection distance. Ideally the flexure's force will vary as a nonlinear function of deflection, allowing micromirror deflection versus voltage profiles similar

to those predicted in Figure 4.21 (Chapter 4). The author successfully constructed micromirror flexures with two distinct spring constants. An example of a tilting micromirror with dual spring constant flexures is the slat used in VBG design number 9.

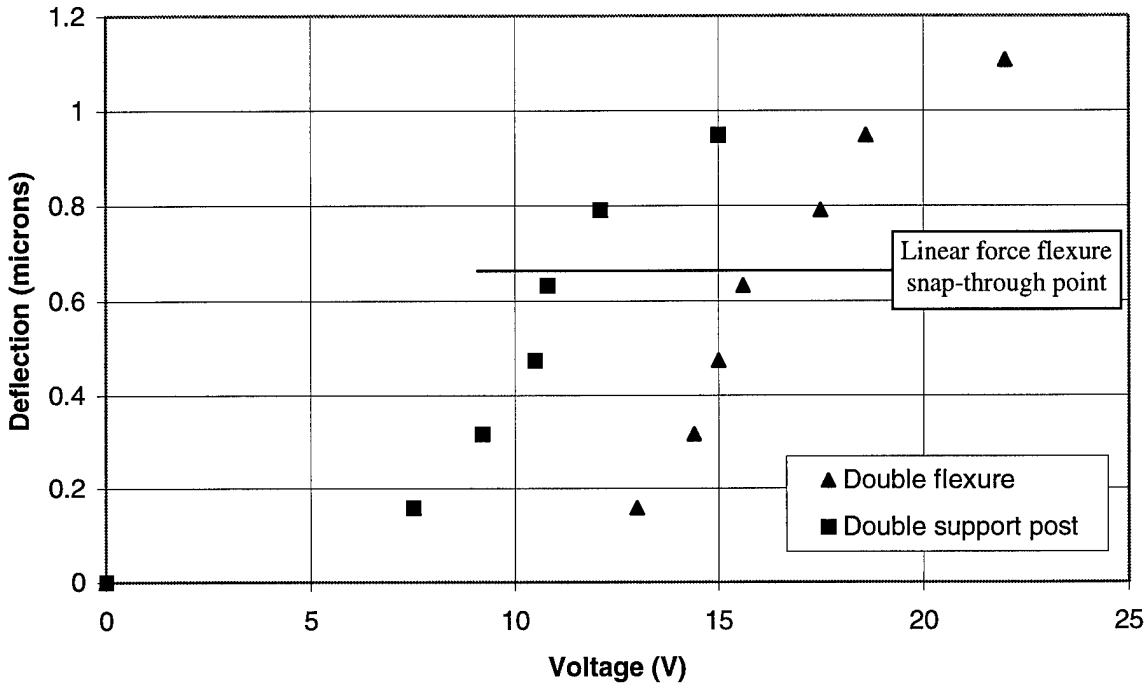

Figure 9.20. Measured deflection versus voltage plot for micromirrors with auxiliary flexures.

Electrostatically actuated variable blaze gratings have a blaze angle that can be changed after construction by tilting each slat towards the substrate using electrostatic attraction between the slat and the substrate. VBG design number 8 used linear force flexures and VBG design number 9 used dual spring constant flexures (VBG design numbers were defined in Table 6.1 in Chapter 6). Slats supported by linear force flexures exhibited snap-through after the edge of the slat traveled one-third of the initial separation distance, limiting the number of diffraction orders that can be supported by the grating. The dual spring constant flexure increased the maximum stable deflection distance for the slat's edge as it was tilted towards the substrate. Figure 9.21 depicts schematic diagrams of variable blaze gratings with linear force (single spring constant) and dual spring constant flexures. Both grating designs used the substrate as the bottom electrode. The slat in Figure 9.21(a) was supported by a linear force torsion flexure. After the edge of the slat opposite the

flexure traveled approximately two-thirds of a micron, it snapped down to the silicon nitride layer. The linear force flexure grating depicted in Figure 9.21(a) supported blaze angles for three diffraction orders.

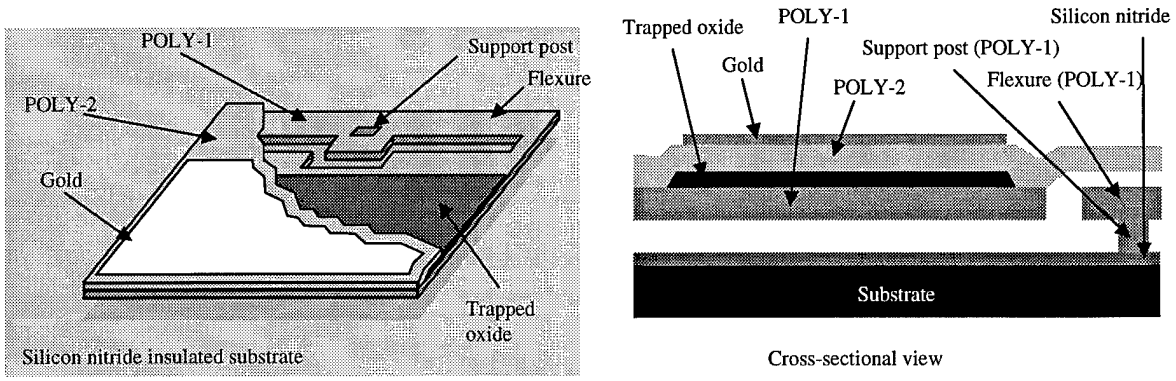

(a) Single spring constant flexure

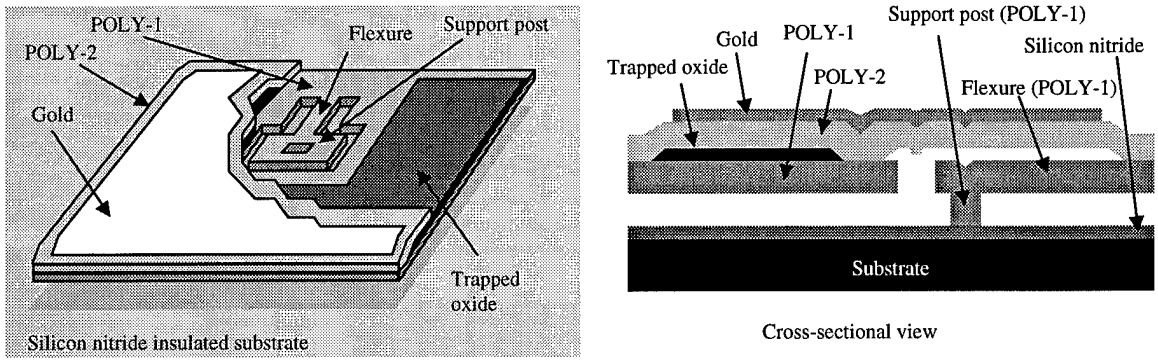

(b) Dual spring constant flexure

Figure 9.21. Schematic diagrams of variable blaze gratings with single and dual spring constant flexures.

Electrostatic force also pulled the edge of the slat opposite the flexure towards the substrate when a voltage was placed between the dual spring constant flexure slat (Figure 9.21(b)) and the substrate. If the voltage was increased, the slat would snap down to rest on the top of the support post. Higher voltages resulted in the slat rotating on top of the support post until the edge of the slat eventually rested on the substrate. The slat did not exhibit snap through until the edge of the slat was less than 300 nm above the silicon nitride layer. The slat's flexure exhibited two distinct spring constants: one value before the slat rested on the support post and a higher value after the slat rested on the support post. The second spring constant was caused by changing the direction and amount of force on the flexure. The flexure bent to counter the electrostatic force before the slat rested on the support post. After the slat rested on the support post, the flexure continued to bend and the edge of the flexure opposite the support post was lifted up.

The nonlinear force flexure grating supports blaze angles for five diffraction orders: two more than the linear force flexure grating. The first additional diffraction order was a result of increasing the range of stable tilt angles. The second additional diffraction order was a result of moving the support post under the slat; the mirror's position on the substrate and support post matched the blaze angle for the next highest diffraction angle after snap-through. Figure 9.22 is a plot of slat edge deflection versus voltage for the grating slats used in VBG design numbers 8 and 9. Measurements for Figure 9.22 were obtained with a HeNe laser (632.8 nm wavelength) in air. Each data point in Figure 9.22 corresponds to an integer diffraction order. Slat edge deflections were calculated based on the observed grating blaze angle.

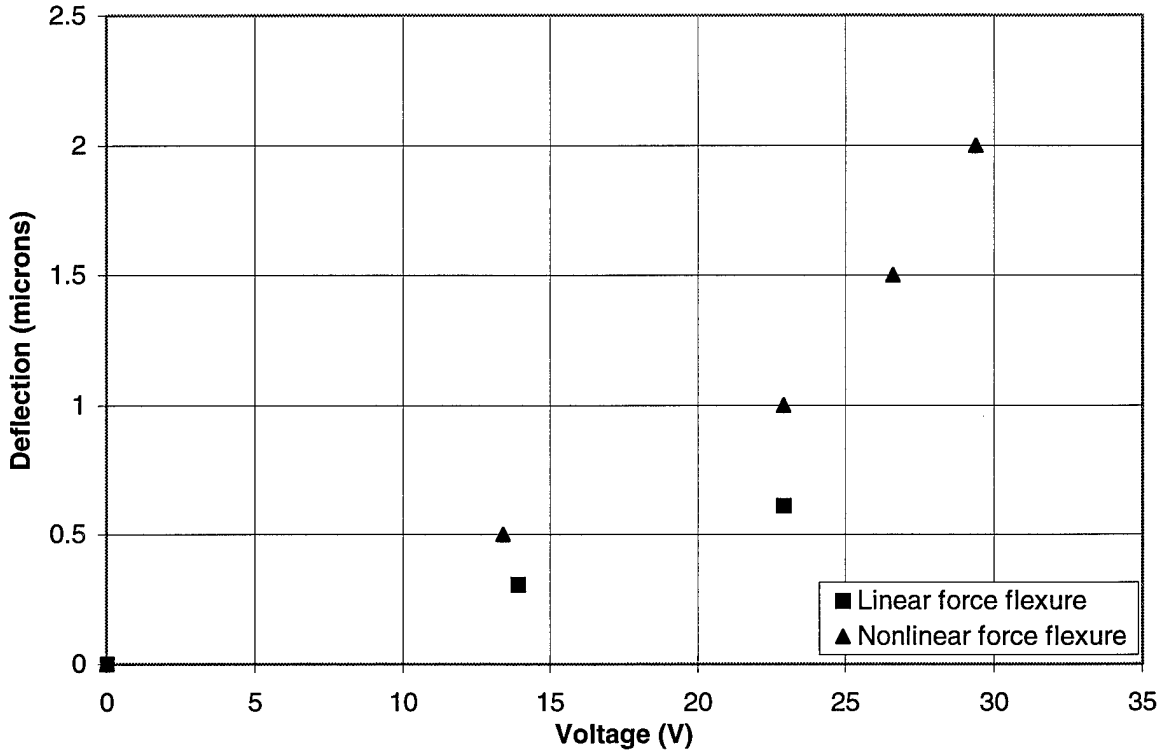

Figure 9.22. Deflection versus voltage plot for variable blaze grating slats suspended by linear and nonlinear flexures.

In addition to an increased useful range of motion, nonlinear flexures provided a fabrication benefit as well; micromirrors with nonlinear flexures tended to suffer stiction to the silicon nitride layer much less than micromirrors with linear flexures. Also micromirrors with auxiliary flexures typically had higher optical power ratings than micromirrors with traditional flexures because the additional flexures assisted in conducting absorbed optical power out of the micromirror.

9.4 Improved Single Use Micromotors

The author's original single use micromotor design was shown in Figure 5.15 (Chapter 5). The author continued to improve the ratchet design used in Figure 5.15. Two of the improved single use micromotors designs are the quad array POLY-1 former remover and the dual array micromirror assembler. These micromotors were an improvement over existing micromotor designs because they required only a single square wave drive voltage. The teeth of the drive rod and drive pawls in all ratchet micromotor designs were angled so that they engaged when the pawl was pushed in the direction of desired movement and slid over each other when the pawl returned to its starting position.

Figure 9.23 depicts a quad array micromotor. The quad array micromotor used two sets of opposed 2-H thermal actuator arrays to pull a POLY-1 former out from under a micromirror. Often the initial stiction between the POLY-1 former and the silicon nitride layer or POLY-2 layer was sufficient to prevent the micromotor in Figure 5.15 from pulling out the POLY-1 former. The quad array micromotor had more than enough force to break the initial stiction and consistently remove the POLY-1 former. Each set of opposed (opposite sides of the drive rod) thermal actuator arrays move in the same direction when the square wave voltage is "on" (12.5 V). The set of opposed thermal actuator arrays in the lower right of Figure 9.23 push their drive pawls up and to the left when the drive voltage is on; the set of opposed thermal actuator arrays in the upper left push their drive pawls down and to the right when the drive voltage is on. All drive pawls return to their initial position when the drive voltage is off. Two sets of opposed thermal actuator arrays provided a continuous pull on the drive rod as the voltage oscillated. The extra two thermal actuator arrays (compared to the author's original design in Figure 5.15) increased the pulling force and improved the tested reliability of this micromotor to nearly 100% for this application. The maximum frequency of the drive voltage was 300 Hz.

The improved dual array micromotor is shown in Figure 9.24 after it was used to assemble a micromirror. The micromotor in Figure 9.24 had four additional thermal actuators and a reduced area drive pawl (to lower friction against the silicon nitride layer) compared to the micromotor in Figure 5.15. The top electrode of the micromirror in Figure 9.24 was formed over a flat region of the die to avoid unintentionally embossing the gold layer by the POLY-0 bottom electrodes. The improved dual array micromotor required 12.0 V at frequencies up to 260 Hz.

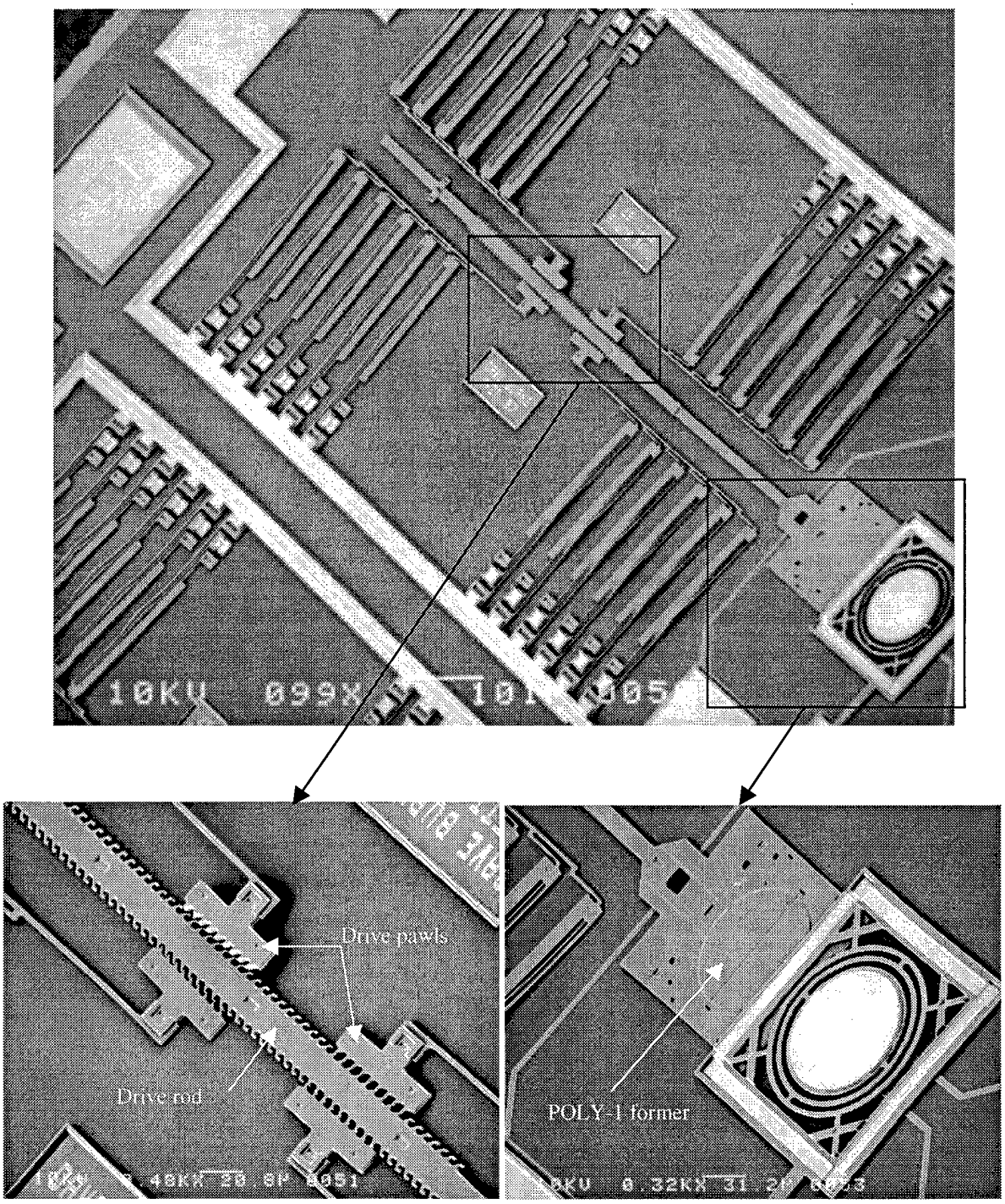

Figure 9.23. A quad thermal array single use micromotor after it was used to remove a POLY-1 former out from under a micromirror (fabricated by the author in MUMPs 20).

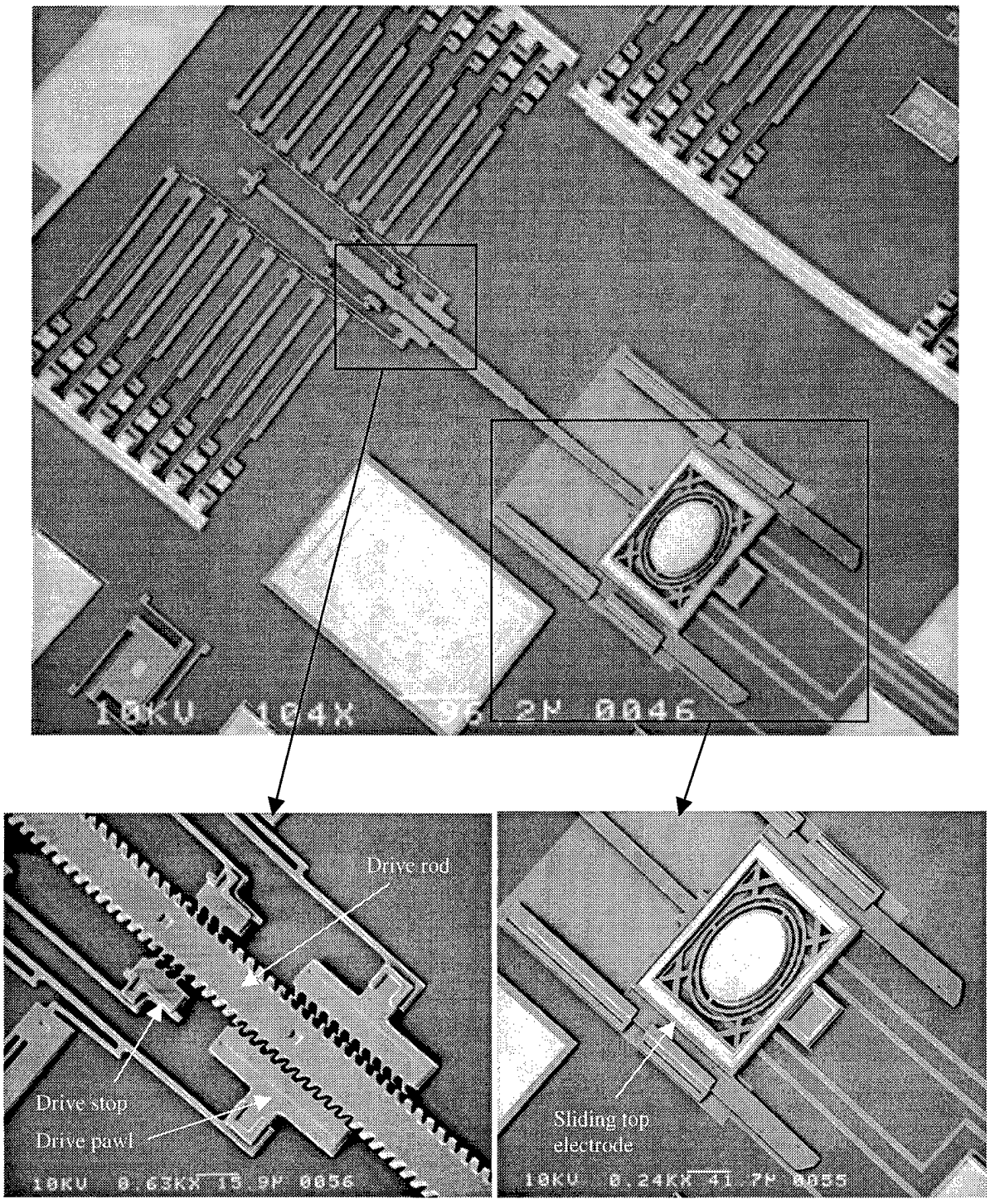

Figure 9.24. A dual thermal array single use micromotor after it was used to assemble a micromirror (fabricated by the author in MUMPs 20).

9.5 Variable Blaze Phased Array Slats

Both optical phased arrays and variable blaze gratings fabricated using state-of-the-art surface micromachining processes have limited optical beam steering capabilities. Optical phased arrays have oscillations in their far field irradiance as a function of steering angle. VBGs are limited to discrete steering angles. The author invented an optical device which has the potential to overcome some of these problems: the Variable Blaze Phased Array (VBPA). VBPAs have slats that can tilt (similar to a VBG) and piston (similar to an optical phased array) simultaneously. Figure 9.25 shows four 60 μm wide and 2.5 mm long VBPA slats designed by the author. The stacked-poly slats use electrostatic attraction to tilt and embedded thermal actuators to piston. Because electrostatic force is dependent on distance, each slat has its own separate POLY-0 bottom electrode to create the electrostatic force required to tilt the slat. The substrate is used to return the current flowing through the thermal actuators. The top electrode is used to pass current into the thermal actuators. Figure 9.26 is a schematic diagram of a VBPA slat.

Each slat in a VBPA can independently tilt and piston giving a VBPA four advantages over VBGs and optical phased arrays: continuous angle beam steering, reduced amplitude oscillations, reduced power secondary steered beams, and beam steering angles beyond the π inter-element phase limit (from Equation (4.8), Chapter 4). Most of the slat is constructed from stacked-poly as shown in Figure 9.26. However the region above the dividing line in Figure 9.26 is constructed only from POLY-2 because the lower POLY-1 layer was used to form slat flexures which also function as thermal actuators. The support post is a substrate contact pad; substrate contact pads can only be fabricated using POLY-2 so an exposed support post (similar to VBG design number 5) was used. Measured peak-to-valley curvature for this device is 72.1 nm. Equations (9.1) and (9.2) define the slat blaze angle, γ, and the slat incremental deflection distance, d, to steer a normally incident plane wave to an angle θ:

$$\gamma = \frac{1}{2}\theta \tag{9.1}$$

$$d = a\sin\theta \tag{9.2}$$

where a is the VBPA period. Equations (9.1) and (9.2) were derived from Equations (4.10) and (4.5) in Chapter 4, respectively.

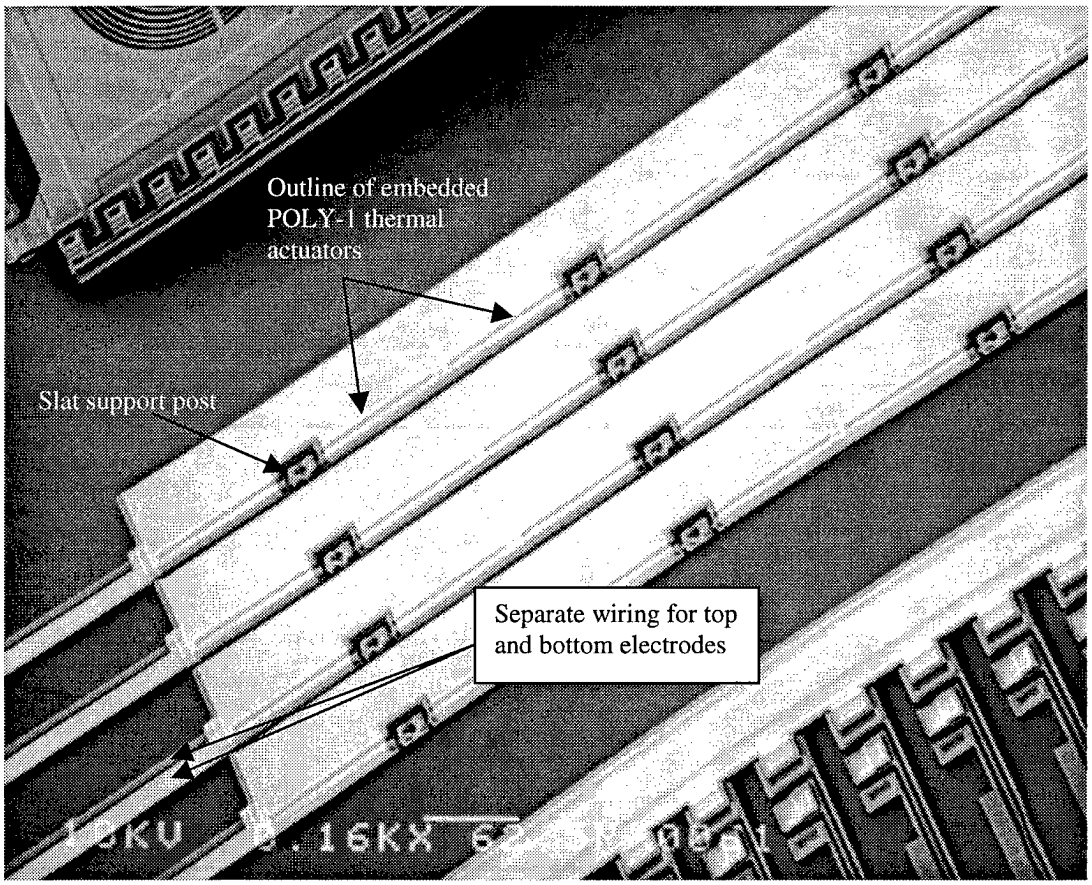

Figure 9.25. Scanning electron micrograph of a VBPA (fabricated by the author in MUMPs 20).

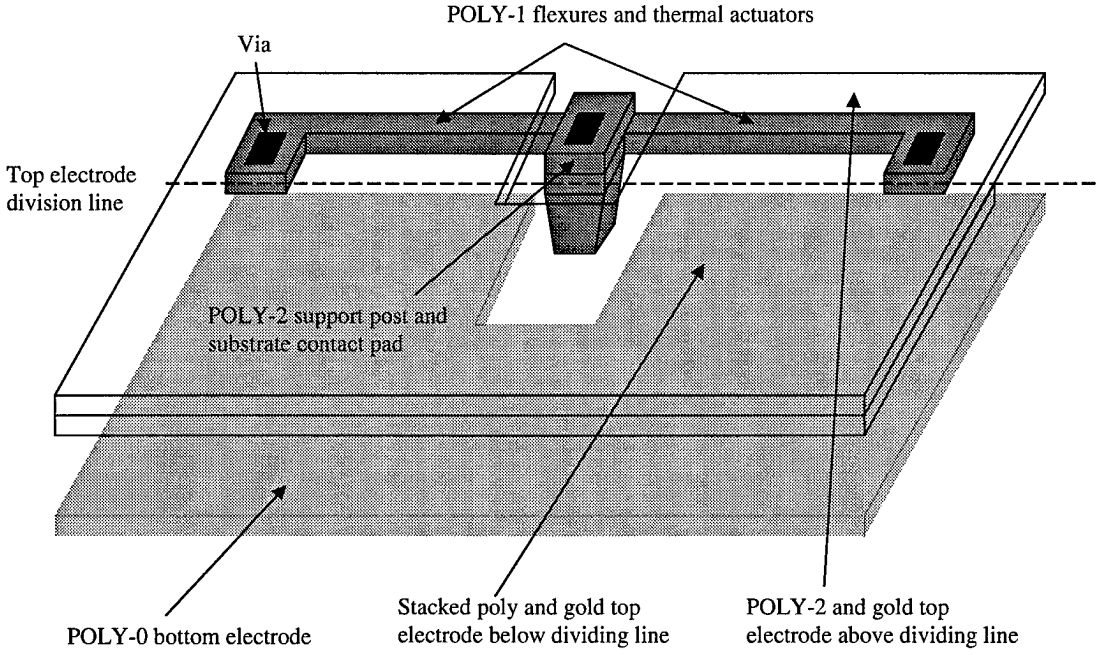

Figure 9.26. Schematic diagram of the actuator and support structure in a VBPA slat. The top electrode was made transparent in order to make the lower layers visible.

Note that in Equations (9.1) and (9.2) all of the slats are tilted to the same angle, γ, however each slat may be pistoned to unique height (a distance d lower than the previous adjacent slat). As in optical phased arrays, the phase can be unwrapped by repeatedly subtracting the distance $\lambda/2$ from d (a round trip phase delay of λ shifts the phase by 2π). Figures 9.27 and 9.28 are FFT simulations of a 36 slat array composed of the VBPA slats shown in Figure 9.25. Figure 9.27 shows the predicted far field irradiance pattern for the VBPA with the slats actuated to steer the incident light to an angle of 0.907° (exactly half way between the first (m=1) and second (m=2) diffraction orders for a VBG with this period). Figure 9.28 is a plot of predicted optical efficiency as a function of VBPA beam steering angle. The maximum stable blaze angle before snap through is 0.637° at the lowest slat height. The optical efficiency is greatly reduced for beam steering angles above twice the maximum stable blaze angle (1.21°).

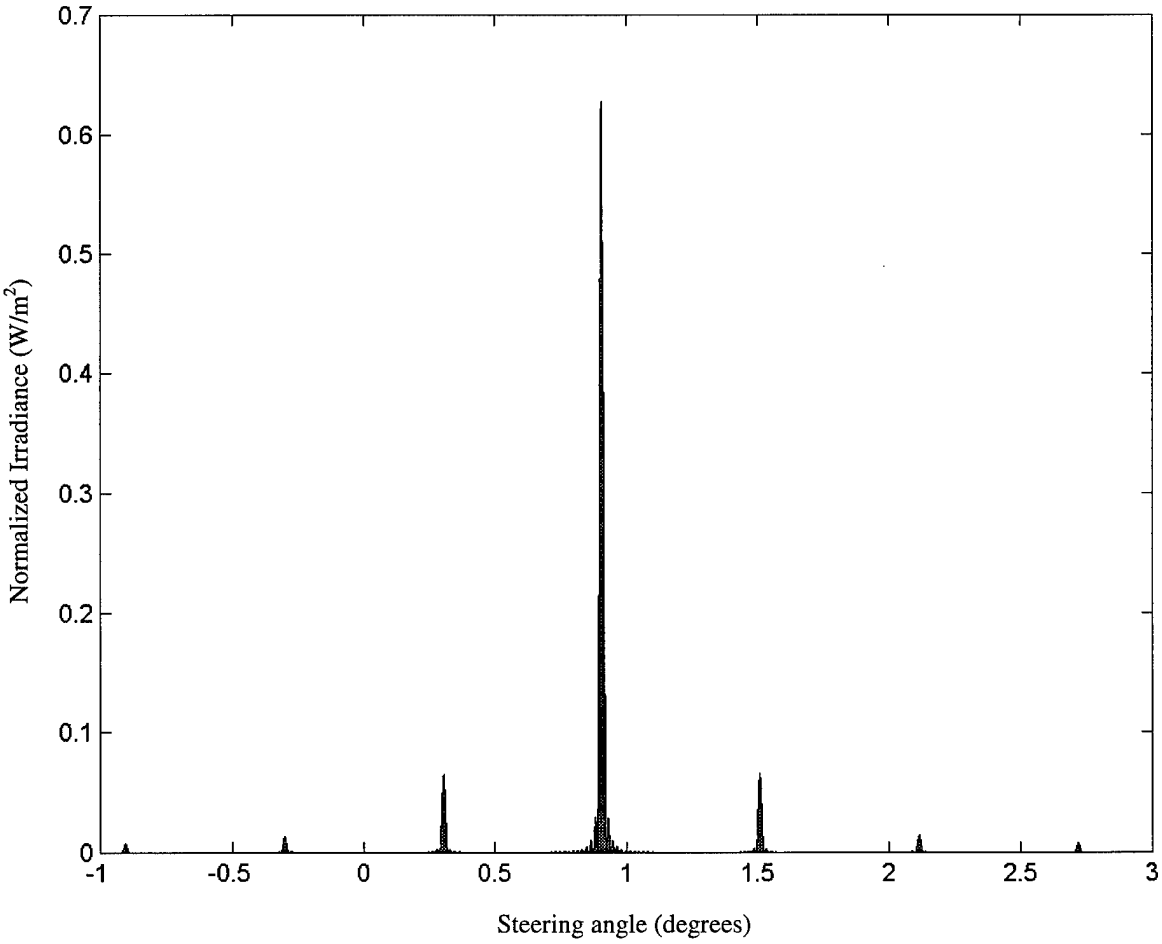

Figure 9.27. Predicted far field irradiance for a 36 slat VBPA illuminated by a coherent normally incident source at a wavelength of 632.8 nm. Slats were tilted and pistoned to select a steering angle of 0.907°.

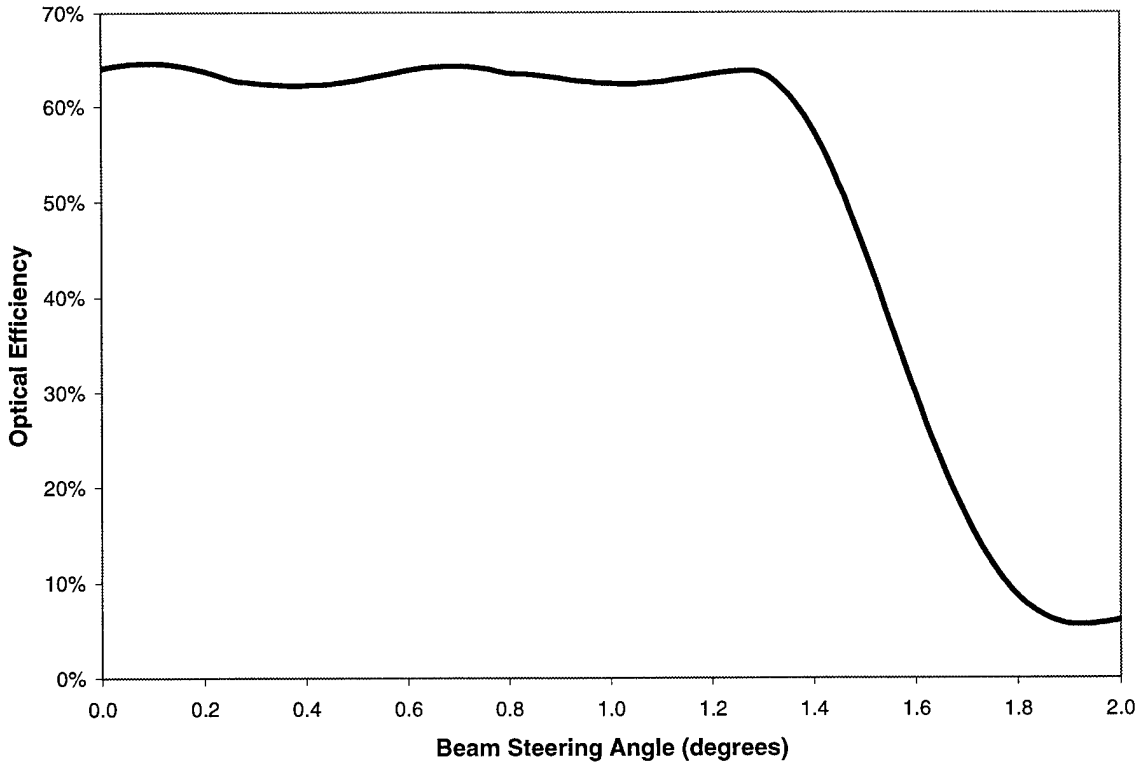

Figure 9.28. Predicted optical efficiency for a 36 slat VBPA illuminated by a normally incident coherent source at a wavelength of 632.8 nm.

Unfortunately combining the best of VBGs and optical phased arrays from an optical beam steering viewpoint resulted in a combination of the worst of electrical drive requirements for these two devices. Each slat in a VBPA requires two unique signals: an electrical current to set the slat height and an electrical potential on the bottom electrode to set the slat blaze angle. In addition, the two signals are inter-related; the electrical potential on the bottom electrode must account for the selected slat height as well as the voltage on the top electrode (resulting from the current flowing through the thermal actuators). Fortunately the two signals for each slat are predictable and could be generated using an integrated control circuit (perhaps fabricated using the silicon on the other side of the die).

The author was able to piston and tilt individual slats in the VBPA shown in Figure 9.25. Slats were capable of pistoning upward more than 316.4 nm using 3.5 V at 60 mA. Slats could be tilted to support a beam steering range of 1.20°, which was the full range before snap through for slats at the lowest height, using 24.2 V

on the bottom electrode and a grounded top electrode. All of these measurements were made using the ZYGO microscope. The VBPA shown in Figure 9.25 is a first generation device; it is possible that the design techniques used to improve the maximum stable blaze angle of the author's VBG designs (such as VBG design number 9) could be applied to improve the performance of future VBPA designs.

9.6 Integrated VCSEL Beam Steering System

The author's initial integrated VCSEL beam steering system design is shown in Figure 9.29 (from the author's dissertation prospectus, Figure 50 [9]). The author worked with Captain Joseph Bouchard [10] to improve and verify the design shown in Figure 9.29. Modifications to the initial design include: a new VCSEL connection technique, a Fresnel microlens, an improved slide-over micromirror, and a larger second stage fan micromirror. The improved integrated VCSEL beam steering system is shown in Figure 9.30. A close-up view of the integrated VCSEL is shown in Figure 9.31.

The original design used a combination of surface and bulk micromachining to etch a 100 μm deep pit for the VCSEL. A flip-wire based on a design by Comtois [11] was used to make contact with the VCSEL. This design proved unusable; all attempts to chemically etch the 100 μm deep pit resulted in damage to the micromirrors on the surface of the die. The improved design used a POLY-2 and gold substrate pad to ground the bottom of the VCSEL and a direct wirebond to connect the top surface of the VCSEL to the power supply (visible in Figure 9.31). Solder was melted between the bottom of the VCSEL and the substrate pad to lower the electrical resistance and to secure the VCSEL in place.

The Fresnel microlens was added to collimate the output of the VCSEL. The diameter of exit aperture of the VCSEL is approximately 10 μm and causes significant beam expansion due to diffraction. The Fresnel microlens is located a distance of 500 μm from the VCSEL's exit aperture (equal to the focal length of the Fresnel microlens). The original slide-over micromirror was not capable of rotating 135°; the top scissor hinge was not large enough to accommodate the rotation. The improved slide-over micromirror was capable of rotating 135° and is visible in Figure 9.31. The size of the second stage fan micromirror was extended both in width and length to increase the beam steering angle. The author's 2-H thermal actuators were used to actuate

the higher mass of the extended fan micromirror. The improved integrated VCSEL beam steering system met all design objectives and was successful is steering the output of the VCSEL [10].

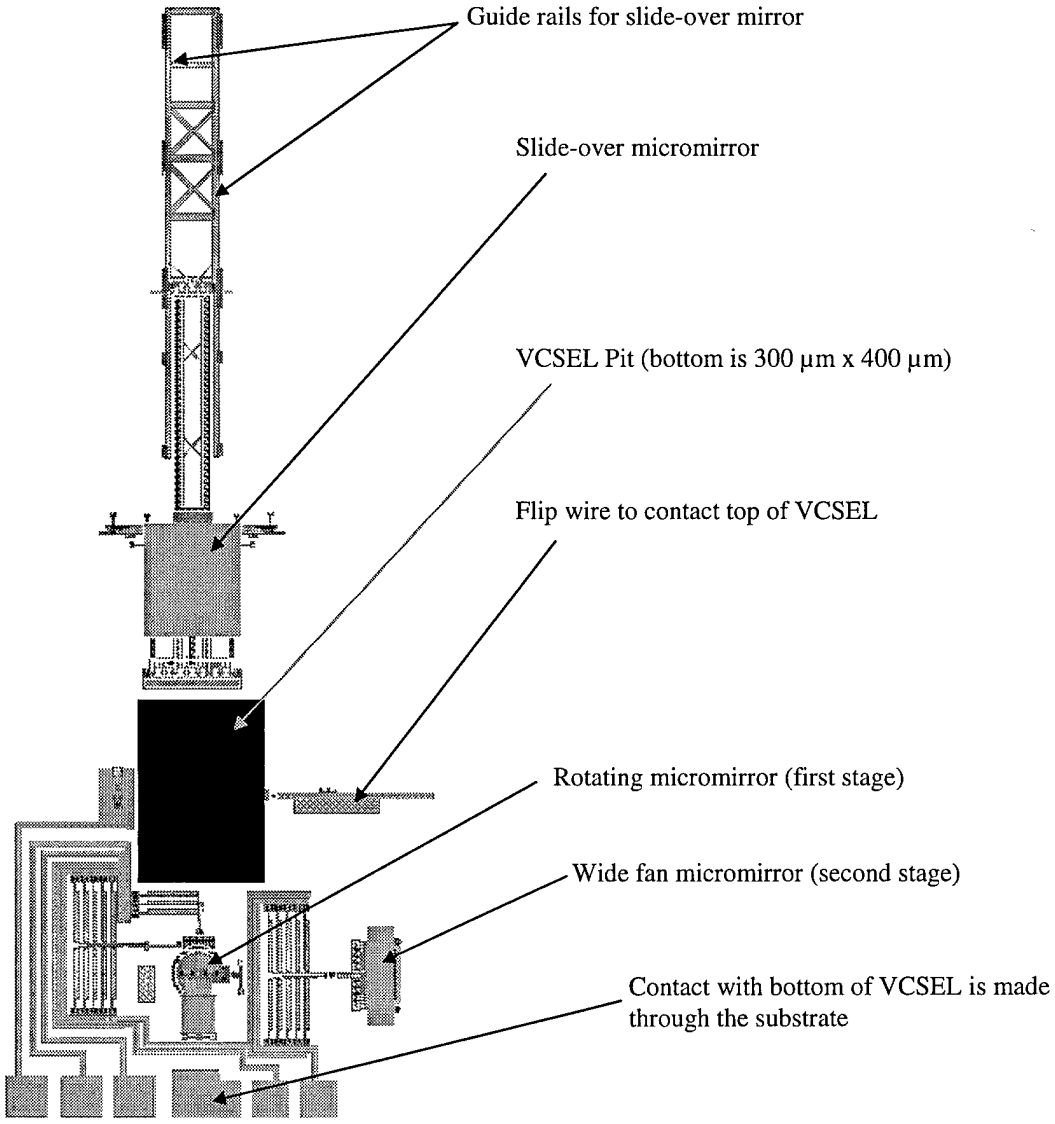

Figure 9.29. Design layout for the integrated VCSEL beam steering system (fabricated by the author in MUMPs 14).

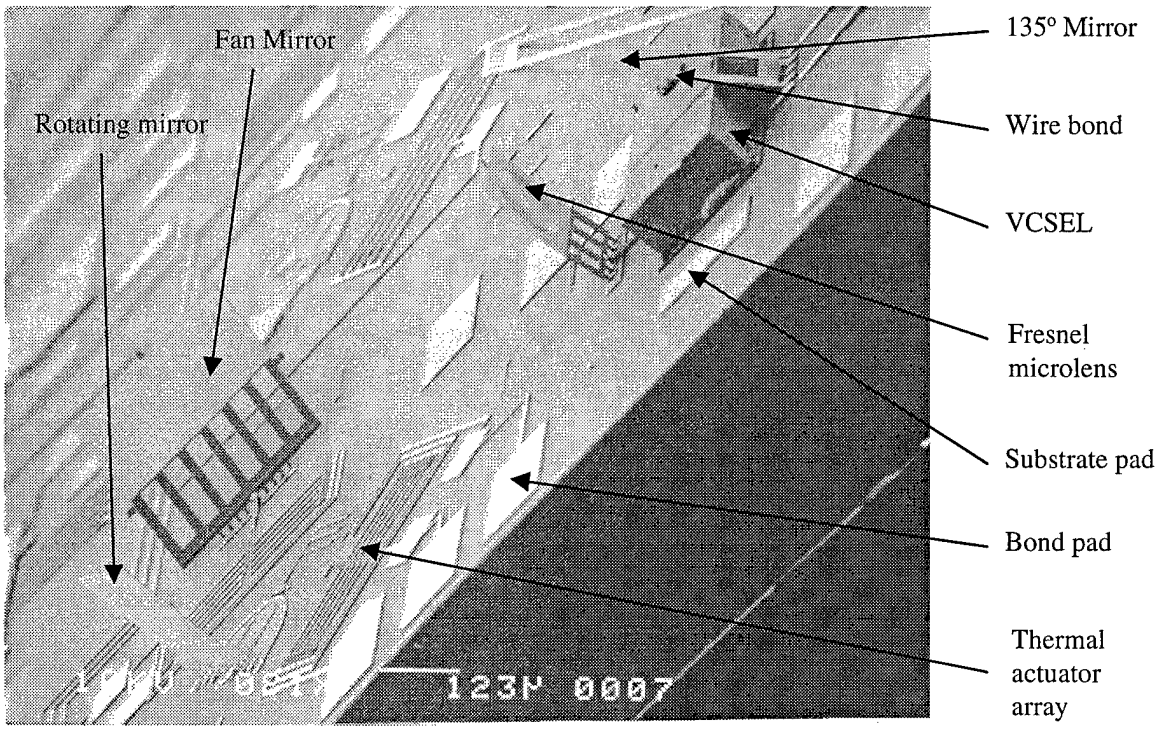

Figure 9.30. An integrated VCSEL beam steering system (fabricated by the author and Bouchard in MUMPs 20) [10].

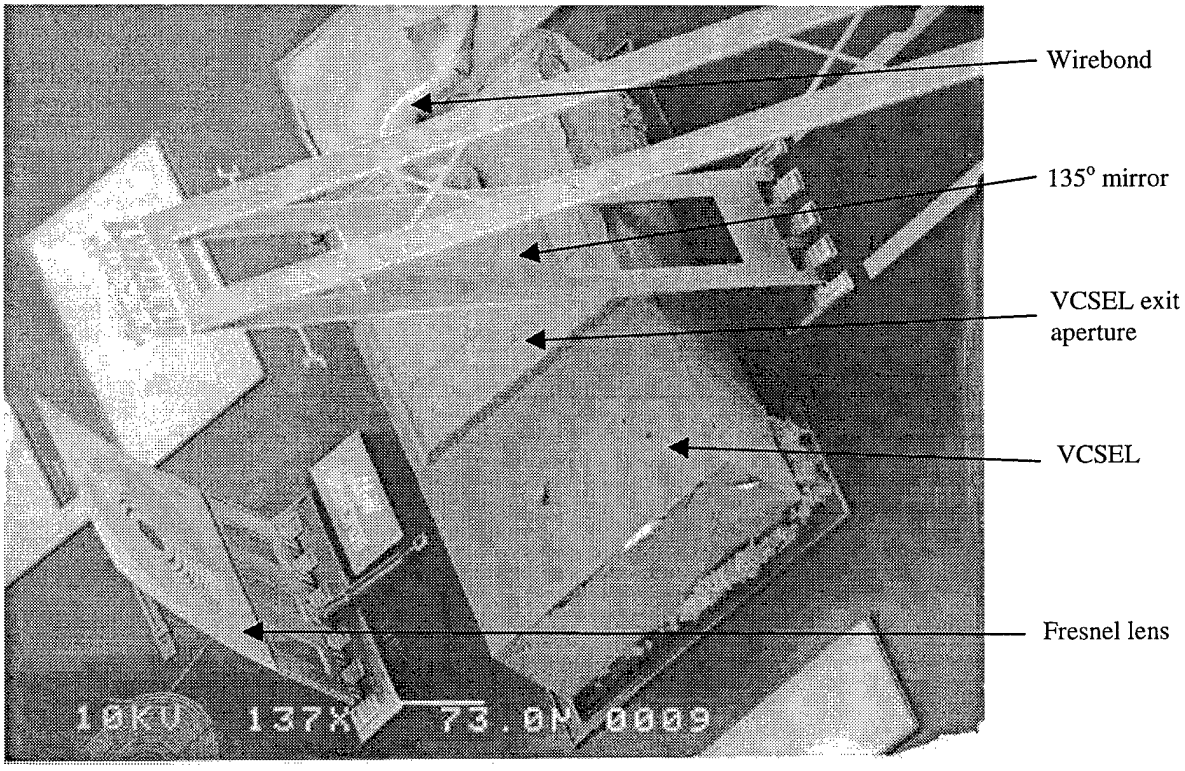

Figure 9.31. Close-up view of an integrated VCSEL (fabricated by the author and Bouchard in MUMPs 20) [8].

9.7 Reference

[1] E. Hecht, *Optics, Second Edition*, Reading, MA: Addison-Wesley Publishing, 1990.

[2] J. H. Comtois and V. M. Bright, "Design techniques for surface-micromachining MEMS processes," *Proc. SPIE*, vol. 2639, pp. 211-222, 1995.

[3] J. R. Reid, V. M Bright, and J. H. Comtois, "Force measurements of polysilicon thermal micro-actuators," *Proc. SPIE*, vol. 2882, pp. 296-306, 1996.

[4] J. T. Butler, V. M. Bright, and W. D. Cowan, "SPICE modeling of polysilicon thermal actuators," *Proc. SPIE*, vol. 3224, pp. 284-293, 1997.

[5] J. H. Comtois and V. M. Bright, "Surface micromachined polysilicon thermal actuator arrays and applications," *Technical Digest, Solid State Sensor and Actuator Workshop*, Hilton Head, SC, pp. 174-177, 1996.

[6] J. R. Reid, V. M. Bright, and J. H. Comtois, "Arrays of thermal micro-actuators coupled to micro-optical components," *Proc. SPIE*, vol. 2865, pp. 74-82, 1996.

[7] J. Heitner, N. G. Shidle, and T. A. Bissel, *Elements of Automotive Mechanics*, New York, NY: D. Van Nostrand Co, Inc., 1946.

[8] Mattress spring image downloaded from the Sealy corporation website at *www.sealy.com* on June 2, 1997.

[9] D. M. Burns, "Microelectromechanical optical beam steering systems design and performance," *Dissertation research prospectus*, Air Force Institute of Technology, AFIT/DSG/ENG/98J, August 29, 1996.

[10] J. G. Bouchard, "Microelectromechanical scanner using a vertical cavity surface emitting laser," *Master's Thesis*, Air Force Institute of Technology, Wright-Patterson AFB, OH, AFIT/GCS/ENG/97D-04, December 1997.

[11] J. H. Comtois, "Structures and techniques for implementing and packaging complex, large scale microelectromechanical systems using foundry fabrication processes," *Doctoral Dissertation*, Air Force Institute of Technology, Wright-Patterson AFB, OH, AFIT/DS/ENG/96-04, May 1996.

10 Summary

This chapter answers the questions:

What accomplishments did the author make in his research? (Section 10.1)

What are the Air Force applications for this research? (Section 10.2)

and recommends areas for further research (Section 10.3).

10.1 Review of significant accomplishments

The author's initial research objectives were listed in Table 1.2 (Chapter 1). The author's accomplishments towards meeting these research objectives are summarized in Table 10.1. The progression of the author's research is depicted in Figure 10.1.

10.2 Air Force Applications

The Air Force has a large number of applications for directing optical energy including: communications, weapon guidance, navigation, range finding, counter-measures, and mapping. A complete discussion of each of these applications is not practical in this document. Instead the author will describe a specific Air Force application of his research: the development of a Micro (less than 100 cm^3 in volume) Air Vehicle (MAV) for targeting and reconnaissance missions. MAVs could be designed to be expendable and fly several meters above the ground for a limited duration (two or three hours). The components of a MAV discussed in this section include: micro laser radars (micro lidars), micro target designators, and micro free space communication transceivers. The technology required to construct practical MAVs should be available in the near future, 2–3 years from the publication date of this dissertation.

Table 10.1. Author's Research Accomplishments.

Research Topic	Accomplishments
HDSI project	1. Improved optical efficiency and fill factor for state-of-the-art optical arrays 2. Developed fast beam steering micromirrors to meet HDSI requirements 3. Invented and validated single use micromotors capable of automatically assembling HDSI fast beam steering micromirrors.
VBGs	1. Invented and validated VBGs for optical beam steering applications 2. Improved diffraction efficiencies by developing and exploiting models of physical and optical construction properties 3. Increased maximum blaze angles by developing nonlinear support flexures
Microlens arrays	1. Investigated the use of polyurethane as a construction material for surface micromachined lenses 2. Validated the use of decentered Fresnel microlens arrays for optical beam steering 3. Developed thermal actuators capable of moving Fresnel microlens arrays
Maximum optical power rating	1. Developed and validated a model to predict the maximum optical power rating for a specific MEMS optical device 2. Determined the maximum operating temperature for a MUMPs micromirror
Integrated VCSEL beam steering	1. Invented a surface micromachined system to steer the output of a VCSEL 2. Developed (with Captain Bouchard) methods for integrating a VCSEL on a MUMPs die
Additional topics	1. Improved predicted optical efficiency by reducing the curvature due to residual material stress in micromirrors 2. Improved the release process used to remove the sacrificial layers in a MUMPs die 3. Invented surface micromachined focusing mirrors compatible with MUMPs 4. Invented VBPAs

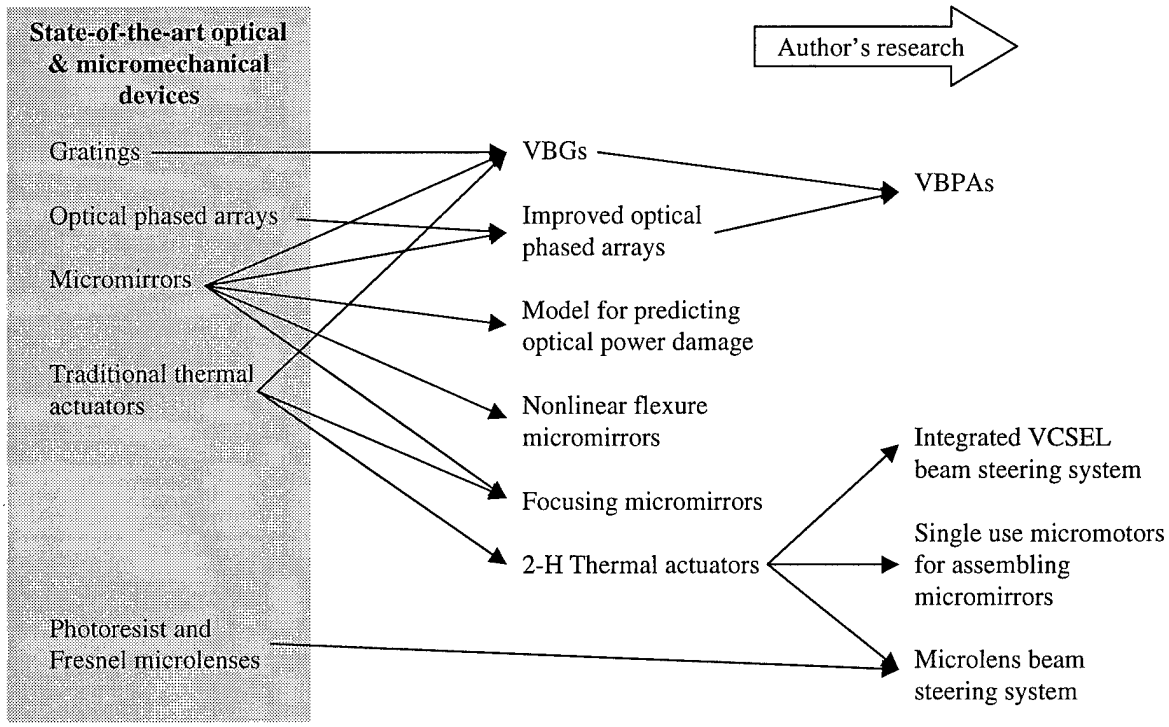

Figure 10.1. Progression of the author's research. Some areas of the author's research, such as the impact of micromirror construction on residual material stress induced curvature, are not shown for clarity; however these areas contributed to the success of many discoveries.

10.2.1 Micro Lidars

A micro lidar is depicted in Figure 10.2 and could be constructed using the technology demonstrated in the author's research (specifically integrated semiconductor lasers and electrostatically driven VBGs). The micro lidar works by steering the output of the semiconductor laser to discrete beam steering angles in a single plane. The micro lidar could be positioned so that it would fan across an arc on the ground a few meters in front of the MAV. The reflected light from the ground would be collected by the VBG and focused into the detector. The micro lidar is highly power efficient because the only moving parts are the VBG slats, which are electrostatically driven. A micro lidar with a five diffraction order VBG could provide altitude, pitch, roll, and collision avoidance data to a MAV's guidance system. A MEMS INU similar to the one shown in Figure 1.2 (Chapter 1) could be used to provide the rest of the data required by the MAV's guidance system.

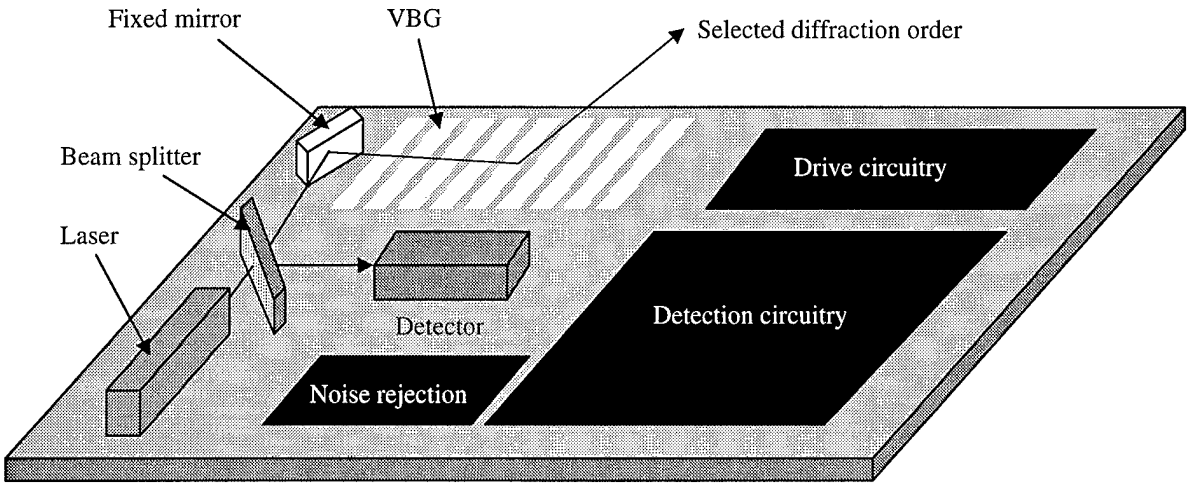

Figure 10.2. Schematic diagram of a single chip micro-lidar.

10.2.2 Micro Target Designators

A micro target designator could be constructed using the integrated VCSEL beam steering system described in Chapter 9. The micro target designator could provide the MAV with a method of illuminating targets for laser guided munitions launched from other platforms (perhaps hundreds of kilometers behind the Forward Edge of the Battle Area (FEBA)). The cooperative concept would increase the safety of aircrews and exploits the expendability of the MAVs. The micro target designator's VCSEL wavelength could be selected so that it would be unique in the battle area; the cooperative platform behind the FEBA could launch its laser guided munitions whenever the VCSEL wavelength is detected, eliminating the requirement for a long distance communication system on the MAV.

10.2.3 Micro Free Space Communication Transceivers

A micro free space communication transceiver could be constructed using an integrated VCSEL and an optical phased array or a VBPA. The transceiver could sweep a laser communications signal across the MAV's horizon; diffraction would spread the signal sufficiently for communication with an adjacent MAV. This

transceiver concept would support a network of MAVs. Each MAV could communicate its target selection with other MAVs in the area and avoid illuminating a target with more than one MAV's laser designator.

10.2.4 MEMS Devices on a MAV

Figure 10.3 depicts a MAV with integrated MEMS devices. MEMS devices for reconnaissance (recce) would be optimized for the MAV's proximity to the ground. Potential reconnaissance sensors would be microphones for detecting tank engines and a galvanometer coupled to a loop antenna for detecting steel. MAV vehicle propulsion and electrical power could be provided by a MEMS-based micro-turbine-engine similar to the micro-turbine-engine depicted in Figure 2.17 (Chapter 2). The fuselage may not be based on conventional airframes such as the model depicted in Figure 10.3; the fuselage could be round. A round shape could hold a single silicon wafer (perhaps 10 cm in diameter) containing all of the MEMS sensors and actuators as well as computer microprocessors and memory. A typical MAV mission could consist of launching hundreds of MAVs in a wave across the FEBA followed 30 minutes later by a salvo of laser guided munitions fired from distant conventional Air Force platforms. Each MAV could orbit its target until the target is destroyed.

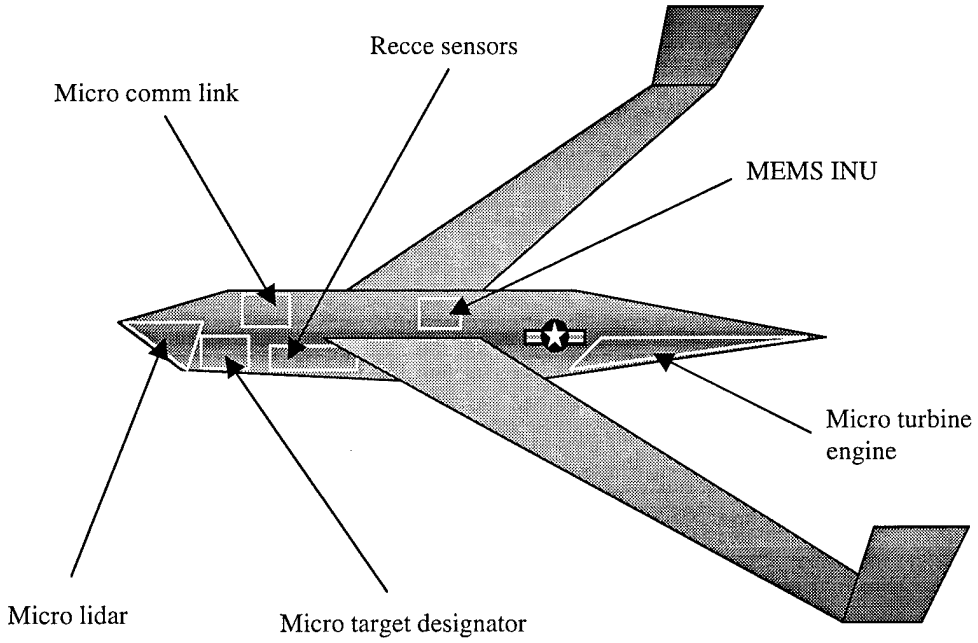

Figure 10.3. A MAV with integrated MEMS.

10.3 Recommendations for Future Research

The author's research was aimed at constructing and verifying methods for steering optical beams with surface micromachined devices. This research resulted in the development of a variety of devices for steering an optical beam; many of these devices were optimized by the author for the surface micromachining process used at AFIT. For example further research would improve the diffraction efficiency of VBGs fabricated in MUMPs by only a few percent according to the author's FFT simulations. Instead future research into VBGs should be directed at developing a VBG for a particular application (period and maximum blaze angle) or for a micromachining process other than MUMPs. However some of the devices developed by the author could benefit from basic research before being directly inserted into an optical system. The devices with the most potential to benefit from future research are: VBPAs, MEMS focusing mirrors, polyurethane microlenses, and decentered microlens beam steering.

10.3.1 VBPAs

Variable blaze phased arrays could be an interim solution for constructing practical optical phased arrays for optical beam steering. Eventually surface micromachined processes will be capable of producing quarter micron (or less) optical phased array element widths; diffraction effects will negate the benefits of blazing these elements. However the development of sub-micron optical phased array periods could be 10–15 years (or more) from the present. VBPAs could be used in the near future, as early as 1–2 years from the present. A VBPA constructed with a currently achievable period (60 μm) would require far fewer control lines than an equivalent surface area sub-micron optical phased array. Even when sub-micron optical phased arrays are available, VBPAs may be better suited for some optical beam steering applications. Future research into VBPAs should address development of a VBPA control system and validate the VBPA concept.

The objective of research into a VBPA control system would be to develop a control system that would accept a single input: the desired beam steering angle. The output of the control system would be two voltages for each slat to simultaneously tilt and deflect that slat. The two voltages for each slat would be inter-related; the voltage required to tilt a slat to a specific angle depends on the slat height. All slats in a VBPA should have the same tilt angle (equal to half the desired beam steering angle for normally incident light); however each slat

may be required to deflect to a unique height. Further research could adapt the control system to accommodate a range of incident light wavelengths.

The VBPA concept could be validated by steering incident light into the nulls between the locations of diffraction orders for a grating with a period equal to the VBPA's period. Halfway between the diffraction orders of a grating are nulls where destructive interference from each grating element cancels out all light. If a VBPA could steer light into a null between adjacent diffraction orders, it would prove that the device functions as a phased array. If the optical efficiency at this location was similar to the predicted value in Figure 9.21 (Chapter 9), it would prove the device functions as a variable blaze phased array. The next step would be to sweep the steered optical beam through an arc using the control system described in the previous paragraph; the amplitude of the steered optical beam should be relative constant.

10.3.2 MEMS focusing mirrors

Future research into MEMS focusing mirrors may make the devices suitable for focusing imagery; focusing imagery for video recorders and digital cameras using MEMS devices could directly benefit future Air Force recce systems. Future research should investigate improving the actuation mechanism (perhaps using electrostatic force), decreasing the width of the rings to as little as 10 μm (to reduce the radius of curvature error), and improving the fill factor by applying gold to the entire surface of each ring.

10.3.3 Polyurethane Microlenses

The author was unable to consistently construct high quality polyurethane microlenses using surface micromachined apertures. Typically the microlenses were destroyed by the adhesion of the polyurethane drop to the probe or hypodermic needle. However bulk micromachined devices should be strong enough to withstand the removal of the probe or hypodermic needle after the drop is formed. The hinges in the author's surface micromachined aperture failed, but the polysilicon plate was strong enough to withstand the drop application process. Future research should investigate the construction of polyurethane microlenses using bulk micromachined apertures or surface micromachined apertures with improved hinges. The quality of the microlenses could be categorized after reliable apertures and construction processes are developed.

10.3.4 Decentered Microlens Beam Steering

The author constructed and verified the operation of linear arrays of surface micromachined Fresnel microlenses. The next step would be to investigate the construction of two dimensional Fresnel microlens arrays using bulk or LIGA micromachining. Figure 10.4 depicts a single chip VCSEL beam steering system using a two dimensional Fresnel microlens plate. The aperture of each VCSEL is shaped as a Fresnel zone blocking plate so that the laser's output immediately converges towards the two dimensional Fresnel microlens plate. The Fresnel microlens plate could be actuated using thermal actuators, SDAs, or electromagnetic actuators (implemented in LIGA micromachining).

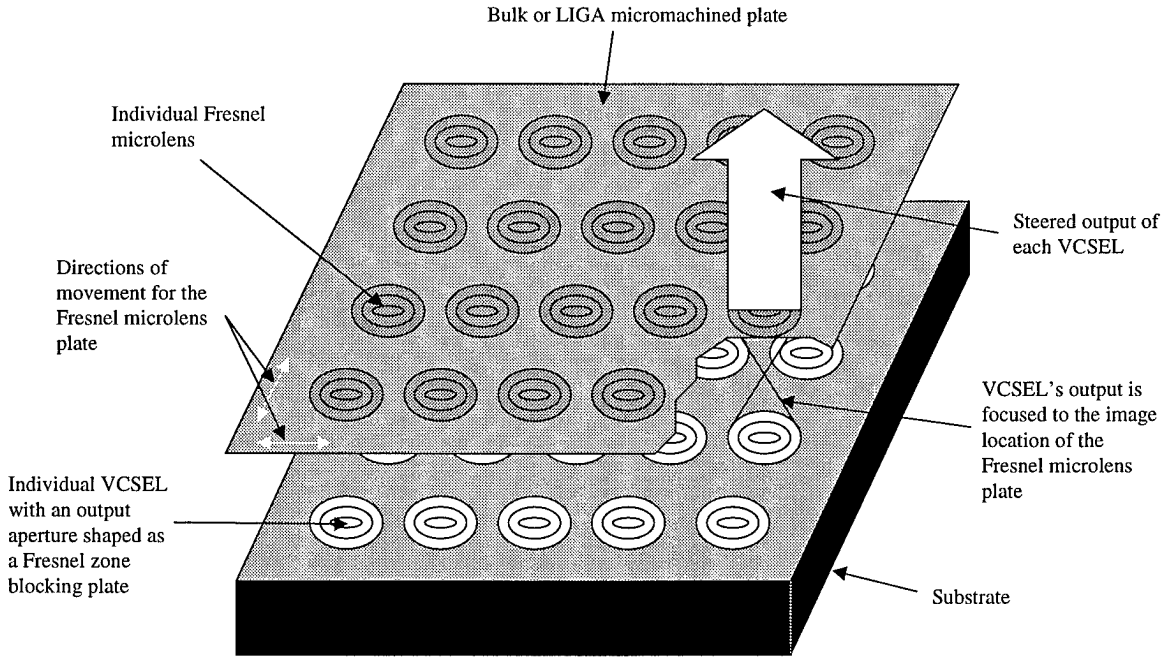

Figure 10.4. A proposed two dimensional decentered microlens beam steering system with integrated VCSELs.

A. MUMPs Material Properties

This appendix lists many properties of the MUMPs structural layers. Reflectivities where measured by the author using the VBG test set-up described in appendix C.

A.1. Nominal Layer Thickness and Measured Reflectivity for MUMPs

TABLE A.1. Nominal Layer Thickness and Measured Reflectivity for MUMPs Structural and Sacrificial Layers.

Layer Name	Nominal Thickness (μm) [1]	Measured Reflectivity (at 632.8 nm)
Nitride (silicon nitride)	0.6	4.95%
Poly-0 (bottom polysilicon layer)	0.5	-
1st Oxide (sacrificial layer - phosphosilicate glass)	2.0	-
Poly-1 (middle polysilicon layer)	2.0	-
2nd Oxide (sacrificial layer - phosphosilicate glass)	0.75	-
Poly-2 (top polysilicon layer)	1.5	34.9%
Gold	0.5	91.5%

A.2. Reflectivity of Gold and Silver as a Function of Wavelength

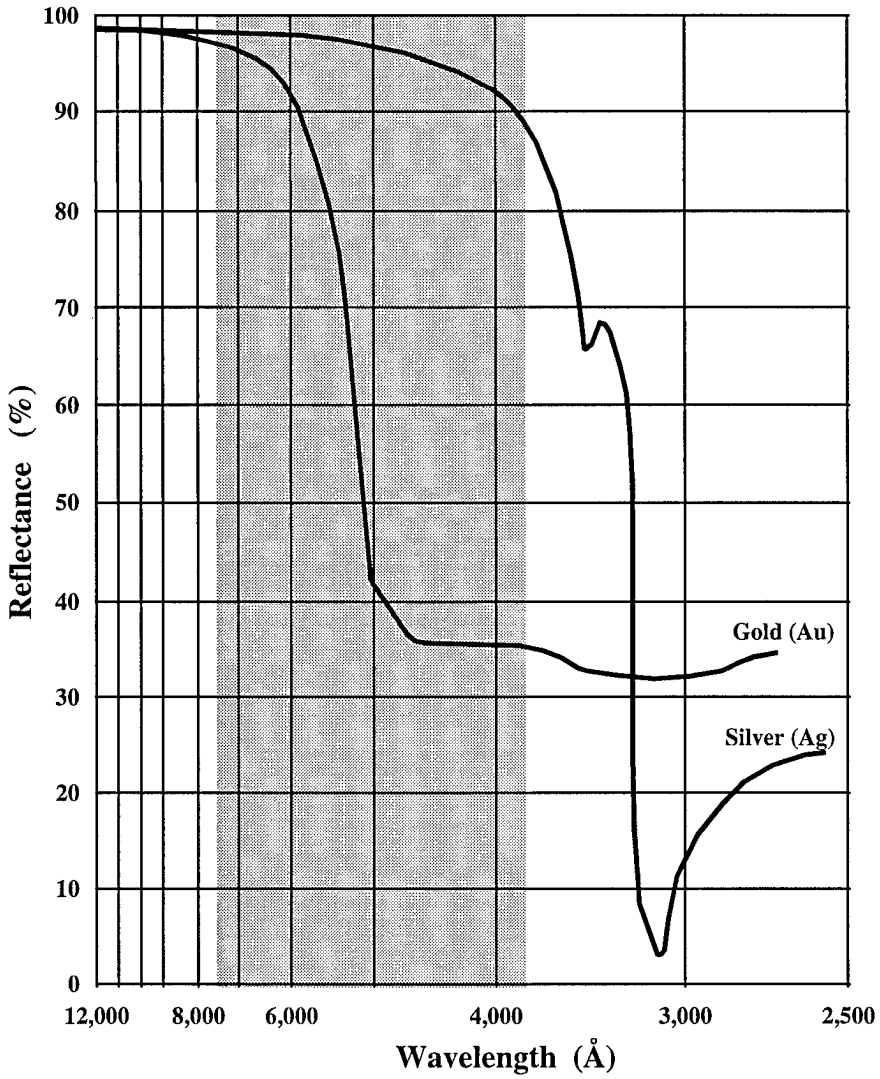

Figure A.1. Reflectivity of gold and silver as a function of wavelength. The shaded area corresponds to the visible spectrum [1].

A.3. Layer Thickness and Stress by MUMPs Run

TABLE A.2. Polysilicon Layer Thickness and Stress Variations by MUMPs Run [2,3].

MUMPs Run	POLY-0 Thickness (nm)	POLY-0 Stress (MPa) (C)	POLY-1 Thickness (nm)	POLY-1 Stress (MPa) (C)	POLY-2 Thickness (nm)	POLY-2 Stress (MPa) (C)
5	545.0	10	2017.5	3	1680.0	8
6	520.0	20	2022.0	5	1565.0	5
7	488.0	-	2010.0	8	1470.6	11
8	469.6	8	1978.0	14	1545.0	10
9	512.2	3	1994.8	3	1504.8	6
10	499.4	4	1972.0	10	1482.5	10
11	498.7	19	1986.9	4	1515.4	11
12	501.6	22	1994.6	10	1544.1	11
13	505.0	16	1995.4	6	1479.4	10
14	506.0	34	1989.9	8	1455.5	10
15	495.7	19	1957.2	12	1495.5	8
16	504.2	24	1970.8	9	1488.2	9
17	501.0	26	1973.9	5	1493.5	6
18	501.7	29	1965.5	9	1537.9	13
19	505.7	31	1964.6	10	1538.4	10
20	500.1	24	1942.8	8	1483.7	9
21	489.1	30	1926.3	8	1464.7	8

TABLE A.3. Material Properties as a Function of the MUMPs Fabrication Run [2,3].

MUMPs Run	Nitride Thickness (nm)	Nitride Stress (MPa) (T)	Gold Thickness (nm)	Gold Stress (MPa) (T)
5	494.0	113	520.0	29.3
6	621.3	19	554.0	-
7	604.9	41	531.8	21
8	558.0	133	520.0	166
9	624.3	67	492.3	5
10	589.8	67	521.5	39
11	605.1	-	534.0	20
12	615.6	184	≈520.0	-
13	580.7	158	473.1	-
14	581.9	116	456.4	57
15	596.6	110	461.9	-
16	599.4	96	450.7	48
17	590.3	105	502.7	68
18	606.0	160	526.2	50
19	569.5	69	484.1	57
20	599.0	132	525.0	95
21	606.0	89	521.3	57

A.4. MUMPs Layer Resistivity

TABLE A.4. Layer Resistivity as a Function of the MUMPs Fabrication Run [2,3].

MUMPs Run	POLY-0 (10^{-3} Ω-cm)	POLY-1 (10^{-3} Ω-cm)	POLY-2 (10^{-3} Ω-cm)	Gold (10^{-6} Ω-cm)
5	2.34	3.33	4.00	2.96
6	1.84	2.58	2.72	3.39
7	*	1.65	1.54	3.30
8	1.5	1.6	2.5	3.5
9	1.5	2.2	3.0	3.0
10	1.6	2.5	3.3	2.9
11	1.96	2.74	2.89	2.87
12	1.72	2.7	3.2	2.99
13	1.65	2.1	3.1	2.78
14	1.5	1.8	2.5	*
15	1.3	1.9	2.1	3.1
16	1.3	1.8	3.4	2.56

* indicates the value was not measured by the manufacturer.

A.5 References

[1] A. Javan, "The optical properties of materials," *Readings from Scientific American*, W. H. Freeman and Company, San Francisco, CA, 1967.

[2] Information downloaded from the MCNC internet web site, WWW.MCNC.ORG, August 1997.

[3] Private communication with David Koester, MUMPs Program Manager, August 15, 1997 and December 3, 1997.

B. Mathematical Calculations and Formulas

B.1. Some Important Properties of the Fourier Transform

The following Fourier transform pairs are presented here as a quick reference for the reader. These Fourier transform properties were used in Section 4.1.1.7.

TABLE B.1. Important Properties of the Fourier Transform.

$f(x)$	$\Im(f(x))$
$c_1 f(x) + c_2 g(x)$	$c_1 F(u) + c_2 G(u)$
$f\left(\frac{x - x_0}{a}\right)$	$\lvert a \rvert e^{-i2\pi x_0 u} F(au)$
$rect(x)$	$sinc(u)$
$e^{\pm i2\pi cx}$	$\delta(u \mp c)$
$\delta(x \pm c)$	$e^{\pm i2\pi cu}$
$f(x)g(x)$	$F(u) * G(u)$
$f(x) * g(x)$	$F(u)G(u)$
$f(x)g(y)$	$F(u)G(v)$

B.2. Prove Equation (4.52)

Equation to be proven:

$$\sum_{n=1}^{N} e^{-i2\pi u\left(n-1-\frac{N-1}{2}\right)a} = \frac{\sin(-N\pi ua)}{\sin(-\pi ua)} \tag{B.1}$$

These calculations are similar to those presented by Klein. Start with the left hand side of Equation (B.1):

$$\sum_{n=1}^{N} e^{-i2\pi u\left(n-1-\frac{N-1}{2}\right)a} = \sum_{n=0}^{N-1} e^{-i2\pi u\left(n-\frac{N-1}{2}\right)a} \tag{B.2}$$

$$= e^{-i2\pi ua\left(\frac{N-1}{2}\right)} \sum_{n=0}^{N-1}\left[e^{-i2\pi ua}\right]^n \tag{B.3}$$

Equation (B.3) has the form of a power series, so the identity in Equation (B.4) can be used to reduce Equation (B.3) into Equation (B.5):

$$\sum_{n=0}^{N-1} r^n = \frac{1-r^n}{1-r} \tag{B.4}$$

$$= e^{-i2\pi ua\left(\frac{N-1}{2}\right)} \frac{1-e^{-i2\pi uaN}}{1-e^{-i2\pi ua}} \tag{B.5}$$

$$= e^{-i2\pi ua\left(\frac{N-1}{2}\right)} \frac{e^{i2\pi ua\frac{N}{2}}\left(e^{-i2\pi ua\frac{N}{2}} - e^{i2\pi ua\frac{N}{2}}\right)}{e^{i2\pi ua\frac{1}{2}}\left(e^{-i2\pi ua\frac{1}{2}} - e^{i2\pi ua\frac{1}{2}}\right)} \tag{B.6}$$

$$= e^{-i2\pi ua\left(\frac{N-1}{2}\right)} e^{i2\pi ua\left(\frac{N-1}{2}\right)} \frac{\sin(-N\pi ua)}{\sin(-\pi ua)} \tag{B.7}$$

$$= \frac{\sin(-N\pi ua)}{\sin(-\pi ua)} \quad \therefore \tag{B.8}$$

B.3. Extend Equation (4.66) to Include Polysilicon and Silicon Nitride layers

Equation (4.66) only includes the reflectance from a VBG's gold layer. Actual VBGs are more complex. Figure (B.1) shows the geometry that will be used to include the reflectances from polysilicon and silicon nitride layers in the formula for VBG Fraunhofer irradiance:

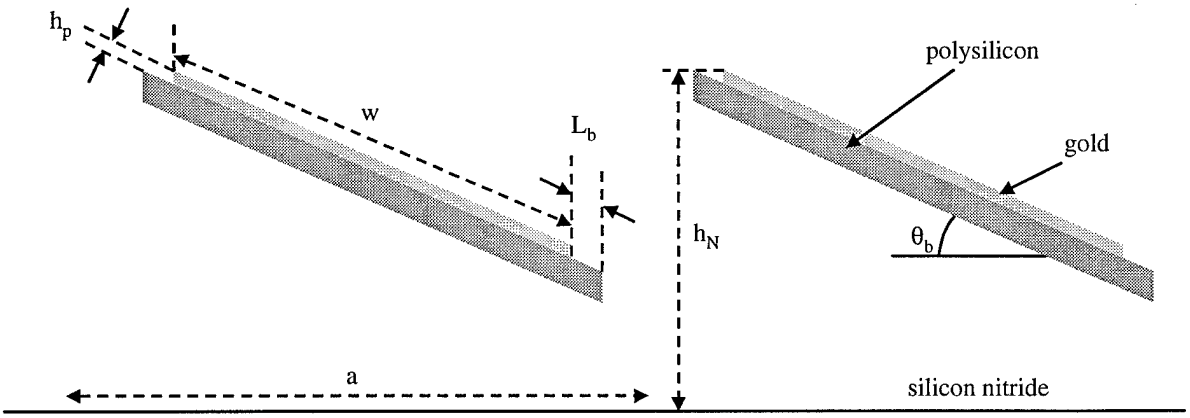

Figure B.1. A cross-sectional view of VBG slats.

where the length of the polysilicon border is L_b, the width of the gold layer is w, the period is a, the thickness of the gold layer is t_p, the initial height of the gold layer above the silicon nitride layer is t_N, and the blaze angle is θ. Projected lengths of the gold layer and polysilicon border are $w \cos \theta$ and $L_b \cos \theta$, respectively. The width of the gap between adjacent slats is $(a - \cos \theta\ (w+2L_b))$. The distance from the center of a slat to the center of the polysilicon border is $\pm\frac{1}{2} \cos \theta\ (w+L_b)$. The distance from the center of a slat to the center of the gap is $a/2$. The number of slats is N, and the number of gaps is N-1. The author's approach to finding an expression for the Fraunhofer irradiance will be to find the Fourier transforms of the polysilicon border and the silicon nitride layer in the gap between slats. Once these transforms are known, they will be added to the Fourier transform for the gold layer (used in Equation (4.66).

The transmittance function for the gold layer (t_{gold}) in a variable blaze grating was shown in Chapter 4 to be:

$$t_{gold}(x,y)=\sqrt{R}\left\{rect\left(\frac{x}{w\cos\theta_b}\right)rect\left(\frac{y}{L}\right)e^{i\frac{2\pi}{\lambda}2x\tan\theta_b}\right\}*\sum_{n=1}^{N}\delta\left(x-(n-1)a\right) \tag{B.9}$$

where L is the length of the slat. Equation (B.9) includes the reflectance (power) of the gold layer, R. Because Equation (B.9) is for the E-field (equal to the square root of the power), the square root of R is used to scale the E-filed reflected off the gold layer.

The transmittance function for the polysilicon border (t_{poly}) on each side of the gold layer is:

$$t_{poly}(x,y)=\sqrt{R_p}e^{i\frac{4\pi}{\lambda}(x\tan\theta_b+h_P)}\left\{\left[rect\left(\frac{x+\frac{\cos\theta_b}{2}(w+L_b)}{L_b\cos\theta_b}\right)+rect\left(\frac{x-\frac{\cos\theta_b}{2}(w+L_b)}{L_b\cos\theta_b}\right)\right]\times rect\left(\frac{y}{L}\right)\right\}*\sum_{n=1}^{N}\delta\left(x-(n-1)a\right) \tag{B.10}$$

where R_p is the reflectance of the polysilicon. The exponent in Equation (B.10) includes the additional distance h_p that light reflecting off the polysilicon travels (compared to the gold layer).

The transmittance function for the gap between slats ($t_{nitride}$) is:

$$t_{nitride}(x,y)=\sqrt{R_N}e^{i\frac{2\pi}{\lambda}2h_N}\left\{rect\left(\frac{x-\frac{a}{2}}{a-\cos\theta_b(w+2L_b)}\right)rect\left(\frac{y}{L}\right)\right\}*\sum_{n=1}^{N-1}\delta\left(x-(n-1)a\right) \tag{B.11}$$

where R_n is the reflectance of the silicon nitride. The exponent in Equation (B.11) includes only the phase delay caused by reflection off the silicon nitride (an additional distance of h_p compared to light reflecting off the highest point on the gold layer). The silicon nitride layer does not tilt, so the phase delay in Equation (B.11) is independent of blaze angle. Note that the number of impulse functions in Equation (B.11) is one less than the number of slats; this corresponds to the number of gaps between the slats.

The Fourier transform of Equations (E.9), (E.10), and (E.11) are given in Equations (B.12), (B.13), and (B.14), respectively:

$$T_{gold}(u,v)=\left|wL\cos\theta_b\right|\sqrt{R}\,\mathrm{sinc}\left(w\cos\theta_b\left(u-\frac{2\tan\theta_b}{\lambda}\right)\right)\mathrm{sinc}(Lv)\frac{\sin(-N\pi ua)}{\sin(-\pi ua)} \tag{B.12}$$

$$T_{poly}(u,v)=\left|L_bL\cos\theta_b\right|\sqrt{R_p}e^{i\frac{2\pi}{\lambda}2h_p}\,\mathrm{sinc}\left(L_b\cos\theta_b\left(u-\frac{2\tan\theta_b}{\lambda}\right)\right)\times$$
$$\left(e^{i2\pi\left(u-\frac{2\tan\theta_b}{\lambda}\right)\left(\frac{\cos\theta_b}{2}(w+L_b)\right)}+e^{-i2\pi\left(u-\frac{2\tan\theta_b}{\lambda}\right)\left(\frac{\cos\theta_b}{2}(w+L_b)\right)}\right)\mathrm{sinc}(Lv)\frac{\sin(-N\pi ua)}{\sin(-\pi ua)} \tag{B.13}$$

$$T_{nitride}(u,v)=\left|L(a-\cos\theta_b(w+2L_b))\right|\sqrt{R_N}e^{i\frac{2\pi}{\lambda}2h_N}\,\mathrm{sinc}((a-\cos\theta_b(w+2L_b))u)\times$$
$$e^{-i2\pi u\frac{a}{2}}\,\mathrm{sinc}(Lv)\frac{\sin(-(N-1)\pi ua)}{\sin(-\pi ua)} \tag{B.14}$$

The sum of the transmittance functions is the transmittance function for the entire VBG ($T(u,v)$):

$$T(u,v)=\left|wL\cos\theta_b\right|\sqrt{R}\,\mathrm{sinc}\left(w\cos\theta_b u-\frac{2w\sin\theta_b}{\lambda}\right)\mathrm{sinc}(Lv)\frac{\sin(-N\pi ua)}{\sin(-\pi ua)}+$$
$$\left|L_bL\cos\theta_b\right|\sqrt{R_p}e^{i\frac{4\pi}{\lambda}h_p}\,\mathrm{sinc}\left(L_b\cos\theta_b u-\frac{2L_b\sin\theta_b}{\lambda}\right)\times$$
$$2\cos\left(\pi\left(u-\frac{2\tan\theta_b}{\lambda}\right)\cos\theta_b(w+L_b)\right)\mathrm{sinc}(Lv)\frac{\sin(-N\pi ua)}{\sin(-\pi ua)}+$$
$$\left|L(a-\cos\theta_b(w+2L_b))\right|\sqrt{R_N}e^{i\frac{4\pi}{\lambda}h_N}\,\mathrm{sinc}((a-\cos\theta_b(w+2L_b))u)\times$$
$$e^{-i\pi ua}\,\mathrm{sinc}(Lv)\frac{\sin(-(N-1)\pi ua)}{\sin(-\pi ua)} \tag{B.15}$$

Solving for the Fraunhofer irradiance gives:

$$E(u,v) = E_s L^2 \left(\frac{1}{z\lambda}\right)^2 \mathrm{sinc}^2\left(\frac{Lv}{z\lambda}\right) \times$$

$$\left| |w\cos\theta_b| \sqrt{R}\,\mathrm{sinc}\left(\frac{w}{\lambda}\left(\cos\theta_b \frac{u}{z} - 2\sin\theta_b\right)\right) \frac{\sin\left(\frac{-N\pi ua}{z\lambda}\right)}{\sin\left(\frac{-\pi ua}{z\lambda}\right)} + \right.$$

$$2|L_b \cos\theta_b| \sqrt{R_p} e^{i\frac{4\pi}{\lambda}h_p}\,\mathrm{sinc}\left(\frac{L_b}{\lambda}\left(\cos\theta_b \frac{u}{z} - 2\sin\theta_b\right)\right) \times$$

$$\cos\left(\frac{\pi}{\lambda}\left(\frac{u}{z} - 2\tan\theta_b\right)\cos\theta_b (w + L_b)\right) \frac{\sin\left(\frac{-N\pi ua}{z\lambda}\right)}{\sin\left(\frac{-\pi ua}{z\lambda}\right)} +$$

$$|a - \cos\theta_b (w + 2L_b)| \sqrt{R_N} e^{i\frac{4\pi}{\lambda}h_N}\,\mathrm{sinc}\left((a - \cos\theta_b (w + 2L_b))\frac{u}{z\lambda}\right) \times$$

$$\left. e^{-i\frac{\pi ua}{z\lambda}} \frac{\sin\left(\frac{-(N-1)\pi ua}{z\lambda}\right)}{\sin\left(\frac{-\pi ua}{z\lambda}\right)} \right|^2 \qquad \text{(B.16)}$$

The VBG we are modeling has a total width equal to N slats (each with a width of $w + 2L_b$) and N-1 gaps (each with a width of a - cosθ (w+2L_b)). The area of the grating, A, is equal to:

$$A = L[(N-1)a + \cos\theta_b (w + 2L_b)] \qquad \text{(B.17)}$$

If we only look at the v=0 plane, substitute $\sin\theta = u/z$, and normalize the irradiance for the area given in Equation (B.17), Equation (B.16) becomes:

$$E(\theta)=\left(\frac{1}{(N-1)a+\cos\theta_b(w+2L_b)}\right)^2\left(\frac{1}{z\lambda}\right)^2\times$$

$$\left|w\cos\theta_b\right|\sqrt{R}\,\mathrm{sinc}\left(\frac{w}{\lambda}(\cos\theta_b\sin\theta-2\sin\theta_b)\right)\frac{\sin\left(\frac{-N\pi a}{\lambda}\sin\theta\right)}{\sin\left(\frac{-\pi a}{\lambda}\sin\theta\right)}+$$

$$2\left|L_b\cos\theta_b\right|\sqrt{R_p}e^{i\frac{4\pi}{\lambda}h_p}\,\mathrm{sinc}\left(\frac{L_b}{\lambda}(\cos\theta_b\sin\theta-2\sin\theta_b)\right)\times$$

$$\cos\left(\frac{\pi}{\lambda}(\cos\theta_b\sin\theta-2\sin\theta_b)(w+L_b)\right)\frac{\sin\left(\frac{-N\pi a}{\lambda}\sin\theta\right)}{\sin\left(\frac{-\pi a}{\lambda}\sin\theta\right)}+$$

$$\left|a-\cos\theta_b(w+2L_b)\right|\sqrt{R_N}e^{i\frac{\pi}{\lambda}(4h_N+a\sin\theta)}\,\mathrm{sinc}\left(\frac{\sin\theta}{\lambda}(a-\cos\theta_b(w+2L_b))\right)\times$$

$$\left.\frac{\sin\left(\frac{-(N-1)\pi a}{\lambda}\sin\theta\right)}{\sin\left(\frac{-\pi a}{\lambda}\sin\theta\right)}\right|^2 \qquad \text{(B.18)}$$

Equation (B.18) is the Fraunhofer irradiance for a VBG with polysilicon borders of length L_b, and gaps allowing reflection off the silicon nitride layer.

C. Test Equipment Used in the Author's Research

All of the specialized test equipment used by the author in his research is listed in this appendix.

C.1 The 145 Pin Grid Array (PGA) Chip Carrier

Figures C.1 and C.2 are pictures of the top and bottom of the 145 PGA used by the author to test MEMS devices on an optical bench. The chip carrier is manufactured by the Kyocera corporation, Kyoto, Japan, and was procured through Spectrum semiconductor materials, Inc., 2027 O'Toole Ave, San Jose, CA 95131. The part number for 145 PGA is: CPG14416. The 145 PGA was selected because the cavity size is 1.2 cm square, so a MUMPs die easily fits inside. Figure C.3 shows a schematic diagram of the 145 PGA and identifies a pin numbering scheme; this pin numbering scheme is used in Table C.1 to relate the pin number in the cavity to the pin on the bottom of the die. Figure C.4 is a Zero Insertion Force (ZIF) socket and breadboard constructed by the author to connect the 145 PGA to control circuitry. The MUMPs die was mounted in the chip carrier with glue and wirebonded to the pads in the cavity with the Kulick and Soffa Industries wire bonder.

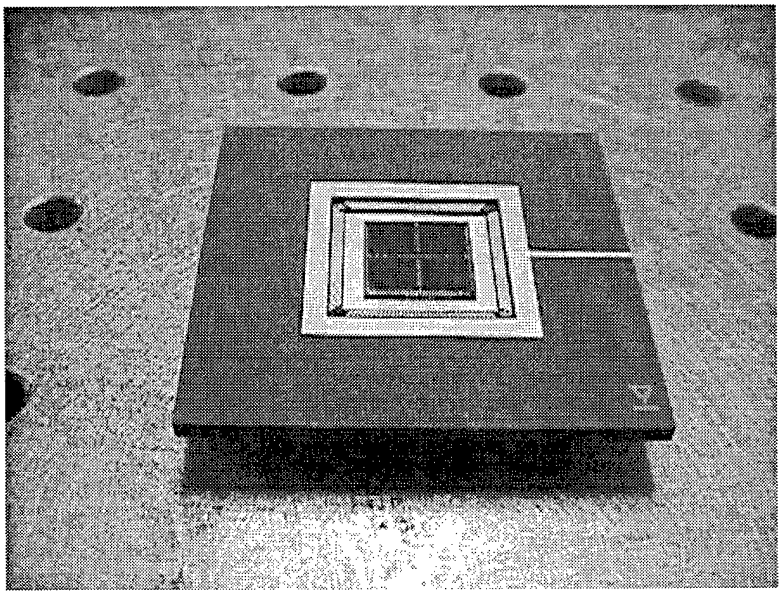

Figure C.1. The top of a 145 PGA chip carrier.

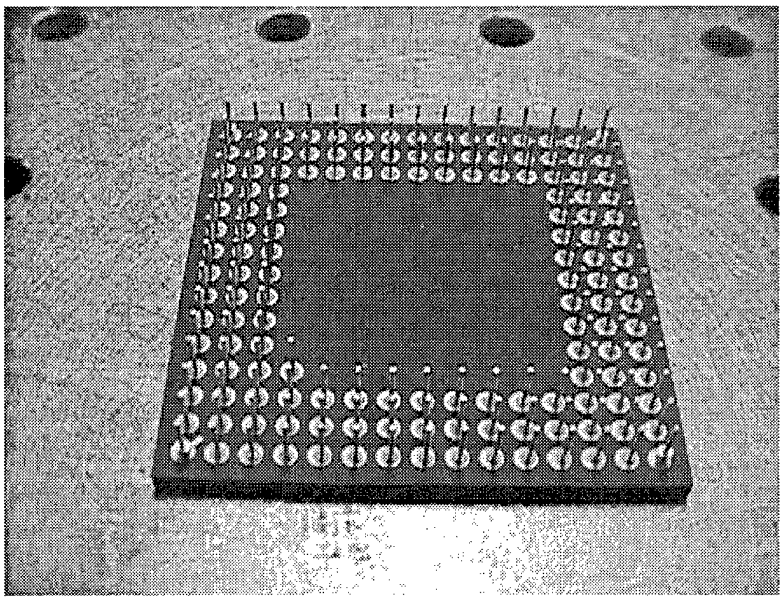

Figure C.2. The bottom of a 145 PGA chip carrier.

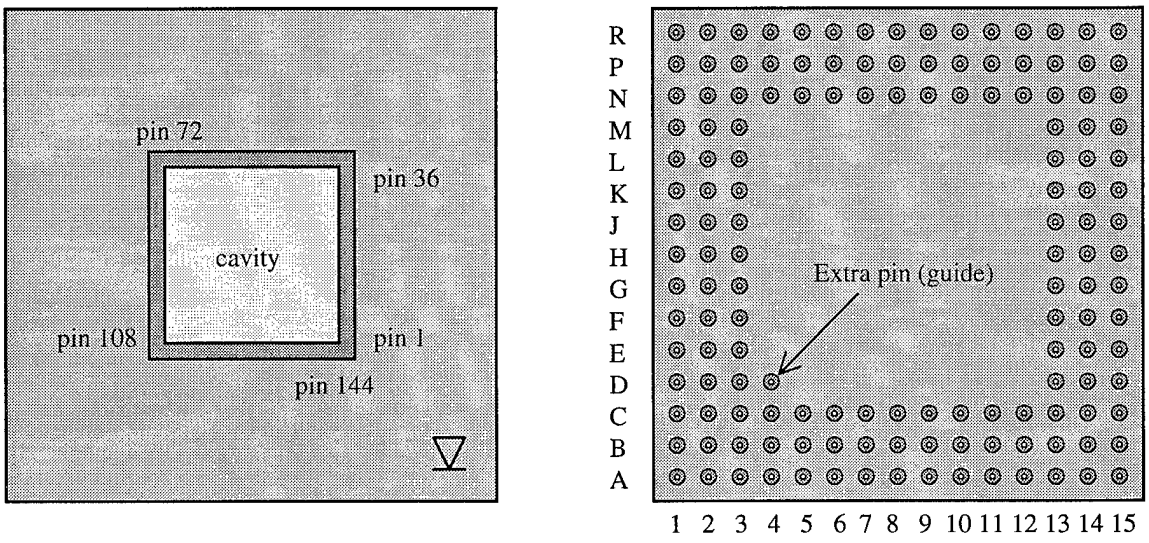

Figure C.3. Schematic diagram of the (a) top and (b) bottom of the 145 PGA.

Table C.1. Wirebond to Pin Number Matrix for the 145 PGA

Wirebond Number	Pin Number
1	D3
2	C2
3	B1
4	D2
5	E3
6	C1
7	E2
8	D1
9	F3
10	F2
11	E1
12	G2
13	G3
14	F1
15	G1
16	H2
17	H1
18	H3
19	J3
20	J1
21	K1
22	J2
23	K2
24	K3
25	L1

Wirebond Number	Pin Number
26	L2
27	M1
28	N1
29	M2
30	L3
31	N2
32	P1
33	M3
34	N3
35	P2
36	R1
37	N4
38	P3
39	R2
40	P4
41	N5
42	R3
43	P5
44	R4
45	N6
46	P6
47	R5
48	P7
49	N7
50	R6

Table C.1. Wirebond to Pin Number Matrix for the 145 PGA (continued)

Wirebond Number	Pin Number
51	R7
52	P8
53	R8
54	N8
55	N9
56	R9
57	R10
58	P9
59	P10
60	N10
61	R11
62	P11
63	R12
64	R13
65	P12
66	N11
67	P13
68	R14
69	N12
70	N13
71	P14
72	R15
73	M13
74	N14
75	P15

Wirebond Number	Pin Number
76	M14
77	L13
78	N15
79	L14
80	M15
81	K13
82	K14
83	L15
84	J14
85	J13
86	K15
87	J15
88	H14
89	H15
90	H13
91	G13
92	G15
93	F15
94	G14
95	F14
96	F13
97	E15
98	E14
99	D15
100	C15

Table C.1. Wirebond to Pin Number Matrix for the 145 PGA (continued)

Wirebond Number	Pin Number
101	D14
102	E13
103	C14
104	B15
105	D13
106	C13
107	B14
108	A15
109	C12
110	B13
111	A14
112	B12
113	C11
114	A13
115	B11
116	A12
117	C10
118	B10
119	A11
120	B9
121	C9
122	A10
123	A9
124	B8
125	A8

Wirebond Number	Pin Number
126	C8
127	C7
128	A7
129	A6
130	B7
131	B6
132	C6
133	A5
134	B5
135	A4
136	A3
137	B4
138	C5
139	B3
140	A2
141	C4
142	C3
143	B2
144	A1

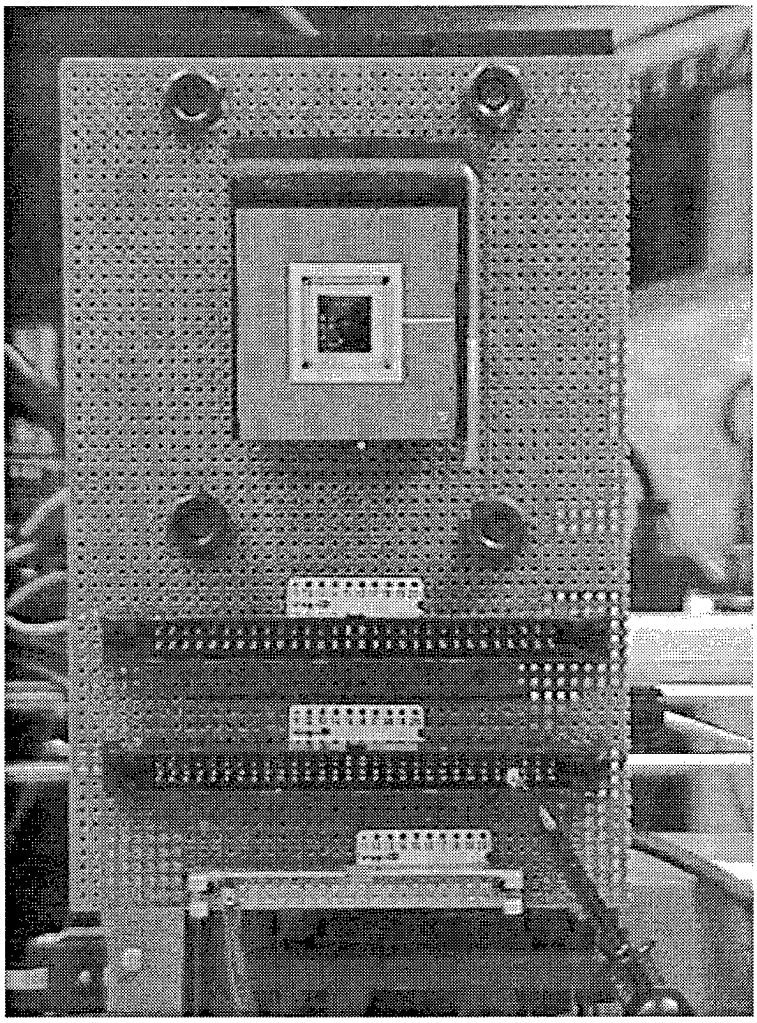

Figure C.4. 145 PGA chip carrier in a ZIF socket mounted to the author's control circuitry breadboard.

C.2 Dektak Surface Profile Measuring System

The Dektak model 2A surface profile measuring system is shown in Figure C.5. This system has a vertical resolution that is better than 100 Å. The Dektak system was used by the author to measure the amount of gold deposited on a MUMPs wafer using the Ladd sputter coater. The Dektak system is manufactured by the Sloan Technology Corporation, P.O. Box 4608, Santa Barbara, CA 93109.

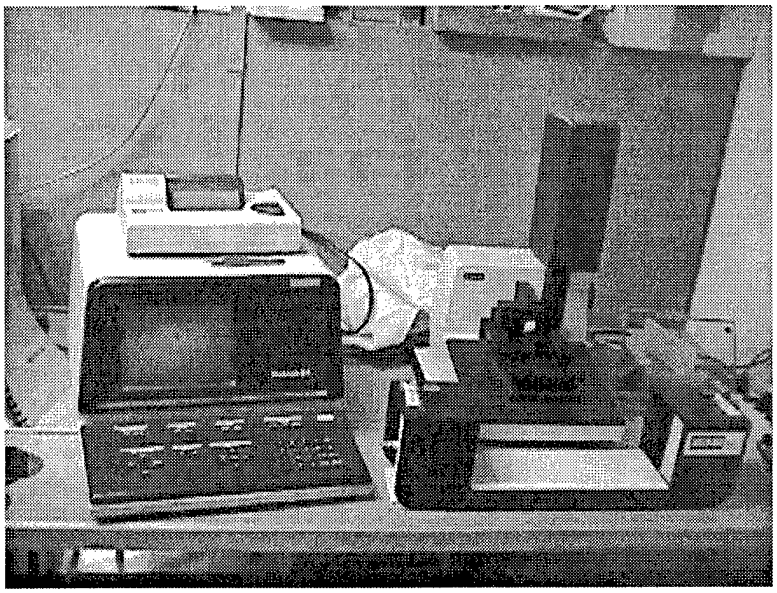

Figure C.5. The Dektak model 2A surface profile measuring system.

C.3 Digital Power Supply

The Hewlett-Packard (HP) model 6624A system DC power supply shown in Figure C.6 was used by the author to drive many of his MEMS devices. The HP power supply is manufactured by the Hewlett-Packard Company, 150 Green Pond Road, Rackaway, NJ 07866. The HP power supply has a fast response time (less than 750 μsec for full range) and has four programmable outputs. Each output has a range of 0 – 80 volts.

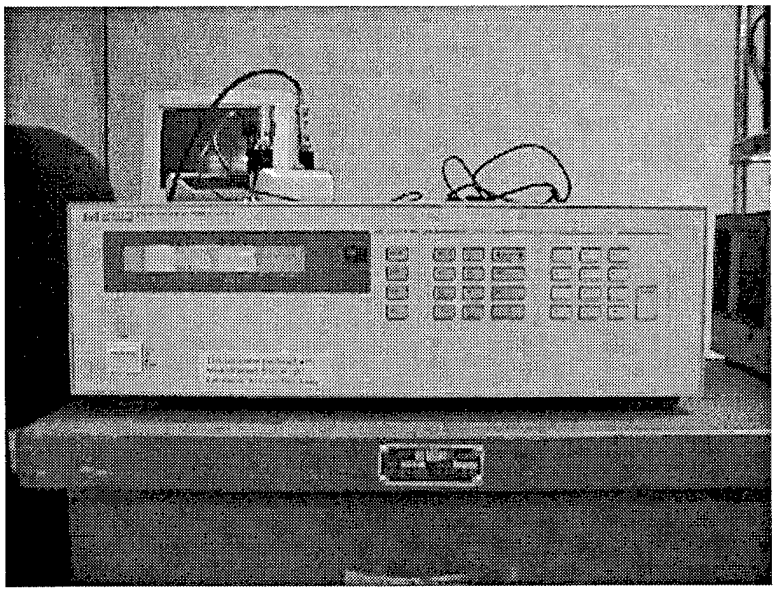

Figure C.6. The Hewlett-Packard programmable DC power supply.

C.4 Electronic Furnace

The author used the Thermolyne type 30400 electronic furnace to bake MUMPs dies and determine the maximum device temperature. The Thermolyne electronic furnace is manufactured by Barnstead/Thermolyne, P.O. Box 797, 2555 Kerper Blvd, Dubuque, IA 52004-0797. The Thermolyne electronic furnace has a range of 100°C to 982°C (continuous operation) and is fully programmable. The Thermolyne furnace will hold the set temperature to within a degree (Celsius) for up to 72 hours. The warm-up time is lengthy; the furnace typically requires 12 hours or more to reach 700°C. The long warm-up time is partly due to the construction of the furnace; the furnace is completely lined with ceramic blocks. Figure C.7 is a picture of the Thermolyne electronic furnace.

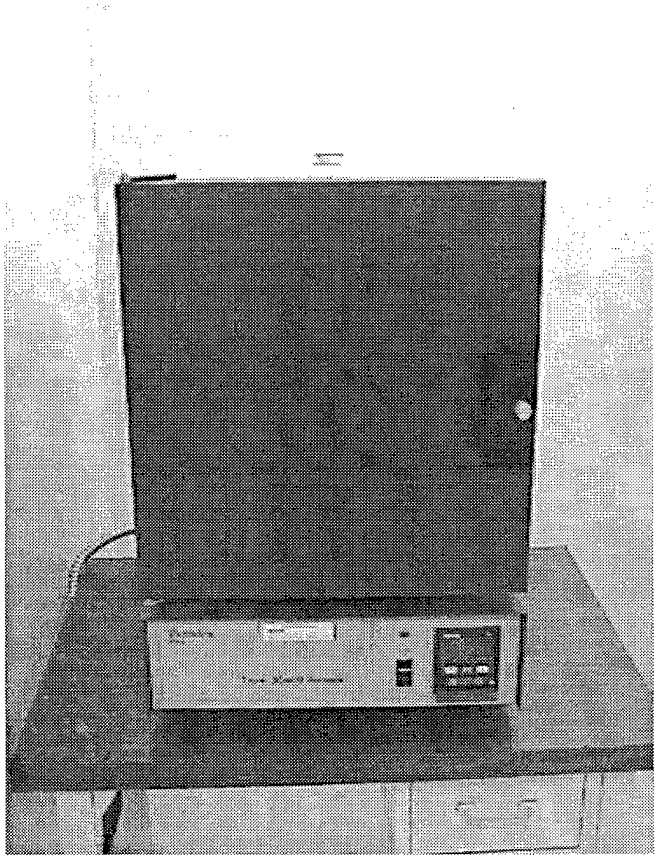

Figure C.7. The Thermolyne type 30400 electronic furnace.

C.5 Fume Hood and Chemical Bench

The fume hood and chemical bench used by the author to release MUMPs die is shown in Figure C.8. The release process involves Hydrofluoric acid, which can emit toxic Fluorine gas, so a fume hood is required for the researcher's safety. The fume hood and chemical bench was manufactured by Duralab Equipment Corporation, 107-23 Farragut Road, Brooklyn, NY 11235.

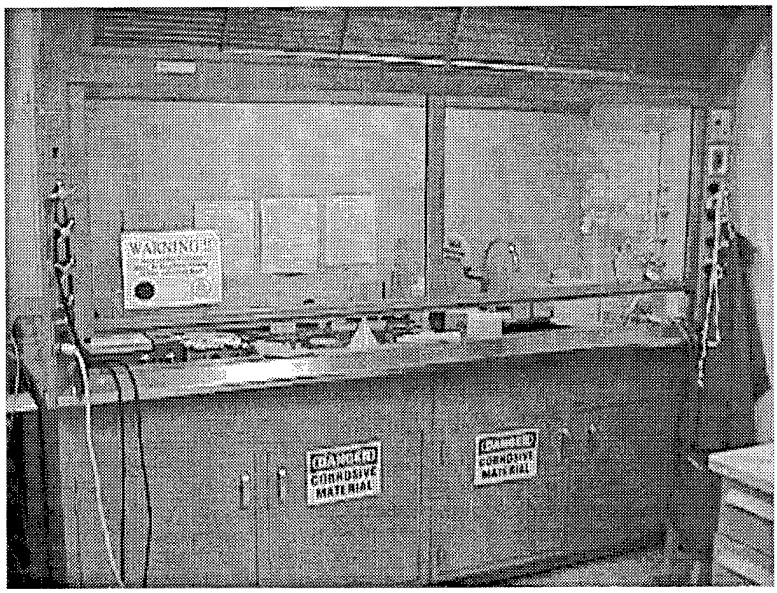

Figure C.8. Fume hood and chemical bench used by the author to release MUMPs die.

C.6 HeNe Lasers

The author used two HeNe lasers during his research. The first HeNe laser is the NEC model: GLG5734 gas laser. The NEC gas laser is approximately 1.2 meters long and is manufactured by NEC corporation, NEC building, 33-1 Shiba, 5-Chome, Minato-Ku, Tokyo, Japan, 108. The NEC gas laser is rated for 50 mW continuous output, however the most that the author was able to get out was 36.5 mW. The NEC gas laser was used by the author in all optical power damage experiments. Figure C.9 is a picture of the NEC gas laser.

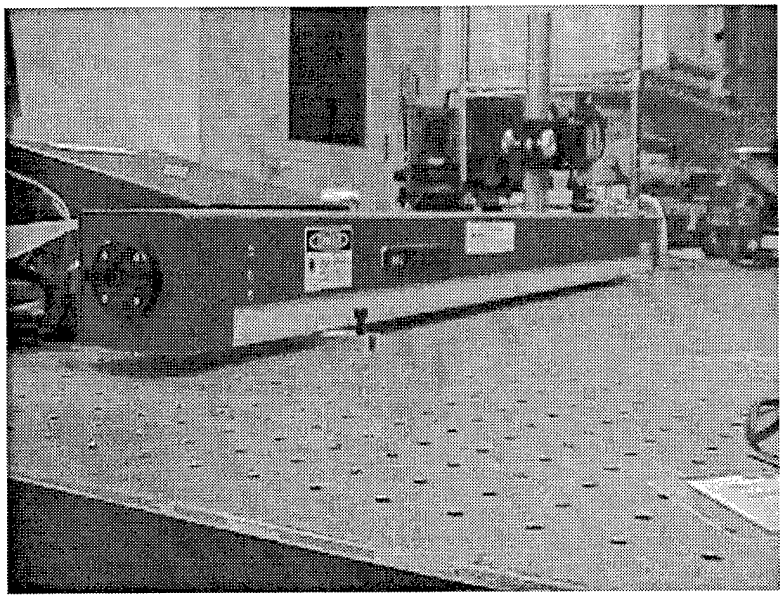

Figure C.9 The NEC gas laser used for optical power damage testing.

Devices such as variable blaze gratings and variable radius of curvature micromirrors were illuminated by a model 106-1 Spectra-Physics HeNe gas laser. The Spectra-Physics gas laser was manufactured at Spectra-Physics, Inc., 959 Terry Street, Eugene, OR 97402. The Spectra-Physics gas laser was rated at 20 mW, and the author was able to get an output power level of 17.0 mW. Figure C.10 is a picture of the Spectra-Physics gas laser.

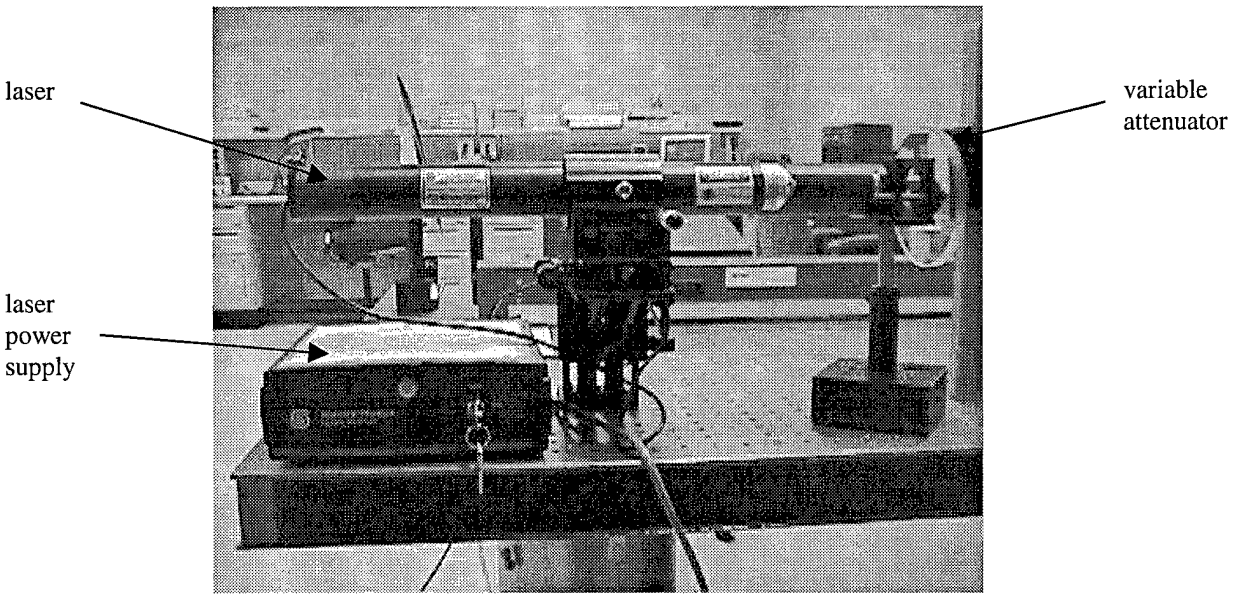

Figure C.10. The Spectra-Physics gas laser used to illuminate MEMS devices on the optical bench.

C.7 Micromanipulator Probe Station

The micromanipulator probe station model 6200 shown in Figure C.11 is the primary method of assembling MEMS structures at AFIT. The micromanipulator probe station rests on an air table to isolate the probe station from random vibrations in the floor of the laboratory caused by other equipment or personnel. The author used the micromanipulator probe station to assemble lenslet arrays and test the electrical and mechanical properties of optical devices before placing the devices on the optical bench. On the top of the microscope assemble is a Sony video camera, which can be used to record imagery. The micromanipulator probe station is manufactured by the Micromanipulator Company, 2801 Arrowhead Drive, Carson City, NV 89701.

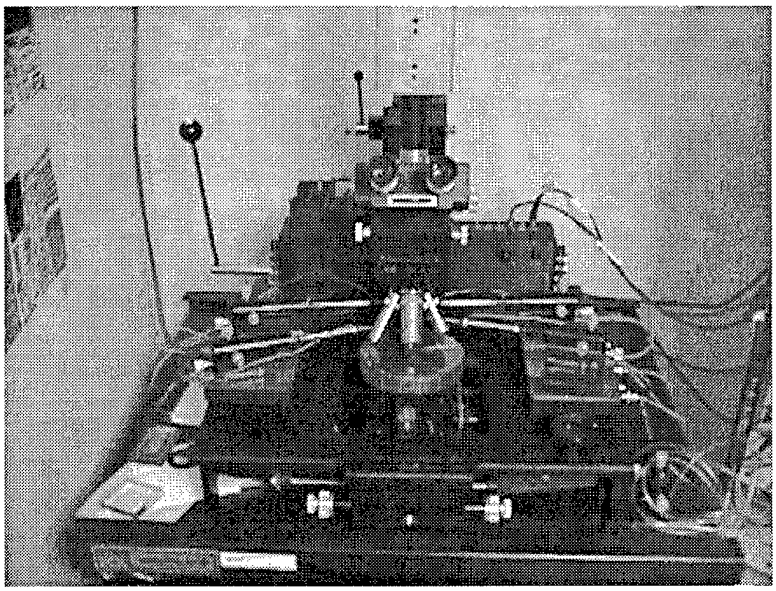

Figure C.11. The model 6200 micromanipulator probe station.

C.8 Optical Power Meter

The author measured all optical power levels and calculated diffraction efficiencies with the Newport Corporation model 835 optical power meter. The optical power meter is manufactured by Newport Corporation, Fountain Valley, CA 92708. The model 835 optical power meter has a range of 1 nW to over 100 mW, with an accuracy of ±0.02 nW. The signal risetime is less than 20 msec. Care must be taken when using the model 835 to ensure that the detector head is normal to the incident laser beam. If the detector head is tilted even slightly, then a lower signal reading will given by the instrument. Figure C.12 is a picture of the Newport model 835 optical power meter.

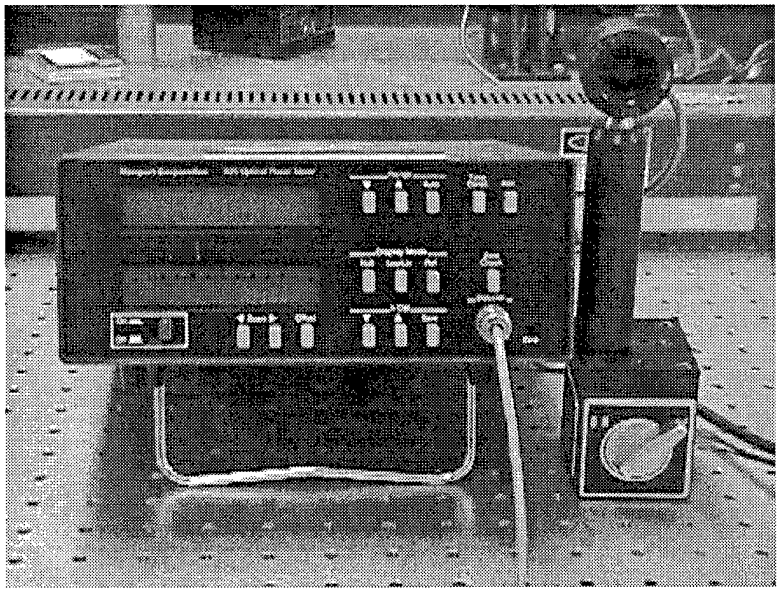

Figure C.12. The Newport model 835 optical power meter and detector head.

C.9 Scanning Electron Microscope.

The International Scientific Instruments model WB-6 Scanning Electron Microscope (SEM) is shown in Figure C.13. The model WB-6 SEM is manufactured by the International Scientific Instruments, Inc., 1457 McCarthy Blvd, Milpitas, CA 95035. The maximum resolution for this SEM is 4 nm. The SEM includes a Polaroid camera that was used to collect all of the author's SEM imagery used in this document.

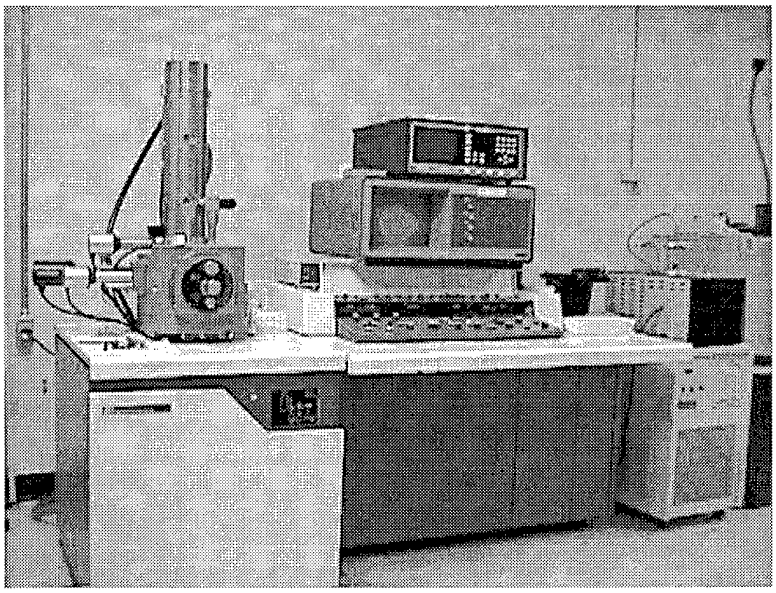

Figure C.13. The AFIT MEMS lab scanning electron microscope.

C.10 Sputter Coater

The Ladd bench top sputter coater, model: 30800, was often used to coat samples for the SEM with a thin layer of gold. The thin gold layer reduces the charge storage effects that reduce image intensity in the SEM. The author typically used a 150 Å thick gold layer. The Ladd bench top sputter coater is manufactured by Ladd Research Industries, Inc., P.O. Box 1005, Burlington, VT 05402. Figure C.14 is a picture of the Ladd sputter coater.

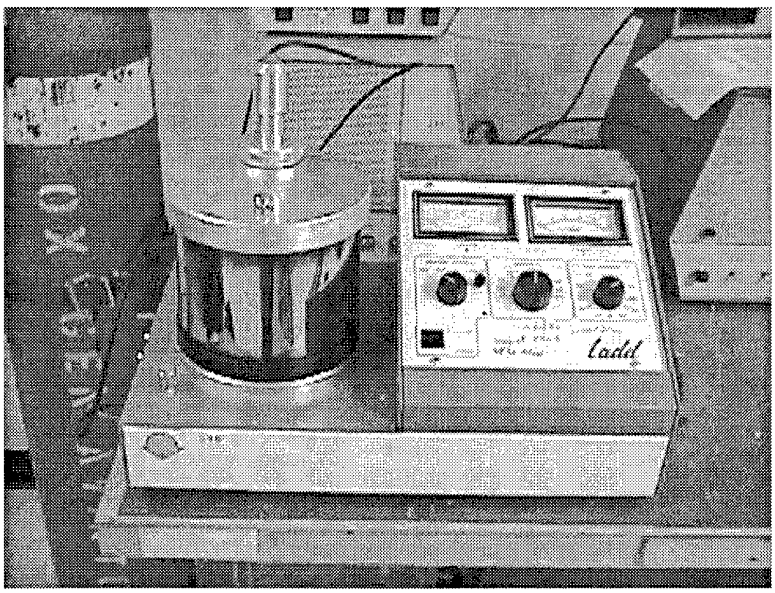

Figure C.14. The Ladd bench top sputter coater.

C.11 VBG Test Set-up

The test set-up used by the author to evaluate his VBGs and variable radius of curvature mirrors is shown in Figure C.15. At the upper left hand corner is the Spectra-Physics 20 mW HeNe laser and a variable attenuator (described in Section C.6), and at the lower right corner is the author's breadboard (see section C.1). A beam expanding lens (lens #1) was used to expand the waist of the laser beam at the aperture. The aperture was used to make the laser's spot round. Earlier experiments by the author used a collimator; the collimator was not necessary and was subsequently removed (to increase the available optical power on the device under test). The steering mirror and focusing lens (lens #2) were used to shape and position the laser's spot on the device under test. The target is located 1.7 meters from the breadboard.

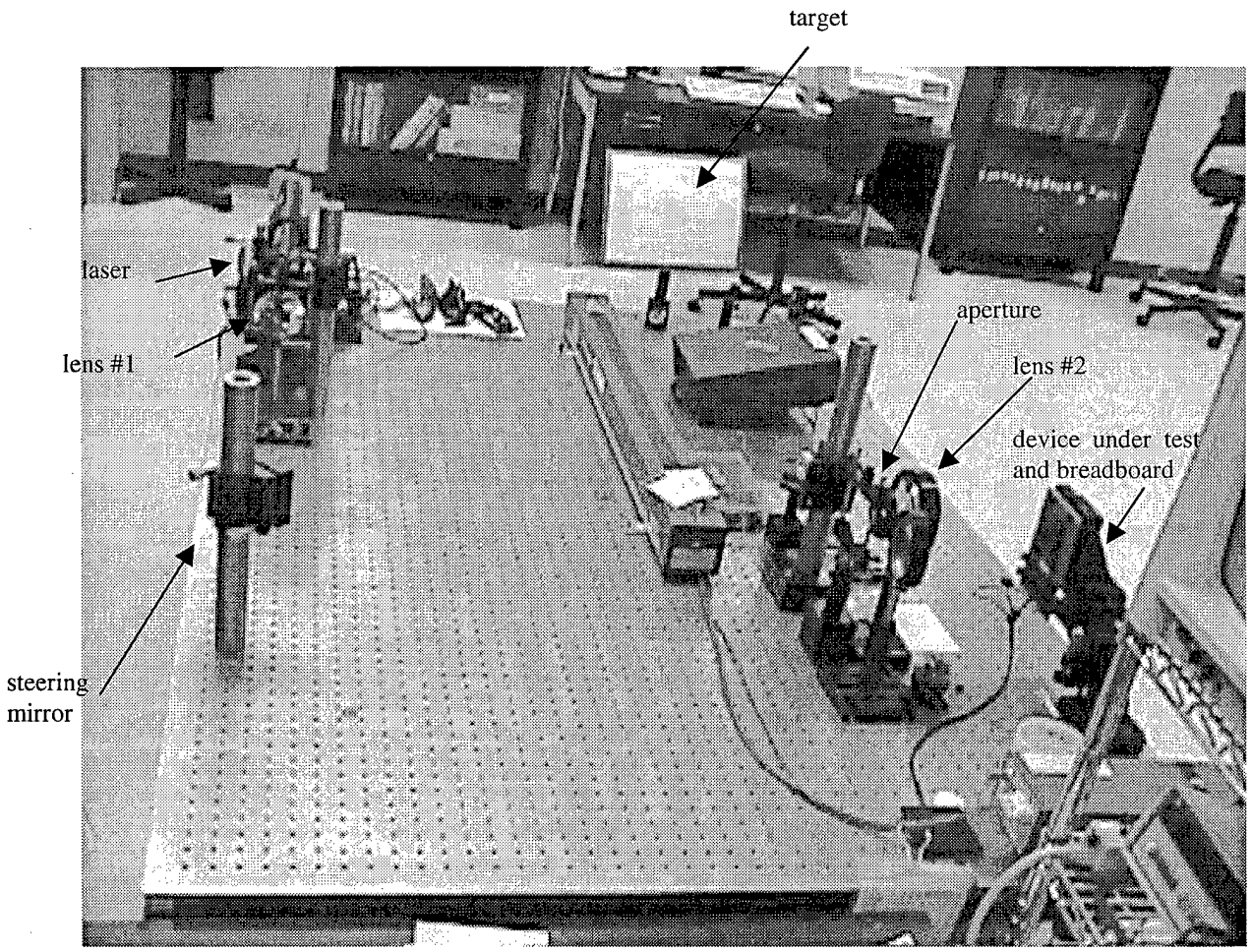

Figure C.15. The author's VBG test set-up.

C.12 Wire Bonder

The wire bonder shown in Figure C.16 is a model 4124 ultrasonic ball bonder. The wire bonder uses 25 μm diameter gold wire to connect pads on the die to pads on the chip carrier. The wire bonder is manufactured by Kulick and Soffa Industries, Inc., 2101 Blair Mill Road, Willow Grove, PA 19090. The wire bonder uses a ball bond on the MEMS die, and a wedge bond on the chip carrier.

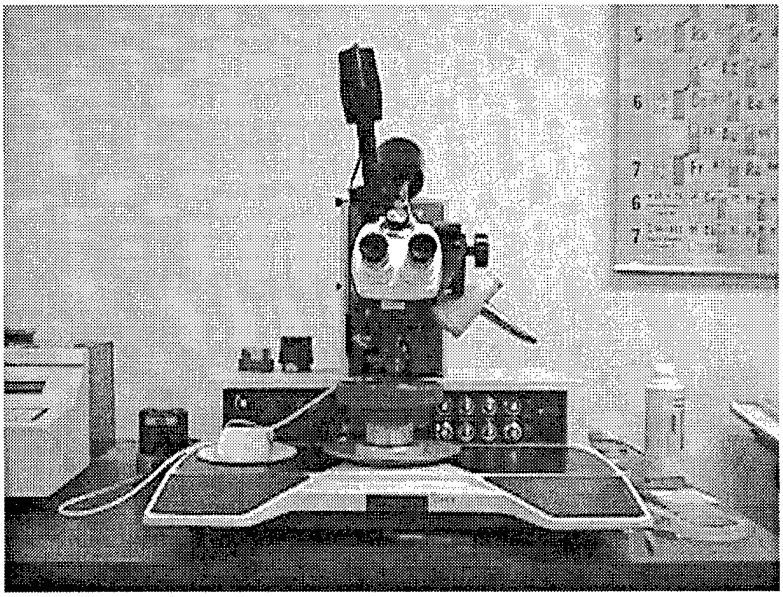

Figure C.16. The Kulick and Soffa industries model 4124 wire bonder.

C.13 Zygo Laser Measurement System

The Zygo model Maxim-3D laser measuring system is shown in Figure C.17. The Zygo model Maxim-3D has a vertical sensitivity of 0.6 nm, and was used by the author to measure the amount of residual stress induced curvature present in MUMPs fabricated micromirrors. The Zygo was also used by the author to measure vertical deflections for electrostatically actuated devices. The Zygo laser measuring system is manufactured by the ZYGO Corporation, Laurel Brook Road, Middlefield, CN 06455. The left side of Figure C.17. is the computer drive unit; the right side is the laser and microscope assembly.

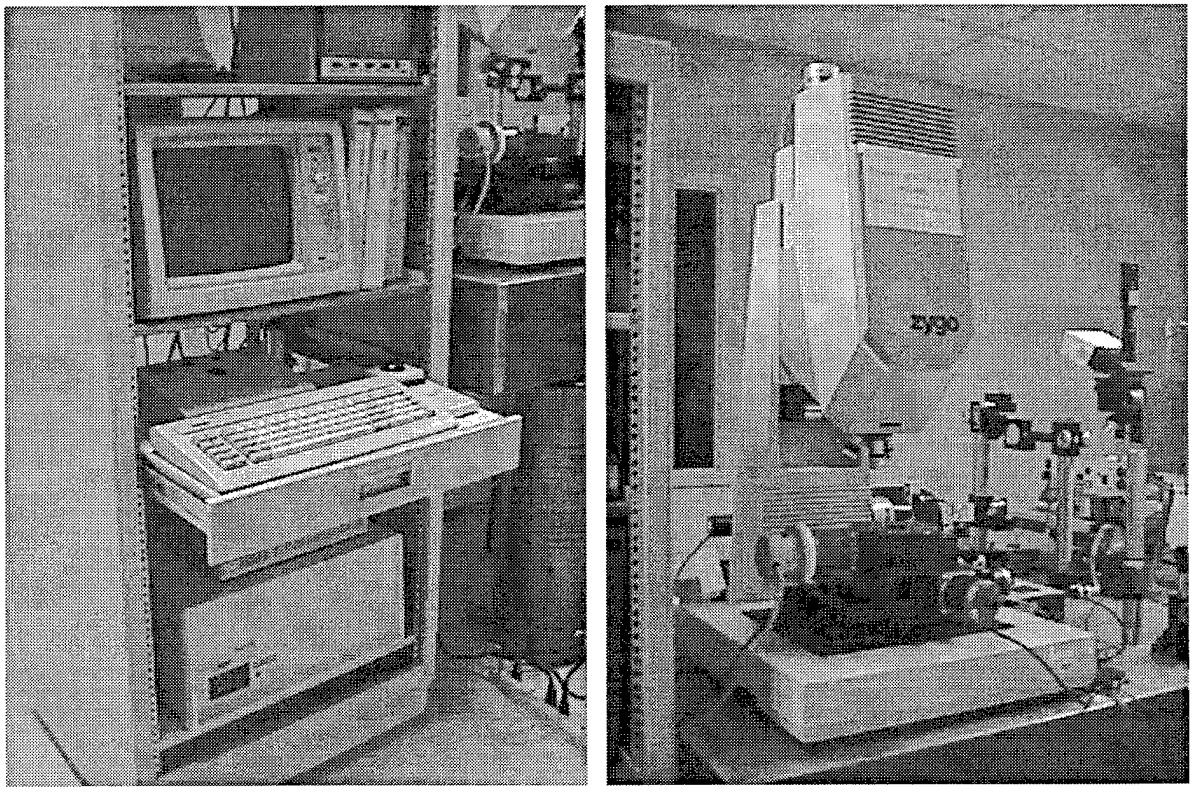

Figure C.17. The Zygo model Maxim-3D laser measuring system.

D. Optical Power Test Procedures

Refer to Figure 8.9 for a schematic diagram of the test set-up. Table D.1 presents the procedures for setting up and conducting an experiment. Safety is very important. The optical power levels used by the author can easily result is damage to human eye. The laboratory should be locked during all testing to prevent exposure of other researchers to high optical power levels. Also, laser eye protection should be worn during all testing.

TABLE D.1. Test Procedures Used by the Author to Measure the Incident Optical Power Required to Damage a Micromirror

1	Close shutter.
2	Turn the variable attenuator so that the minimum attenuation is achieved.
3	Turn on NEC 50 mW laser.
4	Place sample die in vacuum chamber.
5	Turn on vacuum pump for 15 minutes.
6	Backfill vacuum chamber with 0.999 % dry nitrogen.
7	Turn off nitrogen and wait approximate one hour for the vacuum pump to bring the vacuum chamber to a pressure of 20 mTorr. Leave vacuum pump on during testing.
8	Measure laser's output power. The laser's output should be relatively constant (within 5%) for at least 30 minutes before testing is started.
9	Place two 95% opaque neutral density filters between the shutter and the focusing lens.
10	Place the safety cover over both microscope eyepieces, and open the shutter.
11	Measure the laser's output power at the point where the laser's beam enters the focusing lens. If the laser's power at this point is higher than 100 nW, increase the variable attenuator so that the laser beam's power is less than or equal to 100 nW.
12	Remove the cover from the microscope eyepieces, and position the laser spot on the target micromirror. Ensure that the entire laser spot rests on the gold layer and does not illuminate the polysilicon border.
13	Remove the microscope eyepieces and cover the microscope assembly.
14	Set the variable attenuator to its maximum attenuation setting, and remove neutral density filters.
15	Gradually decrease the variable attenuator's attenuation until 2.953 mW illuminates the focusing lens. 33.86% of the optical power illuminating the focusing lens reaches the target micromirror.

16	Remove the cover over the microscope assembly, and measure the optical power exiting the right eyepiece hole. Calculate the initial micromirror reflectivity from this value. 22.93% of the optical power reflected off the target micromirror exits the right eyepiece hole. From step 15, the micromirror should be illuminated with 1 mW of optical power.
17	Replace the safety cover over the microscope assembly.
18	Gradually decrease the variable attenuator's attenuation until the desired testing optical power at the focusing lens is achieved. 33.86% of the optical power illuminating the focusing lens reaches the target micromirror.
19	Monitor testing for one hour.
20	Gradually increase the variable attenuator's attenuation until 2.953 mW illuminates the focusing lens. 33.86% of the optical power illuminating the focusing lens reaches the target micromirror.
21	Remove the cover over the microscope assembly, and measure the optical power exiting the right eyepiece hole. Calculate the final micromirror reflectivity from this value. 22.93% of the optical power reflected off the target micromirror exits the right eyepiece hole. From step 20, the micromirror should be illuminated with 1 mW of optical power. A micromirror is considered damaged when the final reflectivity is 25% or more below the initial reflectivity.
22	Replace the safety cover over the microscope assembly.
23	Place two 95% opaque neutral density filters between the shutter and the focusing lens.
24	Measure the laser's output power at the point where the laser's beam enters the focusing lens. If the laser's power at this point is higher than 100 nW, increase the variable attenuator so that the laser beam's power is less than or equal to 100 nW.
25	Remove the cover over the microscope assembly and replace the microscope eyepieces.
26	Evaluate the micromirror for visible damage.
27	If another test is needed, go to step 13 and increase the target optical power on the test micromirror by 0.5 mW.
28	Turn off laser and vacuum pump.
29	Close shutter.
30	Backfill vacuum chamber with nitrogen.
31	Remove test die from vacuum chamber.

Vita

Major David M. Burns graduated from the United States Air Force Academy with a Bachelor of Science degree in electrical engineering and was commissioned a Second Lieutenant on June 1, 1983. His first assignment was to Wright Patterson Air Force Base, Ohio, where he initially served as a radar engineer and then served as the electronic warfare computer resources director for the Advanced Tactical Fighter (F-22/F-23) program. During this assignment, he earned a Master of Science degree in electromagnetics at the University of Dayton in December, 1985. He was assigned to Hanscom Air Force Base, Massachusetts, in 1988. At Hanscom, he served as the program manager for the development of the B-2's mission planning system. In 1992, he was assigned to the Secretary of the Air Force's Special Programs Office (SAF/AQLJ) at the Pentagon There he managed the development of advanced reconnaissance programs. He was assigned to the Air Force Institute of Technology in 1995 to pursue a Ph.D. in electrical engineering. He was elected and served on the executive boards of both Tau Beta Pi and Eta Kappa Nu engineering honor societies at AFIT.

REPORT DOCUMENTATION PAGE

Form Approved
OMB No. 0704-0188

1. AGENCY USE ONLY *(Leave blank)*	2. REPORT DATE	3. REPORT TYPE AND DATES COVERED
	December 1997	Dissertation July 95 - December 97

4. TITLE AND SUBTITLE
Microelectromechanical Optical Beam Steering Systems

5. FUNDING NUMBERS

6. AUTHOR(S)
David M. Burns

7. PERFORMING ORGANIZATION NAME(S) AND ADDRESS(ES)
Air Force Institute of Technology
Wright Patterson AFB, OH 45433

8. PERFORMING ORGANIZATION REPORT NUMBER
AFIT/DS/ENG/98-01

9. SPONSORING/MONITORING AGENCY NAME(S) AND ADDRESS(ES)
Edward A. Watson, Ph.D.
Jeffrey W. Grantham, Ph.D.
Air Force Research Laboratory
AFRL/AAJT
WPAFB, OH 45433

10. SPONSORING/MONITORING AGENCY REPORT NUMBER

11. SUPPLEMENTARY NOTES

12a. DISTRIBUTION AVAILABILITY STATEMENT
Approved for public release; distribution unlimited

12b. DISTRIBUTION CODE

13. ABSTRACT *(Maximum 200 words)*

The development of microelectromechanical systems (MEMS) has matured to the point where the fabrication of micron-sized devices is feasible. State-of-the-art MEMS construction processes now support the fabrication of novel optical devices that could not previously be built. This dissertation reports on the development of innovative micro-optical devices such as Variable Blaze Gratings (VBGs) using state-of-the-art MEMS construction processes. The principle application of the micro-optical devices described in this dissertation is steering optical beams; however other applications such as spectral analysis are identified. Specific optical beam steering systems developed and characterized in this work include: optical phased arrays, VBGs, decentered microlens arrays, and integrated Vertical Cavity Surface Emitting Laser (VCSEL) micromirror systems. Optical power induced damage to micromachined mirrors is also modeled and tested. In addition a number of new MEMS devices were created during this research including: double hot arm thermal actuators, optical hybrid devices such as variable blaze phased arrays and focusing micromirrors, and nonlinear flexures. Extensive Fourier analysis and optical testing of the micro-optical devices was used to verify device operation.

14. SUBJECT TERMS
Microelectromechanical Systems, Micromachining, Optical Beam Steering, Gratings, Mirrors

15. NUMBER OF PAGES
320

16. PRICE CODE

17. SECURITY CLASSIFICATION OF REPORT	18. SECURITY CLASSIFICATION OF THIS PAGE	19. SECURITY CLASSIFICATION OF ABSTRACT	20. LIMITATION OF ABSTRACT
Unclassified	Unclassified	Unclassified	UL

Standard Form 298 (Rev. 2-89) (EG)
Prescribed by ANSI Std. 239.18
Designed using Perform Pro, WHS/DIOR, Oct 94